TRANSPORT PROPERTIES OF LOW-DIMENSIONAL QUANTUM SPIN SYSTEMS

Von der Gemeinsamen Naturwissenschaftlichen Fakultät
der Technischen Universität Carolo-Wilhelmina
zu Braunschweig

zur Erlangung des Grades eines
Doktors der Naturwissenschaften
(Dr. rer. nat.)

genehmigte

DISSERTATION

von

FABIAN HEIDRICH-MEISNER

aus Hannover

1. Referent: Prof. Dr. W. Brenig
2. Referent: Prof. Dr. D. C. Cabra
Eingereicht am: 13.12.2004
Mündliche Prüfung (Disputation) am: 18.03.2005
2005 (Druckjahr)

TRANSPORT PROPERTIES OF LOW-DIMENSIONAL QUANTUM SPIN SYSTEMS

Von der Gemeinsamen Naturwissenschaftlichen Fakultät
der Technischen Universität Carolo-Wilhelmina
zu Braunschweig

zur Erlangung des Grades eines
Doktors der Naturwissenschaften
(Dr. rer. nat.)

genehmigte

DISSERTATION

von

FABIAN HEIDRICH-MEISNER

aus Hannover

Vorveröffentlichungen der Dissertation

Teilergebnisse aus dieser Arbeit wurden mit Genehmigung der Gemeinsamen Naturwissenschaftlichen Fakultät, vertreten durch den Mentor der Arbeit, in folgenden Beiträgen vorab veröffentlicht:

Publikationen

i. F. Heidrich-Meisner, A. Honecker, D.C. Cabra und W. Brenig:
Thermal conductivity of anisotropic and frustrated spin-1/2 chains,
Phys. Rev. B **66**, 140406(R) (2002).

ii. C. Hess, B. Büchner, U. Ammerahl, L. Colonescu, F. Heidrich-Meisner, W. Brenig und A. Revcolevschi:
Magnon Heat Transport in doped La_2CuO_4,
Phys. Rev. Lett. **90**, 197002 (2003).

iii. F. Heidrich-Meisner, A. Honecker, D.C. Cabra und W. Brenig:
Zero-frequency transport properties of one-dimensional spin-1/2 systems,
Phys. Rev. B **68**, 134436 (2003).

iv. F. Heidrich-Meisner, A. Honecker, D.C. Cabra und W. Brenig:
Comment on "Anomalous thermal conductivity of frustrated Heisenberg spin chains and ladders",
Phys. Rev. Lett. **92**, 069703 (2004).

v. F. Heidrich-Meisner, A. Honecker, D.C. Cabra und W. Brenig:
Transport in dimerized and frustrated spin systems,
Verhandlungen der *International Conference on Magnetism and Magnetic Materials*, Rom 2003.
J. Mag. Mag. Mat. **272-276**, 890-891 (2004).

vi. M. Arlego, W. Brenig, D.C. Cabra, F. Heidrich-Meisner, A. Honecker und G. Rossini:
Bond-impurity induced bound states in disordered spin-1/2 spin ladders,
Phys. Rev. B **70**, 014436 (2004).

vii. M. Arlego, W. Brenig, D.C. Cabra, F. Heidrich-Meisner, A. Honecker und G. Rossini:
Bound states in weakly disordered spin ladders,
Verhandlungen der *International Conference on Strongly Correlated Electron Systems*, Karlsruhe 2004.
Zur Veröffentlichung angenommen bei Physica B; Preprint cond-mat/0411751.

viii. F. Heidrich-Meisner, A. Honecker, D.C. Cabra und W. Brenig:
Thermal conductivity of one-dimensional spin-1/2 systems,
Verhandlungen der *International Conference on Strongly Correlated Electron Systems*, Karlsruhe 2004.
Zur Veröffentlichung angenommen bei Physica B; Preprint cond-mat/0406378.

ix. F. Heidrich-Meisner, A. Honecker und W. Brenig:
Thermal conductivity of the XXZ model in a magnetic field,
Eingereicht bei Phys. Rev. B, Preprint cond-mat/0408529.

Tagungsbeiträge

1. F. Heidrich-Meisner, A. Honecker, W. Brenig, C. Hess und B. Büchner:
Thermische Leitfähigkeit niedrigdimensionaler Spin-1/2 Systeme,
Poster, DPG Frühjahrstagung, 11.3.–15.3.2002, Regensburg.

2. F. Heidrich-Meisner, A. Honecker, D.C. Cabra und W. Brenig:
Transporteigenschaften eindimensionaler Spin-1/2-Systeme,
Poster, Korrelationstage (Workshop), 24.2.–28.2.2003, Dresden.

3. F. Heidrich-Meisner, A. Honecker, D.C. Cabra und W. Brenig:
Heat and spin transport in one-dimensional spin-1/2 systems,
Poster, DPG Frühjahrstagung, 24.3.–28.3.2003, Dresden.

4. F. Heidrich-Meisner, A. Honecker, D.C. Cabra und W. Brenig:
Transport in dimerized und frustrated spin systems,
Poster, *International Conference on Magnetism and Magnetic Materials*, 27.7.–1.8.2003, Rom, Italien.

5. F. Heidrich-Meisner, A. Honecker und W. Brenig:
Thermal transport of one-dimensional spin systems in the presence of a magnetic field,
Poster, DPG Frühjahrstagung 8.3.–12.3.2004, Regensburg.

6. M. Arlego, W. Brenig, D.C. Cabra, F. Heidrich-Meisner, A. Honecker und G. Rossini:
Bound states in weakly disordered spin ladders,
Poster, *International Conference on Strongly Correlated Electron Systems*, 26.7.–30.7.2004, Karlsruhe.

7. F. Heidrich-Meisner, A. Honecker, D.C. Cabra und W. Brenig:
Thermal conductivity of one-dimensional spin-1/2 systems,
Poster, *International Conference on Strongly Correlated Electron Systems*, 26.7.–30.7.2004, Karlsruhe.

Contents

Satz: $\LaTeX2_\varepsilon$

Chapter 1

Introduction

Among the techniques to investigate the properties of condensed matter, transport experiments are particularly interesting as they probe a stationary, but non-equilibrium state in contrast to thermodynamic quantities, which characterize the equilibrium. Measuring the transport coefficients such as the electrical or the thermal conductivity provides for valuable information about the dynamical properties and the interactions of quasi-particles. Probably most prominent, the transition from the normal to the superconducting state of superconducting materials is signaled by a sharp drop of the electrical resistivity [1].

In most insulating materials heat is mainly carried by phonons, i.e., the excitations of the crystal lattice. In metals, charge carriers dominate the heat conduction. Recent experiments on *low-dimensional* magnetic insulators [ii, 2–15] have given strong evidence for the presence of a third channel for heat transport, namely a contribution of *magnetic* excitations. This thesis studies the transport properties of low-dimensional quantum spin models, including transport of spin or magnetization and heat transport. Numerous contributions have been made to this active field of theoretical research both for classical as well as for quantum mechanical systems. For recent reviews, see Refs. [16] and [17], respectively.

The field of low-dimensional magnetism with small spins has attracted the interest of many researchers for a number of reasons. First, in contrast to magnetic systems with classical long-ranged ferro- or antiferromagnetic order, novel ground state properties arise due to the existence of strong quantum fluctuations in reduced dimensions. Therefore, the term *quantum magnetism* is commonly in use for this field of research. In one dimension (1D), where quantum fluctuations are particularly strong, antiferromagnetic order is often suppressed even at zero temperature, but rather so-called spin liquid states are favored [18–21]. Prominent examples are dimerized chains and spin ladders. Second and in particular for one-dimensional systems, many powerful numerical and analytical techniques have been developed, including on the one hand, Density-Matrix-Renormalization-Group methods (DMRG) [22], Quantum-Monte-Carlo simulations (QMC) [23,24], and exact diagonalization (ED) [25], and on the other hand, the Bethe ansatz for integrable models [26] and field-theoretical approaches such as bosonization (see Ref. [27] for a review and references therein). Third, the successful preparation of materials that are good realizations of quasi two- or one-dimensional quantum magnets have rendered possible a fruitful interplay between theory and experiment [18–20, 28, 29]. Finally, the prototype model of quantum magnetism, the Heisenberg model on different topologies, is the effective model that describes low-energy degrees of freedom of correlated electron systems at half filling, i.e., with an average density of one electron per site (see, e.g., Refs. [30, 31]). For instance, the magnetic and electronic properties of the parent compounds of most high-temperature cuprate superconductors [32] are inherent to the CuO_2 planes where each Cu-ion carries a spin-1/2 moment [33, 34]. A typical example is La_2CuO_4. At half filling and due to Coulomb correlations, such systems are insulating, and the low-energy degrees of freedom are magnetic excitations.

In fact, most of the materials for which experimental evidence for magnon thermal conductivity[1] has recently been established belong to the class of cuprates. The most prominent examples are the so-called "telephone-number" compounds (Sr,Ca,La)$_{14}$Cu$_{24}$O$_{41}$ [6–11], the spin chain materials SrCuO$_2$ and Sr$_2$CuO$_3$ [12, 13], and the quasi two-dimensional antiferromagnet La$_2$CuO$_4$ [ii, 2, 3]. In all these cases, the physics of the CuO$_2$ planes dominates the electronic and magnetic properties, with the difference that in (Sr,Ca,La)$_{14}$Cu$_{24}$O$_{41}$ spin chains and two-leg ladders are realized [35], SrCuO$_2$ and Sr$_2$CuO$_3$ contain spin chains, while the magnetism of La$_2$CuO$_4$ is two-dimensional [34].

Historically, magnon thermal conductivity was suggested to be observable at very low temperatures in para- and ferromagnetic insulators [36, 37]. First theoretical publications mostly addressed heat conduction in ferromagnets and within spin-wave theory, and both one [38–41] and higher dimensions [42–50] were studied. Experimentally, magnon thermal conductivity was discussed already long ago for three dimensional magnetic materials such as yttrium (see, e.g., Refs. [46, 51, 52]) as a feature at very low temperatures close to 1 K and also for the spin chain material KCuF$_3$ [53]. The surprising result of the more recent transport experiments is that magnetic excitations do not only contribute to the thermal current, but that such contributions can exceed the heat transport via phonons even at elevated temperatures. This is particularly obvious in the case of (Sr,Ca,La)$_{14}$Cu$_{24}$O$_{41}$ [7, 8], where the magnetic contribution to the thermal conductivity is of the order of 100 WK^{-1}m^{-1} [8] at room temperature. Using phenomenological expressions, many authors have analyzed the experimental data finding surprisingly large values for the mean-free paths of magnetic excitations of the one-dimensional compounds [7, 8, 12–14]. For instance, mean-free paths of several hundred lattice constants have been reported for (Sr,Ca,La)$_{14}$Cu$_{24}$O$_{41}$ [7, 8]. This observation has stimulated an active theoretical discussion about possible ballistic thermal transport in the spin models describing the magnetic properties of these compounds [54–59].

The model systems that are studied in this thesis are motivated by the experimental results, and they include the spin-1/2 XXZ chain, which is a spin chain with nearest neighbor interactions and an exchange anisotropy, the two-leg spin ladders as well as dimerized and frustrated chains. If not stated otherwise, antiferromagnetic interactions are considered. For the interpretation of experiments, one is interested in all possible types of scattering mechanisms, including interactions of the magnetic subsystem with phonons or impurities. In this work, the main focus is on transport properties of pure spin systems. Furthermore, most results are obtained for translationally invariant models, but the influence of bond disorder in spin chains and ladders is also discussed in two examples.

The models are different with respect to several aspects such as ground state properties or elementary excitations, which will be detailed in the following chapters. In this introduction, we emphasize the influence of integrability on transport. The spin-1/2 XXZ chain is an integrable model, which implies that infinitely many conserved quantities are known. A pragmatic definition of integrability in one dimension is that the model is in principle solvable along the lines of the Bethe ansatz [26]. Additional interactions as well as spatial variation of the interactions inducing frustration or dimerization break the integrability. An important line of research is the comparative study of transport properties of integrable in contrast to

---

[1] In this work, the term *magnon thermal conductivity* is used as a general expression to refer to heat transport mediated by magnetic excitations.

nonintegrable systems, since it has been conjectured that integrable systems exhibit ballistic transport [60, 61] within linear response theory [62, 63]. In linear response theory, the transport coefficients are expressed through current-current correlation functions computed in an equilibrium ensemble. Linear response theory is the conceptual framework on which this thesis is based.

A more precise definition of ballistic transport can be given by introducing the Drude weight. To this end, one considers the frequency dependence of the conductivity, denoted by $\sigma(\omega)$. The real part of the conductivity $\sigma(\omega)$ is usually decomposed into a part which is singular at zero frequency $\omega = 0$ and a second part $\sigma_{\text{reg}}(\omega)$ which is regular in the zero-frequency limit and thus called the regular part of $\sigma(\omega)$:

$$\operatorname{Re}\sigma(\omega) = D(T)\delta(\omega) + \sigma_{\text{reg}}(\omega)\,. \tag{1.1}$$

The prefactor $D(T)$ of the delta-function $\delta(\omega)$ is the so-called *Drude weight* and it measures the conserved part of the current. Originally, the Drude weight was introduced by Kohn [64] for zero temperature to characterize an ideal conductor. A finite Drude weight obviously gives rise to a diverging zero-frequency conductivity. The physical reason for finite Drude weights is the existence of conservation laws that prevent the current from decaying (see, e.g., Ref. [61]). A trivial example for systems that possess a finite Drude weight are free particles, for which the particle- and the energy-current operators commute with the Hamiltonian. However, a nonzero Drude weight can also exist in interacting systems such as the one-dimensional Hubbard model (see Ref. [17] and references therein). The Drude weight and the regular part of the spin and the thermal conductivity are the quantities that are analyzed in this work by means of exact diagonalization, mean-field theory, and bosonization.

Frequently, the term ballistic transport is used to describe an experimental situation in which mean-free paths of quasi-particles are larger than sample dimensions. This is different form the definition used in this work, since a finite Drude weight implies an infinite current life-time. Using a phenomenological ansatz to identify the life-time of the current with that of the quasi-particles which carry the current, this diverging life-time translates into infinitely large mean-free paths.

To conclude this introduction, the structure of the thesis and the main results are outlined. In Chapter 2, the basics of transport theory within the framework of linear response theory are summarized. The transport coefficients and expressions for the Drude weight are introduced. Furthermore, the relation of transport and conservation laws as well as the difference between ballistic and diffusive transport are discussed. Chapters 4–6 also contain the expressions for the quantities that are evaluated. Thus, a reader acquainted with the terminology of linear response theory may skip Chapter 2 and can read the following chapters independently.

Chapter 3 provides a survey of experiments for the thermal conductivity of low-dimensional materials. The discussion concentrates on quasi low-dimensional materials, in which magnon thermal conductivity typically dominates at temperatures of the order of several 10 K or even at room temperature. From the experimental point of view, magnon thermal conductivity is best established for $(\mathrm{Sr,Ca,La})_{14}\mathrm{Cu}_{24}\mathrm{O}_{41}$, SrCuO_2, $\mathrm{Sr}_2\mathrm{CuO}_3$, and $\mathrm{La}_2\mathrm{CuO}_4$. Further materials with interesting thermal transport properties such as CuGeO_3 [65–69] and $\mathrm{SrCu}_2(\mathrm{BO}_3)_2$ [69, 70] are briefly discussed. In extension of previous work [8, 71, 72] and as one part of the results of this thesis, the experimental results for Zn-doped $\mathrm{La}_2\mathrm{CuO}_4$ [71] are analyzed using an equation of Boltzmann-type in Sec. 3.4. For the sake of easy reference, theoretical results relevant for the thermal conductivity of the materials mentioned above are reviewed in this chapter in order to describe the emerging picture.

Chapters 4, 5, and 6 contain the main results of this thesis for transport properties of quasi one-dimensional spin systems. The results are divided into three groups: first, the integrable spin-1/2 XXZ chain, exhibiting ballistic transport properties; second, the nonintegrable, but translationally invariant spin systems such as spin ladders, dimerized and frustrated chains and third, bond-disordered systems, namely XY chains with off-diagonal disorder and bond-disordered two-leg ladders. In the case of the XXZ chain, which has finite Drude weights in a large part of its parameter space spanned by exchange anisotropy and magnetic field, the dependence of the Drude weights on temperature, magnetic field, and parameters of the model is investigated. For the nonintegrable models, the main conclusion is that the Drude weights vanish in the thermodynamic limit, indicating normal transport properties.

A theory for spin transport of one-dimensional systems such as the Heisenberg chain or the Hubbard model is a long-standing problem (see, e.g., the reviews presented in Refs. [17, 73]), with strong efforts devoted to transport in the integrable spin-1/2 XXZ chain. The latter is the subject of Chapter 4. The intriguing property of the spin-1/2 XXZ chain is that the energy-current operator is a conserved quantity [61, 74]. While this directly leads to a diverging thermal conductivity, is has also been conjectured that spin transport is anomalous [61], although the corresponding spin-current operator does in general not commute with the Hamiltonian. However, many issues are still unsolved, including the question whether the Drude weight for spin transport is nonzero or not at finite temperatures for the spin-1/2 Heisenberg chain. The spin-1/2 Heisenberg chain is a special case of the XXZ chain which has $SU(2)$ symmetry. The crucial point is that on the one hand, no proof for a finite spin Drude weight at zero magnetic field has been found so far, and on the other hand, despite the integrability of this model, even different Bethe ansatz approaches yield inconsistent results for the spin Drude weight [75–77]. This calls for complementary methods such as exact diagonalization, which is restricted to finite systems, but not biased by approximations.

The XXZ chain has several different ground state regimes, depending on the anisotropy and the magnetic field. There is a gapless phase, a ferromagnetic, and an antiferromagnetic phase, and in the latter cases, a gap exists in the excitation spectrum. In Chapter 4, it is first shown how the Drude weights in the gapless phase can be computed to leading order in temperature using conformal invariance. The results for zero magnetic field reproduce those of Refs. [78–80]. Next, a mean-field theory based on the Jordan-Wigner representation of spin-1/2 operators [81] is used to compute the Drude weights at finite temperatures for zero and finite magnetic fields. This approach, though approximative, agrees well with exact results for the thermal Drude weight in the gapless phase at zero magnetic field [78]. Several expressions are derived for the low-temperature limit at finite magnetic fields. In addition, exact diagonalization is used to compute the thermal Drude weight as a function of anisotropy, temperature, and magnetic field. The comparison with analytically exact results [78, 82] establishes the applicability of the numerical approach. Regarding spin transport at zero magnetic field, the numerical results confirm that the spin Drude weight is finite in the gapless phase at zero magnetic field, which is in agreement with Refs. [75, 83–90]. This includes the $SU(2)$-symmetric case, i.e., the Heisenberg chain. Furthermore, the temperature dependence of the spin Drude weight is discussed and compared to the results of other authors. Finally, preliminary numerical results for the magnetothermal response of the Heisenberg chain are shown. This effect has recently also been studied by QMC simulations combined with exact diagonalization [91] and analytically [92].

Integrability can be broken by either adding interactions with external degrees of freedom such as phonons or impurities to the Hamiltonian, or by adding additional intrinsic interactions such as next-nearest neighbor interactions. The subject of transport in nonintegrable models is covered in Chapter 5, including spin-1/2 systems such as the frustrated chain, the dimerized chain, and the two-leg spin ladder. These models are also relevant for the interpretation of several experiments [7–9].

Many authors have studied the influence of integrability-breaking terms on transport properties [60, 83–88, 93–95]. A conjecture by Zotos and coworkers [83] states that in general, a vanishing Drude weight for either type of transport can be expected for nonintegrable systems at finite temperatures.

Regarding thermal transport, the large thermal conductivities observed for the compounds (Sr,Ca,La)$_{14}$Cu$_{24}$O$_{41}$ have stimulated speculations about dissipationless thermal transport in spin ladders and other nonintegrable systems [54–58]. The results of a first numerical study of the thermal Drude weight of spin ladders and frustrated chains have been interpreted in favor of a finite thermal Drude weight for these systems [54, 58]. Based on the conclusion of this numerical study, effective low-energy theories have been used to investigate the thermal Drude weight of nonintegrable one-dimensional spin systems analytically [55, 56]. Subsequent numerical studies including this thesis, however, arrive at the opposite conclusion of a vanishing Drude weight [57, 96], which can also be corroborated from the point of view of bosonization [59, 95, 97].

In Chapter 5, bosonization is used to argue that generically, vanishing Drude weights are expected. The conclusion of vanishing Drude weights is confirmed by an extensive numerical study of spin and thermal transport for system sizes of up to twenty sites. This also pertains to the frequency dependence of the thermal conductivity. In the high-temperature limit, the dc-conductivity can reliably be extracted from the numerical results. Consequences for the interpretation of recent experiments are discussed for spin ladders.

Finally, interesting physics arises in the presence of impurities. Two cases are studied in Chapter 6: disordered XY chains and bond disorder in two-leg ladders. Bond disorder connotes a random distribution of the magnetic exchange couplings in the Hamiltonian.

XY chains, with or without disorder, correspond to noninteracting spinless lattice fermions. Disorder, as a perturbation, leads to vanishing Drude weights even for a noninteracting system. Thus the focus is on the frequency dependence of the regular part of the thermal and the spin conductivity. First results for the spin conductivity and the thermal conductivity of XY chains are presented for several types of disorder. Large systems of the order of 10^4 sites can be diagonalized numerically since the model is noninteracting.

While the main objective of this work is the theory of transport properties, the final part mainly deals with impurity-induced bound states in two-leg spin ladders. This is of interest, since bond disorder can easily be induced by defects in real materials. Using a mapping on bond-boson operators [98] and applying a projection onto the one particle subspace, it is shown that mid-gap states appear both for diagonal and off-diagonal disorder. The comparison with numerical impurity-averaging reveals that the results obtained in the strong-coupling limit are qualitatively correct in a wide parameter range. For finite concentrations of impurities, diagrammatic techniques are available to compute the density of states of the elementary triplet excitations. The analytical and the numerical results for large systems are in excellent agreement. Possible extensions of this study are discussed, including transport in disordered spin ladders and spectral properties of three-dimensional dimer systems.

The results of this work are summarized in Chapter 7. Open issues and future projects regarding transport in low-dimensional spin systems are outlined.

CHAPTER 2

Transport coefficients

In this chapter, transport theory within the framework of linear response theory is introduced. Thus, Kubo-formulae are used to describe both spin and thermal transport. It is not the purpose of this chapter to derive the expressions for the transport coefficients since this is discussed at length in textbooks. Rather, the chapter lists the quantities that are studied in this thesis, provides for a qualitative discussion, and it serves to fix the notation. A reader acquainted with transport theory may directly continue with Chapter 3 and can use this chapter for easy reference to the equations. The presentation follows Ref. [62] where the theory for transport coefficients in the zero-frequency limit is based on Luttinger's work [99].

2.1 Overview

Alternative approaches

In this thesis, transport is described within linear response theory. Other approaches to study transport properties of quantum spin systems have also been pursued in the literature. For instance, numerical simulations of stationary non-equilibrium states have recently been performed for thermal transport by coupling a finite number of spins to external heat baths [100–104]. The coupling to the external baths is modeled through master-equations. In such theories, interesting questions arise; for instance, the proper definition of temperature on the nanoscale has been debated [104–107]. Also, it is not a priori clear under which conditions a linear gradient in temperature results when a system is coupled to external baths. Furthermore the relation between temperature and internal energy does not necessarily have to be linear. So far, the connection between these approaches and Kubo-type of expressions has not yet been fully elucidated for quantum systems. On the contrary, the understanding of classical systems such as chains of oscillators is further developed. For a review of theoretical work done for thermal transport of classical systems, see Ref. [16].[1]

Another theoretical concept to study transport is the Landauer-Büttiker formalism, which is often used for mesoscopic systems. For instance, magnetization transport of Heisenberg chains of finite length was analyzed in Ref. [120] along the lines of this theory. An introduction and further details can be found in textbooks [121].

The structure of this chapter is the following. In Sec. 2.2, the main concepts as well as the quantities to be studied are introduced, providing the reader with the necessary framework to proceed with the following chapters. This pertains to the relevant correlation functions used

---

[1] For more recent publications on heat transport in classical systems, see Refs. [108–119].

in linear response theory and the definition of the Drude weight. In addition, the appropriate definition of current operators for spin systems is discussed in Sec. 2.2.2. Further details, such as some derivations of specific formulae used for the Drude weights, are deferred to Sec. 2.2.3. Section 2.3 contains a brief discussion of the relation between transport and conservation laws, surveying theoretical concepts that can be found in the literature. For instance, the terms ballistic and diffusive transport are often used to interpret transport experiments. These concepts are introduced in Sec. 2.3.3. For recent reviews on transport properties of low-dimensional quantum systems, the reader may also wish to consult Refs. [17, 73].

A prototype spin Hamiltonian and the Jordan-Wigner transformation

In principle, the transport theory to be outlined in Sec. 2.2 is general and not restricted to specific models. However, we prefer to introduce a spin Hamiltonian which allows us to discuss the transport coefficients with perspective to spin models. In addition, spin-1/2 models can equivalently represented as systems of interacting spinless fermions, which is possible due to the famous Jordan-Wigner transformation [81]. Therefore, an innate analogy exists between spin transport of our spin models on the one hand and particle transport of fermions on the other hand. Extensive use of these equivalent pictures will be made throughout this thesis.

A generic model for the systems studied in Chapters 4, 5, and 6 is a spin-1/2 Heisenberg Hamiltonian on a chain of N spins with antiferromagnetic interactions, i.e., $J_{lj} > 0$, an additional exchange anisotropy, a Zeeman term, and periodic boundary conditions:[2]

$$H = \sum_{l=1}^{N} H_l = \sum_{l=1}^{N} \sum_{j=1}^{r_0} J_{lj} \left[\frac{1}{2} \left(S_l^+ S_{l+j}^- + \text{h.c.} \right) + \Delta S_l^z S_{l+j}^z \right] - h \sum_{l=1}^{N} S_l^z \, . \tag{2.1}$$

N denotes the number of sites, h is the magnetic field, and S_l^μ, $\mu = x, y, z$, is the μ-component of a spin-1/2 operator acting on site l. As usual, $S_l^\pm = S_l^x \pm i S_l^y$ is the spin raising(lowering) operator. The first sum runs over all sites l, and the second over all spins for which the coupling constants $J_{lj} = J(|l-j|)$ are nonzero. The couplings are assumed to be nonzero for $|l-j| \leq r_0$. The exchange anisotropy is denoted by Δ. Equation (2.1) implicitly specifies a choice for the local energy density H_l.

The Hamiltonian (2.1) includes the spin-1/2 XXZ chain ($r_0 = 1$) and the frustrated chain ($r_0 = 2$). In Chapters 4, 5, and 6, at most $r_0 = 2$ will be studied.

Via the Jordan-Wigner transformation [81], the Hamiltonian (2.1) is equivalent to a system of one-dimensional interacting spinless fermions. Here, the Hamiltonian in terms of Jordan-Wigner fermions is given for the case of the dimerized and frustrated Heisenberg chain [$r_0 = 2$ in Eq. (2.1)]. For this limiting case of (2.1), which is studied in Chapters 4 and 5, we introduce the notation $J_l = J_{l1}$ and $\alpha J = J_{l2}$. The index l runs over the sites of spins. Dimerization is introduced through an alternation of the nearest neighbor interaction $J_l = \lambda_l J$, where $\lambda_l = 1$ for l even and $\lambda_l = \lambda$ for l odd. A nonzero α causes frustration. The free parameters of the dimerized and frustrated chain are thus λ, α, and Δ since J can be set to unity.

Expressing the spin operators in terms of Jordan-Wigner fermions gives [81]:

$$S_l^z = c_l^\dagger c_l - \frac{1}{2}; \quad S_l^+ = e^{i\pi\Phi_l} c_l^\dagger \tag{2.2}$$

---

[2] If not stated otherwise, constants such as Plancks's quantum $\hbar$, the Boltzmann constant k_B, Bohr's magneton μ_B, or the elementary charge e are set to unity throughout this work.

with

$$\{c_l\,, c_j^\dagger\} = \delta_{lj}\,. \tag{2.3}$$

$c_l^{(\dagger)}$ destroys(creates) a spinless fermion on site l. $\{.,.\}$ is the anti-commutator. The string-operator Φ_l in Eq. (2.2) is defined by

$$\Phi_l = \sum_{i=1}^{l-1} n_i\,, \tag{2.4}$$

where $n_i = c_i^\dagger c_i$. In terms of spinless fermions, the Hamiltonian reads (see, e.g., Ref. [122]):

$$\begin{aligned} H &= J\sum_{l=1}^{N}\Big[\frac{1}{2}\lambda_l\left\{(c_l^\dagger c_{l+1} + \text{H.c.}) + \Delta(\,c_l^\dagger c_l c_{l+1}^\dagger c_{l+1} - c_l^\dagger c_l + \frac{1}{4})\right\} \\ &\quad +\alpha\{\frac{1}{2}(c_l^\dagger c_{l+2} + \text{H.c.})(1 - c_{l+1}^\dagger c_{l+1}) + \Delta(c_l^\dagger c_l c_{l+2}^\dagger c_{l+2} - c_l^\dagger c_l + \frac{1}{4})\}\Big] \\ &\quad -h\sum_{l=1}^{N} n_l + h\frac{N}{2}\,. \end{aligned} \tag{2.5}$$

Obviously, the magnetic field h acts as a chemical potential for the fermions. In the case of vanishing anisotropy $\Delta = 0$, zero frustration $\alpha = 0$, and no dimerization $\lambda = 1$, (2.5) is a free-fermion model with a nearest neighbor hopping matrix element $t = J/2$. This limiting case is called XY model and its Hamiltonian is diagonal in a momentum-space representation

$$H = \sum_k \epsilon_k c_k^\dagger c_k \tag{2.6}$$

with a cosine band $\epsilon_k = -J\cos(k) - h$, where k is the wavenumber.

2.2 Linear response theory

2.2.1 The regular part and the Drude weights

In this thesis the focus is on transport of heat and spin mediated via magnetic excitations of a typical Heisenberg spin Hamiltonian (2.1). As is obvious from the Jordan-Wigner representation in Eq. (2.5), this can equivalently be viewed as particle and heat transport of spinless fermions. The following equations are not restricted to either one dimension or transport of magnetic systems, but are more generally valid.

Within linear response theory, the spin and the thermal current are related to the gradients ∇h and ∇T of the magnetic field h and the temperature T, respectively, by [62]:

$$\begin{pmatrix} \mathcal{J}_1 \\ \mathcal{J}_2 \end{pmatrix} = \begin{pmatrix} L_{11} & L_{12} \\ L_{21} & L_{22} \end{pmatrix} \begin{pmatrix} \nabla h \\ -\nabla T \end{pmatrix}. \tag{2.7}$$

Here, $\mathcal{J}_i = \langle j_i \rangle$ denotes the thermodynamic expectation value of the current operator j_i taken in the non-equilibrium state and $X_1 = \nabla h$ and $X_2 = \nabla T$ act as external forces X_i $(i = 1, 2)$.[3]

---

[3] Strictly speaking, the forces involve additional factors of T^{-1} [62], which are, however, absorbed in the definition of the coefficients L_{ij} in the present notation.

j_1 is the spin(particle)-current operator and j_2 the thermal current operator, respectively. L_{ij} denote the transport coefficients. For spin models, off-diagonal elements are only nonzero in finite magnetic fields, since $L_{12} = L_{21} = 0$ for $h = 0$ due to particle-hole symmetry [61].

The choice for the current operators and the corresponding forces X_i is ambiguous. As a criterion, the positivity of the net-entropy production is often used [62]:

$$\frac{\partial \mathcal{S}}{\partial t} = \sum_i \mathcal{J}_i X_i > 0 \,. \tag{2.8}$$

In this equation, $\mathcal{S}$ denotes the entropy and t is the time variable.

The currents fulfill equations of continuity, relating the local currents to the magnetization density and the energy density, respectively. Let us consider the example of free particles, i.e., Eq. (2.6), for which the definition of current operators is intuitive. At zero magnetic field $h = 0$, the particle-current operator j_s is given by [62,123]

$$j_\mathrm{s} = \sum_k v_k n_k \tag{2.9}$$

while the energy-current operator j_th reads

$$j_\mathrm{th} = \sum_k \epsilon_k v_k n_k \,. \tag{2.10}$$

Here, $v_k = \partial_k \epsilon_k$ is the velocity, ϵ_k is the one-particle dispersion, and $n_k = c_k^\dagger c_k$. For the case of a vanishing magnetic field (or zero chemical potential for the spinless fermions), the energy current is equal to the thermal current, and we will therefore use both expressions synonymously.

Given the external forces ∇h and ∇T as well as a finite external field, the corresponding current operators are

$$j_1 = j_s; \quad j_2 = j_\mathrm{th} - h j_s \,. \tag{2.11}$$

Hence, in a finite magnetic field, the thermal current is not simply equal to the energy-current $\mathcal{J}_\mathrm{th} = \langle j_\mathrm{th} \rangle$ [124].[4] For free particles, the thermal current is [62]:

$$j_2 = \sum_k (\epsilon_k - h) v_k n_k \,. \tag{2.12}$$

A different choice of currents that fulfill (2.8) is the pair $\mathcal{J}_\mathrm{s} = \langle j_\mathrm{s} \rangle$ and $\mathcal{J}_\mathrm{th} = \langle j_\mathrm{th} \rangle$. These currents correspond to the pair of forces $-\nabla(-h/T)$ and $\nabla(1/T)$ [62]. The derivation of the currents for a given spin model will be discussed in more detail in Sec. 2.2.2. For some of the cases we are interested in, the actual choice for the currents does not matter. For instance, the final result for the thermal conductivity in finite magnetic fields is the same for both pairs of currents.

---

[4] Frequently, j_th is denoted by j_E to emphasize that this operator describes transport of energy. We refrain from this notation to keep the consistency with Refs. [i, iii, iv, v, viii, ix].

Relation to experiments

The coefficients appearing in the transport matrix of Eq. (2.7) can be related to experimentally accessible quantities. First of all, the spin conductivity σ, measured under the condition of $\nabla T = 0$, is equal to the first entry in Eq. (2.7), i.e.,

$$\sigma = L_{11}\,. \tag{2.13}$$

The thermal conductivity κ is usually measured under the condition of zero particle flow, i.e.,

$$\mathcal{J}_1 = \langle j_1 \rangle = 0\,. \tag{2.14}$$

Since the thermal conductivity is defined as

$$\mathcal{J}_2 = -\kappa \nabla T\,, \tag{2.15}$$

one arrives at:

$$\kappa = L_{22} - \frac{1}{T}\frac{L_{21}^2}{L_{11}}\,. \tag{2.16}$$

In zero magnetic field, corresponding to a vanishing chemical potential in the particle picture, this reduces to

$$\kappa = L_{22}\,. \tag{2.17}$$

The second term in Eq. (2.16) arises from the coupling of the thermal current operator j_2 to the spin-current operator j_1, which is linear in the magnetic field h; see Eq. (2.11). This effect is analogous to what happens in metals where a particle current with opposite sign to the electrical currents ensures the condition (2.14). This second contribution will be referred to as the magnetothermal correction. It is often neglected in the case of electrons since it is usually much smaller than L_{22} [123].

The off-diagonal elements can also be related to certain experimental situations, now assuming the presence of a static external magnetic field. Imposing the condition $\mathcal{J}_1 = 0$ and applying a thermal gradient, a gradient ∇h of the magnetic field results:

$$\nabla h = S\,\nabla T; \quad S = \frac{L_{12}}{L_{11}}\,. \tag{2.18}$$

This is the analog to the Seebeck effect for charge carriers, and the constant of proportionality S is called magnetic thermopower, imitating the terminology used for charge carriers.

Finally, also the Peltier effect has its counterpart for magnetic systems. Under the condition of $\nabla T = 0$, the application of a spin current drives a thermal current with

$$\mathcal{J}_2 = \Pi\,\mathcal{J}_1; \quad \Pi = \frac{L_{21}}{L_{11}}\,. \tag{2.19}$$

The coefficients Π and S are not independent but connected via the Onsager relation:

$$\Pi = TS\,. \tag{2.20}$$

For a discussion of magnetothermal effects in spin-1/2 Heisenberg chains, see Refs. [86,91,92] and in the one-dimensional Hubbard model, see Ref. [125].

Transport coefficients and current-current correlation functions

The transport coefficients L_{ij} are related to correlation functions. At finite frequencies ω, the coefficients $L_{ij}(\omega)$ depend on the time-dependent current-current correlation functions via [62]

$$L_{ij}(\omega) = \frac{\beta^r}{N} \int_0^\infty dt\, e^{i(-\omega+i0^+)t} \int_0^\beta d\tau \langle j_i\, j_j(t+i\tau)\rangle_{\text{eq}}\,. \tag{2.21}$$

For a derivation of this equation, see Refs. [79, 126, 127]. In this equation and in Eqs. (2.23) and (2.24), $r = 0$ for $j = 1$ and $r = 1$ for $j = 2$. $\beta = 1/T$ is the inverse temperature and therefore, also τ has units of T^{-1}. $\langle\cdot\rangle_{\text{eq}}$ denotes the thermodynamic expectation value taken within an equilibrium ensemble. Note that $L_{12} = L_{21}/T$ due to Onsager's relation [62]. It is straightforward to show that the real part of $L_{ij}(\omega)$ can be decomposed into a δ-function at $\omega = 0$ with weight D_{ij} and a regular part $L_{ij}^{\text{reg}}(\omega)$:

$$\operatorname{Re} L_{ij}(\omega) = D_{ij}\delta(\omega) + L_{ij}^{\text{reg}}(\omega)\,. \tag{2.22}$$

This equation defines the Drude weights D_{ij} and can be derived by introducing a spectral representation in Eq. (2.21). In terms of such a spectral representation, D_{ij} and the real part of $L_{ij}^{\text{reg}}(\omega)$ are given by [61, 79]:

$$D_{ij}(h,T) = \frac{\pi\beta^{r+1}}{N} \sum_{\substack{m,n\\ E_m=E_n}} p_n \langle n|j_i|m\rangle\langle m|j_j|n\rangle \tag{2.23}$$

and

$$L_{ij}^{\text{reg}}(\omega) = \frac{\pi\beta^r}{N}\frac{1-e^{-\beta\omega}}{\omega} \sum_{\substack{m,n\\ E_m\neq E_n}} p_n \langle n|j_i|m\rangle\langle m|j_j|n\rangle\, \delta(\omega-(E_m-E_n))\,. \tag{2.24}$$

Here, $p_n = \exp(-\beta E_n)/Z$ is the Boltzmann weight, Z denotes the partition function, $|n\rangle$ are eigenstates of the Hamiltonian and E_n are the corresponding eigenenergies. The expression for the Drude weight D_{ij} simplifies if one of the currents is conserved, e.g., $[H, j_i] = 0$

$$D_{ij}(h,T) = \frac{\pi\beta^{r+1}}{N} \sum_n p_n \langle n|j_i j_j|n\rangle\,. \tag{2.25}$$

At this point one can start to give an interpretation of these quantities. For this purpose, we focus on a specific example, which is spin transport within the model defined in Eq. (2.1); the physical picture, however, being applicable to other types of transport as well. The following considerations apply to the thermodynamic limit.

Figure 2.1 shows (a) the real part of the conductivity as a function of frequency and (b) the current $\mathcal{J}_1 = \langle j_1\rangle$ as a function of time. The corresponding Drude weight is D_{11} and the zero-frequency limit of $L_{11}^{\text{reg}}(\omega)$ is denoted by

$$\sigma_{\text{dc}} = \lim_{\omega\to 0} L_{11}^{\text{reg}}(\omega)\,. \tag{2.26}$$

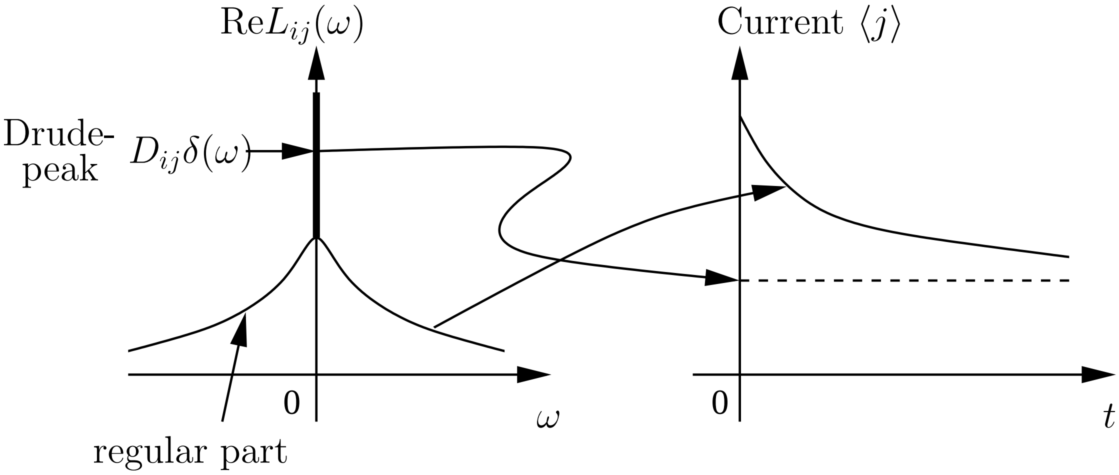

Figure 2.1: Left panel: Sketch of the real part of the conductivity Re $L_{11}(\omega)$ as a function of frequency ω. Three cases can be distinguished: (a) Re $L_{11}(\omega) = D_{11}\delta(\omega)$; (b) the Drude weight D_{11} is finite, but there is also spectral weight at finite frequencies; (c) The Drude weight vanishes in the thermodynamic limit and the zero-frequency limit of Re $L_{11}(\omega)$ determines the dc-conductivity σ_{dc}. In the cases (a) and (b), transport is *ballistic*, while case (c) describes the situation in any real experiment. Right panel: this shows the current $\langle j\rangle$ as a function of time t for case (b). In this picture, it is assumed that an external force, i.e., a gradient of the magnetic field or the chemical potential, was present for $t < 0$, but adiabatically switched of, giving rise to a finite initial value of the current at $t = 0$. In case (a), the current operator itself is exactly conserved, thus, $\langle j\rangle$ does not decay as a function of time. In case (b), the non-conserved part of the current decays, while the long-time limit of $\langle j\rangle$ is nonzero, as indicated by the dashed line in the right panel. Finally, in case (c), an initial current will decay to zero on a characteristic time-scale τ in the absence of external forces (not shown in the figure). This is the situation which is realized in any real experiment as long as the possibility of superconductivity is excluded.

Three main cases can be distinguished at finite temperatures $T > 0$:[5]

$$\begin{array}{lll} (a) & D_{11}(T) > 0; & \sigma_{\mathrm{dc}}(T) = 0 \\ (b) & D_{11}(T) > 0; & \sigma_{\mathrm{dc}}(T) > 0 \\ (c) & D_{11}(T) = 0; & \sigma_{\mathrm{dc}}(T) > 0\,. \end{array} \tag{2.27}$$

In the cases (a) and (b), the Drude weight is finite, leading to an infinite conductivity, irrespective of σ_{dc}. This situation, i.e., $D_{11} > 0$ in the thermodynamic limit, will be referred to as ballistic transport. Case (a) corresponds to an exactly conserved current operator, with no spectral weight at finite frequencies at all. In case (b), the current operator is decomposed into a conserved part j_{c} and a second contribution j_{dec}, which decays on a time scale τ:

$$j_1 = j_{\mathrm{c}} + j_{\mathrm{dec}}\,, \tag{2.28}$$

which is illustrated in the right panel of Fig. 2.1. In a transport experiment, the relevant limit is the long-time limit, thus, the transport coefficient in the zero-frequency limit is determined by j_{c}. In any realistic experiment, dissipation is present giving rise to a complete decay of an initial current in the absence of driving external forces. This is case (c) in Eq. (2.27). Since

---

[5] In principle, a fourth case is also possible which is $D_{11}(T) = 0$ and $\sigma_{\mathrm{dc}}(T) = 0$. However, a dc-conductivity $\sigma_{\mathrm{dc}}(T)$ which is *exactly* zero at finite temperatures is not a very likely case.

a finite temperature is assumed in Eq. (2.27), one can expect the dc-conductivity $\sigma_{\mathrm{dc}}(T>0)$ to be nonzero, even if it might be very small for insulators. Note that the possibility of superconductivity is explicitely excluded here. The presence of impurities or a coupling to the lattice degrees of freedom typically causes dissipation. Therefore, in the absence of superconductivity, one always expects dissipative transport.

Starting from pure spin models, the question is whether intrinsic scattering causes dissipation, rendering the conductivity finite. It turns out that in integrable one-dimensional systems such as the Hubbard model or the Heisenberg chain, transport properties are anomalous, characterized by finite Drude weights [61], giving rise to diverging conductivities. Hence, despite the presence of interactions in both models, intrinsic scattering has no effect on the conductivities. A detailed discussion of the Heisenberg chain is deferred to Chapter 4, while more general aspects will be mentioned in Sec. 2.3.

At zero temperature, the Drude weight can be understood as an indicator of metal-insulator transitions. This viewpoint has been promoted by Kohn [64] and Scalapino et al. [127, 128] in the context of electrical transport. The criteria introduced in Refs. [127, 128] to distinguish metallic and insulating behavior of clean systems at zero temperature are

$$\begin{array}{llrcll} \text{(i)} & \text{Perfect metal:} & D_{11} & > & 0 & \\ \text{(ii)} & \text{Insulator:} & D_{11} & = & 0 & \sigma_{\mathrm{dc}}=0\,. \end{array} \tag{2.29}$$

A prominent example for the Drude weight D_{11} as being an order parameter of a metal-insulator transition is the Mott-Hubbard transition in the one-dimensional Hubbard model[6]

$$H=-t\sum_{\sigma,l}(c^{\dagger}_{\sigma l}c_{\sigma l+1}+\text{h.c.})+U\sum_{l}\left(n_{\uparrow l}-\frac{1}{2}\right)\left(n_{\downarrow l}-\frac{1}{2}\right)\,. \tag{2.30}$$

Here, the Hamiltonian has been written for the one-dimensional case. t denotes the hopping matrix element between next-neighbor sites and U is the onsite Coulomb correlation. $\sigma=\uparrow,\downarrow$ is the spin index. Another parameter of this model is the filling, i.e., the average number of particles per site or band. Both the filling and the U-dependence of the Drude weight are of interest. For zero temperature, this was calculated in Refs. [129–131]. Limiting cases of Eq. (2.30) are (i) the band limit $U=0$ and (ii) the atomic limit of $U=\infty$. Regarding the dependence of the Drude weight on the filling n at zero temperature, the following results can be derived (see, e.g., Ref. [73]):

$$\begin{array}{lrcl} \text{(i)} & D_{11}(n) & = & 4t\sin(\frac{\pi n}{2}) \\ \text{(ii)} & D_{11}(n) & = & 2t|\sin(\pi n)|\,. \end{array} \tag{2.31}$$

In the band limit (i), the Drude weight is finite at half filling $n=1$, while the interactions drive the Mott-Hubbard transition. For $U=\infty$, D_{11} vanishes at half filling, since due to the correlation, double occupancies are forbidden and the fermions essentially act as spinless ones.

---

[6] For this model, D_{11} should be interpreted as the Drude weight corresponding to particle transport, or electrical transport, if multiplied with the charge.

2.2.2 The definition of current operators for spin models

After these general considerations, the setup of the formalism is completed by giving expressions for the current operators

$$j_i = \sum_{l=1}^{N} j_{i,l}\,; \quad i = 1, 2\,. \tag{2.32}$$

The local current operators $j_{1,l}$ and $j_{2,l}$ satisfy equations of continuity [45]

$$\begin{aligned} j_{1,l+1} - j_{1,l} &= -i[H, S_l^z]\,, & (2.33)\\ j_{2,l+1} - j_{2,l} &= -i[H, H_l] & (2.34)\end{aligned}$$

where S_l^z is the local magnetization density and H_l is the local energy density, respectively, with $H = \sum_l H_l$. Note that a discretized version of the divergence $\mathrm{div} j(x) = j_{l+1} - j_l$ is used here. At zero magnetic field[7], the total currents[8] $j_{\mathrm{th[s]}} = \sum_l j_{\mathrm{th[s]},l}$ corresponding to the local magnetization density S_l^z and the energy density H_l from Eq. (2.1), are given by [45, 61, 79]

$$\begin{aligned} j_{\mathrm{s}} &= \sum_{l=1}^{N} j_{\mathrm{s},l} = i \sum_{l=1}^{N} \sum_{n,r=0}^{r_0-1} [H_{l-r-1}, S_{l+n}^z] & (2.35)\\ j_{\mathrm{th}} &= \sum_{l=1}^{N} j_{\mathrm{th},l} = i \sum_{l=1}^{N} \sum_{n,r=0}^{r_0-1} [H_{l-r-1}, H_{l+n}]\,. & (2.36)\end{aligned}$$

This way of writing the currents is particularly convenient, since it is independent of the specific model. Furthermore, in any numerical implementation, only the local densities need to be changed. For the Heisenberg chain, Eqs. (2.35) and (2.36) reduce to

$$\begin{aligned} j_{\mathrm{s}} &= i\frac{J}{2} \sum_{l=1}^{N} (S_l^+ S_{l+1}^- - S_{l+1}^+ S_l^-) & (2.37)\\ j_{\mathrm{th}} &= J^2 \sum_{l=1}^{N} \widetilde{\vec{S}}_l \cdot (\vec{S}_{l+1} \times \widetilde{\vec{S}}_{l+2})\,. & (2.38)\end{aligned}$$

In Eq. (2.38), the abbreviation $\widetilde{\vec{S}} = (S^x, S^y, \Delta S^z)$ is used while $\vec{S}$ is the standard notation. From these expressions for the current operators and from Eq. (2.21), we see that the computation of transport coefficients involve the evaluation of a four-point correlation function of spin operators in the case of spin transport and of a six-point correlation function in the case of thermal transport.

At finite magnetic field, the solutions of the continuity equations are [91]

$$j_1 = j_{\mathrm{s}}; \quad j_2 = j_{\mathrm{th}} - h j_{\mathrm{s}}\,. \tag{2.39}$$

Thus, while the expression for the spin-current operator remains unchanged, the thermal current couples to the spin-current operator. Both sets of current operators, i.e., (j_1, j_2) or

---

[7] Note that for the currents at zero field, the notations $j_1(h = 0) = j_{\mathrm{s}}$ and $j_2(h = 0) = j_{\mathrm{th}}$ will be used throughout the thesis.

[8] Subscripts in brackets $[\cdot]$ refer to spin transport.

$(j_\mathrm{s}, j_\mathrm{th})$, can be used at finite magnetic fields, giving equivalent expressions for the experimentally observable coefficients σ or κ as defined in Eqs. (2.13) and (2.16). What changes are the forces and of course, also the expressions for the entries of the transport matrix (2.7) [see Ref. [62] for further details].

It is often argued that the current operators are not defined unambiguously through the equations of continuity, since different choices for the local densities S_l^z or H_l can be made. This is not so crucial for the spin current because S_l^z involves only local density operators in the fermionic language. From the equation of continuity, generally written for a density operator d_l as

$$\frac{\partial d_l}{\partial t} = -\partial_x j_l\,, \tag{2.40}$$

one can, however, infer that at zero frequency ω, matrix elements of the local current j_l do not depend on the particular choice for d_l [132]. Let E_n, E_m be eigenenergies of the Hamiltonian with eigenstates $|n\rangle$. Then it follows that

$$\langle m|\frac{\partial d_l}{\partial t}|n\rangle = i(E_m - E_n)\langle m|d_l|n\rangle \tag{2.41}$$

since $\partial_t d_l = i[H, d_l]$. For $\omega = E_m - E_n = 0$, Eq. (2.41) yields

$$\partial_x\langle m|j_l|n\rangle = 0. \tag{2.42}$$

Hence, in the zero-frequency limit, j_l is independent of the particular choice for d_l.

Finally, it should be mentioned that the definitions for the current operators given in Eqs. (2.35) and (2.36) apply to the case of a spatially homogenous magnetic field. In general, the spin current has three spatial components in an inhomogeneous magnetic field. Thinking in terms of classical vectors, it becomes obvious that the divergence alone cannot determine the current operator. For a recent discussion of the appropriate way to define the spin-current operator in inhomogeneous magnetic fields; see Refs. [133–136].

2.2.3 Expressions for the Drude weights

An explicit expression for the Drude weights D_{ij}, corresponding to the currents j_1, j_2, has been given in Eq. (2.23). When the currents $(j_\mathrm{s}, j_\mathrm{th})$ are chosen, the analogous expressions for the quantities $D_\mathrm{s}(h,T)$, $D_\mathrm{th}(h,T)$, and $D_\mathrm{th,s}(h,T)$ are [60, 61, 64]:

$$\begin{aligned} D_\mathrm{s}^I(h,T) &= \frac{\pi\beta}{N}\sum_{\substack{m,n\\E_m=E_n}} p_n\,|\langle m|j_\mathrm{s}|n\rangle|^2, & (2.43)\\ D_\mathrm{th}(h,T) &= \frac{\pi\beta^2}{N}\sum_{\substack{m,n\\E_m=E_n}} p_n\,|\langle m|j_\mathrm{th}|n\rangle|^2, & (2.44)\\ D_\mathrm{th,s}(h,T) &= \frac{\pi\beta}{N}\sum_{\substack{m,n\\E_m=E_n}} p_n\,\langle n|j_\mathrm{th}|m\rangle\langle m|j_\mathrm{s}|n\rangle. & (2.45) \end{aligned}$$

For reasons that will become clear below, the spin Drude weight from Eq. (2.43) is denoted by D_s^I instead of simply D_s. In Eqs. (2.43), (2.44), and (2.45), the magnetic field only enters via the Boltzmann weights p_n. In the numerical analysis presented in Chapters 4 and 5, D_{th}, D_{s}, and $D_{\mathrm{th,s}}$ will be evaluated while the coefficients D_{ij} from Eq. (2.23) can be derived if desired since they are linear combinations of $D_{\mathrm{th}}, D_{\mathrm{s}}$, and $D_{\mathrm{th,s}}$:

$$\begin{aligned} D_{11} &= D_{\mathrm{s}}\,, & (2.46)\\ D_{21} &= D_{\mathrm{th,s}} - hD_{\mathrm{s}}\,, & (2.47)\\ D_{22} &= D_{\mathrm{th}} - 2\,\beta h D_{\mathrm{th,s}} + \beta h^2 D_{\mathrm{s}}\,. & (2.48)\end{aligned}$$

For the thermal Drude weight the following notation is used:

$$\mathrm{Re}\,\kappa(\omega,h,T) = K_{\mathrm{th}}(h,T)\delta(\omega) + \kappa_{\mathrm{reg}}(\omega,h,T)\,. \tag{2.49}$$

We introduce the symbol $K_{\mathrm{th}}(h,T)$ for the thermal Drude weight since in finite magnetic fields and under the condition of $\langle j_{\mathrm{s}}\rangle = 0$, the thermal conductivity is composed of L_{22} and the magnetothermal correction [see Eq. (2.16)]. If all Drude weights D_{ij} are finite, then a similar relation holds for the thermal Drude weight

$$K_{\mathrm{th}}(h,T) = D_{22}(h,T) - \frac{1}{T}\frac{D_{21}^2(h,T)}{D_{11}(h,T)}\,. \tag{2.50}$$

If there is no external field, it follows from Eq. (2.50) that

$$K_{\mathrm{th}}(h=0,T) = D_{\mathrm{th}}(h=0,T) = D_{22}(h=0,T)\,. \tag{2.51}$$

High-temperature expansion of the Drude weights

In Chapters 4 and 5, the finite-size scaling of the Drude weights $D_{\mathrm{s}}(T>0)$ and $D_{\mathrm{th}}(T>0)$ is repeatedly analyzed in the high-temperature limit. Such a study allows one to assess whether the Drude weights $D_{\mathrm{s}}(T>0)$ and $D_{\mathrm{th}}(T>0)$ are finite in the thermodynamic limit. The discussion will concentrate on an expansion of the Drude weights in powers of $\beta = 1/T$:

$$D_{\mathrm{s}}(T) = \sum_i \frac{C_{\mathrm{s},i}}{T^i}; \quad D_{\mathrm{th}}(T) = \sum_i \frac{C_{\mathrm{th},i}}{T^{i+1}}; \quad i \geq 1\,, \tag{2.52}$$

where the leading coefficients are denoted by $C_{\mathrm{s}} = C_{\mathrm{s},1}$ and $C_{\mathrm{th}} = C_{\mathrm{th},1}$. These quantities can easily be computed numerically by setting all Boltzmann weights p_n to unity in Eqs. (2.43) and (2.44), which yields

$$C_{\mathrm{th[s]}}(N) = \frac{\pi}{Z_0\,N} \sum_{\substack{m,n\\ E_m=E_n}} |\langle m|j_{\mathrm{th[s]}}|n\rangle|^2\,. \tag{2.53}$$

The partition function $Z_0 = Z(\beta=0)$ is equal to the dimension of the Hilbert space.

Kohn's formula

In the literature, the reader will usually find expressions for the spin Drude weight $D_{11} = D_{\mathrm{s}}$ which are different from Eq. (2.43). First, this includes Kohn's famous formula [64], generalized to finite temperatures [60, 137]

$$D_{\mathrm{s}}^{II}(T) = \pi\, N \sum_n p_n \left. \frac{\partial^2 E_n(\Phi)}{\partial \Phi^2} \right|_{\Phi=0} . \tag{2.54}$$

To arrive at this expression, one considers finite rings of length N being pierced by the flux Φ [138], i.e., a static twist about the z-axis, resulting in a flux-dependent Hamiltonian $H(\Phi)$. Second, one can show that Eq. (2.54) can be written as [60, 79]

$$D_{\mathrm{s}}^{II}(h,T) = \frac{\pi}{N} \left[\langle -\hat{T} \rangle - 2 \sum_{\substack{m,n \\ E_m \neq E_n}} p_n \frac{|\langle m | j_{\mathrm{s}} | n \rangle|^2}{E_m - E_n} \right] . \tag{2.55}$$

The operator $\hat{T}$ is the kinetic energy to be defined below. To allow for an explicit distinction of the Drude weight from Eqs. (2.54) and (2.55) from the one defined in Eq. (2.43), the former will be denoted by D_{s}^{II} and the latter by D_{s}^{I}. Next, three aspects will be explained in more detail: (i) the equivalence of Eqs. (2.54) and (2.55), (ii) the relation of D_{s}^{I} and D_{s}^{II}, and (iii) the optical sum rule.

Derivation of Eq. (2.55) for $D_{\mathrm{s}}^{II}(T)$

The derivation of Eq. (2.55) from Eq. (2.54) within second-order perturbation theory is quite instructive and it is briefly outlined here for the Heisenberg chain expressed in terms of spinless fermions in one dimension [$\alpha = 0, \lambda = 1$ in Eq. (2.5)]. The same procedure applies to the Hubbard model. As a byproduct, the appropriate definitions of $\hat{T}$ and the current operator $j_1 = j_{\mathrm{s}}$ become obvious.

In a static flux Φ the fermion operators c_l acquire a phase shift:

$$c_l \to e^{iAl} c_l \, . \tag{2.56}$$

The vector-potential is given by $A = \Phi/N$; Φ being the total flux. The flux-dependent Hamiltonian $H(\Phi)$ reads

$$H(\Phi) = J \sum_{l=1}^{N} \left\{ -\frac{1}{2} (e^{-iA} c_{l+1}^{\dagger} c_l + e^{iA} c_l^{\dagger} c_{l+1}) + f(\{n_l\}) \right\} . \tag{2.57}$$

Note that the phase cancels in density operators n_l. Thus, generalizing the model, terms containing only density operators n_l are summed up in $f(\{n_l\})$, including a Zeeman term. Furthermore, using a gauge transformation, the phase can completely be shifted to one link, e.g., between sites 1 and N [64]. Therefore, the Drude weight D_{s}^{II} can also be seen as the response to generalized boundary conditions.

Expanding $H(\Phi)$ up to second order in Φ yields [79]

$$H(\Phi) = H(\Phi = 0) + \frac{\Phi}{N} j_{\mathrm{s}} - \frac{\Phi^2}{2\, N^2} \hat{T} \, . \tag{2.58}$$

The expression for the current operator

$$j_{\mathrm{s}} = i \frac{J}{2} \sum_{l=1}^{N} \left(c_{l+1}^{\dagger} c_l - c_l^{\dagger} c_{l+1} \right) \tag{2.59}$$

is equivalent to the one given in Eq. (2.37), where it was derived from the equation of continuity. The kinetic energy $\hat{T}$ is given by

$$\hat{T} = \frac{J}{2} \sum_{l=1}^{N} (c_{l+1}^{\dagger} c_l + c_l^{\dagger} c_{l+1}) \,. \tag{2.60}$$

By applying second-order perturbation theory to $H(\Phi)$ it is straightforward to arrive at Eq. (2.55); see Refs. [79,126]. To this end, one considers an eigenstate $|n(\Phi)\rangle$ of $H(\Phi)$, given as a series in Φ by:

$$|n(\Phi)\rangle = \sum_{r=0}^{N} \Phi^r |n^{(r)}(\Phi)\rangle \,, \tag{2.61}$$

which obeys the normalization condition

$$\langle n|n(\Phi)\rangle = 1; \quad |n\rangle = |n(\Phi = 0)\rangle \quad \Rightarrow \quad \langle n|n^{(r)}(\Phi)\rangle = 0 \,. \tag{2.62}$$

Thus, taking the second derivative of an eigenenergy $E_n(\Phi) = \langle n(\Phi)|H(\Phi)|n(\Phi)\rangle$ with respect to Φ results up to order $O(\Phi^2)$, in

$$\frac{\partial^2 E_n}{\partial \Phi^2} = \left\langle n \left| \frac{\partial^2 H(\Phi)}{\partial \Phi^2} \right| n \right\rangle + 2 \left\langle n \left| \frac{\partial H(\Phi)}{\partial \Phi} \right| n^{(1)} \right\rangle + \left\langle n \left| H(\Phi = 0) \right| n^{(2)} \right\rangle \,. \tag{2.63}$$

The last term $\langle n|H(\Phi = 0)|n^{(2)}\rangle = E_n \langle n|n^{(2)}\rangle$ vanishes due to Eq. (2.62). Inserting Eq. (2.58) into (2.63) yields

$$\left. \frac{\partial^2 E_n}{\partial \Phi^2} \right|_{\Phi=0} = -\frac{1}{N^2} \langle n|\hat{T}|n\rangle + \frac{2}{N} \langle n|j_{\mathrm{s}}|n^{(1)}\rangle \,. \tag{2.64}$$

Using standard perturbation theory with respect to j_{s}, one can compute $|n^{(1)}\rangle$, paying attention to possible degeneracies. The final result is Eq. (2.55).

Two expressions for the spin Drude weight: D_{s}^{I} and D_{s}^{II}

The fact that there are two expressions for the Drude weight in one dimension, Eqs. (2.43) and (2.55), might cause some confusion. The objective of this subsection is to elucidate this issue. The presentation follows Refs. [61,94,127,137].

The two expressions D_{s}^{I} and D_{s}^{II} are equivalent in the thermodynamic limit and one spatial dimension [61,84]:

$$D_{\mathrm{s}} = \lim_{N \to \infty} D_{\mathrm{s}}^{I}(N,T) = \lim_{N \to \infty} D_{\mathrm{s}}^{II}(N,T) \,. \tag{2.65}$$

However, they exhibit differences at low temperatures for finite system sizes [61,84,94]. One might ask what actually is the Drude weight for a finite system. As a definition, the Drude weight is the response to an external flux, incorporated into the Hamiltonian in the way outlined above. Equivalently, it measures the stiffness of the system against twisted boundary conditions [64]. Thus, the physical Drude weight for a finite system in one dimension is given by $D_{\mathrm{s}}^{II}(N,T)$, as defined in Eqs. (2.54) and (2.55). In addition, the sum-rule for the spin conductivity, which is discussed below, is only fulfilled at all temperatures for D_{s}^{II}. One might further ask why one should at all bother about D_{s}^{I}. First, technically, the expressions for D_{s}^{I}

and $D_{\rm th}$ are analogous, which simplifies any numerical implementation. Second, Narozhny et al. [84] have argued that any part of $D_{\rm s}$ that is finite in the thermodynamic limit must be due to $D_{\rm s}^{I}$, since this measures the diagonal matrix elements of the current such as $\langle n|j_{\rm s}|n\rangle$. A detailed comparison of both quantities for the systems of interest in this thesis will be presented in Chapters 4 and 5.

A further insight into this issue can be gained by taking the second derivative of the free energy with respect to the flux Φ:

$$F(\Phi) = -\frac{1}{\beta}\ln Z(\Phi)\,. \tag{2.66}$$

Note the analogies: at zero temperature, Eq. (2.54) gives Kohn's original result [64]:

$$D_{\rm s}^{II}(T=0) = \pi\,N\,\frac{\partial^2 E_0}{\partial^2\Phi}\bigg|_{\Phi=0}\;; \tag{2.67}$$

thus the Drude weight measures the curvature of the ground-state energy level.[9] The intuitive extension to finite temperatures is not correct, which would be to assume that $D_{\rm s}(T)$ is given by the second derivative of F. In fact,

$$\rho_s = \pi\,N\,\frac{\partial^2 F(\Phi)}{\partial\Phi^2}\bigg|_{\Phi=0} \tag{2.68}$$

measures the density of superfluid particles in the thermodynamic limit and in a transverse vector field [94,137], and is usually called the Meissner fraction. Taking the second derivative of F explicitely results in:

$$\frac{\partial^2 F(\Phi)}{\partial\Phi^2}\bigg|_{\Phi=0} = \frac{1}{\pi\,N}D_{\rm s}^{II}(N,T) + \beta\left(\sum_n p_n\,\frac{\partial E_n(\Phi)}{\partial\Phi}\bigg|_{\Phi=0}\right)^2 - \beta\sum_n p_n\left(\frac{\partial E_n(\Phi)}{\partial\Phi}\bigg|_{\Phi=0}\right)^2. \tag{2.69}$$

From the derivation of Eq. (2.55), one knows that the second term on the r.h.s. is equal to:

$$\langle j_{\rm s}\rangle_{\rm eq} = {\rm tr}(j_{\rm s}) = N\sum_n p_n\,\frac{\partial E_n(\Phi)}{\partial\Phi}\bigg|_{\Phi=0}\,. \tag{2.70}$$

Since this is an expectation value taken in equilibrium, $\langle j_{\rm s}\rangle_{\rm eq}$ must vanish in the thermodynamic limit. In other words, no persistent currents exist at finite temperatures in the thermodynamic limit. The third term on the r.h.s., multiplied by $\pi\,N$, can be identified as $D_{\rm s}^{I}$:

$$D_{\rm s}^{I}(N,T) = \pi\,N\,\beta\sum_n p_n\left(\frac{\partial E_n(\Phi)}{\partial\Phi}\bigg|_{\Phi=0}\right)^2. \tag{2.71}$$

To see this, the basis set $\{|n\rangle\}$ is chosen such that $j_{\rm s}$ is diagonal in degenerate subspaces, which can always be achieved by a unitary transformation. From Eq. (2.69) one can then infer that the difference between $D_{\rm s}^{I}$ and $D_{\rm s}^{II}$ is given by the Meissner fraction:

$$\rho_s = D_{\rm s}^{II} - D_{\rm s}^{I}\,. \tag{2.72}$$

In any non-superfluid medium, in one dimension, and for $N \to \infty$, the Meissner fraction vanishes [61,94,137]. This makes the relation between $D_{\rm s}^{I}$ and $D_{\rm s}^{II}$ clear and proves Eq. (2.65).

---

[9] A possible degeneracy of E_0 is neglected here.

Optical sum rule

Another useful quantity is the integrated spectral weight $I(\omega)$, which is defined by:

$$I_{\mathrm{s}}(\omega) = D_{\mathrm{s}} + 2\int_{0^+}^{\omega} d\omega\, \sigma_{\mathrm{reg}}(\omega)\,; \quad I_{\mathrm{th}}(\omega) = D_{\mathrm{th}} + 2\int_{0^+}^{\omega} d\omega\, \kappa_{\mathrm{reg}}(\omega)\,. \tag{2.73}$$

An important result for the optical conductivity

$$\sigma(\omega) = L_{11}(\omega) \tag{2.74}$$

can now be derived, which is the optical sum rule [79, 139, 140]. Integrating Eq. (2.22) over frequency yields the first moment of the real part of the optical conductivity $\mathrm{Re}\,\sigma(\omega)$:

$$\frac{I_0}{2} := \int_0^{\infty} d\omega\, \mathrm{Re}\,\sigma(\omega) = \frac{\pi}{2\,N}\langle -\hat{T}\rangle\,. \tag{2.75}$$

To arrive at this equation, one makes use of the fact that $\mathrm{Re}\,\sigma(\omega)$ is an even function of frequency ω. The rest of the computation is straightforward. This relation is very useful to check numerical implementations. Given a parabolic dispersion, Eq. (2.75) has a very intuitive interpretation. In this case, the mean-value of $\hat{T}$ is replaced by the ratio of density over mass of the carriers, as it is well known from the Drude theory of metals [123]. Thus, the integral over $\mathrm{Re}\,\sigma(\omega)$ is related to the total number of particles in the system.

A similar result for the thermal conductivity relating the first moment of $\mathrm{Re}\,\kappa(\omega)$ to the mean value of a simple observable has not yet been found. In the limit of $\beta \to 0$ and $h = 0$, the weaker condition

$$\frac{I_0}{2} = \int_0^{\infty} d\omega\, \mathrm{Re}\,\kappa(\omega) = \beta^2 \frac{\pi}{2\,N}\langle j_{\mathrm{th}}^2\rangle \tag{2.76}$$

can be derived from Eqs. (2.21), (2.22), and (2.44) [57].

2.3 Transport and conservation laws

2.3.1 Mazur's inequality

The influence of conservation laws on transport properties of low-dimensional quantum systems has been noticed by Zotos and coworkers [61, 141] and has intensely been studied by other authors also [95, 141–144]. For extended reading the reader is referred to Ref. [63]. The presentation in this section follows Refs. [63, 142, 145].

The innate relation of conservation laws and transport becomes obvious if one considers the example of the spin-1/2 Heisenberg chain. A straightforward calculation shows that the energy-current operator j_{th} defined in Eq. (2.36) is a conserved quantity for all exchange anisotropies [61, 74]. From Eqs. (2.21) and (2.16), one can infer that $\kappa(\omega) \propto L_{22}(\omega)$ diverges.

The situation is more interesting when the current operator j itself is not conserved, but when further conservation laws play a role and prevent the current from decaying. One prominent example is spin transport in the XXZ chain where j_{s} is not conserved for any nonzero Δ:

$$[H, j_{\mathrm{s}}] \neq 0 \quad \text{for} \quad \Delta \neq 0\,. \tag{2.77}$$

To be more precise, imagine that $\{Q_l\}$ is the set of all conserved observables in the Liouville space. The Liouville space contains all observables, which act as (hermitian) operators on the original Hilbert space, and it has a scalar product [63]. Then the Drude weight $D_{\rm s} = D_{11}$ can be written as:

$$D_{\rm s}(h,T) = \frac{\pi}{T\,N}\,(j_{\rm s}\,|\,\mathcal{P}j_{\rm s})\,, \tag{2.78}$$

where $\mathcal{P}$ is the projection operator on an orthonormal set of conserved quantities $\{Q_l\}$. The brackets $(.|.)$ denote Mori's scalar product in the Liouville space (see, e.g., Ref. [63]):

$$(A(t)\,|\,B) = \frac{1}{\beta}\int\limits_0^\beta d\tau\,\langle A(t)^\dagger B(i\tau)\rangle\,. \tag{2.79}$$

The interpretation of Eq. (2.78) is that the Drude weight is finite whenever the current has a nonzero projection $j_{\rm c}$ on the subspace of conserved quantities in the Liouville space. The perpendicular component $j_\perp = j_{\rm dec}$ decays.

Since it is in principle difficult to know all conserved quantities, often an inequality is derived from Eq. (2.78). Restricting to a subset $\{Q_m\} \subset \{Q_l\}$ of the conserved quantities, one obtains [61, 146, 147]:

$$D_s(h,T) \geq \frac{\pi}{T\,N}\sum_m \frac{\langle j_{\rm s} Q_m\rangle^2}{\langle Q_m^2\rangle}\,, \tag{2.80}$$

which provides a lower bound for the Drude weight $D_s(h,T)$. In the literature, this relation is often referred to as Mazur's inequality [61, 146, 147]. Several authors [61, 87] have used Eq. (2.80) to infer a finite spin Drude weight for the Heisenberg chain, assuming broken particle-hole symmetry, or the presence of finite magnetic fields, respectively. Only one conserved quantity is often considered in Eq. (2.80), namely $Q_1 = j_{\rm th}$, which has a finite overlap $(j_{\rm s}|j_{\rm th}) > 0$ onto the spin-current operator for $h \neq 0$ [61]. This proves $D_s(h,T) > 0$ for $h \neq 0$. The proof does not apply to the case of zero magnetic field, since $(j_{\rm s}|j_{\rm th}) = 0$ for $h = 0$ due to particle-hole symmetry [61]. A discussion of the problem whether the spin Drude weight is finite or not also at zero magnetic field for the XXZ chain is deferred to Chapter 4.

2.3.2 Integrable versus nonintegrable models

An intensely studied question is whether one can find a criterion for the Drude weight to be finite. Current research focuses on the differences between integrable and nonintegrable systems [60, 83–88, 93], on the relation of transport and level statistics [84, 88], on the role of ergodicity [144], and on topological aspects [148]. Quantum-integrability of one-dimensional models can pragmatically be defined as the model being solvable via the Bethe ansatz. Such models possess an infinite number of conserved quantities. Examples for integrable quantum models are the XXZ chain and the one-dimensional Hubbard model. For a formal proof of the integrability of the Heisenberg chain, relating it to certain limits of the transfer matrices of two-dimensional classical models, see, e.g., Ref. [149].

Spin systems such as the spin-1 chain, the dimerized or frustrated spin-1/2 chain, or spin ladders, are nonintegrable. The issue of level statistics is closely related to the crossover from integrability to non-integrability. The level statistics $P(E)$ of integrable systems follow a Poisson distribution while nonintegrable ones have Wigner statistics [100, 150]. Integrable systems are typically nonergodic due to the existence of many conservation laws.

Regarding transport properties of integrable versus nonintegrable systems, Zotos and coworkers have proposed the following criteria, based on numerical studies of the spinless t–V–W model[10] [61, 83]:

(i) An integrable model is characterized by a finite Drude weight $D_{\mathrm{s}}(T)$ at finite temperatures if $D_{\mathrm{s}}(T=0)>0$. It is therefore an ideal conductor at any temperature.

(ii) An integrable model remains an insulator at finite temperatures with $D_{\mathrm{s}}(T>0)=0$ if $D_{\mathrm{s}}(T=0)=0$.

(iii) Nonintegrable systems have a vanishing Drude weight $D_{\mathrm{s}}(T>0)=0$ and exhibit normal transport behavior.

No formal and general proof for these conjectures exists. For the integrable XXZ chain and the Hubbard model, spin and charge transport are anomalous under certain conditions. See Chapter 4 for a discussion of $D_{\mathrm{s}}(T)$ for the Heisenberg model. Basically, the anomalous transport properties of integrable models regarding both thermal and spin transport are now well accepted in the literature. Note, however, that a counter-example against conjecture (iii) has been given in Ref. [94] and that the second conjecture does also not hold as a general rule. In finite magnetic fields, counter-examples can easily be found for the XXZ chain, for instance, the case of spin transport in the ferromagnetic phase, which is shown in Fig. 4.17(b) and discussed in Sec. 4.5.2.

2.3.3 Diffusive versus ballistic transport

Experiments including transport as well as NMR measurements and neutron scattering are often interpreted in term of diffusive versus ballistic behavior. Here, we provide a definition of these terms, which can often be found in experimental papers. The discussion follows Ref. [17]. Recent studies of spin diffusion in Heisenberg chains can be found in Refs. [151, 152].

Consider an observable $A=\sum_l A_l$, e.g., the magnetization or energy, for which a conservation law holds. Then, an equation of continuity exists, relating the local density A_l to a current j_A:

$$\partial_t A_l + \partial_x j_A(x) = 0\,. \tag{2.81}$$

One is interested in the long-time $t\to\infty$ and short wavelength regime $k\to 0$ of the autocorrelation function

$$S_{AA}(l,t) = \langle\{A_l(t), A_0(0)\}\rangle\,. \tag{2.82}$$

Here, $\{\,.\,,\,.\,\}$ denotes the anti-commutator. According to spin diffusion phenomenology, one expects that correlations $S_{AA}(l,t)$ decay as

$$S_{AA}(l,t) \propto \chi_A\, T \int \frac{dk}{2\pi}\, e^{ikl - D_A k^2 |t|}\,. \tag{2.83}$$

---

[10] This model is equivalent to a XXZ chain with an additional next-nearest neighbor Ising interaction $\sum_l S^z_l S^z_{l+2}$.

χ_A denotes the static susceptibility, D_A is the diffusion constant, and k the wavenumber. For a one-dimensional systems, this results in a typical square root dependence of the autocorrelation function on time [152]

$$S_{AA}(l,t) \propto t^{-1/2} \,. \tag{2.84}$$

Performing a Fourier transformation in Eq. (2.83) yields the expression

$$S_{AA}(k,\omega) \propto \frac{\chi_A D_A k^2}{(D_A k^2)^2 + \omega^2} \,. \tag{2.85}$$

The relation to current-current correlation functions becomes clear if one makes use of the Fourier-transformed continuity equation

$$\omega A_k(\omega) - k j_k(\omega) = 0 \,. \tag{2.86}$$

Thus, for the current-current correlation function one obtains

$$S_{j_A j_A}(k,\omega) \propto \frac{\chi_A D_A \omega^2}{(D_A k^2)^2 + \omega^2} \,, \tag{2.87}$$

i.e., a Lorentzian in frequency space. This is the form of the correlation function that characterizes *diffusive* behavior.

In contrast to diffusive transport, *ballistic* transport is characterized by a δ-function in $S_{j_A j_A}$ in this case:

$$S_{j_A j_A} \propto \delta(\omega - vk) \,. \tag{2.88}$$

v is the characteristic velocity of excitations. In the limit of $k \to 0$, the δ-function moves to $\omega = 0$, and its weight $C_{j_A j_A}$ is given by the long-time asymptotic value of the current-current correlations:

$$C_{j_A j_A} = \lim_{t\to\infty} S_{j_A j_A}(k=0,t) \,. \tag{2.89}$$

Ballistic behavior of the current-current correlation function translates directly into the presence of a finite Drude weight, since the transport coefficients can be expressed in terms of the symmetrized product $\{\,.\,,\,.\,\}$ [45]:

$$L_{ij}(\omega) \propto S_{j_A j_A} \,. \tag{2.90}$$

Finally, it should be mentioned that ill-defined zero-frequency transport coefficients may also arise as a consequence of peculiar long-time tales in $S_{AA}(l,t)$, even if the Drude weight vanishes (see Ref. [17] for a discussion and Ref. [152] for a potential example).

CHAPTER 3

Survey of experimental results

This chapter provides an survey of the numerous recent experiments on magnetic transport properties of quasi one- and two-dimensional materials. This includes the following materials: $(Sr,Ca,La)_{14}Cu_{24}O_{41}$ [6–11,71,153,154], Sr_2CuO_3 [12,13], $SrCuO_2$ [13], $BaCu_2Si_2O_7$ [14], $AgVP_2S_6$ [15], $CuGeO_3$ [65–69], $SrCu_2(BO_3)_2$ [69,70], Nd_2CuO_4 [4,155], and La_2CuO_4 [ii,2,3]. Furthermore, the approaches used to gain a quantitative description and interpretation of experimental results are outlined. These are mainly based on phenomenological expressions. A particular focus is on the magnetic mean-free paths, which can be extracted from experimental data. The mean-free paths turn out to be extremely large in many examples [7,8,12,13]. Several possible scattering mechanisms are discussed and it is shown that the magnetic mean-free paths can be tuned through Zn-doping [ii, 154]. We also provide for references to theoretical studies that are relevant for the materials listed above. For a recent review of the experimental situation, the reader may consult [156].

3.1 Overview

The first section of this chapter contains a brief summary of materials and results of transport measurement that have attracted attention during the last years.[1] The focus of this survey is on thermal transport measurements of spin-1/2 systems. Some representative examples will be described in more detail, namely the spin ladder compounds $(Sr,Ca,La)_{14}Cu_{24}O_{41}$ [6–11,71,153,154] in Sec. 3.2, which is probably the most spectacular and best studied system, the spin chain compounds $SrCuO_2$ and Sr_2CuO_3 [12, 13] in Sec. 3.3.1, and finally, the two-dimensional antiferromagnet La_2CuO_4 [ii, 2, 71] in Sec. 3.4. Theoretical studies relevant for the interpretation of these experiments will be mentioned.

These materials have been chosen because for them, broad experimental evidence for magnon thermal conductivity exists. In particular, the results have been reproduced by different groups. Therefore, they can be regarded as paradigms for thermal transport in spin ladders, spin chains, or square lattice antiferromagnets. Further materials with interesting thermal transport properties, $CuGeO_3$ [65–69] and $SrCu_2(BO_3)_2$ [69, 70], are discussed in Sec. 3.5.

The telephone-number compound $La_5Ca_9Cu_{24}O_{41}$ exhibits the largest absolute values of κ_{mag} observed so far being of the order of 100 $\mathrm{WK^{-1}m^{-1}}$ at room temperature $T \approx 300$ K [8], which is remarkable for an insulating material. Note that the thermal conductivity of a typical metal is of the order of $10 \ldots 400$ $\mathrm{WK^{-1}m^{-1}}$ [123] while that of an typical insulator

---

[1] Note that a possible magnetic contribution to the thermal conductivity was very early discussed for the spin chain material $KCuF_3$ in Ref. [53].

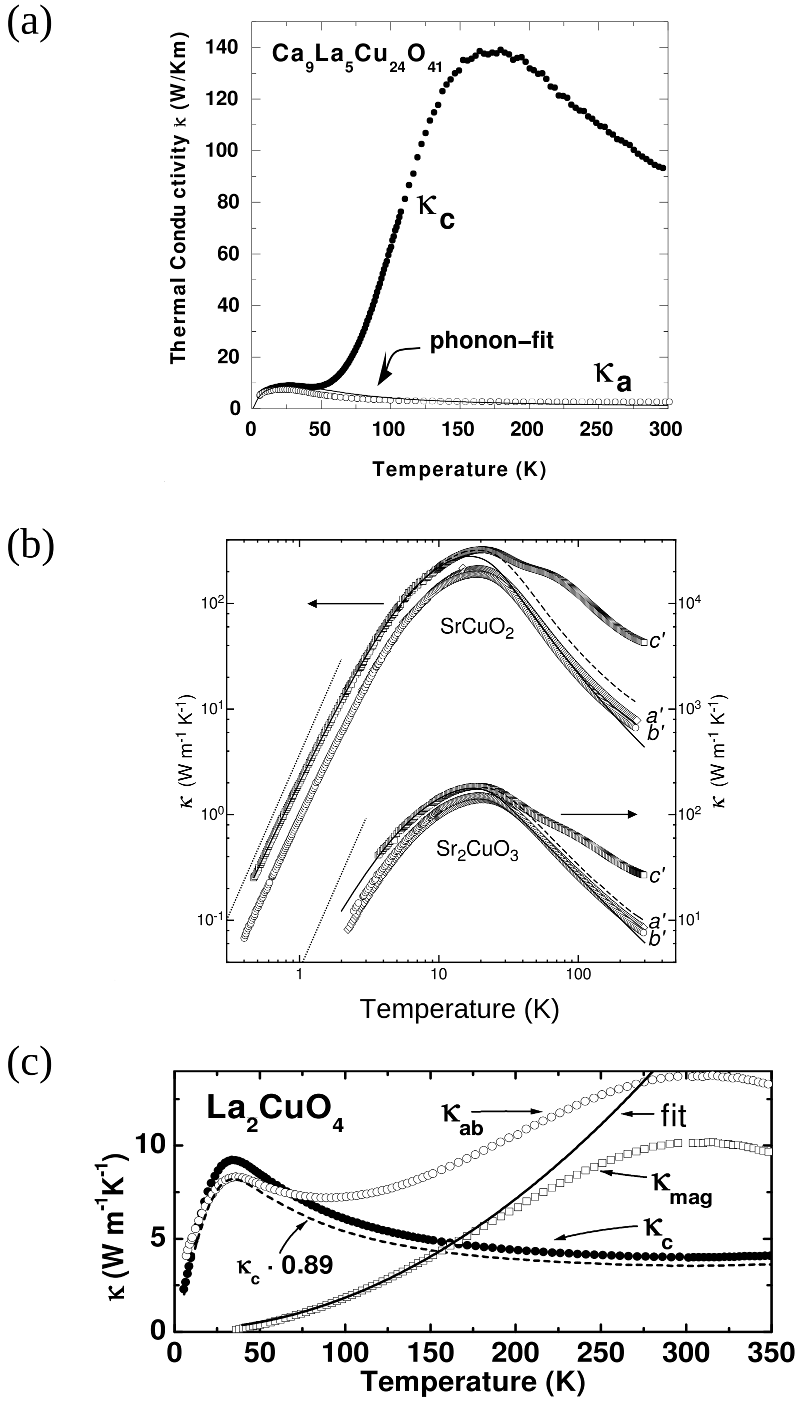

Figure 3.1: Thermal conductivity of $La_5Ca_9Cu_{24}O_{41}$ [8] [panel (a)], $SrCuO_2$ and Sr_2CuO_3 [13] [panel (b)], and La_2CuO_4 [ii] [panel (c)]. (a): κ_c has been measured along the direction of ladders in $La_5Ca_9Cu_{24}O_{41}$, while κ_a is the thermal conductivity of one of the other crystal axes. While the low-temperature peaks, originating from acoustical phonons [8], are similar in both directions parallel (c-axis) and perpendicular to the ladders (a-axis), the remarkably large second maximum around 170 K is only present in κ_c. (b): The data denoted by c' have been measured in the direction of chains in both compounds; a' and b' denote the perpendicular directions. Note that both axes are scaled logarithmically. For both materials, i.e., $SrCuO_2$ and Sr_2CuO_3, a shoulder is visible in $\kappa_{c'}$. (c): κ_{ab} which is the thermal conductivity measured inplane exhibits the usual phonon maximum around 30 K and a second maximum at room temperature. The latter is not present if κ is measured perpendicular to the CuO_2 planes, which is denoted by κ_c in (c). For a discussion of the additional fit lines in panels (a), (b), and (c), the reader is referred to Secs. 3.2, 3.3, and 3.4, respectively. Reproduced from Refs. [8], [13], [ii], with permission from the authors.

such as quartz (SiO_2) is of the order of 10 $WK^{-1}m^{-1}$ [157]. For this family of materials, i.e., $(Sr,Ca,La)_{14}Cu_{24}O_{41}$, several doping experiments have been performed, which show that: (i) the phonon contribution to κ can selectively be reduced [7,8,71,153]; (ii) enhancing the hole concentration in the ladders by substituting Sr by Ca strongly suppresses κ_{mag}; and (iii) Zn-doping, replacing magnetic Cu^{2+} by nonmagnetic ions, leads to a gradual reduction of κ_{mag} with the magnetic mean-free paths being linear in the inverse Zn-concentration [71,154].

$SrCuO_2$ and Sr_2CuO_3 are the paradigms for heat transport via spinons, i.e., for thermal transport in Heisenberg chains. Additionally, most of the theoretical studies [59,78,158,159] addressing transport in Heisenberg chains have discussed their results with perspective on $SrCuO_2$ or Sr_2CuO_3. Finally, the quasi-two-dimensional system La_2CuO_4 is a well studied material among the cuprates regarding thermal transport properties and can be viewed as a paradigm for these materials. Similar to the case of the telephone-number compounds, a consistent picture arises since replacing Cu by Zn again allows for a controlled suppression of the magnetic mean-free paths [ii].

The phenomenological indications for magnon thermal conductivity are first, the spatial anisotropy of the κ tensor and second, a typical double-peak structure observed when κ is measured either in the direction of chains or ladders or inplane in the case of quasi-2D materials. This is clearly seen in the cases of $La_5Ca_9Cu_{24}O_{41}$ [8] shown in Fig. 3.1(a) and of La_2CuO_4 [ii] shown in Fig. 3.1(c), while the thermal conductivity of for $SrCuO_2$ and Sr_2CuO_3 [13] only exhibits a shoulder, as is evident from Fig. 3.1(b). As will be discussed in more detail in the following sections of this chapter, for these three materials there is profound evidence that the contribution from magnetic excitations is substantial. For instance, if the phonon contribution κ_{ph} is subtracted from the total thermal conductivity observed in the c-direction for $La_5Ca_9Cu_{24}O_{41}$, which is the direction parallel to the spin ladders, assuming

$$\kappa_c = \kappa_{\mathrm{ph}} + \kappa_{\mathrm{mag}} \, , \tag{3.1}$$

then the resulting κ_{mag} is exponentially activated at low-temperatures, i.e., κ_{mag} is proportional to $\exp(-\Delta_{\mathrm{sp}}/T)$. The value obtained for the gap Δ_{sp} is in excellent agreement with values for the spin gap of the ladders known from other experiments [160–163]. Similarly, for La_2CuO_4, κ_{mag}, i.e., the magnetic contribution to the inplane thermal conductivity κ_{ab}, almost exhibits a T^2-dependence at low temperatures, which is the expected behavior for two-dimensional quasi-particles with a linear dispersion ϵ_k for small wavenumbers k.

In some of the other materials where a double-peak structure in one crystallographic direction is observed the situation is less clear, partially even controversial, and in some cases, a different scenario explains the experimental observations. For instance, the thermal conductivities of $CuGeO_3$ [65–69], which is a spin-1/2 chain material, and of $SrCu_2(BO_3)_2$ [69,70], which provides a realization of the two-dimensional Shastry-Sutherland lattice [164], have a very interesting behavior in magnetic fields. In the case of $SrCu_2(BO_3)_2$, the observed double-peak structure is not a reflection of two different quasi-particles with different energy scales contributing to the thermal transport, but rather a consequence of resonant scattering of a purely phononic thermal current on localized triplet excitations of the Shastry-Sutherland model [70]. In addition, there is a number of quasi-one dimensional materials, for instance, $BaCu_2Si_2O_7$ [14] or $La_2Cu_2O_5$ [165,166], where κ is anisotropic, i.e., the conductivity in one crystallographic direction exceeds the conductivity of the other directions, but no double-peak structure in $\kappa(T)$ is found in either direction. See, for instance the case of the spin chain $BaCu_2Si_2O_7$ [14] shown in Fig. 3.13. While an excess conductivity observed parallel to spin chain or ladder structures might hint at a possible extra contribution from magnetic excitations, a separation of κ_{ph} and κ_{mag} is complicated in this example. The example of the spin-1/2 chain material $BaCu_2Si_2O_7$, where the exchange coupling is smaller than in $SrCuO_2$, will be covered in Sec. 3.3.2. Experimentalists have also succeeded in measuring the thermal conductivity of spin-1 chains, i.e., Haldane systems. So far results are published for $AgVP_2S_6$ [15], which will be mentioned in some detail in Sec. 3.3.3 and contrasted against spin-1/2 chain materials. Finally, Table 3.1 contains a list of materials with interesting thermal transport properties, lists the references, and compares the coupling constants.

The experiments are frequently discussed with respect to possible *ballistic* transport in contrast to *diffusive* transport. In the literature, the term ballistic often means that the mean-free paths are larger than the sample dimensions. However, in most theoretical studies addressing transport in one-dimensional systems[2] and in this thesis as well, transport is called ballistic, if the respective Drude weight[3] is finite. Roughly speaking, the Drude weight measures that part of the current[4] which is exactly conserved and which will hence not decay as a function of time.

The models investigated in Chapters 4 and 5 are relevant for the description of the magnetic properties of the quasi one-dimensional materials discussed in this chapter: the XXZ chain, dimerized and frustrated chains, and spin ladders. From the theoretical point of view, the Hamiltonians are divided into two groups: first, the integrable XXZ model, in particular including the spin-1/2 Heisenberg chain with exchange coupling anisotropy $\Delta = 1$, and secondly, nonintegrable models such as the dimerized chain, the frustrated chain, or spin ladders. The intriguing property of the spin-1/2 XXZ chain is that its energy-current operator is exactly conserved [61, 74], leading to a finite thermal Drude weight for this model and therefore, the prediction of anomalous thermal transport properties.[5] In fact, some authors frequently claim that the large magnetic mean-free paths derived from the experimental data mostly using phenomenological expressions of the Boltzmann type reflect the divergence of the conductivity of the underlying pure spin model [12–15, 166, 167]. The proposed picture is that the divergence of κ_{mag} is screened by weak residual scattering on, e.g., impurities and phonons. This scenario has even been suggested to describe the thermal transport in the spin ladder system $(Sr,Ca,La)_{14}Cu_{24}O_{41}$, exhibiting the largest absolute values of κ_{mag}, although this system is nonintegrable. One of the objectives of this thesis is to clarify the differences between transport in integrable and nonintegrable models, in particular, with respect to possible ballistic transport in the latter ones.[6] Let us state, in a nutshell, our viewpoint based on the results of this study as outlined in the following chapters: first of all, for the nonintegrable models, we find no indication for ballistic thermal transport; on the contrary, the thermal Drude weight is very likely to vanish in the thermodynamic limit. This is in agreement with the conclusions of Refs. [57, 59]. Thus, the interactions of magnetic excitations of either type, e.g., spinons for frustrated chains, or triplets for spin ladders, render the thermal conductivity κ_{mag} of pure nonintegrable spin systems finite, irrespective of the presence of a spin gap. The large absolute values may rather be a simple consequence of the very large exchange couplings which has also been concluded by Zotos [57]. External scattering mechanisms such as acoustical or optical phonons, impurities, or charge carriers modify the thermal conductivity $\kappa_{\mathrm{mag}}(T)$ of the pure spin model. Given very large exchange couplings and a large spin gap of

---

[2] See, e.g., Ref. [61].

[3] See Chapter 2 for a definition of this quantity.

[4] Either charge, energy, particle, or spin current.

[5] See also Chapter 4 for an extended discussion.

[6] See Chapters 4-6.

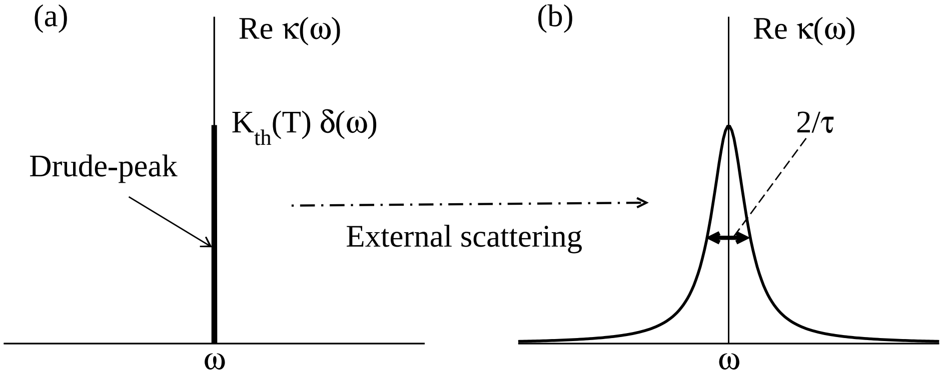

Figure 3.2: (a): Sketch of the real part of the thermal conductivity $\kappa(\omega)$ of the Heisenberg chain as a function of frequency ω. The conductivity is given by $\mathrm{Re}\,\kappa(\omega) = K_{\mathrm{th}}(T)\delta(\omega)$ due to the exact conservation of the energy-current operator [61,74]. Thus, the thermal Drude weight K_{th} is nonzero at any finite temperature, and any contribution at finite frequencies vanishes. (b): In a real experiment for spin chain materials, one may expect the Drude weight to be broadened into, e.g., a Lorentzian in frequency space by external scattering. τ is the inverse width of such Lorentzian, and it is related to the life time of the current, or the inverse scattering rate, respectively.

the order of 400 K in (Sr,Ca,La)$_{14}$Cu$_{24}$O$_{41}$, compared to the typical energy scales of acoustical phonons, we can expect this particular scattering channel to be weak. Consequently, and in particular for La$_5$Ca$_9$Cu$_{24}$O$_{41}$, one may speculate that the experimental κ_{mag} follows a similar temperature dependence as the intrinsic κ_{mag} of the pure spin ladder in a wide temperature range.

For materials that contain Heisenberg chains, one proposal is that the thermal conductivity is, roughly, given by

$$\kappa_{\mathrm{mag}}(T) \propto K_{\mathrm{th}}(T)\,\tau(T)\,, \tag{3.2}$$

where $K_{\mathrm{th}}(T)$ is the thermal Drude weight of the pure system, broadened to a Lorentzian with width $1/\tau$ in frequency space by external scattering [14, 54, 91]. Figure 3.2 provides an illustration. Writing down Eq. (3.2) in this form, an energy dependence of τ is neglected. This, however, has been argued to be a strong and unrealistic approximation [55].

Since the thermal Drude weight is exactly known for arbitrary temperatures and exchange anisotropies [i, iii, 78, 82], Eq. (3.2) can be used to estimate the external scattering rate τ^{-1}. One should be aware of the fact that this is, strictly speaking, not a microscopic theory for κ_{mag}, since firstly, the validity of Eq. (3.2) is based on the assumption of energy-independent scattering rates, and secondly, the scattering rates themselves are *not* modeled.

Regarding the absolute value of κ_{mag}, it is clear that it will strongly be influenced by $\tau(T)$. Whether or not one observes a thermal conductivity $\kappa_{\mathrm{mag}}(T)$ with a temperature dependence which is mostly dominated by that of $K_{\mathrm{th}}(T)$ probably depends on the relevant energy scales. In fact, recent theoretical studies taking into account spin-phonon coupling [59, 158, 159] and scattering on impurities [158, 159] predict a temperature dependence of $\kappa_{\mathrm{mag}}(T)$ that is, even at low temperatures, governed by the temperature dependence of the respective scattering rates $1/\tau$. Finally, one should keep in mind that, despite the impressively consistent picture that arises for La$_2$CuO$_4$ [ii, 71] or (Sr,Ca,La)$_{14}$Cu$_{24}$O$_{41}$ [8, 10, 11, 153, 154], the extremely large magnetic mean-free paths derived from experiments are based on phenomenological expressions (see, e.g., Refs. [ii, 7–9, 11–14, 153, 154]). The phenomenological models lack a profound theoretical justification at present, e.g., for spin ladders.

The phenomenological expression used to describe the magnon thermal conductivity of La_2CuO_4 is part of the work done in this thesis. Its application to Zn-doped La_2CuO_4 has been published in Ref. [ii].

Material	Refs.	Geometry	Coupling-constants
Quasi-1D spin-1/2 chains			
$CuGeO_3$	[65–69]	(frustrated) chains	$J = 120$ K [168], INS α=0.35 [169, 170]
$SrCuO_2$	[13]	chains	$J = 2600$ K [171], INS
Sr_2CuO_3	[12, 13]	chains	$J = (2200 \pm 200)$ K [172], $\chi(T)$; [173], OPT $J = (2600 \pm 200)$ K [174], $\chi(T)$
$BaCu_2Si_2O_7$	[14]	chains	$J = 280$ K [175], $\chi(T)$
Quasi-1D spin-1 chains			
$AgVP_2S_6$	[15]	chains	$J = 780$ K [176]
Spin-1/2 ladder systems			
$Sr_{14}Cu_{24}O_{41}$	[6–9]	2-leg ladder	$J_\perp = 1508$ K $J_\parallel = 835$ K [162], INS
$Sr_{14-x}Ca_xCu_{24}O_{41}$	[7, 10, 11]	2-leg ladder	
$La_5Ca_9Cu_{24}O_{41}$	[8, 153]	2-leg ladder	$J_\perp \approx J_\parallel$, $J_{\mathrm{ring}}/J_\perp \approx 0.1$ $J_\perp = 1280$ [177], INS $J_\perp = 1550$ [178], OPT
$Sr_{14}Cu_{24-x}Zn_xO_{41}$	[71, 154]	2-leg ladder	
$La_2Cu_2O_5$	[165, 166]	4-leg ladder	
Quasi-2D materials: R_2CuO_4; R=La,Nd,Pr			
La_2CuO_4	[ii, 2, 3]	square lattice	$J = 1550$ K [179]
$La_2Cu_{1-z}Zn_zO_4$	[ii, 3]	square lattice	
$La_{2-x}Eu_xCuO_4$	[ii, 180]	square lattice	
$La_{2-x}Sr_xCuO_4$	[3, 71]	square lattice	
Nd_2CuO_4	[4, 155]	square lattice	$J = 1500$ K [155]
Further quasi-2D materials			
$Sr_2CuO_2Cl_3$	[5]	square lattice	$J = 1225$ K [5]
$K_2V_3O_8$	[155, 181]	square lattice, V^{4+} ions	$J = 12.6$ K [182]
$SrCu_2(BO_3)_2$	[69, 70]	Shastry-Sutherland lattice	$J_1 = 72$ K; $J_2 = 43$ K [183]

Table 3.1: This table contains a list of thermal conductivity measurements of materials that are discussed in this chapter. For most of them, magnon thermal conductivity has been proposed. For $SrCu_2(BO_3)_2$ and $K_2V_3O_8$, a magnetic contribution to κ has been excluded [69, 155]. The case of $CuGeO_3$ is still under controversial discussion; see Sec. 3.5.1. See Eq. (2.5) for a definition of α, Fig. 3.18 for J_1, J_2, and Fig. 3.3 for a definition of $J_\perp$ and $J_\parallel$. J_{ring} measures a four-spin ring exchange term [177, 178]. If available, experimental values for the exchange couplings are given together with the respective reference. The following abbreviations are introduced to denote the experimental technique used to determine J: INS: inelastic neutron scattering; $\chi(T)$: magnetic susceptibility; OPT: optical spectroscopy.

3.2 The spin ladder compounds (Sr,Ca,La)$_{14}$Cu$_{24}$O$_{41}$

Structural and magnetic properties

The compounds of the family (Sr,Ca,La)$_{14}$Cu$_{24}$O$_{41}$ are often called *telephone-number compounds* because of the six digits in the structural formula. The structure of the parent compound Sr$_{14}$Cu$_{24}$O$_{41}$ is depicted in the upper panel of Fig. 3.3. It consists of alternating layers [35]: (i) the cation-planes; (ii) the CuO$_2$ containing chains shown in the lower-left panel of Fig. 3.3; and (iii) the Cu$_2$O$_3$ planes containing two-leg ladders shown in the lower-right panel of Fig. 3.3. The ladders and chains can be regarded as quasi-one dimensional structures, since the interactions between chains and ladders, respectively, in the same plane are frustrated while the interplane interaction is weak. Both ladders and chains extend in the c-direction as can be seen in Fig. 3.3, but the structure is incommensurate since $c_L \approx 3.9$ Å and $c_K \approx (10/7)c_K$. The lattice constants in the other directions are $a \approx 11.3$ Å and $b \approx 12.6$ Å. For a detailed discussion of structural, thermodynamic, and magnetic properties of spin ladder systems in general, the reader is referred to the article by Johnston et al. [28] and the review by Dagotto [19]. For (Sr,Ca,La)$_{14}$Cu$_{24}$O$_{41}$, Ref. [184] also provides a wealth of details.

Here, we are primarily interested in the properties of the spin ladders, because excitations of the spin chains are very unlikely to contribute to the thermal conductivity; for arguments given below. For the exchange couplings along the legs of the ladders $J_{\|}$ and along the rungs $J_{\perp}$ of Sr$_{14}$Cu$_{24}$O$_{41}$ (see Fig. 3.3) different values are reported in the literature. The values are listed in Table 3.1. Most recent studies find $J_{\|} \approx J_{\perp}$ with $J_{\perp} \approx 1280$K [177] or $J_{\perp} \approx 1550$K [178]. To obtain these results from inelastic neutron-scattering [177] and optical spectroscopy [178], respectively, a four-spin ring exchange term of roughly $J_{\mathrm{ring}} \approx 0.1 J_{\perp}$ has to be taken into account.

Note that Sr$_{14}$Cu$_{24}$O$_{41}$ is intrinsically hole-doped in the CuO planes, with an average valency of Cu$^{2.25+}$. For the hole concentration in the chains, a value of 0.6 holes per Cu-site has been proposed [185, 186], while only one hole per structural unit resides in the ladders [187]. Thus, most of the holes can be found in the CuO$_2$ chains, where at low temperatures, indications for charge ordering are found [184, 188–190]. The picture proposed for this charge ordering is that the remaining spin-1/2 moments, alternatingly separated by either one or two holes, form dimers with a spin gap of 140K [160].

Upon isovalent Ca-doping, holes are transferred from the chains into the ladders [185,186]. In fact, these materials have attracted particular interest since superconductivity under high pressure was found in Sr$_{14-x}$Ca$_x$Cu$_{24}$O$_{41}$ for large Ca-contents $x \approx 12$ [191,192]. Before, large superconducting correlations were theoretically predicted for hole-doped two-leg ladders [193] triggering the experimental quest for superconductivity. With respect to the hole content, the compound La$_6$Ca$_8$Cu$_{24}$O$_{41}$ is special because the CuO planes would be hole free. However, the preparation of single-crystals turns out to be difficult for this stoichiometry, and therefore the best suited example to study transport properties of pure spin ladders is La$_5$Ca$_9$Cu$_{24}$O$_{41}$. A detailed discussion of thermal transport properties of the telephone-number compounds can be found in [71].

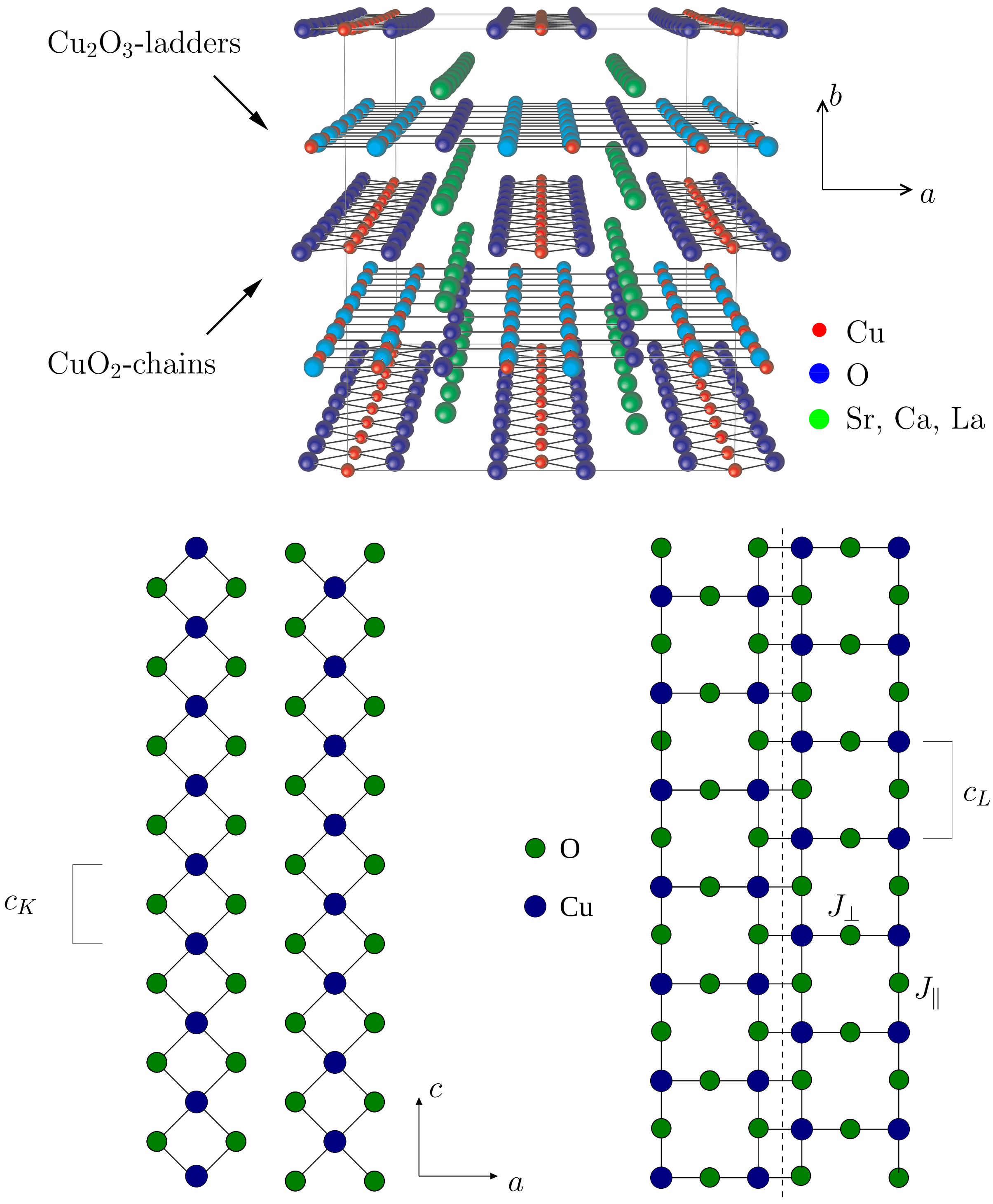

Figure 3.3: Upper panel: Crystal structure of (Sr,Ca,La)$_{14}$Cu$_{24}$O$_{41}$. The material is built up of alternating layers: CuO$_2$ planes, Cu$_2$O$_3$ planes, and in between, layers containing the (Sr,Ca,La)-ions. Lower panel, left: top view on the CuO$_2$ planes containing chains. Lower panel, right: Top-view on the Cu$_2$O$_3$ planes containing ladders. In the CuO$_2$ planes, adjacent chains are shifted against each other by half a unit cell. Exchange couplings along the rungs of the ladder are denoted by $J_\perp$ and along the legs of the ladder by $J_\parallel$, respectively. Adapted from [177].

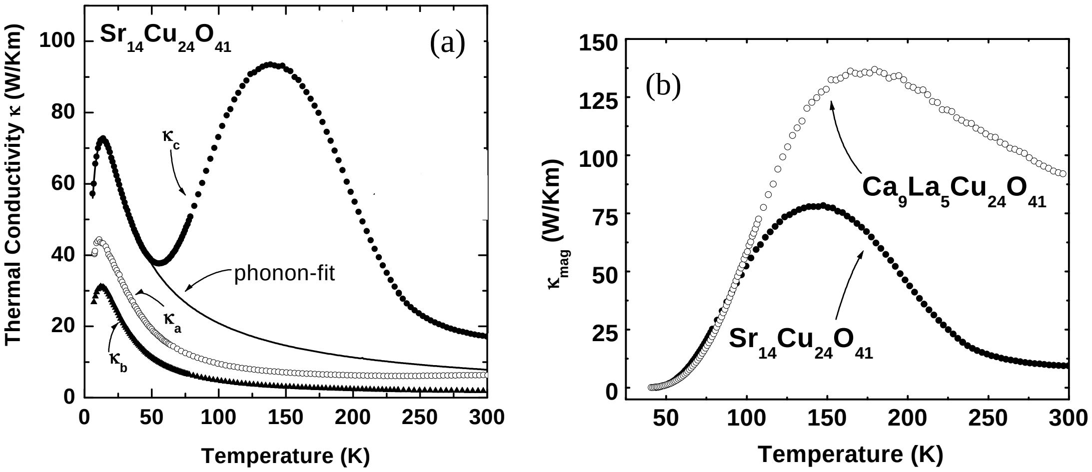

Figure 3.4: (a): Thermal conductivity of $Sr_{14}Cu_{24}O_{41}$ measured parallel (κ_c) and perpendicular to the ladders and chains ($\kappa_{a,b}$). The solid line is a fit to the low-temperature peak to describe the phonon contribution to the thermal conductivity κ_c. (b): Magnon thermal conductivity $\kappa_{\rm mag}$ of $Sr_{14}Cu_{24}O_{41}$ and $La_5Ca_9Cu_{24}O_{41}$, compare Fig. 3.1(a), obtained by subtracting the phonon thermal conductivity $\kappa_{\rm ph}$ [solid line in panel(a)] from the total κ_c; see text for further details. Reproduced from [8].

3.2.1 Thermal conductivity of $Sr_{14}Cu_{24}O_{41}$ and $La_5Ca_9Cu_{24}O_{41}$

Results for the thermal conductivity of $Sr_{14}Cu_{24}O_{41}$ have independently been reported by Sologubenko et al. [7], Hess et al. [8], and Kudo et al. [6, 9]. Figure 3.4(a) depicts the results of Hess et al. [8] for κ of $Sr_{14}Cu_{24}O_{41}$. The main features, also seen in the case of $La_5Ca_9Cu_{24}O_{41}$ shown in Fig. 3.1(a), are:

(i) The anisotropy between the thermal conductivity κ_c measured *parallel* to chains and ladders and the conductivity $\kappa_{a,b}$ measured perpendicular to the ladder and chain planes, both regarding the magnitude of κ and its temperature dependence. κ_c clearly exceeds $\kappa_{a,b}$ and it exhibits a double-peak structure, which is only seen in the c-direction.

(ii) The absolute values of κ_c are very large and remarkable for a practically insulating material. A typical metal, e.g., Cu, has a thermal conductivity of 385 $WK^{-1}m^{-1}$ at $T = 273$ K [123] and diamond, the best known thermal conductor, has a thermal conductivity of 1000 $WK^{-1}m^{-1}$ at $T = 300$ K.[7] This has to be compared to $\kappa_c = 100$ $WK^{-1}m^{-1}$ at room temperature observed in the case of $La_5Ca_9Cu_{24}O_{41}$.

The low-temperature peak is explained in terms of standard phonon thermal conductivity [7,8]. Intuitively the huge second maximum around 170K seen in κ_c is related to magnetic excitations. Acoustical phonons are excluded as the elastic constants cannot explain the anisotropy [7,8]. All authors also argue that the second maximum is not of electronic origin, as the contribution from charge carriers estimated via the Wiedemann-Franz law would be far below the observed values for κ [7–9].

In principle, both excitations of the spin chains and the ladders could give rise to the

---

[7] http://www.cvd-diamond.com/tfdiprth/frames_d.htm.

excess conductivity. However, the excitations of the spin chains in $Sr_{14}Cu_{24}O_{41}$ are practically dispersionless [188]. Furthermore, in $Sr_{14}Cu_{24}O_{41}$, the effect of charge ordering at low temperatures occurs [188–190], which is not the case for $La_5Ca_9Cu_{24}O_{41}$. As the magnetic thermal conductivity of both compounds at low temperatures is very similar, the chains are unlikely to carry the extra amount of heat. To allow for a quantitative analysis, it is necessary to separate the phonon contribution $\kappa_{\rm ph}$ and the possible magnon contribution $\kappa_{\rm mag}$. This is a crucial step in the analysis of the experimental data, as it largely determines the error. The procedure applied in Ref. [8] is briefly outlined. There, the low-temperature peak in κ_c is fitted by a Callaway model [194] and then, this fit is extrapolated to high temperatures. In $Sr_{14}Cu_{24}O_{41}$, unfortunately, already the phonon peak around 40 K is highly anisotropic, thus κ_a and κ_b cannot be used to deduce the phonon contribution. The situation is better in $La_5Ca_9Cu_{24}O_{41}$, where the low-temperature maxima in κ_a and κ_c are almost identical, which can be seen in Fig. 3.1(a). Note that the phonon maximum in $La_5Ca_9Cu_{24}O_{41}$ is smaller than in $Sr_{14}Cu_{24}O_{41}$, which is ascribed to two reasons. Firstly, $La_5Ca_9Cu_{24}O_{41}$ contains both La and Ca-ions, which are randomly distributed, causing scattering centers for phonons. Secondly, in $La_5Ca_9Cu_{24}O_{41}$ the chains are structurally disordered, i.e., they are shifted against each other in the CuO_2 planes [8].

Before turning to the quantitative analysis of the experimental data, a special feature of the thermal conductivity must be mentioned. The peculiar observation is that thermal transport measurements in these materials are *irreversible*, i.e., different absolute values for the *second* maximum of κ_c are obtained if the samples are cooled or heated during the measurement [71]. This amazing effect is so far unexplained. It does, however, explain the slightly different values of κ_c observed in [7] and [8], since the data have apparently been taken under different conditions. A similar observation has recently been reported for the Haldane compound $AgVP_2S_6$ [15] and was also found for $CaCu_2O_3$ [195]; thus it might be an intrinsic feature of magnon thermal transport. For a discussion of possible explanations, the reader is referred to Ref. [71].

Quantitative analysis of $\kappa_{\rm mag}$

The results for $\kappa_{\rm mag} = \kappa_c - \kappa_{\rm ph}$ are shown in Fig. 3.4(b). At low temperatures, the $\kappa_{\rm mag}$ of both compounds are almost identical, while at higher temperatures, the data for $La_5Ca_9Cu_{24}O_{41}$ clearly exceed that for $Sr_{14}Cu_{24}O_{41}$ by more than a factor of two at $T = 300$ K. The most important evidence for magnon thermal conductivity from triplet excitations is the exponentially activated behavior seen at low temperatures, i.e.,

$$\kappa_{\rm mag} \propto e^{-\Delta_{\rm sp}/T} \,. \tag{3.3}$$

This is illustrated in Fig. 3.5. It is also noteworthy that the temperature dependence of $\kappa_{\rm mag}$ of $La_5Ca_9Cu_{24}O_{41}$ is at least compatible with a $\kappa_{\rm mag} \propto T^{-2}$ at very high temperatures. This form is expected for intrinsic magnetic thermal transport without modifications due to external scattering. Alvarez and Gros [54] have given a fit formula for $\kappa_{\rm mag}$ of $La_5Ca_9Cu_{24}O_{41}$ which describes the experimental data quite well. When extrapolated to high temperature, their fit yields $\kappa_{\rm mag} \propto T^{-2}$.

In order to estimate the constant $\Delta_{\rm sp}$ in Eq. (3.3), one can either fit a simple activation law to the data, or choose a somewhat better description in terms of a Boltzmann-type of

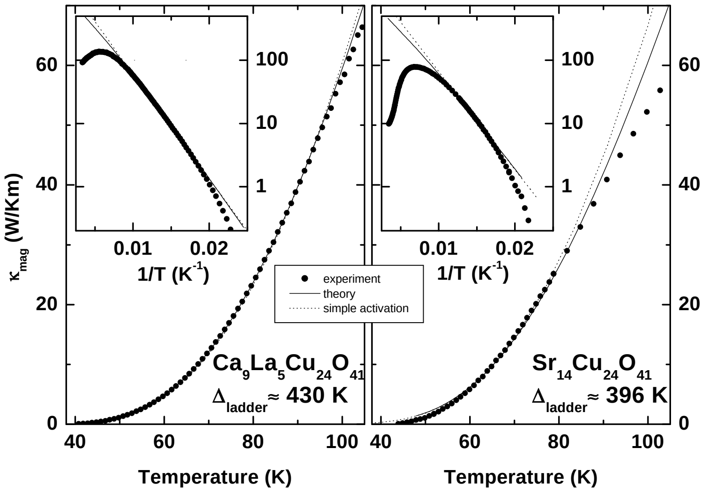

Figure 3.5: Magnetic part κ_{mag} of the thermal conductivity of $\mathrm{La_5Ca_9Cu_{24}O_{41}}$ and $\mathrm{Sr_{14}Cu_{24}O_{41}}$ at low temperatures. Here, $\kappa_{\mathrm{mag}} \propto \exp(-\Delta_{\mathrm{sp}}/T)$ is found at low temperatures, and Δ_{sp} is in good agreement with the spin gap of the ladder subsystem, determined with other experimental techniques. The thin, dotted lines display a simple activation behavior according to Eq. (3.3), while the solid lines stem from Eq. (3.9). Reproduced from Ref. [8].

equation [7, 8], which we outline now. The starting point is

$$\kappa_{\mathrm{mag}}(T) = \sum_k C_{V,k}\, v_k\, l_{\mathrm{mag},k} \tag{3.4}$$

where k denotes the wavenumber, $C_{V,k}$ is the specific heat per k-space volume, $v_k = \partial_k \epsilon_k$ is the velocity, ϵ_k the dispersion, and $l_{\mathrm{mag},k}$ is the mean-free path.

Before turning to the discussion of experimental results, note that in general and in particular for gapped systems, $\kappa_{\mathrm{mag}} \not\propto C_V$, where C_V is the total specific heat of the magnetic subsystem. A proportionality between the thermal conductivity and the specific heat can be established under the condition of $\epsilon_k \propto k$ in the low-temperature limit [123], as it is the case for electrons close to the Fermi-surface or for spinons, being the elementary excitations of the XXZ chain [78] (see also Chapter 4). Furthermore, we need to assume the mean-free path $l_{\mathrm{mag,k}}$ to be independent of wavenumber k, which is a reasonable assumption for scattering on impurities or sample boundaries. To illustrate this aspect, the following dispersion ϵ_k for the elementary triplet excitation is assumed:

$$\epsilon_k = \frac{1}{\sqrt{2}}\sqrt{(\Delta_{\mathrm{sp}}^2 + \epsilon_{\mathrm{max}}^2) + (\Delta_{\mathrm{sp}}^2 - \epsilon_{\mathrm{max}}^2)\cos(k)}\,. \tag{3.5}$$

This dispersion was also used in Ref. [54] to fit the experimental data and it takes into account the finite spin gap Δ_{sp}. ϵ_{max} is the upper boundary of the triplet band. We may then write for the average velocity $v = \langle v_k \rangle$ and the specific heat C_V

$$C_V = -\frac{1}{TN}\sum_k \epsilon_k^2 \frac{dn(\epsilon_k)}{d\epsilon_k} \tag{3.6}$$

$$v = \frac{1}{N}\sum_k v_k n(\epsilon_k)\,. \tag{3.7}$$

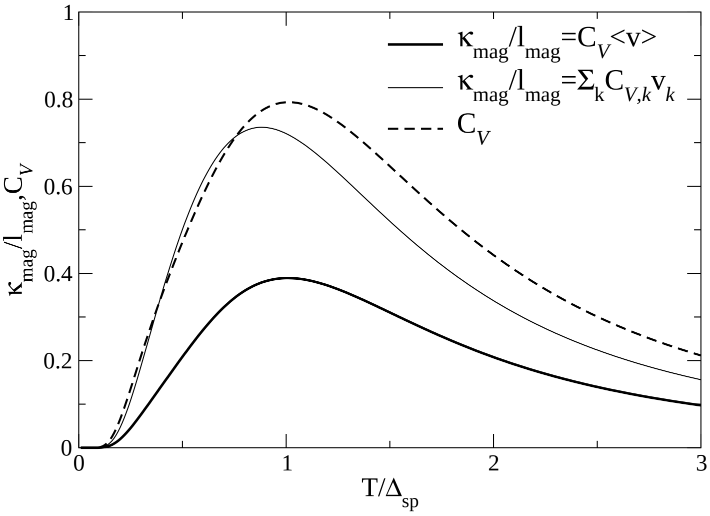

Figure 3.6: Comparison of two phenomenological expressions for the thermal conductivity carried by the elementary triplet excitations of a spin ladder; Eqs. (3.9) and (3.10); denoted by the thin and thick solid line, respectively. The temperature T is measured in units of the spin gap Δ_{sp}. The dashed line is the specific heat C_V of a gas of free massive triplets with the dispersion Eq. (3.5). The comparison reveals that the relation $\kappa_{\mathrm{mag}} \propto C_V$ is not valid in gapped systems. One should rather integrate over the contributions from each volume element in momentum space.

For the distribution function $n(\epsilon)$, we use the form

$$n(\epsilon) = \frac{3}{e^{\epsilon/T} + 3}\,, \tag{3.8}$$

which takes into account that the triplet excitations are threefold degenerate hardcore bosons.[8] This deviates from the usual statistics of bosons since the triplets are subject to the additional constraint that double occupancies of one rung site are forbidden [98]. Under the assumption that the magnetic mean-free paths do not depend on the wavenumber, i.e., $l_{\mathrm{mag}} \neq l_{\mathrm{mag}}(k)$, Eq. (3.4) can be written as[9]

$$\kappa_{\mathrm{mag}}(T) = -\frac{3\,l_{\mathrm{mag}}}{\pi T} \int\limits_{\Delta_{\mathrm{sp}}}^{\epsilon_{\mathrm{max}}} d\epsilon\, \epsilon\, \frac{dn(\epsilon)}{d\epsilon}\,. \tag{3.9}$$

Since this is a one-dimensional integral, Eq. (3.9) is independent of the specific form of the dispersion relation ϵ_k, i.e., v_k drops out of the integral.

Combining Eqs. (3.6) and (3.7) yields a relation often claimed to be generally valid in one-dimensional systems

$$\kappa_{\mathrm{mag}} = C_V\, v\, l_{\mathrm{mag}}\,. \tag{3.10}$$

This quantity is compared to κ_{mag} from Eq. (3.9) in Fig. 3.6, where $\kappa_{\mathrm{mag}}/l_{\mathrm{mag}}$ and C_V are plotted versus temperature. The two curves for κ_{mag} have their maxima at different positions and they are quantitatively different. Thus, we prefer not to adopt the very strong

---

[8] Equation (3.8) for n_k is exact in the limit of $J_\parallel = 0$. It has been argued that it also holds for finite interdimer couplings, see Ref. [196, 197].

[9] See also the discussion in Ref. [72].

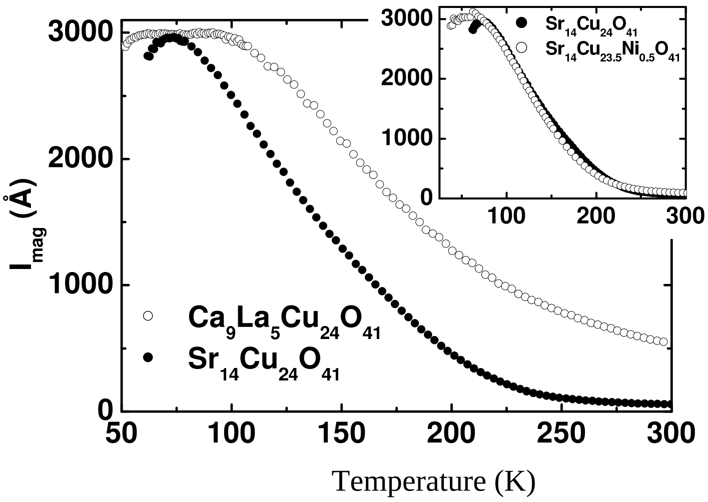

Figure 3.7: Main panel: Mean-free paths l_{mag} extracted from κ_{mag} using Eq. (3.10) for $Sr_{14}Cu_{24}O_{41}$ and $La_5Ca_9Cu_{24}O_{41}$. The inset shows a comparison of the mean-free paths of $Sr_{14}Cu_{24}O_{41}$ and $Sr_{14}Cu_{23.5}Ni_{0.5}O_{41}$ [71]. Doping with Ni induces both structural and magnetic defects, since Ni-ions carry a spin-1 moment. Since the mean-free path l_{mag} and κ_{mag} (not shown here) are practically unaffected by Ni-doping, one can conclude that Ni ions reside within the chains and not on ladder Cu-sites [71]. Reproduced from Ref. [71] with permission from the author.

approximation of $\kappa_{\mathrm{mag}} \propto C_V$ and continue with Eq. (3.9).

In order to fit the experimental data some prefactors have to be added in Eq. (3.9) since the experimental κ_{mag} is the thermal conductivity of an array of spin ladders embedded in a three dimensional environment. Thus, we have

$$\kappa_{\mathrm{mag}}(T) \to \frac{N_L}{\hbar\, k_B} \kappa_{\mathrm{mag}}(T) \quad \text{and} \quad T \to k_B T\,, \tag{3.11}$$

where N_L is the number of ladders per unit area, $\hbar$ is Planck's quantum, and k_B is the Boltzmann constant.

Since ϵ_{max} does not affect the results for temperatures $T < 300$ K, it is set to $\epsilon_{\mathrm{max}} = 200$ meV [162, 177]. Assuming a temperature independent mean-free path at low temperatures,[10] the fit can be performed and the resulting curves are depicted in the left panel of Fig. 3.5 for $La_5Ca_9Cu_{24}O_{41}$ and in the right panel of Fig. 3.5 for $Sr_{14}Cu_{24}O_{41}$ [8]. The values for the spin gap that can be extracted are $\Delta_{\mathrm{sp}} = 396$ K for $Sr_{14}Cu_{24}O_{41}$ and $\Delta_{\mathrm{sp}} = 415 \ldots 430$ K for $La_5Ca_9Cu_{24}O_{41}$, which is in good agreement with values for the spin gap extracted from neutron scattering data [162]. This result is very important, because it establishes a *positive* experimental proof for magnon thermal conductivity in (Sr,Ca,La)$_{14}$Cu$_{24}$O$_{41}$ in contrast to many other materials where the conclusion of magnon thermal conductivity can only be drawn by giving reasons to *exclude* other possible heat carriers.

Next, the result for Δ_{sp} and the low-temperature limit of l_{mag} can be used to estimate the temperature dependence of l_{mag} for $T < 300$ K. The results are shown for both samples in Fig. 3.7. First of all, note the extremely large mean-free paths l_{mag} of approximately 3000 Å at low temperatures, which corresponds to roughly 700 lattice constants. Secondly, l_{mag} is

---

[10] The precise fit-intervals are listed in Refs. [8, 71].

smaller for $\mathrm{Sr}_{14}\mathrm{Cu}_{24}\mathrm{O}_{41}$ at high temperatures, which is a consequence of the smaller κ_c. Possible reasons for this quantitative difference between $\mathrm{Sr}_{14}\mathrm{Cu}_{24}\mathrm{O}_{41}$ and $\mathrm{La}_5\mathrm{Ca}_9\mathrm{Cu}_{24}\mathrm{O}_{41}$ are discussed in Sec. 3.2.2.

Possible ballistic transport in spin ladders materials?

The observation of extremely large magnetic mean-free paths has stimulated many researchers to speculate about possible ballistic thermal transport in spin ladders [54–56, 58]. As mentioned in Sec. 3.1, ballistic thermal transport is characterized by the existence of a finite thermal Drude weight. A finite Drude weight is related to conservation laws that prevent the energy current from decaying [61, 63, 95, 145]. In a first numerical study of thermal transport in spin ladders and frustrated chains [54], Alvarez and Gros claimed that the thermal Drude weight $K_{\mathrm{th}}(T)$ is finite in the thermodynamic limit for spin ladders and more generally, for dimerized chains and frustrated chains also. Based on this conjecture, they analyzed the experimental data for κ_{mag} of $\mathrm{La}_5\mathrm{Ca}_9\mathrm{Cu}_{24}\mathrm{O}_{41}$ by dividing κ_{mag} by their numerical results for $K_{\mathrm{th}}(T)$, which allows one to estimate the external scattering rates via

$$\tau_{\mathrm{ext}} \propto \kappa_{\mathrm{mag}}(T)/K_{\mathrm{th}}(T)\,. \tag{3.12}$$

In their theory, intrinsic scattering due to triplet-triplet interactions is of course absent for thermal transport. They used the dispersion relation given in Eq. (3.5) to extract the magnetic mean-free path

$$l_{\mathrm{mag}}(T) = \langle v_k(T)\rangle\ \tau_{\mathrm{ext}}(T)\,. \tag{3.13}$$

The mean velocity $\langle v_k(T)\rangle$ was defined in Eq. (3.7). In comparison with the results of Hess et al., they find much smaller values for l_{mag}; e.g., for $T = 100$ K, they report $l_{\mathrm{mag}} \approx 176$ Å in contrast to $l_{\mathrm{mag}} \approx 3000$ Å given in Ref. [8]. On the one hand, the kinematic approach of Ref. [8] might be oversimplified, and therefore, the large magnetic mean-free paths should be interpreted with some caution. On the other hand, the magnetic mean-free paths of Zn-doped samples scale linearly with the Zn-distance (see Ref. [154] and the discussion in Sec. 3.2.3), which, from the experimental point of view, rather supports the large mean-free paths of Ref. [8]. From the theoretical point of view, the main conclusion of Ref. [54], i.e., the existence of a finite Drude weight for spin ladders, however, has to be questioned in view of the results for the thermal conductivity of Ref. [57] and of this thesis [i, iii, iv, v]. In Chapter 5, an extensive numerical study will be presented that supports the conclusion of a vanishing thermal Drude weight. This conclusion is in agreement with a recent numerical study by Zotos [57] and it can be further corroborated by field-theoretical arguments along the lines of Ref. [95]; see Sec. 5.2. The emerging picture is that instead of the Drude weight, the thermal conductivity is just the usual zero-frequency limit of a broad nonsingular function $\kappa_{\mathrm{reg}}(T,\omega)$, ω being the frequency,

$$\kappa(T) = \lim_{\omega\to 0} \kappa_{\mathrm{reg}}(T,\omega)\,. \tag{3.14}$$

Note, however, that despite the fact that in nonintegrable models such as spin ladders or frustrated chains, all relevant conservation laws are broken [iii, 59, 95], Rosch and coworkers argue that the large absolute values of κ_{mag} are mainly a consequence of the presence of *approximately* conserved currents [59, 97]. In contrast to this point of view, two alternative reasons are suggested: (i) κ_{mag} is large simply because the exchange couplings are large, and

(ii) external scattering processes are much weaker in the telephone-number compounds than in, e.g., $SrCuO_2$. In fact, recent theoretical studies [59, 158, 159] indicate that basically, the external scattering rates $1/\tau$ dominate the temperature dependence and limit the magnitude of κ_{mag} in $SrCuO_2$.

Scattering mechanisms

This leads directly to the discussion of the relevant scattering processes from the experimental point of view. Possible scattering mechanisms are: (i) intrinsic scattering, i.e., triplet-triplet interactions or (ii) external scattering, involving other quasi-particles such as acoustical phonons, optical phonons, charge carriers, or scattering on localized structural impurities, sample boundaries, or magnetic impurities.

While some authors consider scattering between acoustical phonons and triplets as a very likely process [14], Hess et al. [153] argue that due to spin conservation, such processes would require at least two triplets with opposite spin and one phonon. Since the spin gap is very large $\Delta_{\mathrm{sp}} \sim 400$ K, the energy ΔE transferred in such scattering event must be larger than 800 K. Typical energies of acoustical phonons, however, are much smaller in the cuprates; thus, on these grounds, Hess et al. conclude that acoustical phonons can be excluded as being a relevant scattering channel. Optical phonons, on the contrary, are found to have the right energies of the order of 800 K. Note that this is the energy of a Cu−O−Cu bond stretching mode in $La_5Ca_9Cu_{24}O_{41}$. One can push the analysis of the mean-free paths a little bit further by assuming [153]

$$l_{\mathrm{mag}}^{-1} = l_0^{-1} + \gamma_{\mathrm{trip}}\, d_{\mathrm{trip}}^{-1} + \gamma_{\mathrm{opt}}\, d_{\mathrm{opt}}^{-1} \,. \tag{3.15}$$

Here, scattering on impurities and sample boundaries is summarized in a temperature independent constant $1/l_0$ while d_{trip} and d_{opt} are measures of the mean distances of triplets and optical phonons, respectively. The prefactors γ_{trip} and γ_{opt} are introduced to account for different scattering probabilities. Next, the mean distances are related to the particle densities via $l_{\mathrm{trip,x}}^{-1} \propto n_x$ with n_x being the distribution function of the quasi-particles of species x. This procedure, taking the γ_x as fit parameters, results in a consistent fit of l_{mag} if only optical phonons are taken into account and a less good agreement if only triplet-triplet interactions are considered. Therefore, Hess et al. suggest that scattering between optical phonons and triplets is the most relevant process in $La_5Ca_9Cu_{41}O_{41}$ [153]. This would also explain why the thermal conductivity in this compound can be so large, since the relevant scattering channels involve high-energy processes.

3.2.2 Thermal conductivity of $Sr_{14-x}Ca_xCu_{24}O_{41}$

The differences in $\kappa_{\mathrm{mag}}(T)$ between $Sr_{14}Cu_{24}O_{41}$ and $La_5Ca_9Cu_{24}O_{41}$ at high temperatures, which are evident from Fig. 3.4(b), hint at triplet-hole scattering being efficient in suppressing the magnon thermal conductivity since $La_5Ca_9Cu_{41}O_{41}$ contains only very few holes. Regarding the hole content in the ladders of $Sr_{14}Cu_{24}O_{41}$, it has not yet fully been clarified whether this quantity is constant as a function of temperature or not [198, 199]. In any case, the observation of a low-temperature thermal conductivity κ_{mag}, which is almost identical in both samples, is consistent with the conclusion that triplet-hole scattering is very strong at high

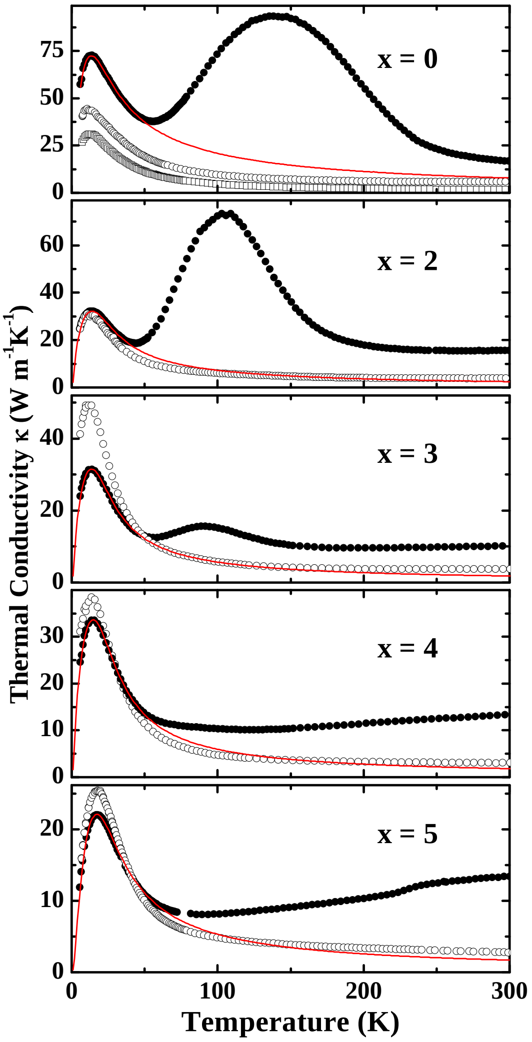

Figure 3.8: Thermal conductivity κ of Sr$_{14-x}$Ca$_x$Cu$_{24}$O$_{41}$ for $x = 0, 2, 3, 4, 5$. Solid symbols denote the thermal conductivity κ_c measured parallel to the ladders, while open symbols denote the conductivity κ_a measured perpendicular to the ladder planes. See Fig. 3.3 for the crystal structure. The upper-most panel also contains κ_b. The solid line in the latter panel is the usual fit of the low-temperature phonon maximum according to the Callaway model [194]. Reproduced from [11] with permission from the author.

but unimportant at low temperatures. This pictures has been further substantiated by a series of thermal transport measurements on Ca-doped samples, i.e., Sr$_{14-x}$Ca$_x$Cu$_{24}$O$_{41}$, which probe the scattering processes in more detail [10,11]. The results for κ of such measurements are shown in Fig. 3.8 for $x = 0, 2, 3, 4, 5$, where solid symbols denote κ_c and open symbols κ_a. The main observations are: (i) an overall suppression of κ_c and (ii) the high-temperature maximum is stronger reduced upon Ca-doping than the low-temperature peak. It eventually disappears for $x \geq 4$ and changes into a weak decrease of κ_c for $T > 80$ K. Since the replacement of Sr by Ca introduces randomness into the lattice, it is obvious that the phononic background is reduced. Note that different ions on Sr sites are not expected to have a strong effect on κ_{mag} since by replacing Sr by La, κ_{mag} rather increases at high temperatures while

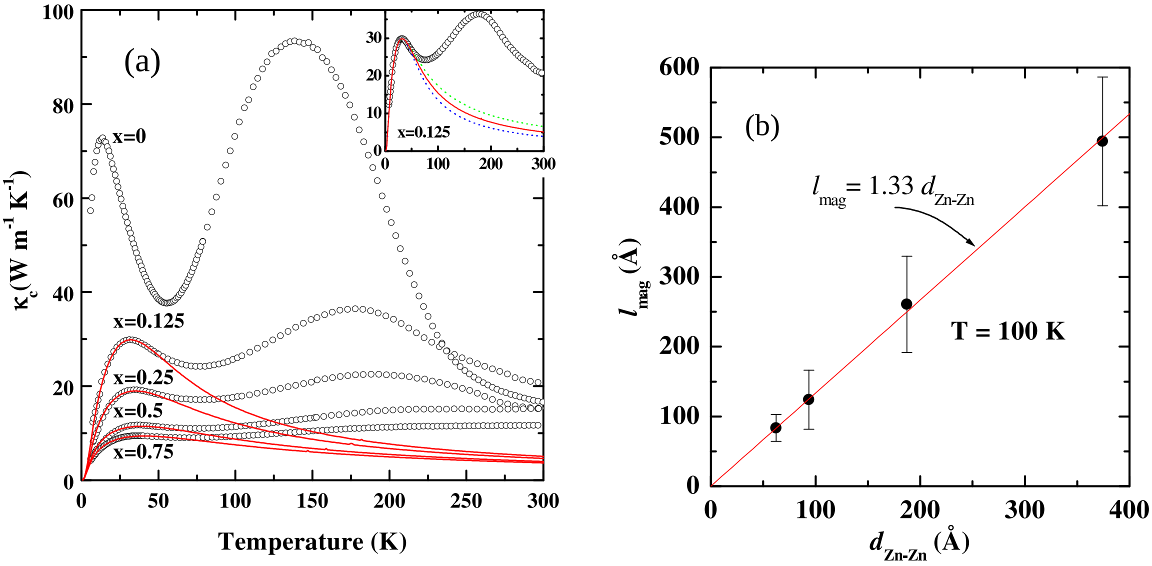

Figure 3.9: Thermal conductivity of Zn-doped $Sr_{14}Cu_{24-x}Zn_xO_{41}$. (a): κ_c for $x = 0.125, 0.25, 0.5, 0.75$. In the inset, κ_c is shown for the case of $x = 0.125$ and the dotted and solid lines illustrate the uncertainties in determining the phonon contribution. (b): Preliminary data for the magnetic mean-free paths $l_{\rm mag}$ of the Zn-doped samples versus inverse mean Zn-Zn distance at $T = 100$ K [154].

it is identical at low temperatures $T < 100$ K for both compounds; see Fig. 3.4(b) again.

In addition, some experimental studies [185, 186] suggest that the hole content in the ladders increases upon Ca-doping, from which one can infer that triplet-hole scattering efficiently relaxes the thermal current. Strong triplet-hole scattering seems to set in above a typical temperature T^* [11], and is apparently weaker at low temperatures as can already be inferred from the comparison of $Sr_{14}Cu_{24}O_{41}$ and $La_5Ca_9Cu_{24}O_{41}$. Based on this observation, Hess et al. discuss two possible scenarios [11]. On the one hand, the hole concentration in the ladders could be a function of temperature, increasing at higher T. This could be explained by a temperature-dependent transfer of holes from chains to ladders in $Sr_{14-x}Ca_xCu_{24}O_{41}$, which is supported by ^{17}O NMR measurements [198, 200]. On the other hand, inactive triplet-hole scattering may be a consequence of charge ordering in the ladders at low temperatures, with the hole concentration being constant as a function of temperature. The latter picture is corroborated by unpublished x-ray absorption spectroscopy data [199].

In summary, Hess et al. report experimental evidence for a temperature-dependent scattering probability for triplet-hole scattering in $Sr_{14-x}Ca_xCu_{24}O_{41}$ [11]. Further experiments seem to be necessary to substantiate one of the two proposals mentioned above. Finally, note that the investigation of charge ordering is interesting from a more general point of view, as a possible competition of charge ordered ground states and superconductivity is discussed for the cuprates; both for two- (see, e.g., Ref. [201]) and one-dimensional representatives [20, 193].

3.2.3 Thermal conductivity of Zn-doped $Sr_{14}Cu_{24}O_{41}$

Finally, doping the CuO planes with Zn allows for a study of the influence of nonmagnetic impurities on transport properties, since for each Zn-ion, one spin-1/2 moment is effectively removed. Here, results from Ref. [154] for the thermal conductivity of $\mathrm{Sr}_{14}\mathrm{Cu}_{24-x}\mathrm{Zn}_x\mathrm{O}_{41}$ with $x = 0.125, 0.25, 0.5, 0.75$ are summarized. $\kappa_c(T)$ is shown in Fig. 3.9(a). While the curves for small impurity concentrations display the typical double-peak structure, these features become less pronounced at higher doping levels and the extra contribution arising from magnetic excitations is rather seen as a slow increase of κ_c for temperatures $T \gtrsim 100$ K and, e.g., $x = 0.75$. An overall suppression of κ_c is evident from Fig. 3.9(a), as one would expect it since on the one hand, the Zn-ions on Cu sites induce phonon-impurity scattering, and on the other hand, magnetic excitations are likely to be scattered on nonmagnetic impurities.

Applying the analysis based on Eq. (3.9) one can extract the mean-free paths. For details as to how the phonon background is separated from κ_c,the reader may consult Ref. [154] The magnon thermal conductivity κ_{mag} is fitted along the lines of Ref. [8], assuming that the spin gap Δ_{sp} does not change upon Zn doping in first approximation. Scattering on holes must also be accounted for,[11] however, only at temperatures above roughly 100 K [11]. To this end, the ansatz

$$l_{\mathrm{mag}}^{-1} = l_0^{-1} + l_{\mathrm{h}}^{-1} \tag{3.16}$$

is made where l_0 is due to static defects and l_{h}^{-1} measures triplet-hole scattering. Knowing $l_{\mathrm{h}}(T)$ from Ref. [11], the authors assume this quantity not to be different in the Zn-doped samples and can then conclude that triplet-hole scattering is irrelevant for $T \lesssim 100$ K.

The mean-free paths l_{mag} are plotted versus the mean Zn-Zn distance $d_{\mathrm{Zn-Zn}}$ in Fig. 3.9(b). Very interestingly, the mean-free paths l_{mag} of the doped samples are found to scale linearly with the mean Zn distance $d_{\mathrm{Zn-Zn}}$, i.e.,

$$l_{\mathrm{mag}} = \mathrm{const}\, d_{\mathrm{Zn-Zn}} \tag{3.17}$$

where the constant is close to unity. In other words, these experiments show that Zn-doping is a tool to tune the magnetic mean-free paths in a controlled way. In summary, a consistent picture for the interpretation of the heat-transport measurements of these spin ladder compounds arises. The notion of magnon thermal conductivity in $(\mathrm{Sr,Ca,La})_{14}\mathrm{Cu}_{24}\mathrm{O}_{41}$ is strongly corroborated by the experiments on Zn-doped samples, since l_{mag} and, through Eq. (3.9), also κ_{mag} are linear in the Zn-Zn distance, as one would expect it in a quasi-particle picture for the magnon thermal conductivity.

3.2.4 Summary and other spin ladder compounds

In summary, broad experimental evidence exists supporting the conclusion of magnon thermal conductivity in $(\mathrm{Sr,Ca,La})_{14}\mathrm{Cu}_{24}\mathrm{O}_{41}$ [ii, 7–9, 11, 154] as a feature of the $\mathrm{Cu}_2\mathrm{O}_3$ spin ladder planes. The observed absolute values are very large, calling for an investigation of scattering mechanisms. An analysis of magnetic mean-free paths based on a kinetic model of Boltzmann type results in several interesting conclusions. Firstly, scattering on acoustical phonons can be ruled out on grounds of an energetic argument [153]. Thus, in the case of $\mathrm{La}_5\mathrm{Ca}_9\mathrm{Cu}_{24}\mathrm{O}_{41}$, the large values for κ_{mag} seem to be a consequence of both the very large exchange couplings and apparently weak external scattering mechanisms. While theoretical studies indicate that triplet-triplet scattering should lead to a relaxation of the thermal current (see Ref. [57] and Chapter 5), this channel could be weaker than scattering on optical phonons [153]. Secondly,

---

[11] See the previous section on thermal transport properties of $\mathrm{Sr}_{14-x}\mathrm{Ca}_x\mathrm{Cu}_{24}\mathrm{O}_{41}$, Sec. 3.2.2.

experiments on Ca-doped samples and the comparison with the compound $La_5Ca_9Cu_{24}O_{41}$ reveal that triplet-hole interactions efficiently reduce the thermal conductivity. Hess et al. suggest thermal conductivity measurements as a tool to probe these interactions and propose the existence of charge ordering in the ladders [11]. Thirdly, it is found that the magnetic mean-free paths, defined in terms of Eq. (3.9), can directly be tuned by doping the Cu_2O_3 planes with nonmagnetic Zn-ions, strongly supporting the notion of magnon thermal conductivity [154].

It is, however, somewhat unsatisfactory that such very large values of κ have so far only been reported for this particular family of materials. Transport measurements for other potential ladder materials[12] such as $CaCu_2O_3$ also find indications for anisotropic thermal transport hinting at a magnetic contribution, however, with significantly smaller absolute values of κ observed [195]. Recently, Kudo et al. [165,166] have reported experimental results for the thermal conductivity of $La_2Cu_2O_5$. A strong anisotropy of the κ tensor is observed, but no double-peak structure. One should also mention that, while the structure of $La_2Cu_2O_5$ suggests that four-leg ladders are realized in this material, the system does not have a spin gap, but rather orders antiferromagnetically with a Néel temperature of $T_N = 130$ K [203]. Thus the magnetic properties are different from those of $(Sr,Ca,La)_{14}Cu_{24}O_{41}$, in particular, since $La_2Cu_2O_5$ has gapless instead of massive excitations, as it has been pointed out in Refs. [165,166].

Coming back to $(Sr,Ca,La)_{14}Cu_{24}O_{41}$, it seems that the large thermal conductivity is a consequence of a large intrinsic conductivity which is only weakly reduced by external scattering. The strength of external scattering mechanisms is likely to strongly depend on material specific parameters.

3.2.5 Discussion of theoretical results for spin ladder materials

As mentioned above, in a first numerical study on thermal transport in nonintegrable spin systems, Alvarez and Gros conjectured that a finite thermal Drude weight exists in the thermodynamic limit for two-leg spin ladders and frustrated as well as dimerized chains [54,58]. Stimulated by their work, Orignac et al. studied the thermal Drude weight of effective low-energy models based on a representation of the spin ladder Hamiltonian in terms of Majorana fermions [55]. They have analyzed the magnetic field dependence of the thermal Drude weight and the influence of impurities on the thermal Drude weight. This study does not provide for a proof of a finite Drude weight, since the finite Drude weight is a consequence of the mapping onto noninteracting particles.

A subsequent numerical study [57] as well as the results of this thesis indicate that the picture of ballistic thermal transport is not supported by either numerical results or field theoretical arguments. Rather, the relevant quantity seems to be the regular part of $\mathrm{Re}\,\kappa(\omega)$. For an extended discussion, the reader is referred to Chapter 5.

From the theoretical point of view, it would be desirable to predict the size and temperature dependence of κ_{mag} for pure spin ladders for the experimentally relevant temperature and parameter range. Using numerical techniques, this is currently possible by extrapolating

---

[12] Note that optical spectroscopy measurements performed on $CaCu_2O_3$ samples indicate that this is rather a spin chain material with non-negligible three dimensional interchain couplings [202].

the numerical results for κ_{mag} obtained from $\mathrm{Re}\,\kappa_{\mathrm{reg}}(\omega)$;

$$\kappa_{\mathrm{mag}} = \lim_{\omega \to 0} \mathrm{Re}\,\kappa_{\mathrm{reg}}(\omega)\,, \tag{3.18}$$

from the high-temperature limit down to temperatures accessible by experiments. While such comparison presumes some assumptions as to how to perform the extrapolation, the absolute values of the theoretical results for κ_{mag} turn out to be of the same order of magnitude as the experimental data (see [57] and Sec. 5.6). Thus, the conclusion of magnon thermal conductivity drawn from the experimental data is consistent with the available theoretical work.

The thermal conductivity of hole-doped ladders, relevant for $Sr_{14-x}Ca_xCu_{24}O_{41}$ and large doping levels x, was studied in Ref. [204].[13] In their theory dressed holons and spinons are introduced and a mean-field type of approximation is applied to decouple the holon and spinon sector as well as to separate the thermal current into a purely holon and a spinon contribution. Phonons are not taken into account and the authors propose, based on a comparison of their results with experimental data from Ref. [7], that the thermal conductivity in the Ca-doped samples is dominated by the contribution from dressed spinons [204].

3.3 Thermal conductivity of spin chain compounds

In this section, results for the thermal conductivity of four materials are summarized: $SrCuO_2$, Sr_2CuO_3, $BaCu_2Si_2O_7$, and $AgVP_2S_6$ [12–15, 206]. In the first three cases, spin-1/2 chains are realized, while $AgVP_2S_6$ is a Haldane compound with spin-1. $SrCuO_2$ and Sr_2CuO_3 are materials with a large energy scale of the magnetic systems since the exchange coupling is of the order of 2000 K. This has to be contrasted against $BaCu_2Si_2O_7$, where the exchange coupling is one order of magnitude smaller.

3.3.1 Spin chain compounds with large J: $SrCuO_2$ and Sr_2CuO_3

Structural and magnetic properties

For the spin chain compounds $SrCuO_2$ and Sr_2CuO_3, experimental results on the thermal conductivity have been reported by Sologubenko et al. [12, 13] and more recently also by Ribeiro et al. for Ca-doped samples [206], i.e., $Sr_{1-x}Ca_xCuO_2$.

In both $SrCuO_2$ and Sr_2CuO_3, spin chains are realized [207, 208]; with the difference that the chains in Sr_2CuO_3 are linearly aligned, while in $SrCuO_2$, there are zig-zag, or double chains. The units cells are depicted in Fig. 3.10. The interchain coupling in Sr_2CuO_3, denoted by J' in Fig. 3.10, but not drawn for this material, is very small compared to the intrachain coupling J, being of the order of 2000–3000 K for both materials. Therefore the exchange couplings are of comparable magnitude as those of $Sr_{14}Cu_{24}O_{41}$. A major difference between these two materials and the spin ladder compound $Sr_{14}Cu_{24}O_{41}$ is that the spectrum of the former ones is gapless while the elementary excitations of the ladder subsystem of $Sr_{14}Cu_{24}O_{41}$ are massive triplet excitations. Note that the spectrum of $SrCuO_2$ remains gapless despite

---

[13] Within the same theory, the optical conductivity of hole-doped spin ladders was analyzed in Ref. [205].

of the weak interchain coupling $|J'| \sim 0.1J$ [209], since J' is a ferromagnetic interaction [210]. The elementary excitations of Heisenberg spin chains are spin-1/2 quantities, named spinons [211]. Since spinons can only be created in pairs, the spectrum is a continuum of two-particle excitations. The dispersion relation of a single spinon excitation is the well-known Cloizeaux-Pearson dispersion [212]

$$\epsilon_k = \frac{\pi}{2} J |\sin(ka)| \,, \tag{3.19}$$

where a denotes the lattice spacing along the chain. For an extended review of spin chain materials and their properties, the reader is referred to, e.g., the paper by Johnston et al. [29] and further references therein.

Experimental results for the thermal conductivity

As mentioned in Sec. 3.1, the thermal conductivity of both compounds is anisotropic with a larger conductivity found if κ is measured parallel to the chains. This is the c'-direction, see Figs. 3.1 and 3.10. In comparison with $Sr_{14}Cu_{24}O_{41}$, $\kappa_{c'}$ does not exhibit a clear double-peak structure, but rather, the additional contribution in the c'-direction is signaled by a shoulder in the high-temperature side of the phonon maximum. The phonon maximum is located around 20 K for both compounds. All authors agree that this first maximum is of phononic origin [12,13,206]. Regarding possible explanations for the shoulder seen in κ_c, electrons are excluded since both materials are insulating [13]. Anisotropic phonon-phonon scattering is ruled out since the elastic constants are only weakly anisotropic [13]. Thus, the remaining transport channels are optical phonons or spinons. The first possibility is argued to be less likely on the basis of the results for Ca-doped $SrCuO_2$, i.e., $Sr_{1-x}Ca_xCuO_2$ [206]. Thus we are left with thermal transport mediated by spinons by applying the principle of *working by exclusion*.

A further quantitative analysis of the magnon thermal conductivity is more complicated than for the ladder materials. In the latter ones, the existence of the large spin gap of the order of 400 K gave good reason to assume that κ_{mag} is negligible in the entire temperature range where κ_{ph} is large. In the spin chain materials, the maxima of κ_{mag} and κ_{ph} apparently merge, which renders a straightforward separation of the two contributions difficult.

Quantitative analysis of the experimental data

Let us now discuss how the separation of the phonon and magnetic contribution was done for $SrCuO_2$ and Sr_2CuO_3. Sologubenko et al. used the Debye-model [194] to model the phonon thermal conductivity both parallel and perpendicular to the chains

$$\kappa_{\text{ph}}(T) = \frac{k_k}{2\pi^2 v_{\text{ph}}} \left(\frac{k_B}{\hbar}\right)^2 \int\limits_0^{\Theta_D/T} dx\, \frac{x^4 e^x}{(e^x-1)^2}\, \tau(x(\omega),T) \,. \tag{3.20}$$

In this equation, v_{ph} denotes the sound velocity, Θ_D is the Debye temperature, ω is the phonon energy or frequency, respectively, $x = \hbar\omega/k_BT$, and $\tau(\omega,T)$ is the relaxation time. By including a number of scattering processes into $\tau(\omega,T)$ such as scattering on sample

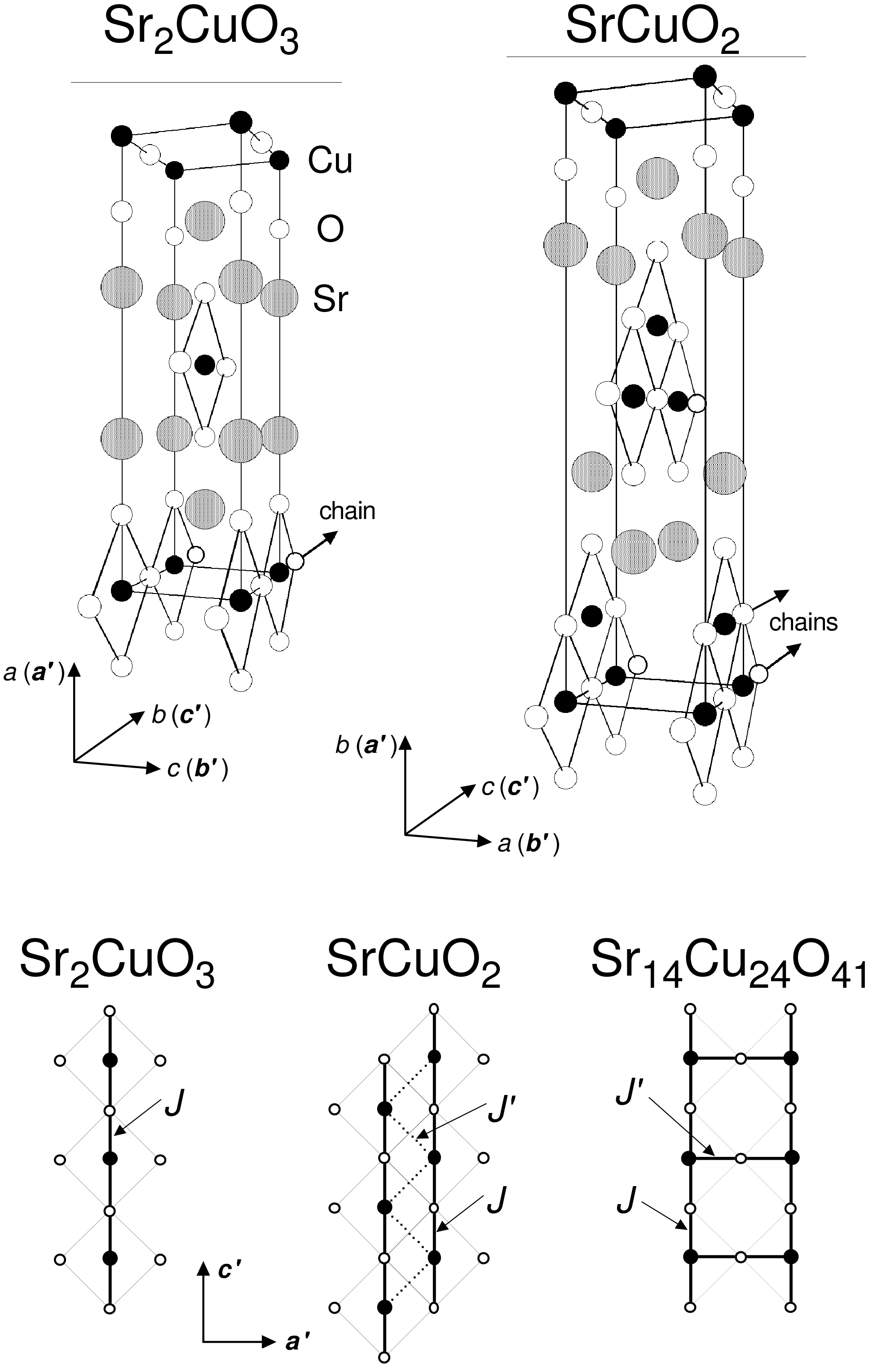

Figure 3.10: The schematic unit cell of Sr_2CuO_3 and $SrCuO_2$ is shown in the upper left and upper right panel, respectively. Small solid circles represent Cu-atoms, while small open circles indicate the position of O-atoms. Lower panel: CuO chains in Sr_2CuO_3 and $SrCuO_2$, compared to the ladders in $Sr_{14}Cu_{24}O_{41}$. Note the labeling of the axes. The labels (a', b', c') are in the following used to distinguish between measurements parallel to the chains (c'-direction) or perpendicular to the chains (a', b'-direction). For $SrCuO_2$ and Sr_2CuO_3, J denotes the coupling along the chain direction, while J' is the interchain coupling. For $(Sr,Ca,La)_{14}Cu_{24}O_{41}$, J is the coupling along the legs of the two-leg ladder, and J' is the rung coupling. Reproduced from [13] with permission from the author; the structures are known from Refs. [207, 208].

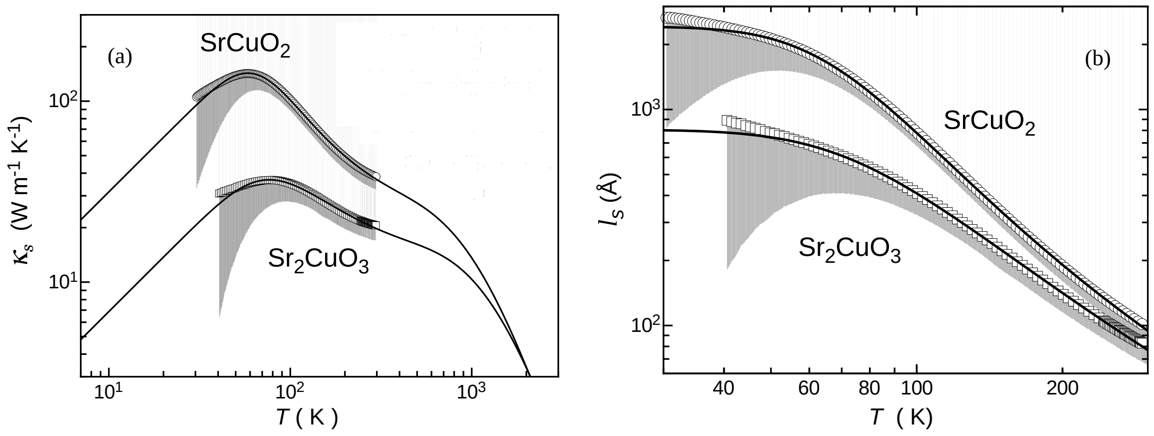

Figure 3.11: (a): Magnetic contribution to the thermal conductivity of $\mathrm{SrCuO_2}$ and $\mathrm{Sr_2CuO_3}$ obtained by subtracting the phonon background from the conductivity measured parallel to the chains. See Ref. [13] for further details. The shaded areas indicate the uncertainties in the determination of κ_{mag} (denoted by κ_s in Refs. [12] and [13]). Note that both axes are scaled logarithmically. (b): Mean-free paths for $\mathrm{SrCuO_2}$ and $\mathrm{Sr_2CuO_3}$; obtained from κ_{mag} by using Eq. (3.22). Reproduced from Ref. [13] with permission from the author.

boundaries, on point defects, phonon-phonon umklapp processes, and resonant scattering, several free fit parameters are introduced. A fair description for the directions perpendicular to the chains could be achieved in Ref. [13], while this approach failed for the direction parallel to the chains. In order to extract the possible spinon contribution to $\kappa_{c'}$, $\kappa_{c'}$ was fitted below $T = 10$ K, partially fixing some of the free parameters to the values obtained for the perpendicular directions.[14] This procedure yields an estimate for $\kappa_{c',\mathrm{ph}}$, and results for κ_{mag} obtained from $\kappa_{\mathrm{mag}} = \kappa_{c'} - \kappa_{c',\mathrm{ph}}$ are shown in Fig. 3.11(a) for both materials.[15]

Note the values: the maximum total κ_c of $\mathrm{SrCuO_2}$ is of the order of 300 K [13, 206] and κ_{mag} still reaches values of 150 K as can be seen in Fig. 3.11(a). This even exceeds the values reported for $\mathrm{La_5Ca_9Cu_{24}O_{41}}$ [8], but at room temperature the thermal conductivity of the spin ladder compounds is clearly larger than in the spin chain materials. Similar to the telephone-number compounds, practically no variation of κ_c in magnetic fields of up to 14 T is found [213].

In the following, we shall discuss some aspects of a quantitative analysis of κ_{mag}. Firstly, the results for the magnetic mean-free paths l_{mag} reported in Ref. [13] are discussed, which have been derived from the experimental data using Eq. (3.4). Finally, we show that Eq. (3.4) is equivalent to

$$\kappa_{\mathrm{mag}} = K_{\mathrm{th}}(T)\tau(T)/\pi \tag{3.21}$$

in the low-temperature limit. K_{th} is the thermal Drude weight, which is exactly known from Ref. [78].[16] Via $l_{\mathrm{mag}} = v_s\tau(T)$, the mean relaxation time is directly proportional to the mean-free path.

We turn to a closer inspection of the experimental results for κ_{mag} of $\mathrm{SrCuO_2}$ and $\mathrm{Sr_2CuO_3}$ and a discussion of magnetic mean-free paths; keeping in mind that the results for κ_{mag} shown

---

[14] See Ref. [13] for the exact definition of all fit parameters.

[15] In this chapter, the thermal conductivity mediated via magnetic excitations is uniquely denoted by κ_{mag}, while Refs. [12] and [13] use the symbol κ_s instead.

[16] See Chapter 4 for a discussion of the thermal Drude weight of spin-1/2 XXZ chains.

in Fig. 3.11(a) may be affected by possible systematic errors inherent to the procedure of determining κ_{ph}.

In Ref. [13], the authors start their analysis of κ_{mag} by writing down the one-dimensional analog to the Debye-type of model used to describe the phonon thermal conductivity:

$$\kappa_{\mathrm{mag}} = \frac{2n_s k_B^2}{\pi\hbar} T \int\limits_0^{\pi J k_B/(2T)} \frac{x^2 e^x}{(e^x+1)^2}\, l_{\mathrm{mag}}(x(\epsilon),T)\, dx\,. \tag{3.22}$$

Here, $x = \epsilon/k_B T$ is dimensionless and n_s denotes the number of spin chains per unit area. The underlying assumption of a linear dispersion for the spinons is justified for a nearest neighbor chain. Below, we shall argue that in a wide temperature range, any dispersion effects can be neglected for these materials since the exchange couplings are so large.

Lacking a theory for $l_{\mathrm{mag}}(x(\epsilon),T)$, the energy dependence of $l_{\mathrm{mag}}(x(\epsilon),T)$ was neglected in Ref. [13] and $l_{\mathrm{mag}}(T)$ was taken in front of the integral. The resulting expression is analogous to Eq. (3.9), with the only differences that first, in Eq. (3.22) the Fermi-function is the correct distribution function and that second, the boundaries are different. The results for l_{mag} are depicted in Fig. 3.11(b). At low temperatures, values of $l_{\mathrm{mag}} \sim 2500$ Å are found for $\mathrm{SrCuO_2}$. This corresponds to roughly 650 lattice constants, since $c = c' = 3.9$ Å [171]. The mean-free paths for $\mathrm{Sr_2CuO_3}$ are slightly smaller, but they are as large as those found for the telephone-number compounds. In contrast to the case of spin ladders, there are no adjustable parameters in Eq. (3.22).

Furthermore, the authors of Ref. [13] report the following temperature dependence of the mean-free paths

$$l_{\mathrm{mag}}^{-1} = l_{\mathrm{sp}}^{-1} + l_{\mathrm{sd}}^{-1} = A_{\mathrm{sp}}\, T\, e^{-T^*/T} + L_{\mathrm{sd}}^{-1}\,. \tag{3.23}$$

Note that the T-dependences of l_{mag} and κ_{mag} only differ by a factor of T in the low-temperature regime. In Ref. [59], a theory of spin-1/2 Heisenberg chains coupled to three dimensional phonons was developed. The authors predict a temperature dependence of κ_{mag} similar to Eq. (3.23). The experimentally determined T^* is roughly equal to $\Theta_D/2$.

Finally, some comments follow on the relation of Eq. (3.22) to the thermal Drude weight. Under the assumption of a frequency-independent scattering rate $1/\tau$ and in the low-temperature limit, Eq. (3.21) is equivalent to Eq. (3.22). The thermal Drude weight of the $S = 1/2$ Heisenberg chain at low temperatures is given by [78, 80]

$$K_{\mathrm{th}}(T) = \frac{\pi^2}{3} v\, T\,. \tag{3.24}$$

For $\mathrm{SrCuO_2}$ and $\mathrm{Sr_2CuO_3}$, deviations from this linear temperature dependence of the Drude weight would only become relevant beyond the temperature interval that is accessed by experiments since the exchange couplings are that large. The maximum of the thermal Drude weight is located at $0.3J \sim 600$ K given a coupling of $J \sim 2000$ K, in contrast to the experimental κ_{mag}, which has its maximum at 60. . . 80 K $\sim J/30$. This is illustrated in Fig. 3.12(a), where K_{th} is plotted versus temperature in units of J. Figure 3.12(b) shows the one-spinon dispersion, which is linear in k at small wavenumbers. The fact that the Drude weight is linear in temperature below room temperature tells us that the temperature dependence of κ_{mag} is strongly dominated by that of the external scattering rates $1/\tau(T)$. In particular, one can expect the high-temperature behavior to deviate from $\kappa \propto 1/T^2$. This is in agreement with recent theoretical work [59, 158, 159] studying the thermal conductivity of Heisenberg

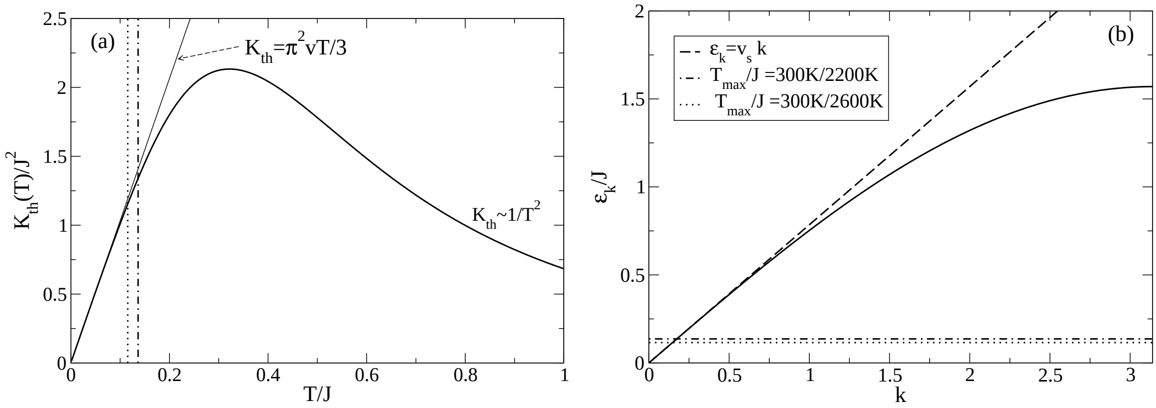

Figure 3.12: (a): Thermal Drude weight K_{th} of the Heisenberg chain versus temperature from Ref. [78]. Both axes are scaled in units of the exchange coupling J. The data shown here are exact in the thermodynamic limit. (b): One-spinon dispersion of the Heisenberg chain [212]. The dashed line shows $\epsilon_k = vk$. The dot-dashed and dotted horizontal lines denote the maximum temperature $T_{\max} = 300$ K accessed in experiment, normalized on $J = 2200$ K (dot-dashed lines) and $J = 2600$ K (dotted lines), respectively.

chains coupled to phonons and/or impurities.

Since at low temperatures, one can expect spinon-phonon scattering to be frozen out, the remaining source for scattering are impurities and boundaries of the sample. For this type of scattering, it is often assumed that the mean-free path is a constant, independent of momentum and energy. This results in a constant scattering rate

$$l_{\mathrm{mag}} = v_s\tau = \mathrm{const} \quad \Rightarrow \quad 1/\tau = \mathrm{const}\,, \tag{3.25}$$

since the spinon velocity $v_s = \langle v_k \rangle$ is a constant at low temperatures. Hence one expects κ_{mag} to be proportional to the specific heat, i.e., $\kappa_{\mathrm{mag}} \propto C_V$.

Inserting on the one hand Eq. (3.24) in Eq. (3.21) and plugging in the necessary prefactors to obtain correct units and to account for the geometry, one finds:

$$l_{\mathrm{mag}} = \frac{3}{\pi}\frac{\hbar}{k_B^2 n_s}\frac{\kappa_{\mathrm{mag}}}{T}\,. \tag{3.26}$$

where $n_s = 1/(14.6\ \mathring{\mathrm{A}}^2)$ is the number of spin chains per unit area [171]. On the other hand, setting the upper limit of the integral in Eq. (3.22) to infinity, the integral can easily by computed for constant l_{mag}, yielding $\pi^2/6$. Then, it is obvious that Eq. (3.21) and Eq. (3.22) are equivalent.

Finally, the main results are summarized as they arise from the analysis of the experimental data: (i) In both compounds, κ is anisotropic, with a larger thermal conductivity observed parallel to the chains [13,206]. (ii) In contrast to the ladders there are no direct experimental proofs for the magnetic origin of the anisotropy. (iii) Using a kinetic model and assuming a k-independent mean-free path l_{mag} to analyze the magnetic contribution to κ_c, large values for l_{mag} are found, similar to the case of the spin ladders. (iv) For the gapless system, the kinetic model is equivalent to the form $\kappa_{\mathrm{mag}} = K_{\mathrm{th}}\tau/\pi$ at low temperatures, with $K_{\mathrm{th}} \propto C_V$. (v) In the temperature range accessed by experiments, the thermal Drude weight is linear in temperature because of the size of the exchange couplings. Therefore, one can conclude that the temperature dependence is dominated by that of the scattering rates, or relaxation times, respectively.

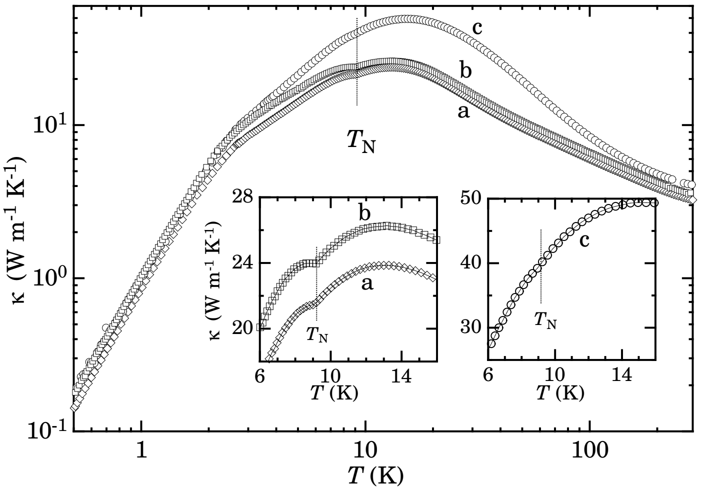

Figure 3.13: Thermal conductivity of the spin chain compound $BaCu_2Si_2O_7$. κ was measured both parallel (c-direction) and perpendicular to the chains (a, b-direction). The material exhibits antiferromagnetic order at low temperatures; T_N denotes the Néel temperature. The insets shows zooms around T_N. Note that the axes are scaled logarithmically. Reproduced from Ref. [14] with permission from the author.

Thermal conductivity of $Sr_{1-x}Ca_xCuO_2$

Very recently, Ribeiro et al. have performed thermal transport measurements on the series $Sr_{1-x}Ca_xCuO_2$ with $x = 0, 0.05$ [206]. Both the thermal conductivity parallel (κ_c) and perpendicular (κ_a) to the chains have been measured. In a nutshell, their main results are: (i) The presence of anisotropic thermal transport in all samples is confirmed. (ii) By excluding other possible origins of the shoulder in κ_c the authors explain the shoulder in terms of magnon thermal conductivity in addition to the phonon contribution. (iii) Upon Ca-doping, the phonon thermal conductivity is suppressed in the vicinity of its maximum, as is seen in the thermal conductivity perpendicular to the chains. Conversely, the temperature dependence of the thermal conductivity parallel to the chain direction is altered at all temperatures upon Ca-doping. At room temperature, however, the same value for κ_c is reached in both the doped and undoped sample. (iv) The Ca-doped samples exhibit a constant thermal conductivity $\kappa_c \approx 50$ WK^{-1}m^{-1} along the chain direction for $T > 100$ K. Moreover, the thermal conductivity κ_a is of the order of $\kappa_a \lesssim 25$ WK^{-1}m^{-1} for $T > 100$ K, being smaller by a factor of two than κ_c in a wide temperature range, from which the authors infer that a magnetic contribution to the thermal conductivity is present in the c-direction.

3.3.2 A spin chain compound with small J: $BaCu_2Si_2O_7$

Among the three examples discussed in this section, $BaCu_2Si_2O_7$, which is another spin-1/2 chain material, is the only one where $\kappa(T)$ does not show a pronounced double-peak structure when measured along the chain direction. This can be seen in Fig. 3.13. The material contains antiferromagnetic spin chains, however, with an exchange coupling of $J = 230 \ldots 280$ K along the chains [175] compared to $SrCuO_2$ where $J = 2600$ K [171]. Thus, we do not expect a

Material	Refs.	$l_{\mathrm{mag,max}}$ [Å]	l_{mag} [Å] (T=300 K)
$BaCu_2Si_2O_7$	[14]	2160±2	10
$SrCuO_2$	[12]	3250±10	70
Sr_2CuO_3	[12, 13]	810±20	77
$La_5Ca_9Cu_{24}O_{41}$	[71]	3000±10	600

Table 3.2: Comparison of magnetic mean-free paths l_{mag} for some materials. The table lists the maximum value of $l_{\mathrm{mag}}(T)$ and the value at room temperature $T = 300$ K. The magnetic mean-free paths have been extracted from the experimental results by using either Eq. (3.2) or Eq. (3.4).

clear separation of the phononic energy scale, the Debye temperature Θ_D, and the magnetic scale set by J. Indeed, in experiment, only an enhancement of κ_c is observed in the c-direction along the chains, compared to the perpendicular directions, but neither a double-peak structure nor a shoulder in $\kappa(T)$ is found. The labels a, b, c denote the crystallographic directions. In the chain direction, κ_c exceeds κ_{ab} by a factor of two [14]. This anisotropy is attributed to magnon thermal conductivity by excluding other possible reasons, such as, e.g., anisotropic elastic constants, or anisotropies in the scattering strength between phonons and spinons. Determining the magnetic part of κ_c by subtracting the average conductivity of the perpendicular directions, i.e.,

$$\kappa_{\mathrm{mag}} = \kappa_c - \frac{\kappa_a + \kappa_b}{2} \tag{3.27}$$

results in a maximum value of approximately 25 $\mathrm{WK^{-1}m^{-1}}$ for κ_{mag} [14]. In order to extract the magnetic mean-free paths, Sologubenko et al. [14] have assumed

$$\kappa_{\mathrm{mag}} = K_{\mathrm{th}}(T)\,\tau/\pi; \quad l_{\mathrm{mag}} = v_s(T)\tau \tag{3.28}$$

where $K_{\mathrm{th}}(T)$ is the thermal Drude weight, τ the relaxation rate and $v_s(T)$ the spinon velocity. Note that the Drude weight has its maximum at roughly 80 K for this value of J. Thus, in contrast to $SrCuO_2$, the Drude weight depends nonlinearly on temperature in the experimentally relevant temperature range. The experimentally observed κ_{mag} has its maximum at sufficiently lower temperatures and decreases monotonously for $T > 20$ K. Taking the results of Ref. [78] for $K_{\mathrm{th}}(T)$ the authors find a maximum value of $l_{\mathrm{mag}} \approx 2000$ Å [14], consistent with the results found for other spin chain materials. See also Refs. [12,13] and Table 3.2 for a comparison of magnetic mean-free paths of the quasi-one dimensional materials $(Sr,Ca,La)_{14}Cu_{24}O_{41}$, $SrCuO_2$, Sr_2CuO_3, and $BaCu_2Si_2O_7$.

3.3.3 A spin-1 Haldane chain: $AgVP_2S_6$

Apart from spin-1/2 chains, results for the thermal conductivity of the Haldane compound $AgVP_2S_6$ have recently been reported by Sologubenko et al. [15]. The magnetic properties of this material are described by a next-nearest Heisenberg term plus a single-ion anisotropy:

$$H = J \sum_l \vec{S}_l \cdot \vec{S}_{l+1} + D \sum_l (S_l^z)^2 \,. \tag{3.29}$$

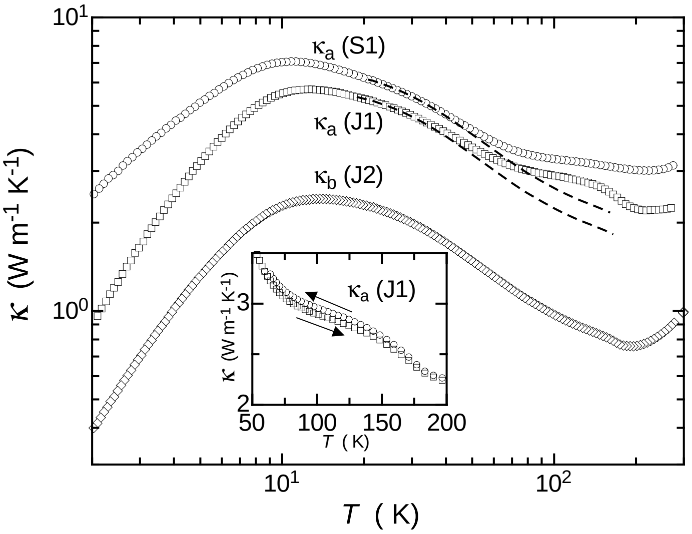

Figure 3.14: Thermal conductivity of the Haldane compound $AgVP_2S_6$ for two samples (S,J); measured parallel (a-direction) and perpendicular (b-direction) to the chains. The inset shows the hysteresis in κ_a at high temperatures, which has also been observed for $(Sr,Ca,La)_{14}Cu_{24}O_{41}$ [71] and $CaCu_2O_3$ [195]. Reproduced from Ref. [15] with permission from the author.

Among the four materials discussed in this section, $AgVP_2S_6$ is a special case, since the model Hamiltonian Eq. (3.29) is nonintegrable, both since it describes a spin-1 chain and due to the single-ion anisotropy. Thus, the underlying physics is already different as compared to, e.g., $SrCuO_2$.

For the constants J and D, the values $J = 780$ K and $D/J = 5.8 \cdot 10^{-3}$ are reported in Ref. [15], while the interchain coupling $J'/J \sim 10^{-5}$ is very weak. In contrast to spin-1/2 chains, the spectrum of an integer-spin chain is gapped [214], and for spin-1 chains, a gap of $0.41J$ is expected from theory [215]. For energy transport, the approximative treatment of Huber et al. [39, 40] predicted diffusive behavior for $S = 1$. This picture has recently been confirmed by a numerical study of thermal transport in a spin-1 chain finding indications of a vanishing thermal Drude weight in the thermodynamic limit, excluding ballistic transport [96]. Interestingly, the case of spin transport in Haldane chains is still debated quite controversially in the literature [96, 216–222]. Experimentally, NMR measurements rather point to the presence of diffusive spin transport [223].

The results for κ, measured both parallel (κ_a) and perpendicular (κ_b) to the chain direction are shown in the left panel of Fig. 3.14. The figure contains results from measurements on different samples, denoted by J and S in the figure. The magnitude of κ being of the order of $\lesssim 10$ WK^{-1}m^{-1} is, in general, much smaller than in the case of spin-1/2 chain materials. κ_a exceeds κ_b by a factor of two and exhibits a shoulder at temperatures $T \gtrsim 50$ K, and the latter effect is ascribed to magnon thermal conductivity present in this system [15]. Reference [15] mainly focuses on a analysis of the energy diffusion constant

$$D_E = \kappa_{\mathrm{mag}}/C_V \tag{3.30}$$

in comparison with the spin diffusion constant D_S, which is experimentally known for this compound from Ref. [223]. These two quantities turn out to be of the same order of magnitude with $D_E \approx 2\,D_S$. An additional analysis of the magnetic mean-free paths resulted in very small values of 60 Å and led to the conclusion of diffusive transport in this Haldane compound.

The apparent strong difference of the magnitude of κ_{mag} between $S = 1/2$ and $S = 1$ chains calls for a theoretical explanation. For the $S = 1$ chain, being nonintegrable, one expects intrinsic scattering to be more relevant than in spin-1/2 Heisenberg chains. An interesting extension of the existing theoretical work would pertain to a comparative study of the thermal conductivity of ladders and Haldane chains since it is at present unclear why the magnon thermal conductivity is so much larger in the telephone-number compounds.

3.3.4 Discussion of theoretical results for spin chain materials

The last part of this section summarizes the theoretical work that has been devoted to the thermal conductivity of Heisenberg chains, with a particular focus on $SrCuO_2$ and Sr_2CuO_3. Many studies have concentrated on the notion of diffusive transport [38–40], the study of the thermal Drude weight $K_{\mathrm{th}}(h,T)$ as a function of temperature and magnetic field [i,iii,ix,54,78, 82], or external scattering mechanisms suchs as phonons [59,158,159] and impurities [158,159]. The thermal Drude weight will be discussed in Chapter 4. Here we concentrate on the concept of diffusive transport and those papers that have made predictions for the temperature dependence of the external scattering rates [59, 158, 159].

In the first papers on thermal conductivity of $SrCuO_2$ and Sr_2CuO_3 [12,13], some attention was paid to the question of possible diffusive versus ballistic transport. These terms have been introduced in Sec. 2.3.3. First theoretical studies on energy transport in ferromagnetic and antiferromagnetic spin-S chains [38–40] focused on the computation of the energy diffusion constant D_E [39], which is defined by

$$\kappa_{\mathrm{mag}} = C_V\, D_E\,, \tag{3.31}$$

where C_V is the specific heat per volume. As a result Huber et al. found that energy transport is nondiffusive[17] for $S = 1/2$ and diffusive for $S > 1/2$ [39, 40]. This is reflected in the result for the diffusion constant from Ref. [39]:

$$D_E = \mathrm{const}\frac{\sqrt{S(S+1)}}{1-3/[4-S(S+1)]}\,. \tag{3.32}$$

Obviously, D_E diverges for $S \to \infty$. While the results of these early papers [38–40] where based on some approximations,[18] the qualitative picture came out correctly. It was further argued that next-nearest neighbor interactions or interchain interactions are expected to restore diffusive transport even for spin-1/2 chains [41].

Later on it was shown that, for $S = 1/2$, the energy-current operator is a conserved quantity [61, 74], which directly leads to a diverging conductivity. Therefore, the relation

$$\mathrm{Re}\,\kappa_{\mathrm{mag}}(\omega) = K_{\mathrm{th}}(T)\delta(\omega) \tag{3.33}$$

holds, where $K_{\mathrm{mag}}(T)$ is the thermal Drude weight. The temperature dependence of this quantity has been computed exactly [78], and it turns out that the implicit assumption of

---

[17] This result has not been noticed in Ref. [38], where a finite thermal conductivity for a ferromagnetic chain was found. This incorrect result is due to the approximative, equation-of-motion type of method applied in Ref. [38].

[18] Basically, the six-point spin correlation function appearing in the Kubo formula, since j_{th} is a product of three spin operators, was decomposed in a product of three two-point functions.

Eq. (3.31), i.e., a proportionality of κ and the specific heat C_V, is valid for the thermal Drude weight at low temperatures only [78]:

$$K_{\mathrm{th}}(T) \propto C_V \, . \tag{3.34}$$

Finally, the results of Refs. [59] and [158, 159] are briefly summarized. In Ref. [59], heat transport in spin-1/2 Heisenberg chains coupled to acoustical phonons is studied within the framework of the Mori-Zwanzig projection formalism. No transverse coupling between the spin chains is included in this work. The main ingredient of the analysis presented in Ref. [59] is the presence of softly violated conservation laws, which prevent a certain part of the thermal current from decaying. The theory is designed to be valid close to the Hamiltonian's fixed point, i.e., the Luttinger liquid. Sufficiently many irrelevant corrections, including both spinon-spinon and spinon-phonon interactions, are added to the Luttinger liquid which degrade the thermal current, the strongest ones being umklapp scattering terms [59]. Thus, while the Drude weights vanish in this theory, the large magnitude of the experimentally observed κ_{mag} is ascribed to slowly decaying parts of the thermal current. Qualitatively, $\kappa \propto \exp(T^*/T)$ with $T^* \sim \Theta_D/2$ is derived as a main result, in agreement with the experimental observation Eq. (3.23).

However, the theory presented in Ref. [59] can apparently not predict the magnitude of κ_{mag}, since it is designed as a theory close to the Luttinger-liquid fixed point. For the Heisenberg chain there is already one marginally relevant operator. Moreover, the numerical values of coupling constants in front of irrelevant operators are mostly unknown, rendering a quantitative statement very difficult. In principle, such constants can be derived from numerical solutions of the Bethe ansatz equations, but only a few of these constants have been computed. See, e.g., the review by Cabra and Pujol [27] for details and further references. Finally, it is not clear why spinon-spinon interactions are considered as a source of scattering in Ref. [59] since for pure Heisenberg chains, the thermal current is exactly conserved, irrespective of any interactions. To account for this fact, one would have to implement the conservation of the pure magnetic thermal current with respect to the pure magnetic part of the Hamiltonian for any order of perturbations added to the Luttinger liquid, the order measured in powers of the lattice constants. In other words, the quantitative relation of the results of Ref. [59] to the case of the Heisenberg chain possessing a finite thermal Drude weight is not obvious.

In Ref. [158, 159], a different approach is chosen, namely the Boltzmann equation is solved in order to determine the thermal conductivity. The external scattering mechanisms considered in this work are scattering on phonons and impurities. Combining the results for the respective scattering rates, the authors find

$$\kappa_{\mathrm{mag}}(T) \propto \begin{cases} T^2 & T \ll T_m \\ T^{-1} \quad \text{for} & T_m \ll T \ll \tilde{\Theta}_D \\ T^0 & T \gg \Theta_D \end{cases} \, . \tag{3.35}$$

T_m denotes the position of the single maximum of $\kappa_{\mathrm{mag}}(T)$ and $\tilde{\Theta}_D$ is introduced as a spin-phonon scattering crossover scale, roughly given by $\tilde{\Theta}_D \approx \Theta_D/4$. At low temperatures impurity scattering dominates, and in Ref. [158, 159] a respective scattering rate of $1/\tau_{\mathrm{imp}} \propto T^{-1}$ is predicted, which yields the T^2-dependence, when combined with the linear temperature dependence of the Drude weight K_{th}. Thus, according to Ref. [158, 159], the scattering rates have a significant influence on the temperature dependence even at low temperatures and the temperature dependence of the thermal Drude weight would never directly be seen in experiment. Further research is necessary to clarify whether a constant mean-free path or scattering rate at low temperatures is realized or whether the predictions of Refs. [158, 159] are valid.

3.4 The two-dimensional antiferromagnet La_2CuO_4

In this section it is demonstrated that magnon thermal conductivity is present and experimentally evident for two-dimensional materials. The main focus will be on La_2CuO_4. This material is well known, being one of the parent compounds for HT_C superconductors. The electronic and magnetic properties are dominated by the CuO_2 planes, where Cu^{2+} ions carry a spin-1/2 moment and form a square lattice. Details about the structure and electronic as well as superconducting properties can be found in Ref. [34] and further references mentioned therein.

The magnetic properties of La_2CuO_4 are described by a Heisenberg Hamiltonian on a two dimensional square lattice

$$H = J \sum_{\langle i,j \rangle} \vec{S}_i \cdot \vec{S}_j \tag{3.36}$$

where $\langle i, j \rangle$ denotes a pair of nearest neighbors. For the exchange coupling J, values of 1550 K are reported in the literature [179, 224–226]. The inter-plane coupling is weak $J'/J \sim 10^{-5}$ [227]. Due to the inter-plane coupling the material develops antiferromagnetic order below $T_N \approx 325$ K (see Ref. [71] and references therein). Note that it has been shown that an additional four-spin ring exchange term must be included into the Hamiltonian to arrive at a consistent description of inelastic neutron scattering data [228]. In the following discussion, this effect will be neglected.

Results for the thermal conductivity of La_2CuO_4 single-crystals [ii, 2], Eu-doped La_2CuO_4 [ii, 71, 153], $La_2Cu_{1-z}Zn_zO_4$ [3, 11, 71], and $La_{2-x}Sr_xCuO_4$ [3, 71] have been reported in the literature.[19] We first concentrate on the pure material La_2CuO_4 in comparison to $La_{1.8}Eu_{0.2}CuO_4$ and $La_{2-x}Sr_xCuO_4$ and second, we turn to the case of Zn-doped La_2CuO_4. An extended discussion of experimental results of pure and doped La_2CuO_4 can be found in [71]. Finally, experimental results for the thermal conductivity of further two-dimensional material can be found in the literature: $K_2V_3O_8$ [155, 181], $Sr_2CuO_2Cl_2$ [5], Pr_2CuO_4 [155], $Pr_{1.3-x}La_{0.7}Ce_xCuO_4$ [229], and Nd_2CuO_4 [4, 155]. These materials have been suggested as candidates for magnon thermal conductivity.

3.4.1 Thermal conductivity of La_2CuO_4 and $La_{1.8}Eu_{0.2}CuO_4$

The thermal conductivity of La_2CuO_4 is shown in the lower panel of Fig. 3.15, which is taken from Ref. [ii]. The discussion is mainly based on Refs. [ii] and [71]. The data shown in Fig. 3.15 are in good quantitative agreement with the first data reported for κ by Nakamura et al. [2]. In the following, the inplane conductivity is denoted by κ_{ab} and the conductivity

---

[19] Thermal transport measurements for Eu-doped La_2CuO_4 were also done in Ref. [180], however, mainly focusing on the physics of stripes.

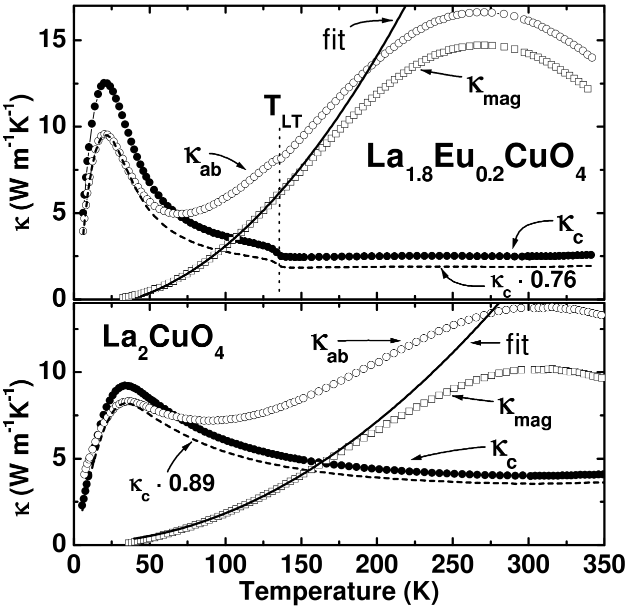

Figure 3.15: Thermal conductivity of $La_{1.8}Eu_{0.2}CuO_4$ (upper panel) and La_2CuO_4 (lower panel). The inplane conductivity is denoted by κ_{ab}; the perpendicular direction by κ_c. T_{LT} is the transition temperature of a structural transition of $La_{1.8}Eu_{0.2}CuO_4$; see Ref. [71] for further details and references. The plots also contain $\kappa_{\mathrm{mag}} = \kappa_{ab} - \kappa_{\mathrm{ph}}$. The determination of κ_{ph} is discussed in the text. The solid lines are fits to κ_{mag} according to Eq. (3.40). Reproduced from Ref. [ii].

in the perpendicular direction by κ_c.

First of all, the anisotropy of κ is obvious from the experimental data: κ_{ab} exhibits two maxima, one at 30 K and a second, very broad one around 300 K, while in κ_c, only the low-temperature peak is present. The low-temperature peak is ascribed to usual phonon heat conduction via acoustical phonons. Possible origins for the second maximum could be a contribution from magnetic excitations, optical phonons, or charge carriers. One might also think of an entirely phononic heat conduction, where the structures arise due to strongly temperature-dependent scattering. We shall argue that in the case of La_2CuO_4 positive indications for magnon thermal conductivity exist, rendering the latter scenario less likely. A contribution from charge carriers can be ruled out since La_2CuO_4 is an insulating material. To decide whether optical phonons plays a role, it is helpful to take the thermal conductivity of Eu- and Sr-doped La_2CuO_4 into consideration.

The upper panel of Fig. 3.15 shows the thermal conductivity of $La_{1.8}Eu_{0.2}CuO_4$ taken from Refs. [ii, 71]. Although Eu-doping introduces structural defects, remarkably, the conductivity is enhanced upon doping both in the c-direction and inplane. This effect is due to structural particularities in the cuprates, and the reader is referred to Ref. [71] for a more elaborate discussion of the phonon thermal conductivity. In relation with possible magnon thermal conductivity, it is noteworthy that the high-temperature maximum is not only present in the Eu-doped sample, but exceeds that of La_2CuO_4. This should be contrasted against the thermal conductivity of Sr-doped samples, i.e., $La_{2-x}Sr_xCuO_4$. As already noticed by Nakamura et al. [2], even a tiny amount of Sr leads to a complete suppression of the high-temperature maximum. Both Eu-ions and Sr-ions induce structural impurities, but the effect on the high-temperature maximum of κ_{ab} is apparently very different. The difference between these two dopants is that Sr-doping leads to hole doping of the CuO_2-planes while the latter are unaffected by Eu-doping. From the experiments on the thermal conductivity of $Sr_{14-x}Ca_xCu_{24}O_{41}$ (see Sec. 3.2.2), it is known that holes serve as efficient scatters for magnetic excitations at high temperatures, causing a strong reduction of the thermal conductivity. Therefore, a contribution from optical phonons to κ_{ab} can be excluded on grounds of the results from the measurements on the doped samples. As is further outlined below, a very consistent interpretation of the experimental data arises if the high-temperature maximum is explained in terms of magnons.

Quantitative analysis of the experimental data

In order to gain a better understanding of scattering mechanisms and to substantiate the conclusion of magnon thermal conductivity in La_2CuO_4, a quantitative analysis of the experimental data has been performed along the lines of Sec. 3.2, based on Eq. (3.4). Prior to that, the magnon contribution has to be separated from the total thermal conductivity, i.e., $\kappa_{\mathrm{mag}} = \kappa_{ab} - \kappa_{ab,\mathrm{ph}}$. To this end, it was assumed [ii, 71] that $\kappa_{ab,\mathrm{ph}} \propto \kappa_c$ holds, where κ_c is of pure phononic nature. The constant of proportionality was estimated by taking κ_c/κ_{ab} in the vicinity of the low-temperature maximum, resulting in $\kappa_{ab} = 0.89\,\kappa_c$ [ii, 71]. As a result, the magnetic contribution κ_{mag} is obtained and shown in the lower panel of Fig. 3.15 (open squares). The maximum is located at 300 K with a maximum value of approximately 10 $\mathrm{WK^{-1}m^{-1}}$. An important observation can directly be made from this curve. In the low-temperature limit, κ_{mag} follows a power-law according to

$$\kappa_{\mathrm{mag}} \propto T^2 \,. \tag{3.37}$$

This is a strong indication that this contribution to κ_c arises from magnon thermal transport. Given a dispersion of elementary excitations with a power-law dependence on momentum k, i.e., $\epsilon_k \propto k^\nu$ in d dimensions, one expects that the specific heat C_V in the low-temperature limit follows

$$C_V \propto T^{d/\nu} \,. \tag{3.38}$$

In first approximation,[20] the dispersion of the elementary excitations of a square-lattice antiferromagnet is linear in k; thus $\kappa_{\mathrm{mag}} \propto C_V$ holds at low temperature, leading to Eq. (3.37).

It is desirable to derive an estimate of magnetic mean-free paths l_{mag} from the experimental data, which is achieved by applying the Boltzmann-type of equation Eq. (3.4) under the assumption of a momentum independent l_{mag}. In contrast to the one-dimensional case Eq. (3.9), the integral over momentum k is not independent of the precise form of the dispersion. To achieve a realistic modeling of the dispersion of La_2CuO_4, the form

$$\epsilon_k^i = \sqrt{\Delta_i^2 + (\hbar v_0 k)^2} \tag{3.39}$$

is used, which gives a good quantitative description of dispersions measured by inelastic neutron scattering at small k [228, 230]. Two magnon branches (denoted by $i = 1, 2$) with

---

[20] In real quasi two-dimensional materials, exchange anisotropies cause the opening of gaps; see, e.g., Ref. [33].

small gaps Δ_i exist. The thermal conductivity of each branch can be cast into the form

$$\kappa^i_{\mathrm{mag}} = \frac{v_0 k_B l_{\mathrm{mag}}}{2a^2 c} \frac{T^2}{\Theta_M^2} \int\limits_{x_{0,i}}^{x_{\max}} dx\, x^2 \sqrt{x^2 - x_{0,i}^2} \frac{dn(x)}{dx} . \qquad (3.40)$$

$v_0 = 1.287 \cdot 10^5$ m/s denotes the velocity of elementary excitations [179], $a = 3.8$ Å is the lattice constant within the CuO_2 planes, $c = 13.2$ Å is the lattice constant perpendicular to the planes, $n(x)$ denotes the Bose function, $\Theta_M = (\hbar v_0 \sqrt{\pi})/(a k_B)$ has units of temperature, and $x_{0,i} = \Delta_i/(k_B T)$ is a dimensionless number. The upper boundary of the integral $x_{\max}$ can be set to infinity without changing the results for l_{mag}. The values for the gaps are $\Delta_1 \approx 26$ K and $\Delta_2 \approx 58$ K [230]. Note that the gaps could be neglected without any large error. An additional factor of $2/c$ appears in Eq. (3.40) counting the number of planes per unit cell.

Except for l_{mag}, all quantities in Eq. (3.40) are known and no adjustable parameters are left.[21] The fit-interval 70K $< T <$ 140 K was chosen since the error in determining κ_{mag} is larger at low temperatures and for very high temperatures, magnon-magnon interactions are known to become relevant, causing a renormalization of the dispersion. The results for the single-crystals La_2CuO_4 and $La_{1.8}Eu_{0.2}CuO_4$ are $l_{\mathrm{mag}} = (558 \pm 140)$ Å and $l_{\mathrm{mag}} = (1157 \pm 60)$ Å, respectively [ii, 71]. These values are smaller than those listed in Table 3.2 for the quasi one-dimensional materials, but at least for $La_{1.8}Eu_{0.2}CuO_4$, the same order of magnitude is reached. The fit-curves themselves (solid lines) are included in the lower panel of Fig. 3.15 for La_2CuO_4 and the upper panel of Fig. 3.15 for $La_{1.8}Eu_{0.2}CuO_4$. Obviously a consistent description of the experimental data is obtained.

Next, one would like to gain a better understanding of the relevant scattering mechanisms. In the next section, a closer inspection of the thermal conductivity of $La_2Cu_{1-z}Zn_zO_4$ is presented. Since doping with Zn-ions, which substitute Cu-ions in the planes, introduces nonmagnetic impurities, this should shed some light on magnon-impurity scattering.

3.4.2 Thermal conductivity of $La_2Cu_{1-z}Zn_zO_4$

The thermal conductivity of Zn-doped $La_2Cu_{1-z}Zn_zO_4$ samples is shown in Fig. 3.16 for $z = 0, 0.005, 0, 01, 0, 05$ [ii, 71]. For the Zn-doped samples, polycrystals were used. Compared to pure La_2CuO_4, one observes (i) that κ is gradually suppressed upon doping; (ii) that the double-peak structure is still visible even for high doping levels; and (iii) that the high-temperature maximum is stronger suppressed than the phonon peak.

Since Zn-ions induce both structural and nonmagnetic defects, it is clear that both phonons and magnons are scattered at Zn-sites, which explains the overall suppression of κ. For a quantitative analysis, the same procedure as for La_2CuO_4 can in principle be applied. However, since only polycrystals are available for the doped cases, a different way of separating κ_{ph} and κ_{mag} must be chosen. In Ref. [ii], κ_{ph} was estimated by fitting $\kappa_{\mathrm{ph}} = \alpha/T + \beta$ to the falling edge of the low-temperature maximum and extrapolated to higher temperatures. κ_{ph} is likely to be systematically overestimated by this procedure for the polycrystalline samples; however, the desired quantity would be κ_{ph} of Zn-doped single crystals, where one would

---

[21] Note, however, that an additional, free additive constant to κ_{mag} was introduced in Refs. [ii, 71] and used to fit the experimental data to account for uncertainties in the determination of κ_{mag} due to the subtraction of the phonon background.

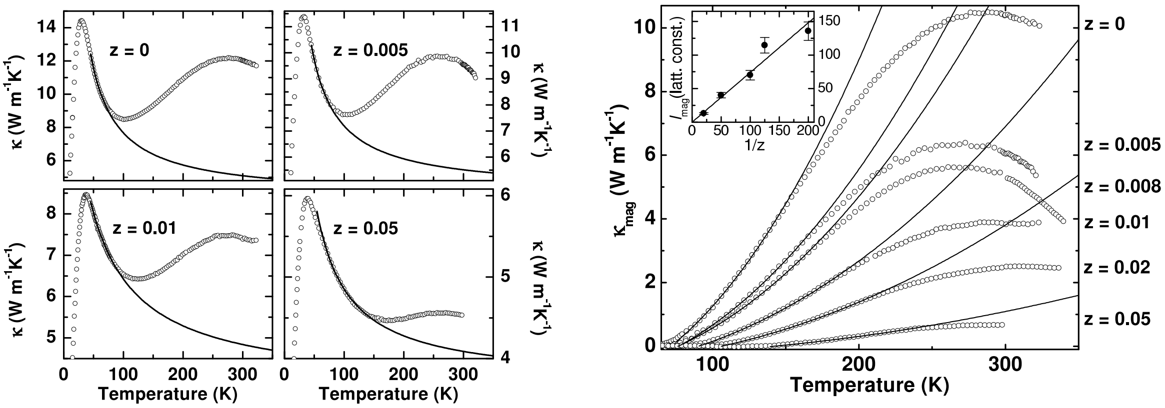

Figure 3.16: Left panel: Thermal conductivity of $La_2Cu_{1-z}Zn_zO_4$ for $z = 0, 0.005, 0.01, 0.05$. For $z = 0$, a single crystal was available, and therefore, the corresponding panel shows the inplane conductivity, while the data for $z > 0$ were taken from polycrystals. Right panel: Magnetic mean-free paths of Zn-doped $La_2Cu_{1-z}Zn_zO_4$ versus $1/z$. The mean-free paths have been extracted by fitting Eq. (3.40) to κ_{mag}, obtained from the total κ by subtracting the phonon background. In the inset, l_{mag} is plotted versus the inverse Zn-content $1/z$, which is a measure of the mean Zn-Zn distance. Reproduced from Ref. [ii].

expect κ_{ph} to be larger than in the case of the polycrystals. Finally, the desired κ_{mag} is defined by $(3/2)\kappa_{\text{mag}}^{\text{poly}}$ since in the polycrystalline samples, all directions are averaged in the measured $\kappa_{\text{mag}}^{\text{poly}}$.

Using κ_{mag} determined along these lines allows one to calculate l_{mag} for the Zn-doped samples from Eq. (3.40). A slight reduction of the spin-wave velocity due to the dopants [231] is neglected, since the resulting error is expected to be smaller than the experimental uncertainties. The results for κ_{mag} and the respective fit-curves according to Eq. (3.40) are shown in the right panel of Fig. 3.16 for $z = 0, 0.005, 0.008, 0.01, 0.02, 0.05$. In all cases, κ_{mag} is very small below 100 K, indicating that κ_{mag} might be underestimated as a consequence of the difficulties to determine κ_{ph}.

The inset of the right panel of Fig. 3.16 contains the most important result. The mean-free paths turn out to be proportional to the inverse Zn-content, $1/z$:

$$l_{\text{mag}} \approx 0.74\, a/z\,. \tag{3.41}$$

$1/z$ is a measure of the mean distance of the Zn impurities in the direction of heat transport. Hence, the experimental data show on the one hand, that the magnetic mean-free paths can directly be tuned by Zn-doping. On the other hand, the values obtained for l_{mag} turn out to be of the order of magnitude of the mean distance of impurities, indicating that the Zn-ions are the dominant source of scattering. This provides a convincing and consistent picture strongly supporting the conclusion that magnon thermal conductivity is present in the cuprates.

3.4.3 Further quasi two-dimensional systems with square lattice geometry

Finally, we stress that a similar phenomenology has been observed for other layered cuprates with the stoichiometry R_2CuO_4, where R is a rare earth ion, e.g., R = Pr, Nd, Sm, Eu and

R	$\kappa_{ab}^{\max}$ [$\mathrm{WK}^{-1}\mathrm{m}^{-1}$]	$T_{\max}$ [K]	Ref.
La	17	300	[ii, 2]
Pr	12	250	[232]
Nd	18	250	[4]

Table 3.3: Maximum value $\kappa_{ab}^{\max}$ of the high-temperature peak of the inplane thermal conductivity κ_{ab} for several cuprates with the structural formula R_2CuO_4, where R denotes a rare earth ion; R=La,Pr,Nd. $T_{\max}$ is the position of the high-temperature maximum.

Gd. A double-peak structure in the inplane thermal conductivity has also been found and published for Nd_2CuO_4 [4, 155]. Similar results have been reported[22] for Pr, Nd, Sm, Eu and Gd [232]. For comparison, Table 3.3 summarizes the maximum value of the high-temperature peak of the inplane thermal conductivity κ_{ab} and the position of the maximum for those materials for which data are published. Note that the magnetism in some of these cuprates is more complicated than in La_2CuO_4 since the rare earth ions carry a finite magnetic moment themselves. This is, for instance, the case for Pr and Nd; see Ref. [155] and references therein.

The oxochlorid $Sr_2CuO_2Cl_2$ is structurally similar to La_2CuO_4, but does not exhibit any structural distortions. It contains CuO_2 layers and it also has a large exchange coupling $J \approx 2225$ K [5]. Its thermal conductivity exhibits the usual double-peak structure with a weak second maximum around 250 K of the order of approximately 15 $\mathrm{WK}^{-1}\mathrm{m}^{-1}$. Thus, the experimental results are very similar to the cuprates of the family R_2CuO_4.

All two dimensional materials mentioned so far are similar since the exchange coupling is of comparable size and quite large; $J \sim 1000$ K. In $K_2V_3O_8$, a two dimensional AFM on a square lattice is also realized, but the coupling is two orders of magnitude smaller; $J \approx 12.5$ K [182]. Originally, it was suggested that magnetic excitations contribute to the thermal conductivity of this material [4]. More recent theoretical work by Chernyshev indicates that the heat transport is only carried by phonons. The reader is referred to the discussion in Ref. [155] for further details.

3.5 Further examples: strong effects in magnetic fields

Figure 3.17 shows the thermal conductivity of the spin chain compound $CuGeO_3$ [65] in panel (a) and of the quasi two-dimensional system $SrCu_2(BO_3)_2$ [69, 70], in panel (b). The low-temperature peak is ascribed to phonons and then described with standard expressions for phonon heat conduction [194]. As the additional, second maximum visible in the experimental data for $\kappa(T)$ appears when the measurement is performed along the direction of chains or inplane for the two-dimensional material, the intuitive conjecture is to relate its origin to magnetic excitations. We shall, however, see that this picture does not hold for the present examples.

---

[22] Note that the high-temperature maximum in Pr_2CuO_4 is only very weakly developed. Still, a larger κ_{ab} as compared to κ_c is evident [232].

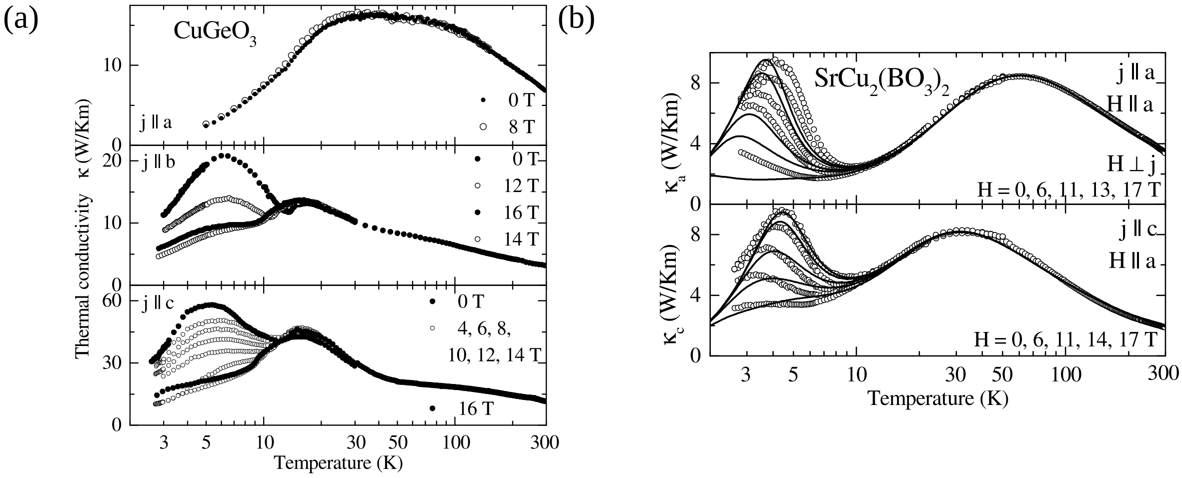

Figure 3.17: Thermal conductivity of $CuGeO_3$ [panel (a)] and $SrCu_2(BO_3)_2$ [panel(b)]. Panel (a) and (b): For both materials, a double-peak structure is present in κ if measured parallel to the chains of $CuGeO_3$ or inplane in the case of $SrCu_2(BO_3)_2$. However, in contrast to all examples shown in Fig. 3.1, the peak at low temperatures is highly sensitive to the application of an external magnetic field, which is denoted by H in this figure. The symbol j denotes the thermal current. The figures are reproduced from Ref. [69] with permission from the author.

3.5.1 The inorganic Spin-Peierls system $CuGeO_3$

Turning now to the case of the Spin-Peierls material $CuGeO_3$, apparently, there is up to now no agreement in the literature about the origin for the double-peak structure. This material is an inorganic Spin-Peierls compound [233], with a transition temperature of $T_{\mathrm{SP}} = 14$ K [233] and it contains spin-1/2 chains. In the Spin-Peierls phase, the spins form singlets due to the dimerization induced by the Peierls mechanism. Thus, below T_{SP}, the magnetic properties are described by the Hamiltonian of a dimerized and frustrated chain and therefore, the excitation spectrum is gapped with a gap of $\Delta_{\mathrm{sp}} = 23$ K [168]. For temperatures above T_{SP}, a model including a next-nearest neighbor interaction αJ has been proposed [169,234]. Since $\alpha \approx 0.35$ for $CuGeO_3$ [169,170], the system is in the massive regime of the frustrated chain $\alpha > \alpha_{\mathrm{crit}} \approx 0.241$ and still gapped (see, e.g., Refs. [234,235]). As can be seen in Fig. 3.17(a), κ measured along the chain direction at zero magnetic field $h = 0$ has a double-peak structure with one maximum around 5 K and a second one around 22 K. Ando et al. [65] suggest that the low-temperature thermal conductivity below 12 K is dominated by phonons while the second one is explained by a contribution from magnetic excitations to the thermal current. The most striking experimental result is the strong field dependence of the low-temperature peak. While the second maximum is practically not affected by the application of a magnetic field of up to 16 T, the maximum at 5 K is strongly suppressed by magnetic fields with $h \lesssim 12.5$ T, and increases again in larger fields. This behavior is explained as follows: the magnetic field closes the gap in the Spin-Peierls phase and in consequence, the density of magnetic excitations that can scatter phonons is increased [65]. Other authors have partially reproduced the experimental results. Vasi'lev et al. [68] have measured κ both parallel (c-axis) and perpendicular to the chains (b-axis), and κ_c exceeds κ_b by a factor of 2.5. However, no indication of the peak around 5.5 K was found which might be ascribed to a lower sample quality [65]. Vasil'ev et al., consequently, discuss the entire thermal conductivity of $CuGeO_3$ in terms of phonons. Hofmann et al. [69] find the same temperature and field dependence of $\kappa_c(T)$ as Ando et al. in the temperature range $0 < T < 30$ K. However, a double-peak structure is also found by this group in the *b*-direction perpendicular to the chains while only one peak is seen in the *a*-direction. Both the sound velocities $v_c \approx 3\, v_b$ and the dispersion of magnetic excitations turn out to be anisotropic [168, 236] comparing the *b*- and *c*-directions. Since the anisotropy ratio of the velocities as well as of κ_b and κ_c is of the order of 3, a sizeable contribution of magnetic excitations to κ can neither be confirmed nor excluded [70]. One might even infer from the lower-most panel of Fig. 3.17(a) that in $CuGeO_3$, there are not only two maxima but three in total. The third one might be located at roughly 90–100 K.

Possible explanations of these observations could be: (i) The thermal conductivity is entirely phononic, and the minima in κ_b and κ_c are due to reduced or enhanced scattering of phonons on magnetic excitations. (ii) The low-temperature features, i.e., the peaks at 5.5 K and 22 K, are phononic and the minimum between these peaks as well as the field dependence are a consequence of the presence of the gap, which is closed in the magnetic field, thus increasing the density of magnetic excitations as scatterers for phonons. (iii) The low-temperature contributions stem from magnetic excitations, while the phonon heat conduction dominates at high temperatures.

Briefly, arguments against or in favor of these three proposals are discussed. First of all, considering the anisotropy of the sound velocities v_c/v_b, which is of the same order as κ_c/κ_b, case (i) would be consistent with the experimental data. As a separation of κ into a phononic and a possible magnetic contribution is difficult [69], there are unfortunately no direct indications for magnetic heat transport as it is for instance the case for the spin ladder compound $La_5Ca_9Cu_{24}O_{41}$. The second scenario, which partially overlaps with the picture developed in Ref. [65], resembles the situation that is observed in $La_5Ca_9Cu_{24}O_{41}$ or $SrCuO_2$, where magnetic heat transport also dominates at high temperatures. It would be very helpful to compare the Debye temperatures, the coupling constants, and the positions of the observed maxima of these materials to decide where one would expect the magnetic thermal conductivity to dominate. Finally, regarding the third scenario, it is noteworthy that the low-temperature features are suppressed upon Zn-doping, which introduces nonmagnetic defects in the chains. Thus, one expects the mean-free paths of magnetic excitations to be strongly suppressed and consistent with the observation, κ to decrease. Note that a strong reduction of the magnon thermal conductivity κ_{mag} upon Zn-doping has been observed both in the system $Sr_{14}Cu_{24-x}Zn_xO_{41}$ [154] and in $La_2Cu_{1-z}Zn_zO_4$ [ii]. Still, replacing Cu by Zn also induces scattering centers for phonons and thus, the analogy does not unambiguously support the third scenario. In summary, despite being one of the first quasi one-dimensional materials for which magnon thermal conductivity was suggested, a complete understanding of the experimental data has not yet been established.

3.5.2 A realization of the Shastry-Sutherland model: $SrCu_2(BO_3)_2$

In connection with the field dependence of κ_c observed for $CuGeO_3$, it is enlightening to discuss the example of $SrCu_2(BO_3)_2$ [70], which shows a similar behavior as can be seen in Fig. 3.17(b). $SrCu_2(BO_3)_2$ constitutes a realization of the Shastry-Sutherland model [164], which is a two-dimensional lattice with inherent geometrical frustration. The lattice is sketched in Fig. 3.18. The ground-state is a dimerized spin singlet state, separated by a

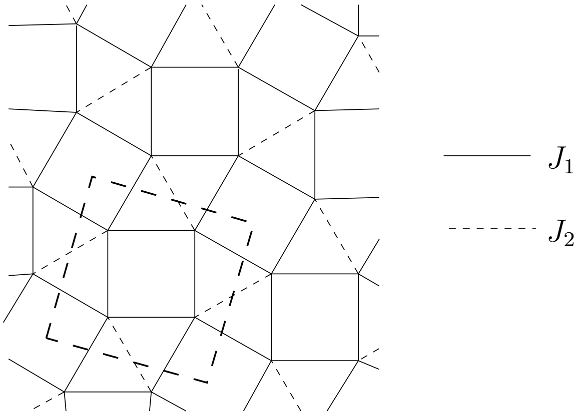

Figure 3.18: Sketch of the Shastry-Sutherland model [164]. Spins are located at the corner of squares. The ground state is a product state of singlets for $J_2 > 2J_1$ and spin 1/2 [164].

spin gap of $\Delta_{\mathrm{sp}} = 35$ K from excited triplet states [237, 238]. In fact, the ground state is a pure product state of singlets formed on the diagonal bonds, denoted by the thin dashed lines in Fig. 3.18. Furthermore, results from inelastic neutron scattering indicate that the one-triplet excitation in this material is dispersionless [238] and therefore, no sizeable magnetic contribution to κ_{mag} is expected. This conclusion is corroborated by the fact that κ shows a similar temperature and field dependence both inplane and perpendicular to the planes [70]. Interestingly, the magnetic specific heat peaks precisely at the minimum seen in $\kappa(T)$ [70]. On grounds of these arguments, Hofmann et al. have developed a model for the phonon heat conductivity taking into account phonon-triplet scattering via a relaxation time ansatz. The scattering rate τ^{-1} is described in terms of resonant scattering of phonons on localized triplet excitations, resulting in a convincing comparison of this model with the experimental data. Thus, in this material, the *minimum* in $\kappa(T)$ is caused by resonant scattering of phonons on triplet excitations, and a contribution of magnetic excitations to the thermal conductivity can be excluded. Note, however, that very recently, it has been argued that multi-triplet excitations might contribute to κ_{mag} in high magnetic fields [239].

3.6 Summary

To conclude this chapter, the most important results from the experimental side are summarized. Thermal transport properties are best understood for the spin ladder materials (Sr,Ca,La)$_{14}$Cu$_{24}$O$_{41}$, the spin chain compounds SrCuO$_2$ and Sr$_2$CuO$_3$, and the two-dimensional system La$_2$CuO$_4$. In these cases, strong experimental evidence supports the conclusion that magnon thermal conductivity is a feature of these materials. The magnon thermal conductivity reaches remarkably large values, and the magnetic mean-free paths extracted from phenomenological expressions are typically of the order of several hundred lattice constants [7, 8, 12–14]. In the case of spin chain materials, the temperature dependence is strongly dominated by the scattering rates, screening the temperature dependence of the pure thermal Drude weight of the Heisenberg chain in a wide temperature range. On the contrary, in the case of spin ladders, energetical arguments as well as the analysis of magnetic mean-free paths suggest that external scattering processes are weak in this case [71, 153], allowing the thermal conductivity to reach large values. For both the spin ladder materials [154] and La_2CuO_4 [ii], a consistent interpretation of transport measurements on Zn-doped samples arises on the basis of the kinetic model from Eq. (3.4). For the two-dimensional systems, in particular the family of R_2CuO_4, the phenomenology of the thermal conductivity is quite the same for many rare earth ions R, allowing for the conjecture that magnon thermal conductivity plays a role in all of these compounds.

Open questions for future theoretical research regarding these materials are: (i) The hysteresis observed for $(Sr,Ca,La)_{14}Cu_{24}O_{41}$ [71] is not understood. (ii) The problem of triplet-hole scattering in Ca-doped $Sr_{14}Cu_{24}O_{41}$, where hole doping strongly suppresses the thermal conductivity, constitutes an interesting problem (see, e.g., Ref. [204]). More generally, a theory for the scattering rates for the spin ladder materials is desirable and one would like to understand theoretically why triplet-phonon scattering is irrelevant for acoustical phonons. (iii) A profound theoretical justification of the phenomenological approaches used to fit experiments is lacking, including for instance Eq. (3.4). In particular, one might want to gain a better understanding to which extent a description of magnon thermal transport in spin ladders in terms of quasi-particles is justified. (iv) The influence of ring exchange on transport properties has not been investigated so far. Note that an additional ring exchange term needs to be added to the Hamiltonian of a two-leg ladder to describe optical [178] as well as neutron-scattering experiments [177] accurately. (v) Theoretical predictions for the thermal conductivity of a two-dimensional antiferromagnet remain an open issue, which has only been studied in few publications [240].

Among the other compounds mentioned in this chapter, $SrCu_2(BO_3)_2$ and $CuGeO_3$ are of particular interest. In both cases, an interesting magnetic field dependence has stimulated strong theoretical and experimental efforts. For $SrCu_2(BO_3)_2$, resonant scattering of acoustical phonons on the localized one-triplet excitations explains the experimental data [70]. For $CuGeO_3$, however, the strong magnetoelastic coupling complicates the physics of this materials, and a consistent interpretation of the experimental results for κ is still lacking.

The investigation of Haldane systems indicates that on the one hand, magnon thermal conductivity might still be present [15], but on the other hand, the magnitude of possible magnetic contributions to κ is strongly reduced as compared to spin-1/2 systems. A comparative study of transport in spin-1/2 and spin-1 systems may shed some light on this issue.

Finally, one type of magnetic transport has not been covered in this chapter, the spin transport. Experimentally, quantities such as the spin diffusion constant are accessible via NMR. Interesting effects might arise in finite magnetic fields where the thermal and the spin current should couple, provided that the respective equation of continuity holds (see Sec. 2.2.2). This might turn out to be an interesting field for future experiments.

Chapter 4

Transport properties of the XXZ chain

In this chapter, transport properties of the integrable spin-1/2 XXZ chain are studied using conformal field theory (CFT), mean-field theory (MF), and exact diagonalization (ED). The XXZ chain possesses a finite thermal Drude weight for any exchange anisotropy both at finite and zero magnetic field [61, 78, 82, 92] and a finite spin Drude weight in a large fraction of its parameter space spanned by magnetic field h and exchange anisotropy Δ. Detailed results are presented for the field, temperature, and anisotropy dependence of the thermal and the spin Drude weight and compared to the existing literature. The methods are complementary, since several expressions for the low-temperature behavior of the Drude weights can be derived from CFT and MF, while ED data are best converged with respect to system size at high temperatures. In particular, ED is shown to be a useful tool to study transport coefficients.

4.1 Overview: the model and the current operators

The Hamiltonian of the XXZ chain is given by

$$H = J\sum_{l=1}^{N}\left\{\frac{1}{2}\left(S_l^+S_{l+1}^- + \text{H.c.}\right) + \Delta S_l^z S_{l+1}^z\right\} - h\sum_{l=1}^{N} S_l^z \,. \tag{4.1}$$

Note that $J > 0$ is assumed. For details on the notation, compare the discussion below Eq. (2.1).

The ground state phase diagram of the XXZ chain in the (Δ, h) plane is depicted in Fig. 4.1. At zero magnetic field there are three different regimes:

$$\begin{array}{lrc} \text{(i)} & \Delta < -1: & \text{ferromagnetic, gapped regime;} \\ \text{(ii)} & |\Delta| \leq 1: & \text{gapless regime;} \\ \text{(iii)} & \Delta > 1: & \text{antiferromagnetic, gapped regime.} \end{array} \tag{4.2}$$

The model has $SU(2)$-symmetry at $\Delta = \pm 1$. Simple limiting cases are the XY model ($\Delta = 0$), corresponding to free, spinless lattice fermions via the Jordan-Wigner transformation, and the Ising-limit, $\Delta/J \to \infty$, where at $h = 0$, the Hamiltonian becomes:

$$H \propto \sum_{l=1}^{N} S_l^z S_{l+1}^z \,. \tag{4.3}$$

The phases (i)–(iii) extend into the (Δ, h) plane at finite magnetic field and they are separated by the quantum critical lines $h_{c1} = h_{c1}(\Delta)$, separating the antiferromagnetic regime (iii) from

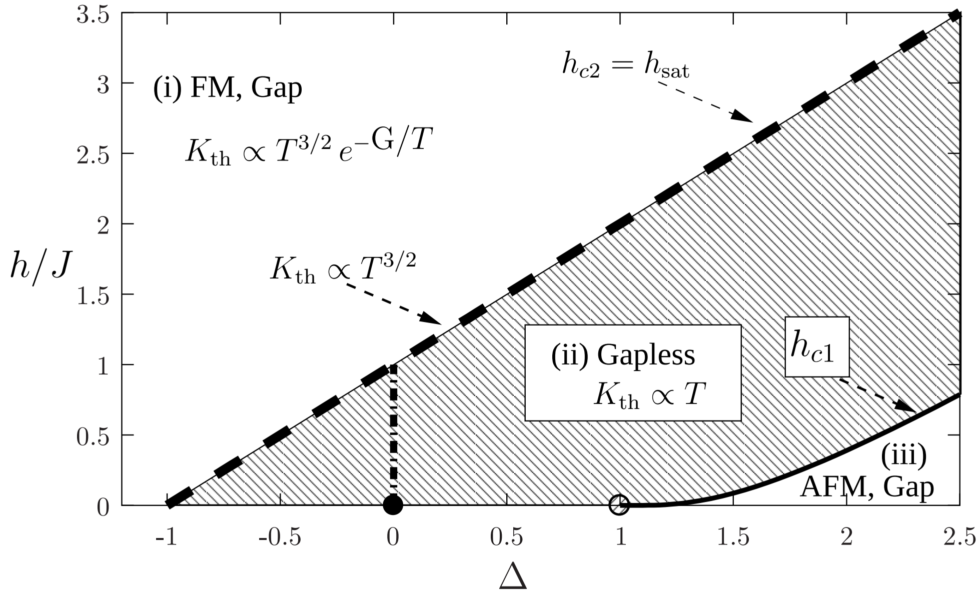

Figure 4.1: Ground state phase diagram of the spin-1/2 XXZ chain in the (Δ, h) plane. Along the dashed and the dot-dashed line, a description in terms of free fermions is valid. This includes the XY model ($\Delta = 0$). The solid line, starting at $\Delta = 1$, denotes the critical field $h = h_{c1}$, separating the massless from the antiferromagnetic regime. The second boundary of the massless phase is given by the saturation field $h = h_{c2} = h_{\mathrm{sat}} = J(1 + \Delta)$ [dashed line]. $G = h - h_{c2}$ is the gap in the fully polarized state. Adapted from Ref. [243] with permission from the author.

the massless one (ii), and $h_{c2} = h_{c2}(\Delta)$, separating the fully polarized state (i) from the massless regime (ii). Thus, h_{c2} is the saturation field h_{sat}, for which a simple expression can be found (see, e.g., Refs. [241, 242]):

$$h_{c2} = h_{\mathrm{sat}} = J(1 + \Delta)\,. \tag{4.4}$$

The gap in the ferromagnetic state is given by $G = h - h_{c2}$. The critical field h_{c1} grows exponentially slowly as a function of the anisotropy Δ for $\Delta > 1$.[1]

Being an integrable quantum model, the XXZ chain possesses infinitely many nontrivial conservation laws (see, e.g., Refs. [61, 78, 244]). For a review on the integrability of the XXZ chain, its properties, and appropriate analytical methods, see Refs. [149, 245].

One of the conserved quantities is the energy-current operator that has been derived in Sec. 2.2.2 (see also Refs. [38, 61, 74]), which is explicitely given by:

$$j_{\mathrm{th}} = iJ^2 \sum_{l=1}^{N} \tilde{\vec{S}}_l \cdot (\vec{S}_{l+1} \times \tilde{\vec{S}}_{l+2})\,. \tag{4.5}$$

As usual, $\vec{S} = (S^x, S^y, S^z)$, but the definition $\tilde{\vec{S}} = (S^x, S^y, \Delta S^z)$ is introduced to achieve a compact notation in Eq. (4.5). Due to the conservation of j_{th}, i.e., $[H, j_{\mathrm{th}}] = 0$, the thermal conductivity diverges and $\kappa(\omega)$ is given by:

$$\mathrm{Re}\,\kappa(\omega) = K_{\mathrm{th}}(h, T)\,\delta(\omega) + \kappa_{\mathrm{reg}}(\omega)\,. \tag{4.6}$$

---

[1] For a discussion of the exact dependence on Δ, see Ref. [27] and references therein.

The thermal Drude weight $K_{\text{th}}(h,T)$ is finite for all temperatures T, all magnetic fields h, and all exchange anisotropies Δ. Without a magnetic field, the regular part $\kappa_{\text{reg}}(\omega)$ vanishes for all frequencies ω. For $h \neq 0$, there is spectral weight at finite frequencies due to the linear coupling of the energy-current to the spin-current operator Eq. (2.39). Finally, note that the energy-current operator is even conserved for the more general XYZ chain [61, 74]:

$$H = \sum_{l=1}^{N} (J_x S_l^x S_{l+1}^x + J_y S_l^y S_{l+1}^y + J_z S_l^z S_{l+1}^z) \,. \tag{4.7}$$

For the sake of quick reference, we quote those equations for the Drude weights from Chapter 2 that will be evaluated in this chapter. The Drude weights corresponding to the pair of current operators j_{s} (spin current) and j_{th} (energy current) are:[2]

$$\begin{aligned}
D_{\text{s}}^{I}(h,T) &= \frac{\pi\beta}{N} \sum_{\substack{m,n \\ E_m=E_n}} p_n \, |\langle m|j_{\text{s}}|n\rangle|^2 \,, && (4.8)\\
D_{\text{s}}^{II}(h,T) &= \frac{\pi}{N}\left[\langle -\hat{T}\rangle - 2 \sum_{\substack{m,n \\ E_m\neq E_n}} p_n \frac{|\langle m|j_{\text{s}}|n\rangle|^2}{E_m - E_n} \right] , && (4.9)\\
D_{\text{th}}(h,T) &= \frac{\pi\beta^2}{N} \sum_n p_n \, \langle n|j_{\text{th}}^2|n\rangle, && (4.10)\\
D_{\text{th,s}}(h,T) &= \frac{\pi\beta}{N} \sum_n p_n \, \langle n|j_{\text{th}} \, j_{\text{s}}|n\rangle \,. && (4.11)
\end{aligned}$$

If the pair of currents $j_1 = j_{\text{s}}$ and $j_2 = j_{\text{th}} - h j_{\text{s}}$ (current operators for finite magnetic fields) is chosen, the Drude weights D_{ij} are [see Eq. (2.23)]:[3]

$$D_{ij}(h,T) = \frac{\pi\beta^{r+1}}{N} \sum_{\substack{m,n \\ E_m=E_n}} p_n \langle n|j_i|m\rangle\langle m|j_j|n\rangle \,. \tag{4.12}$$

The Drude weights D_{ij} are linear combinations of D_{s}, $D_{\text{th,s}}$, and D_{th} [see Eqs. (2.46)–(2.48)]:

$$\begin{aligned}
D_{11} &= D_{\text{s}} \,, && (4.13)\\
D_{21} &= D_{\text{th,s}} - h D_{\text{s}} \,, && (4.14)\\
D_{22} &= D_{\text{th}} - 2\,\beta h D_{\text{th,s}} + \beta h^2 D_{\text{s}} \,. && (4.15)
\end{aligned}$$

In our computations, we choose that set of operators which in each case is most convenient.

At zero magnetic field but finite temperatures, the thermal Drude weight $K_{\text{th}}(h=0,T) = D_{\text{th}}(h=0,T)$ was computed using Bethe ansatz techniques for $0 < \Delta \leq 1$ [78] and $|\Delta| > 1$ [82]. Combined with the numerical results to be presented in this chapter for representative values of Δ, a complete picture of the temperature dependence of the thermal Drude weight arises for all anisotropies. Further results for the magnetic field dependence of the thermal Drude weight are also discussed in this chapter. In finite magnetic fields, the thermal current

---

[2] See Sec. 2.2.3 for a discussion and details on the notation. We also exploit that j_{th} is conserved for the spin-1/2 XXZ chain, i.e., $[H, j_{\text{th}}] = 0$.

[3] $r = 0$ for $j = 1$ and $r = 1$ for $j = 2$.

couples to the spin current and magnetothermal effects must be accounted for. Furthermore, as was shown in Refs. [61, 87], all Drude weights are finite since $[H, j_{\mathrm{th}}] = 0$ and $\langle j_{\mathrm{th}} j_{\mathrm{s}} \rangle > 0$ (see the discussion in Sec. 2.3.1). The latter holds only for $h \neq 0$, since $\langle j_{\mathrm{th}} j_{\mathrm{s}} \rangle = 0$ at $h = 0$ as a consequence of particle-hole symmetry. Here, we mainly focus on the thermal Drude weight K_{th} under the condition of $\langle j_{\mathrm{s}} \rangle = 0$. This is the physical situation that applies if spin currents fulfill the equation of continuity [123]. The two explicit expressions for K_{th}, using either the Drude weights D_{ij} or $D_{\mathrm{th}}, D_{\mathrm{th,s}}$, and D_{s}, are

$$K_{\mathrm{th}}(h, T) = D_{22}(h, T) - \beta \, \frac{D_{21}^2(h, T)}{D_{11}(h, T)} \tag{4.16}$$

or

$$K_{\mathrm{th}}(h, T) = D_{\mathrm{th}}(h, T) - \beta \, \frac{D_{\mathrm{th,s}}^2(h, T)}{D_{\mathrm{s}}(h, T)} \,. \tag{4.17}$$

Therefore, two competing terms contribute to $K_{\mathrm{th}}(h, T)$ in Eq. (4.17): the“pure” thermal Drude weight D_{th} and the “magnetothermal correction”, $\beta D_{\mathrm{th,s}}^2 / D_{\mathrm{s}}$. The magnetothermal response itself, i.e.,

$$S = \frac{D_{12}}{D_{11}} = \frac{1}{T} \frac{D_{21}}{D_{22}} \tag{4.18}$$

has been studied by Louis and Gros both analytically and numerically with Quantum-Monte-Carlo simulations and exact diagonalization in the limit of small fields [91]. Very recently, D_{th}, $D_{\mathrm{th,s}}$, and S have also been studied using Bethe ansatz techniques for $h > 0$ by Sakai and Klümper [92]. Within this approach, D_{th} and $D_{\mathrm{th,s}}$ can be determined, but the spin Drude weight D_{s} apparently still eludes an analytical treatment. Therefore, results for K_{th} and S are restricted to the limit of $T/J \ll 1$ in that work.

Shimshoni et al. [59] have argued that the spin conservation in any *realistic material* is usually *broken*, which would imply that no magnetothermal effects contribute to κ, or K_{th}, respectively. To decide whether this picture is correct may require further experimental results. For comparison, the *pure* thermal Drude weight $D_{\mathrm{th}}(h, T)$ will intensely be studied and its behavior in contrast to K_{th} will be discussed in Sec. 4.6.

The situation is less clear for spin transport at zero magnetic field than for thermal transport. Except for the case of $\Delta = 0$ the spin-current operator

$$j_{\mathrm{s}} = i \frac{J}{2} \sum_{l=1}^{N} (S_l^+ S_{l+1}^- - S_{l+1}^+ S_l^-) \tag{4.19}$$

does not commute with the Hamiltonian (4.1).

At zero temperature and vanishing field, the Drude weight $D_{\mathrm{s}}(T = 0)$ is well known from the work of Shastry and Sutherland [79]. It vanishes for $|\Delta| > 1$, while it is finite for $|\Delta| < 1$, with a jump at $\Delta \pm 1$. Therefore the Drude weight D_{s} signals the metal-insulator type of transition between the regimes (ii) on the one hand and (i) and (iii) on the other hand. The exact expression reads:

$$D_{\mathrm{s}}(h = 0, T = 0) = \frac{\pi^2}{4} \frac{\sin(\gamma)}{\gamma(\pi - \gamma)} \,. \tag{4.20}$$

In this equation, Δ is parameterized via $\Delta = \cos(\gamma)$.

Regarding finite temperatures it should be stressed that the proof[4] of $D_{\mathrm{s}}(h > 0, T > 0) > 0$

---

[4] See Sec. 2.3.1.

breaks down at zero field due to particle-hole symmetry; and no other formal proof for either result, $D_\mathrm{s}(T > 0, h = 0) = 0$ or $D_\mathrm{s}(T > 0, h = 0) > 0$, has been found so far.

In principle, since the XXZ chain is an integrable model, one might expect that it should be possible to compute the Drude weight along the lines of the Bethe ansatz. In fact, such computation has been performed both by Zotos [75], based on an approach developed by Fujimoto and Kawakami [246] for the 1D Hubbard model, and by Klümper and coworkers [76, 247]. However, different results are found for both the temperature dependence of D_s in the massless regime and for the Drude weight at $\Delta = 1$; one work predicting a vanishing Drude weight in this case, the other finding a finite one. In this context, one should be aware of the fact that in both Bethe ansatz calculations, *not* all *micro*states are included at a given energy, and the approaches precisely differ in the choice of the representative states. A numerical solution of the Bethe ansatz equations [76], probing different microstates, has shed some light onto this puzzling situation, showing that for microstates differing only slightly in energy, inconsistent results for D_s are obtained. Thus, it seems that a fundamental problem underlies the computation of D_s in contrast to the very successful application of Bethe ansatz techniques to thermodynamic quantities [78, 248, 249]. Note that the thermal Drude weight[5]

$$K_\mathrm{th}(h = 0, T) = D_\mathrm{th}(h = 0, T) \propto \langle j_\mathrm{th}^2 \rangle \tag{4.21}$$

of the XXZ chain is similar to thermodynamic quantities, i.e., it is a static expectation value, which can be expressed as a second derivative of the free energy of a generalized statistical ensemble $\exp(-\beta H + \Lambda j_\mathrm{th})/Z$, where Λ is a parameter [78]:[6]

$$\left.\frac{\partial^2 Z}{\partial \Lambda^2}\right|_{\Lambda=0} = \langle j_\mathrm{th}^2 \rangle\,. \tag{4.22}$$

On the contrary, the spin Drude weight is in general *not* given by a static correlator

$$D_\mathrm{s} \not\propto \langle j_\mathrm{s}^2 \rangle\,. \tag{4.23}$$

This situation calls for solid numerical investigations which are unbiased and which provide a profound basis to test analytical methods, even if restricted to finite system sizes.

Briefly, the relevant literature is reviewed. Table 4.1 contains a list of contributions to transport properties of the XXZ chain including the methods and the main results.

It is widely agreed that $D_\mathrm{s}(h = 0, T > 0) > 0$ for $|\Delta| < 1$ [83–90]. However, regarding the temperature dependence of $D_\mathrm{s}(T > 0)$ in this regime, contradicting results are reported from the Bethe ansatz computations mentioned above [75, 247], from QMC simulations [85, 86], and from a field-theoretical approach [87]. These results will be further discussed in the following sections and compared to numerical data. No agreement exists regarding the question whether D_s is finite or not for the $SU(2)$-symmetric cases $\Delta = \pm 1$. On the one hand, these are the most relevant cases with respect to experiments and on the other hand, they are special, since they separate different regimes in the ground-state phase diagram of the model shown in Fig. 4.1. The discrepancies of the various Bethe ansatz approaches have already been mentioned, but even the other methods result in inconsistent conclusions. Alvarez and Gros [85, 86] as well as Fujimoto and Kawakami [87] find a finite Drude weight for $\Delta = 1$.

---

[5] This relation, i.e., $K_\mathrm{th}(h = 0, T) \propto \langle j_\mathrm{th}^2 \rangle$ does hold due to $[H, j_\mathrm{th}] = 0$, but is in general not valid for nonintegrable models.

[6] Note that $\langle j_\mathrm{th} \rangle$ vanishes in equilibrium.

Exact diagonalization studies [84, 88, 90, 152] are also interpreted in different ways. Among these papers, there is one work that uses a finite-temperature Lanczos method making system sizes of up to $N = 28$ sites accessible [90]. However, this approach also constructs a single state at given energy, and in fact, the results for D_{s} and $\beta = 0$ seem to be at odds with those obtained from smaller system sizes $N \leq 20$, using *full* exact diagonalization. A comparison is presented in Sec. 4.5. The absence of the spin diffusion pole for the Heisenberg chain was found by Narozhny [151] using bosonization and diagrammatic techniques and numerically by Fabricius and McCoy [152].

Regarding the gapped regimes (i) and (iii), i.e., $|\Delta| > 1$, most authors argue that the Drude weight vanishes here [83, 89, 250, 251]. The scaling with system size will be revisited for $N \leq 19$ using exact diagonalization. Within numerical precision, the conjecture of $D_{\mathrm{s}}(T > 0) = 0$ can clearly be confirmed for $\Delta \gtrsim 1.5$, while the interpretation is less obvious for $1 < \Delta < 1.5$. In particular, the possibility of an exponential suppression of the Drude weight, i.e., $D_{\mathrm{s}} \propto e^{-\mathrm{const}\,\Delta}$ cannot be ruled out on grounds of our numerical data.

Finally, it should be stressed that this survey of the literature is certainly incomplete. Studies of charge transport in the one-dimensional Hubbard [94, 127, 128, 246, 252–254], which is an integrable model as well, and of transport properties of the Luttinger liquid [255–258] are closely related and certainly of great importance. Relevant work will be referred to where appropriate. Finally, note that in principle further integrable spin-1/2 chains can be generated by adding one of the conserved quantities to the Hamiltonian H of the XXZ chain. For instance, thermodynamics as well as thermal transport properties of the Hamiltonian $\tilde{H} = H - j_{\mathrm{th}}$ have recently been investigated in Ref. [259] for the case of $\Delta = 0$.

The structure of this chapter is the following. First, as an introduction to the numerical analysis, some important remarks on the technical procedure are summarized in Sec. 4.2. This comes at the beginning of this chapter since exact diagonalization will already be used in Sec. 4.4 for comparison with mean-field results. Second, in Sec. 4.3, it is outlined how both Drude weights[7] can be computed for the Luttinger-liquid Hamiltonian exploiting the conformal invariance of the model. The Luttinger-liquid Hamiltonian provides a low-energy approximation to the Hamiltonian (4.1). Results are discussed for both zero and finite magnetic fields. Third, in Sec. 4.4, the Drude weights are computed within mean-field theory, based on a mapping onto Jordan-Wigner fermions. The comparison with the Bethe ansatz [78] for $h = 0$ and with exact diagonalization for $\Delta \ll 1$ and $h \ll h_{c2}$ as well as $h \sim h_{c2}$ reveals that this is in fact a quite good approximation to the exact results. Fourth, numerical results for the spin Drude weight are presented in Sec. 4.5 and discussed as a function of temperature T, magnetic field h, and exchange anisotropy Δ. Finally, analogous results for the thermal Drude weight K_{th} are contained in Sec. 4.6.

Some of the results to be presented in this chapter have already been published in Refs. [i, iii] and [ix].

---

[7] The results for D_{th} and D_{s} agree with Ref. [78] and Ref. [79], respectively.

Authors, Reference	(Δ, h)	Method	Results
Thermal Drude weight			
Kane, Fisher [80]		BOS	$K_{\text{th}} = (\pi^2/3)v(\Delta)T$
Klümper, Sakai [78]	$0 \leq \Delta \leq 1$	BA	$K_{\text{th}} = K_{\text{th}}(h = 0, T)$ $K_{\text{th}} = (\pi^2/3)v(\Delta)T \ [T \ll J]$ $K_{\text{th}} = C_{\text{th}}(\Delta)/T^2 \ [T \gg J]$
Alvarez, Gros [54]	$\Delta = 1$	ED	$K_{\text{th}}(h = 0, T)$; $N \leq 14$
Sakai, Klümper [82]	$\|\Delta\| > 1$	BA	$K_{\text{th}} = K_{\text{th}}(h = 0, T)$
Sakai, Klümper [92]	$\Delta = 1$, $h \neq 0$	BA	D_{th}, $D_{\text{th,s}}$, $S = D_{12}/D_{11}$
H.-M. et al. [i, iii, ix]	arb. Δ, $h \geq 0$	ED, MF, BOS	D_{th}, $D_{\text{th,s}}$, D_{22}, K_{th}
Spin Drude weight			
$T = 0$			
Shastry, Sutherland [79]	$\|\Delta\| \leq 1$	BA	$D_{\text{s}} = D_{\text{s}}(\Delta)$
Bonča et al. [260]	$\Delta = 1$	ED, $N \leq 20$	$D_{\text{s}}/J \approx 0.27$, $S^z_{\text{tot}} = 0$
Laflorencie et al. [261]	$\|\Delta\| \leq 1$	BA, BOS	$D_{\text{s}} = D_{\text{s}}(N)$
Gu et al. [262]	$\Delta > 1$	BA, ED	$D_{\text{s}} = D_{\text{s}}(N)$
$T > 0$			
Zotos, Prelovšek [83]	$0 < \Delta < 1$ $1 < \Delta$	ED, $N \leq 16$ ED, $N \leq 16$	$D_{\text{s}} > 0$ $D_{\text{s}} > 0$
Zotos el al. [61]	arb. Δ, $h > 0$	ED, proof	$D_{\text{s}}(h > 0) > 0 \ \forall \Delta$
Fabricius, McCoy [152]	$\Delta > 0$	ED, $N \leq 16$	S^{zz} correlations no diffusion for $\Delta \leq 1$
Naef, Zotos [89]	$0 \leq \Delta < 1$ $1 \leq \Delta$	ED, $N \leq 16$	$D_{\text{s}} > 0$ for $N \to \infty$ $D_{\text{s}} = 0$ for $N \to \infty$
Narozhny et al. [84]	$0 \leq \Delta \leq 1$	ED, $N \leq 14$	$D_{\text{s}} > 0$ for $\Delta \neq 1$ $D^I_{\text{s}} = D^I_{\text{s}}(T)$
Zotos [75]	$0 \leq \Delta < 1$ $\Delta = 1$	BA	$D_{\text{s}} = D_{\text{s}}(T)$ $D_{\text{s}} = 0$
Alvarez, Gros [85, 86]	$0 \leq \Delta \leq 1$	QMC	$D_{\text{s}} > 0$ for $T/J \ll 1$
Fujimoto, Kawakami [87]	$-1 < \Delta \leq 1$	BOS	$D_{\text{s}} > 0$ for $T/J \ll 1$
Long et al. [90]	$\|\Delta\| < 1$ $\Delta = 1$	ED, MCLM, $N \leq 28$	$D_{\text{s}} > 0$ $D_{\text{s}} \to 0$ for $N \to \infty$
Rabson et al. [88]	$0 \leq \Delta \leq 1$	ED, $N \leq 20$	$D_{\text{s}} \to 0$ for $\Delta \neq 1$
Prelovšek et al. [251]	$\Delta > 1$	MCLM	$D_{\text{s}} \to 0$, σ_{dc}
Peres et al. [250]	$\Delta \gg 1$	BA	$D_{\text{s}} = 0$
Louis, Gros [91]	$0 \leq \Delta$, $h \neq 0$	QMC, BA	$S = D_{12}/D_{11}$
H.-M. et al. [iii, ix]	arb. Δ, $h \geq 0$	ED, MF	$D_{\text{s}} = D_{\text{s}}(N, \Delta)$

Table 4.1: This table lists theoretical studies of the Drude weights of the XXZ chain or related models of spinless fermions. If not stated otherwise, $h = 0$ was considered. The following abbreviations are used: ED (exact diagonalization), BA (Bethe ansatz techniques), QMC (Quantum Monte Carlo simulations), BOS (bosonization), MCLM (micro-canonical Lanczos method).

4.2 Technical remarks on exact diagonalization

Before turning to the discussion of analytical results, some remarks on *exact diagonalization* are necessary, since exact diagonalization results will already be used in Sec. 4.4 to validate the mean-field theory. The following technical remarks on the numerical procedure are relevant for both the integrable and the nonintegrable models, which will be discussed in Chapter 5.

The numerical method applied in this thesis is complete diagonalization of the full spectrum for chains with $N \leq 20$ sites. This is only possible by exploiting conservation of the z-component $S^z_{\text{tot}} = \sum_l S^z_l$ of the total spin, translational invariance and spin-inversion symmetry in the $S^z = 0$ subspaces of systems with even N.[8] The latter symmetry is respected by the energy-current operator j_{th} but not by the spin-current operator j_{s}. The dimensions of the largest subspaces for a given momentum k are 8400 for $S^z_{\text{tot}} = 1$ and 9000 for $S^z_{\text{tot}} = 0$ at $N = 20$.[9] In the latter case, the dimension is almost reduced by a factor of two by spin-inversion symmetry for the subspaces with odd and even sign under this symmetry. The requirements from the hardware side are, for the largest system sizes, a maximum of 4GB of RAM. The computations were done on standard PCs and on a COMPAQ compute server provided by the Rechenzentrum of the TU Braunschweig.[10]

Another important aspect is the identification of degenerate states, i.e., states with $E_n = E_m$, in subspaces labeled by S^z_{tot} and momentum k. This is necessary in the evaluation of Eqs. (4.8), (4.9) and (4.12) but becomes irrelevant if the respective current operator is conserved, leading to simpler expressions such as Eq. (4.10) or (4.11). The latter is possible for thermal transport in the XXZ model, i.e., this applies to D_{th} and $D_{\text{th,s}}$.

For spin transport, however, we have $[H, j_{\text{s}}] \neq 0$ for $\Delta \neq 0$, and a careful treatment of degenerate states becomes necessary for the quantities $D_{11} = D_{\text{s}}$ as well as D_{21}, D_{22} and K_{th}. The integrated distribution $I(\epsilon)$ of level spacings ΔE_n is shown in Fig. 4.2. There, the number $I(\epsilon)$ of level spacings $\Delta E_n = E_{n+1} - E_n, E_n < E_{n+1}$ of adjacent energy levels being smaller than a given value of ϵ is plotted versus ϵ for $\Delta = 0.5$:

$$I(\epsilon) = \sum_{(S^z_{\text{tot}},k)} \sum_{\Delta E_n < \epsilon} 1 \,. \tag{4.24}$$

$I(\epsilon)$ can also be written as an integral over a continuous distribution of the level spacings, which we denote by $P(\epsilon)$:

$$I(\epsilon) \propto \int_0^{\epsilon} d\epsilon' P(\epsilon') \,. \tag{4.25}$$

It is sufficient to analyze all subspaces with given S^z_{tot} and momentum k separately and sum over all subspaces thereafter. This is indicated by the first sum in Eq. (4.24).

The spectrum displays some characteristic features: first, the value of $I(\epsilon)$ for $\epsilon \to \infty$

---

[8] For the purpose of this thesis we have adapted a program written by A. Honecker to the present problem, which sets up the Hamiltonian in a basis respecting translational invariance, conservation of S^z_{tot}, and spin-inversion symmetry, where possible. The program has been extended by the present author to set up current operators in the same basis also.

[9] The program used to diagonalize the largest subspaces is the package *diagonalize* written by A. Honecker [263]. The most recent version of this program uses standard *LaPack* routines. See, e.g., http://www.netlib.org/lapack.

[10] The CFGAUSS is a COMPAQ ES45 compute server with 10 nodes equipped with 4 CPUs each and a maximum of 32 GB RAM per node. For further information, see http://www.tu-braunschweig.de/rz/services/compute/cfgauss.

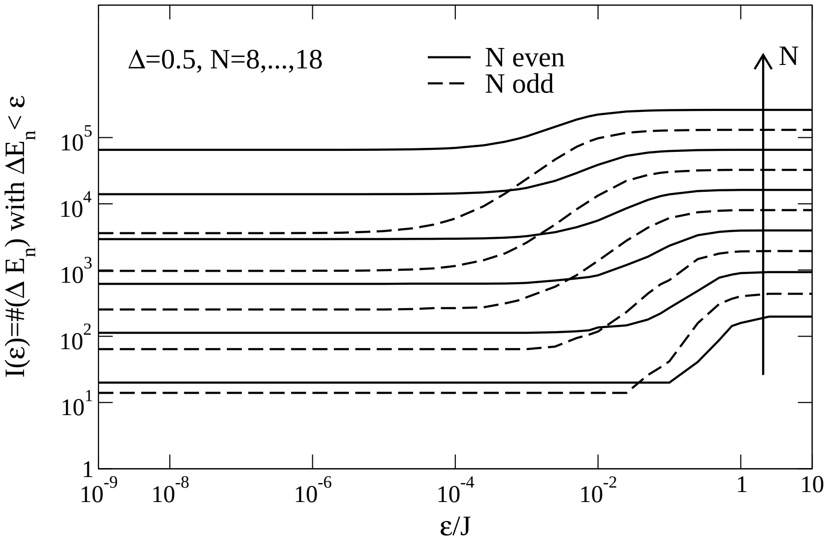

Figure 4.2: Distribution of level spacings in the spectrum of finite XXZ chains with $8 \leq N \leq 18$ (bottom to top as indicated by the arrow) for $\Delta = 0.5$ (solid lines: N even, dashed lines: N odd). ΔE_n is the difference of adjacent energy levels in subspaces classified by total $S^z_{\rm tot}$ and momentum k. The number $I(\epsilon)$ of ΔE_n with $\Delta E_n < \epsilon$ summed over all subspaces is plotted versus ϵ; see Eq. (4.24). From Ref. [iii].

equals the dimension of the Hilbert space 2^N minus the number of subspaces $(S^z_{\rm tot}, k)$. Second, a large fraction of degenerate states is present and third, the integrated distribution of level spacings is constant for $10^{-9} \lesssim \epsilon/J \lesssim 10^{-6}$ for the system sizes investigated. This suggests that adjacent energy levels are typically separated by $\Delta E_n/J \lesssim 10^{-9}$ if they are degenerate. This separation allows for an identification of degenerate states by imposing the following criterion in the numerical analysis: energy levels with $|E_{n+1} - E_n| < \epsilon_{\rm cut} = 10^{-8}J$ are degenerate. By evaluation of Eq. (2.44), which does not make use of $[H, j_{\rm th}] = 0$, for the thermal Drude weight $D_{\rm th}(h = 0, T)$ we find agreement with Eq. (4.10), which exploits $[H, j_{\rm th}] = 0$, and the Bethe ansatz [78] for this choice of $\epsilon_{\rm cut}$. Significant deviations at temperatures $T/J \sim 1$ appear if larger or lower values for the cut-off energy are used. In principle, the sum in Eq. (2.25) can be reduced to a trace, if the current operators are diagonal in degenerate subspaces. This does, however, not make the determination of degenerate states superfluous. The best way to reduce the number of degeneracies would be to exploit further symmetries of the model.

In this context, note that the level-spacing distribution $P(\epsilon)$ has recently been intensely studied, focusing on the transition from integrable to nonintegrable models as reflected in $P(\epsilon)$. For more details and further references, the reader is referred to the recent publications Refs. [88, 264–266].

4.3 Conformal field theory

Luttinger-liquid Hamiltonian for the XXZ chain

In the continuum limit, the spin-1/2 XXZ maps onto a Luttinger liquid in the massless phase (see Fig. 4.1). Thus the low-energy degrees of freedom are described by the effective Hamiltonian:

$$H = \frac{v}{2}\int dx\,\left(K(\partial_x\theta)^2 + \frac{1}{K}(\partial_x\phi)^2\right)\,. \tag{4.26}$$

where ϕ is a free, massless, bosonic field in $1+1$-dimensions and θ is its dual field

$$\partial_x\theta = \frac{1}{v\,K}\partial_t\phi\,. \tag{4.27}$$

K is the so-called Luttinger parameter, and v is the velocity of the elementary excitations.

An important symmetry of (4.26) is its invariance under conformal transformations.[11] The fields generally depend on two variables, x and time t. Equivalently, the fields can be written as functions of complex variables

$$\phi(x,t) = \phi(z,\bar{z}); \quad z = x + it\,. \tag{4.28}$$

Let $z \to z + \zeta(z)$ be a general mapping of the complex plane into itself. Such transformations obey local conformal invariance if $\zeta(z)$ is an analytical function, i.e., the requirement is that $\zeta(z)$ fulfills the Cauchy-Riemann differential equations [267]. The great advantage of conformal invariance is that it already determines certain correlation functions such as the two-point function of the field ϕ [27, 267]. Exploiting conformal invariance to obtain correlation functions one can determine the precise dependence of v and K on the anisotropy Δ by comparing with the exact solution derived from the Bethe ansatz for finite system size N. This results in:

$$v = \frac{\pi}{2}\frac{\sin\gamma}{\gamma}; \quad K = \frac{\pi}{2(\pi-\gamma)}; \quad \Delta = \cos(\gamma)\,. \tag{4.29}$$

The objective of this section is to compute the transport coefficients for a Luttinger liquid. Before, a brief sketch of the derivation of the Luttinger-liquid Hamiltonian for the XXZ chain is given. We follow the presentation of Ref. [27], which also contains further references.[12]

To illustrate the mapping of a lattice model onto a continuum theory, it is instructive to consider the XY case [$\Delta = 0$ in Eq. (4.1)]. First, we apply a Jordan-Wigner transformation, which leads to a representation of the Hamiltonian in terms of spinless fermions $c_l^{(\dagger)}$ (see the discussion in Sec. 2.1 and in Sec. 4.4). The model is diagonal in momentum space with a cosine dispersion [see Eq. (2.6)]. In the low-energy limit, it is sufficient to keep only the modes in the vicinity of the two Fermi points, which are $k_{\mathrm{F}} = \pm\pi/2$ at vanishing magnetic field, i..e., the dispersion is linearized around the Fermi points. To this end, the fermion operators $c(x) = c_l$ are expressed by slowly varying fermionic fields:

$$\frac{c(x)}{\sqrt{a}} \approx e^{ik_{\mathrm{F}}x}\psi_{\mathrm{L}}(x) + e^{-ik_{\mathrm{F}}x}\psi_{\mathrm{R}}(x)\,. \tag{4.30}$$

---

[11] See Refs. [267, 268] for further details.

[12] Regarding the notation, note that we fix constants such that the Luttinger parameter of free fermions (XY case, $\Delta = 0$) is $K = 1$.

In this equation we have introduced a continuous spatial variable via $la \to x$, which replaces the integer site index l. a is the lattice constant. $\psi_{\mathrm{L}}(x)$ and $\psi_{\mathrm{R}}(x)$ are the left and right moving fields, respectively. Using Eq. (4.30), one arrives at the continuum version of the XY model:

$$H = iv \int dx \, [\psi_{\mathrm{R}}^\dagger \partial_x \psi_{\mathrm{R}}^\dagger - \psi_{\mathrm{L}}^\dagger \partial_x \psi_{\mathrm{L}}^\dagger] \,. \tag{4.31}$$

v is the velocity at the Fermi points. This Hamiltonian can equivalently be expressed in terms of bosonic fields $\phi_{\mathrm{R,L}}(x)$ by applying bosonization. We are not going into the details of the procedure, which can be found in the literature [269, 270], but prefer to quote the results. Essentially, one realizes that the fermionic fields can be expressed in terms of exponentials of bosonic ones:[13]

$$\psi_{\mathrm{R,L}}(x) \propto : e^{\pm i\sqrt{4\pi}\phi_{\mathrm{R,L}}(x)} : \,. \tag{4.32}$$

The plus(minus) has to be used for the right(left) moving fields. The dots : . : denote normal ordering. Using the bosonization procedure one arrives at Eq. (4.26). In addition, one can find expressions for the spin operators in terms of the bosonic fields:

$$S_x^z \approx \frac{1}{\sqrt{\pi}} \partial_x \phi + a : \cos(2k_{\mathrm{F}} x + 2\sqrt{\pi}\phi) : + \frac{\langle m \rangle}{2} \,. \tag{4.33}$$

The corresponding expression for $S_x^\pm$ reads:

$$S_x^\pm \approx (-1)^x \; : e^{\pm i\sqrt{\pi}\theta} [b \cos(2k_{\mathrm{F}} x + 2\sqrt{\pi}\phi) + c] : \,. \tag{4.34}$$

$\langle m \rangle$ is the magnetization, and a, b, c are nonuniversal constants, i.e., they depend on parameters of the model such as Δ. Normal ordering with respect to the ground state with magnetization $\langle m \rangle$ is indicated by : . :.

So far we have discussed the noninteracting XY case only. The consideration of interactions also allows us to give a qualitative discussion of the ground-state phases of Fig. 4.1. The crucial point is that interactions arising for $-1 < \Delta < 1$ are incorporated into the Hamiltonian *without* changing its form. The effect of the interactions is a renormalization of the parameters of (4.26), i.e., K and v, which acquire a dependence on the anisotropy Δ. In the limit of small $\Delta \ll 1$, this can be seen by treating the interactions perturbatively, which results to first order in Δ in:[14]

$$v = 1 + \frac{2\Delta}{\pi}; \quad K = 1 - \frac{2\Delta}{\pi} \,. \tag{4.35}$$

One way to see which perturbations in principle arise for $\Delta \neq 0$ but $\Delta \ll 1$ is to insert the expression for S_l^z Eq. (4.33) into $H^{zz} \propto \Delta S_l^z S_{l+1}^z$, and to expand the result in powers of the lattice constant. To leading order one finds an operator of the type:

$$\mathcal{O}(x) = \cos\left(4\sqrt{\pi}\phi(x)\right) \,. \tag{4.36}$$

There are two criteria that have to be considered to decide whether an operator may affect the low-energy physics or not. First of all, the operators are classified as relevant, marginal, or irrelevant in the renormalization group sense. This means that the couplings in front of a

---

[13] We omit the Klein-factors which appear in this equation to ensure commutation relations. See Ref. [27] for a discussion.

[14] See, e.g., Ref. [27].

perturbation increase, stay constant, or scale to zero during the renormalization flow.[15] For instance, the operator from Eq. (4.36) is irrelevant for $|\Delta| < 1$, marginal for $\Delta = 1$, and relevant for $\Delta > 1$, where it gives rise to the opening of a gap.

The second criterion is the commensurability of an operator. Terms that oscillate rapidly on short length-scales are incommensurate and are thus usually discarded. As an example we consider the case of finite magnetic fields $h > 0$. From the Zeeman contribution $h \sum_l S_l^z$ and Eq. (4.33), one infers the presence of a term of the form $h\, a : \cos(2k_{\mathrm{F}}x + \sqrt{\pi}\phi) :$. This operator gives rise to the opening of the gap for $h \geq h_{c2}$, where it becomes commensurate, since in general, the Fermi points are $k_{\mathrm{F}} = \pm(\pi/2)(1 + \langle m\rangle)$. In the massive phase, we have $\langle m\rangle$ and therefore $k_{\mathrm{F}} = \pm\pi$. In the massless phase, however, it is an incommensurate perturbation [27], which is thus neglected, even though it is a relevant perturbation in both the massless and the massive regime.

Zero magnetic field

Equation (4.26) describes a free bosonic field in (1+1) dimensions. Therefore, the transport coefficients of this model diverge, characterized by finite Drude weights. The local current operators $j_{\mathrm{th}}(x)$ and $j_{\mathrm{s}}(x)$ are chosen such that they fulfill equations of continuity:

$$\begin{aligned} \partial_x j_{\mathrm{s}}(x) &= -\partial_t m(x) && (4.37)\\ \partial_x j_{\mathrm{th}}(x) &= -\partial_t H(x) && (4.38) \end{aligned}$$

where $m(x)$ is the local magnetization and $H(x)$ the local energy density. One finds for the total currents [i, 87, 95, 269]

$$\begin{aligned} j_{\mathrm{s}} &= \frac{-vK}{\sqrt{\pi}} \int dx\, \partial_x\theta(x)\,, && (4.39)\\ j_{\mathrm{th}} &= v^2 \int dx\, \partial_x\phi(x)\partial_x\theta(x)\,. && (4.40) \end{aligned}$$

The Drude weights follow from

$$D_{\mathrm{th[s]}} = \pi\beta^r \langle j^2_{\mathrm{th[s]}}\rangle / N \tag{4.41}$$

with $r = 1$ for D_{s} and $r = 2$ for D_{th}. Thus, in order to obtain the Drude weight one has to evaluate the two-point function

$$\langle j_{\mathrm{th[s]}}(x,t) j_{\mathrm{th[s]}}(0,0)\rangle\,, \tag{4.42}$$

t being the imaginary time variable. The computation is performed along the lines of Ref. [248] where the susceptibility was calculated, and a sketch of it is given for the case of $K_{\mathrm{th}} = D_{\mathrm{th}}$. First, coordinates are changed via $z = vt + ix$ and $\bar{z} = vt - ix$. By decomposing $\phi(z,\bar{z}) = \varphi(z) + \bar{\varphi}(\bar{z})$ into its chiral parts and using the respective two-point functions[16] such as

$$\langle\varphi(z)\varphi(w)\rangle = -\frac{K}{4\pi}\ln(z - w) \tag{4.43}$$

---

[15] We skip a discussion of the scaling dimension of operators which is nevertheless important in this context and refer the reader to the literature instead [27].

[16] These correlation functions directly follow from the conformal invariance of the model. For further details, see [27, 267].

one arrives at

$$\langle j_{\mathrm{th}}(x,t) j_{\mathrm{th}}(0,0)\rangle = -2\,\frac{v^2}{(4\pi)^2}\left(\frac{1}{z^4}+\frac{1}{\bar{z}^4}\right). \tag{4.44}$$

Before performing the space-integration the imaginary time direction is compactified by mapping the complex plane, i.e. z, into the strip, parameterized by ζ, using $z(\zeta) = \exp(2\pi\zeta/\beta)$ leading to the following replacement in Eq. (4.44):

$$vt \pm ix \to \frac{v\beta}{\pi}\sin\left(\pi\frac{vt \pm ix}{v\beta}\right). \tag{4.45}$$

After a change of variables

$$u = \tan\left(\frac{\pi t}{\beta}\right); \quad w = -i\tan\left(\frac{i\pi x}{v\beta}\right) \tag{4.46}$$

one finally finds:

$$D_{\mathrm{th}}(T) = \frac{\pi^2}{3}\,v\,T. \tag{4.47}$$

This coincides with Klümper's and Sakai's expression [78], also found by Kane and Fisher [80], for the low-temperature limit of the XXZ chain if the velocity v is equal to $v = (J\pi/2)\frac{\sin\gamma}{\gamma}$. However, the result is more generally valid for models for which the continuum limit is given by the Luttinger-liquid Hamiltonian, supposed the Drude weight can be shown to be finite for the original lattice model.

In analogy to the case of the thermal Drude weight, the spin Drude weight is derived as [79]

$$D_{\mathrm{s}}(T) = v\,K = \mathrm{const}\,. \tag{4.48}$$

Thus, as noticed in Ref. [78], the Drude weights fulfill a Wiedemann-Franz type of relation

$$\frac{D_{\mathrm{th}}(T)}{D_{\mathrm{s}}(T)} = L_0\,T \quad \text{with} \quad L_0 = \frac{\pi^2}{3\,K}\,. \tag{4.49}$$

Furthermore, the relation

$$\frac{D_{\mathrm{th}}}{C_V} = \pi v^2 \tag{4.50}$$

holds at low temperatures [78], since $C_V = (\pi/3v)\,T$ [271].

Finite magnetic fields

At finite magnetic fields, the Hamiltonian acquires an additional term due to the Zeeman contribution $h\sum_l S^z_l$. Using Eq. (4.33) one finds for the massless regime

$$H = \frac{v}{2}\int dx\left(K(\partial_x\theta)^2 + \frac{1}{K}(\partial_x\phi)^2\right) - \frac{h}{\sqrt{\pi}}\int dx\,\partial_x\phi\,. \tag{4.51}$$

By introducing a shifted field $\tilde{\phi}$ via

$$\tilde{\phi} = \phi - \frac{K}{v}\frac{h}{\sqrt{\pi}}\,x \tag{4.52}$$

and by realizing that $\tilde{\theta} = \theta$ through Eq. (4.27), the Zeeman term can be absorbed and the Hamiltonian is, up to an additive constant, of the same form as at zero magnetic field

$$H = \frac{v}{2} \int dx \left(K(\partial_x \theta)^2 + \frac{1}{K}(\partial_x \tilde{\phi})^2 \right) . \tag{4.53}$$

For $h \neq 0$, the velocity v and the Luttinger parameter K acquire an additional dependence on h, i.e., we have $K = K(\Delta, h)$ and $v = v(\Delta, h)$. Both parameters, i.e., $K(\Delta, h)$ and $v(\Delta, h)$, can be computed exactly by solving the Bethe ansatz equations [272]. The velocity $v = v(\Delta, h)$ was calculated for $\Delta = 1$ in Ref. [273]. Further numerical values for these parameters can be found in, e.g., Ref. [274].

The form of the Hamiltonian implies that the expressions for the Drude weights $D_{11} = D_{\mathrm{s}}$ and D_{22} can directly be copied from the zero-field case:

$$\begin{aligned} D_{\mathrm{s}}(h) &= v(\Delta, h)\, K(\Delta, h) && (4.54) \\ D_{22}(h) &= \frac{\pi^2}{3}\, v(\Delta, h)\, T\, . && (4.55) \end{aligned}$$

To see why one is now dealing with D_{22} instead of D_{th}, it is instructive to replace $\tilde{\phi}$ in the expression for the thermal current $\tilde{j}_{\mathrm{th}}$ corresponding to Eq. (4.53):

$$\tilde{j}_{\mathrm{th}} = v^2(h) \int dx\, \partial_x \left(\phi - \frac{K}{v} \frac{h}{\sqrt{\pi}} x \right) \partial_x \theta = j_{\mathrm{th}} - h j_{\mathrm{s}} \, . \tag{4.56}$$

Since particle-hole symmetry is restored for the Hamiltonian written in terms of the shifted $\tilde{\phi}$ [275], it follows that $D_{21} = 0$. From Eqs. (4.13)–(4.15) and Eqs. (4.54)–(4.55), one also finds an expression for the low-temperature limit of D_{th}, in agreement with Ref. [92]:

$$D_{\mathrm{th}} = D_{22} + h^2 D_{\mathrm{s}}/T \, . \tag{4.57}$$

4.4 Mean-field theory

4.4.1 Mean-field Hamiltonian

Next, a Hartree-Fock type of approximation to the Hamiltonian Eq. (4.1) is discussed, which is used to compute the Drude weights D_{ij}. The spin operators S^z_l and $S^{\pm}_l$ are first mapped onto spinless fermions via the Jordan-Wigner transformation [62, 81]:

$$S^z_l = c^{\dagger}_l c_l - \frac{1}{2}; \quad S^+_l = e^{i\pi\Phi_l} c^{\dagger}_l . \tag{4.58}$$

Here, $c^{(\dagger)}_l$ destroys(creates) a fermion on site l. The string operator Φ_l reads $\Phi_l = \sum_{i=1}^{l-1} n_i$ with $n_i = c^{\dagger}_i c_i$. This leads to the following form of the Hamiltonian:

$$H = J \sum_{l=1}^{N} \left[-\frac{1}{2}\big(c^{\dagger}_{l+1} c_l + \mathrm{H.c.}\big) + \Delta\big(n_l n_{l+1} - n_l + \frac{1}{4}\big) \right] - h \sum_{l=1}^{N} n_l + h\, \frac{N}{2} \, . \tag{4.59}$$

A mapping onto Jordan-Wigner fermions has widely been used to study one-dimensional models and an accurate account of the relevant literature is beyond the scope of this thesis.

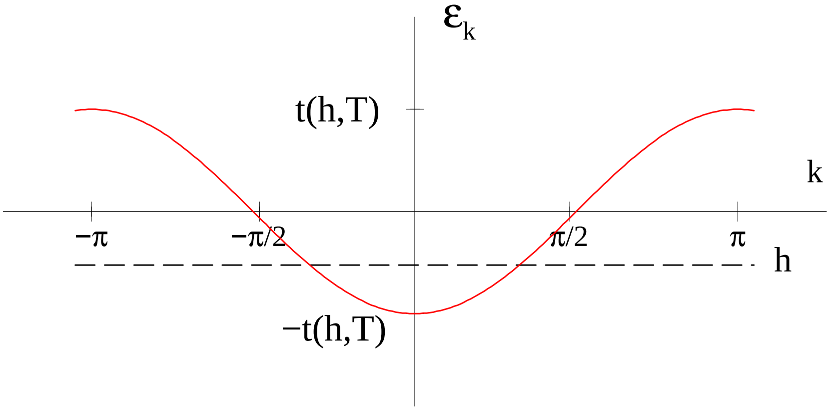

Figure 4.3: Sketch of the mean-field dispersion ϵ_k [Eq. (4.61)] with the field h acting as the chemical potential. For $h = 0$, the Fermi points are $k_{\mathrm{F}} = \pm\pi/2$. For $0 < |h| < h_{\mathrm{sat}}$, $\pi/2 > k_{\mathrm{F}} > 0$, and the dispersion is always linear in the vicinity of the Fermi-level, i.e., $\epsilon_k \propto k$, leading to $K_{\mathrm{th}} \propto T$ at low temperatures in the massless regime. At the saturation field, $k_{\mathrm{F}} = 0$, and $\epsilon_k \propto k^2$. In the fully polarized state, the dispersion can be approximated by $\epsilon_k \propto (k^2 + G)$; $G = h - J$ denoting the gap. $h > 0$ is assumed here.

The notation follows Ref. [122].

The procedure will be outlined incorporating the magnetic field. The interaction term $\Delta n_l n_{l+1}$ appearing in the fermionic representation is treated by a Hartree-Fock decomposition leading to an effective mean-field Hamiltonian

$$H_{\mathrm{MF}} = \sum_k \epsilon_k c_k^\dagger c_k \tag{4.60}$$

with the mean-field dispersion

$$\epsilon_k = -J(1 + 2\Delta\Omega)\cos(k) - h + 2J\Delta(n - 1/2). \tag{4.61}$$

The dispersion is sketched in Fig. 4.3. The quantities to be determined self-consistently are:

$$\Omega(h,T) \quad = \quad \langle c_{l+1}^\dagger c_l \rangle = \frac{1}{\pi}\int_0^\pi dk\, \cos(k) f(\epsilon_k) \tag{4.62}$$

$$n(h,T) \quad = \quad \langle c_l^\dagger c_l \rangle = \frac{1}{\pi}\int_0^\pi dk\, f(\epsilon_k) \tag{4.63}$$

where the latter is related to the average local magnetization m via $\langle S_l^z \rangle = m = n - 1/2$. Both parameters are site independent since no order occurs in the massless phase at finite temperatures due to the Mermin-Wagner theorem.[17] The temperature and field dependence of the self-consistent solutions for Ω and m are shown in Fig. 4.4 for $\Delta = 0.1$.

---

[17] See, e.g., Chapter 6 in Ref. [30].

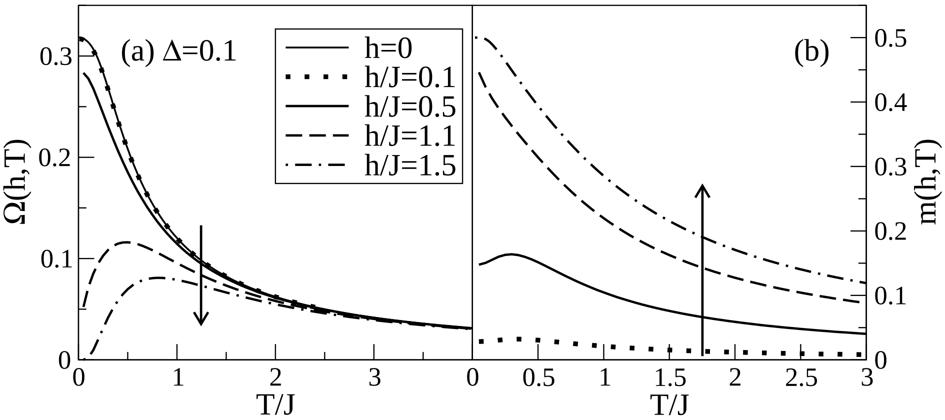

Figure 4.4: Mean-field parameter $\Omega = \Omega(h,T)$ [panel (a)] and local magnetization $m(h,T)$ [panel (b)] versus temperature for various fields $h/J = 0.1, 0.5, 1.1, 1.5$ at $\Delta = 0.1$. Arrows indicate increasing magnetic field.

The Drude weights can be obtained from

$$D_{11} = \frac{\pi\beta}{N}\langle j_1^2\rangle = \frac{\beta}{2}\int_{-\pi}^{\pi} dk\, v_k^2 f^2(\epsilon_k) e^{\beta\epsilon_k}; \tag{4.64}$$

$$D_{21} = \frac{\pi\beta}{N}\langle j_2 j_1\rangle = \frac{\beta}{2}\int_{-\pi}^{\pi} dk\, \epsilon_k v_k^2 f^2(\epsilon_k) e^{\beta\epsilon_k}; \tag{4.65}$$

$$D_{22} = \frac{\pi\beta^2}{N}\langle j_2^2\rangle = \frac{\beta^2}{2}\int_{-\pi}^{\pi} dk\, (\epsilon_k v_k)^2 f^2(\epsilon_k) e^{\beta\epsilon_k}\,. \tag{4.66}$$

since the current operators, which are given by

$$j_1 = \sum_k v_k c_k^\dagger c_k; \quad j_2 = \sum_k \epsilon_k v_k c_k^\dagger c_k\,, \tag{4.67}$$

are both conserved within this approximation. In Eq. (4.67), $v_k = \partial_k \epsilon_k$ denotes the velocity and $f(\epsilon) = 1/(\exp(\epsilon/T)+1)$ is the Fermi function. Note that in general, v_k depends on temperature. In the massless regime, $\epsilon_k = vk$ where $v = v_k(T=0)$. In the case of noninteracting particles, which is effectively realized within mean-field theory, the transport coefficients can already be determined from all single-particle eigenenergies.

Note that the mean-field approach is of course exact for $\Delta = 0$, thus providing a reference case to check the numerical implementation of the current operators for the latter use of exact diagonalization. Moreover, it is also possible to evaluate Eqs. (4.64)–(4.66) on finite systems also by either recursively computing all many-particle states or by explicitely rewriting all transport coefficients in terms of single-particle eigenenergies only. The latter procedure will be used in Chapter 6 to study transport properties of disordered XY chains.

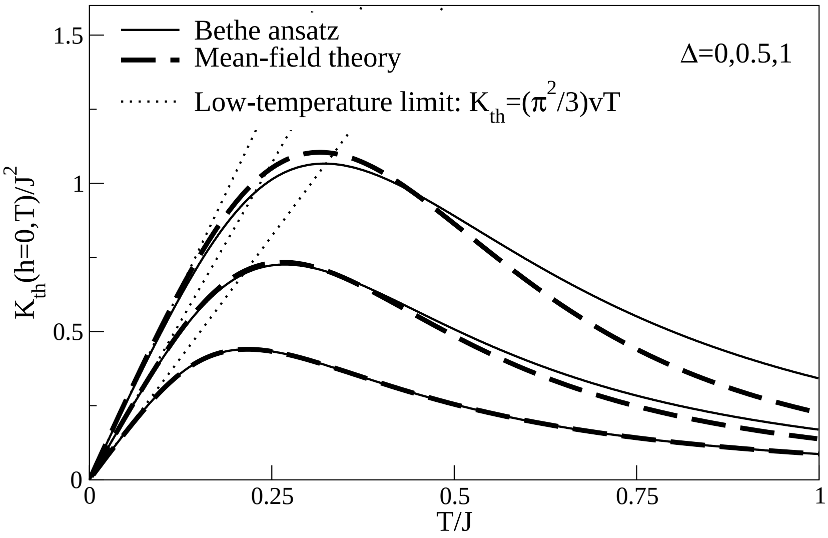

Figure 4.5: Thermal Drude weight $K_{\text{th}}(h=0,T) = D_{\text{th}}(h=0,T)$, mean-field theory [i]. Comparison with the exact result from Ref. [78] for $\Delta = 1, 0.5, 0$ and $h = 0$ (top to bottom). The low-temperature asymptotic $K_{\text{th}} = D_{\text{th}} \propto T$ according to Eq. (4.47) is also included (thin dotted lines).

4.4.2 Zero magnetic field

Results for the thermal Drude weight[18] $K_{\text{th}}(h=0,T)$ from the mean-field approximation are shown in Fig. 4.5 and compared to the exact curves from Ref. [78] for $\Delta = 0, 0.5, 1$. The approach works in this form for $0 \leq \Delta \leq 1$. Note that $n = 1/2$ since the magnetization vanishes at any temperature without an external field.

In the case of $\Delta = 0$, corresponding to free fermions, both approaches coincide. The agreement is still very good for larger values of Δ. In particular, the position of the maximum is well reproduced by the mean-field approach, even for $\Delta = 1$. At high temperatures, the thermal Drude weight is underestimated by the mean-field approximation due to the neglect of many-particle excitations. In the low-temperature limit one obtains

$$K_{\text{th}}(h=0,T) = D_{\text{th}}(h=0,T) = \frac{\pi^2}{3} v^{\text{MF}}\, T \tag{4.68}$$

where the constant velocity is given by [122]

$$v^{\text{MF}} = J\left(1 + \frac{2\Delta}{\pi}\right) . \tag{4.69}$$

This agrees with the expansion of the exact result for the velocity Eq. (4.29) to first order in Δ. Therefore, the temperature dependence comes out correctly, but the prefactor would be renormalized if interactions were properly accounted for; compare Eq. (4.47).

Nevertheless, mean-field theory provides a surprisingly good approximation to the thermal Drude weight. For finite magnetic fields, no analytically exact results are available. Since exact diagonalization on system sizes $N \leq 20$ can usually not give a good description of low energy features, mean-field theory will be used for $h > 0$ as a complementary method to study the low-temperature regime.

Before turning to the case of finite magnetic fields where magnetothermal corrections

---

[18] One should keep in mind that at vanishing magnetic field $K_{\text{th}}(h=0,T) = D_{\text{th}}(h=0,T) = D_{22}(h=0,T)$.

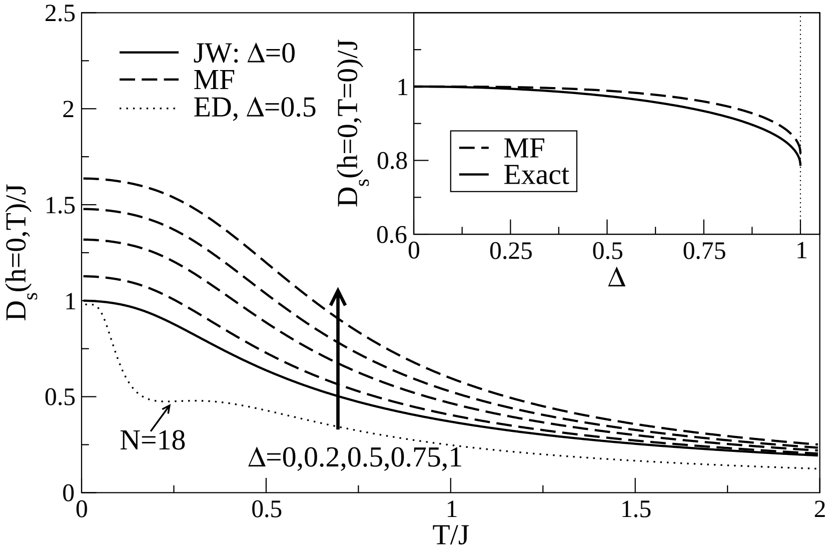

Figure 4.6: Spin Drude weight, mean-field theory. $D_\mathrm{s}(h = 0, T)$ versus temperature for $\Delta = 0, 0.2, 0.5, 0.75, 1$ at zero magnetic field $h = 0$. Increasing Δ is indicated by the arrow. The curve for $\Delta = 0$ (solid line) is exact in the limit $N \to \infty$. Dashed curves denote mean-field results (MF); the dotted line is ED data for $N = 18$ and $\Delta = 0.5$. Inset: Drude weight $D_\mathrm{s}(T = 0)$, comparison of the mean-field result (dashed curve) with the exact expression from Eq. (4.20) [solid line, [79]].

arise [see Eq. (4.16) and (4.17)] the spin Drude weight $D_\mathrm{s} = D_{11}$ as obtained from mean-field theory is compared to exact results. This is shown in Fig. 4.6, where the main panel contains the curves for $\Delta = 0, 0.2, 0.75, 1$ at finite temperatures and the inset contains $D_\mathrm{s}(T = 0)$ from mean-field theory (dashed line) and the exact result from Eq. (4.20) [solid line]. Starting with the case of low temperatures, note that mean-field theory results in

$$D_\mathrm{s}^\mathrm{MF}(h = 0, T = 0) = v^\mathrm{MF}(\Delta) \propto \langle -\hat{T} \rangle \,. \tag{4.70}$$

Thus, D_s^MF essentially measures the mean kinetic energy, or the bandwidth $2(1 + 2\Delta/\pi)$, which increases with increasing Δ [see Eq. (4.61)]. Therefore, one finds

$$D_\mathrm{s}^\mathrm{MF}(T = 0) > D_\mathrm{s}(T = 0)\,, \tag{4.71}$$

which can be seen in the inset of Fig. 4.6 and which still holds at finite temperatures. The latter is evident from the comparison of D_s^MF to exact diagonalization data for $N = 18$ and $\Delta = 0.5$ shown in the main panel of Fig. 4.6. One can therefore conclude that mean-field theory predicts the wrong qualitative dependence on the anisotropy Δ, i.e., an increase instead of a decrease both at finite and zero temperature. In fact, D_s mostly decreases monotonously with Δ, as will be shown in Sec. 4.5.

4.4.3 Finite magnetic fields

The discussion can easily be extended to the case of finite magnetic fields. First, the low temperature limit will be analyzed in the regimes (i) and (ii) of the phase diagram depicted in Fig. 4.1. Second, the spin Drude weight $D_\mathrm{s}(h, T)$ is computed from mean-field theory for $\Delta = 0.1$ and compared to exact diagonalization. Finally, it is shown that for the thermal

Drude weight $K_{\rm th}(h,T)$ at small magnetic fields and for small Δ as well as for fields larger than the saturation, i.e., $h \geq h_{c2}$, a good agreement with ED is found.

Free-fermion case $\Delta = 0$

The discussion starts with the free-fermion case $\Delta = 0$. For illustration, a cosine-dispersion is sketched in Fig. 4.3. For $\Delta = 0$, one finds from Eqs. (4.64)–(4.66) and (4.16):

$$\begin{aligned} K_{\rm th}(h,T) &= D_{22} = \frac{\pi^2}{3} v(h)\, T \;\text{ for }\; 0 \leq h < h_{c2}\,; & (4.72)\\ K_{\rm th}(h,T) &= \left(A_{22} - \frac{A_{21}^2}{A_{11}}\right) T^{3/2} \;\text{ for }\; h = h_{c2}\,; & (4.73)\\ K_{\rm th}(h,T) &= \frac{3}{4}\sqrt{2\pi}\, T^{3/2} e^{-G/T} \;\text{ for }\; h > h_{c2}\,. & (4.74) \end{aligned}$$

To arrive at Eq. (4.72), one should realize that the leading contribution to $K_{\rm th}$ at low temperatures comes from D_{22} in the massless regime; thus $K_{\rm th} \approx D_{22}$. The velocity v for $k = k_{\rm F}$, $k_{\rm F} = \arccos(h/J)$ being the Fermi wavevector, is given by $v = J\sin(k_{\rm F}) = \sqrt{J^2 - h^2}$. The coefficients appearing in Eq. (4.73) are

$$\begin{aligned} A_{11} &= \sqrt{\frac{\pi}{2}}(1-\sqrt{2})\,\zeta(1/2)\,,\\ A_{21} &= \frac{3}{4}\sqrt{\frac{\pi}{2}}(2-\sqrt{2})\,\zeta(3/2)\,, \qquad (4.75)\\ A_{22} &= \frac{15}{16}\sqrt{\frac{\pi}{2}}(4-\sqrt{2})\,\zeta(5/2)\,. \end{aligned}$$

$\zeta(x)$ is the Riemann-Zeta function. The key ingredient to obtain the $T^{3/2}$-dependence of $K_{\rm th}$ is the fact that $\epsilon_k \propto k^2$ for $h = h_{\rm sat}$. Note that the spin Drude weight at $T = 0$ is finite for $0 \leq h < h_{c2}$ and vanishes for $h \geq h_{c2}$. At low temperatures and for $h = h_{c2}$, we find

$$D_{11}(h,T) = A_{11}\sqrt{T}\,. \qquad (4.76)$$

For the quantum critical line $h = h_{c2}$, one can infer from Eqs. (4.14), (4.15), (4.73), and (4.75) that the pure thermal Drude weight also diverges for $T \to 0$ with $D_{\rm th} \propto T^{-1/2}$ ($J = 1$)

$$D_{\rm th} = D_{22} + 2\beta h D_{21} + \beta h^2 D_{11} = A_{11}\frac{h_{c2}^2}{\sqrt{T}} - 2h_{c2}A_{21}\sqrt{T} + A_{22}T^{3/2}\,. \qquad (4.77)$$

To leading order in temperature, the Drude weights D_{ij} in the polarized state are ($\epsilon_k \approx Jk^2/2 + G; G = |h| - J$):

$$\begin{aligned} D_{11}(h,T) &= \sqrt{2\,J\,T}\, e^{-G/T} c_1\,, & (4.78)\\ D_{21}(h,T) &= \sqrt{2\,J\,T}\, e^{-G/T}(Gc_1 + Tc_2)\,, & (4.79)\\ D_{22}(h,T) &= \sqrt{\frac{2\,J}{T}}\, e^{-G/T}(G^2c_1 + 2TGc_2 + c_3T^2) & (4.80) \end{aligned}$$

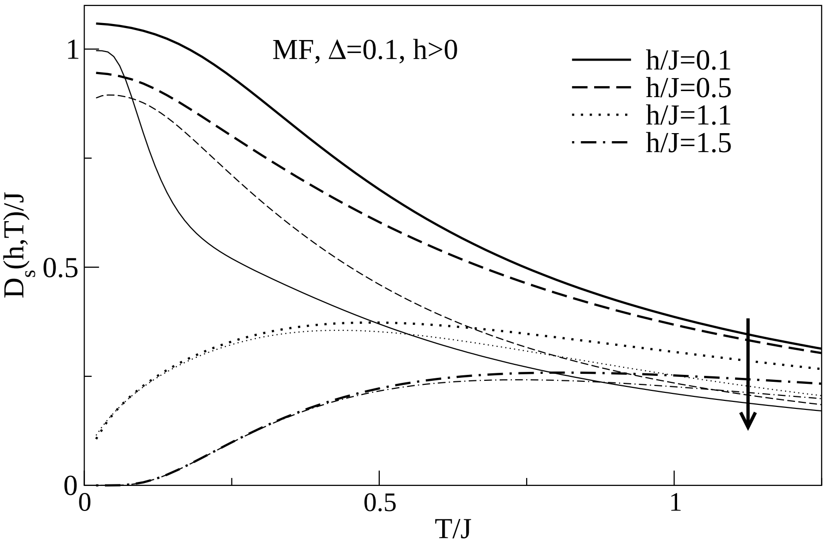

Figure 4.7: Spin Drude weight, mean-field theory for finite magnetic fields. $D_\mathrm{s}(h,T)$ versus temperature for $\Delta = 0.1$ and various magnetic fields $h/J = 0.1$ (solid lines), 0.5 (dashed lines), 1.1 (dotted lines), and 1.5 (dot-dashed lines). Thin lines denote ED results from $N = 18$ sites. The arrow indicates increasing magnetic field.

with

$$c_i = \int_0^\infty dx\, x^{(2i-1)/2}\, e^{-x} = \Gamma\left(i + \frac{1}{2}\right) , \tag{4.81}$$

where $\Gamma(x)$ denotes the Gamma function and i is an integer number. Thus, both the leading and next-to-leading order in T cancel in Eq. (4.16), leading to Eq. (4.74).

The results summarized in Eqs. (4.72)–(4.74), (4.48), (4.76), and (4.78) for the massless state, the saturation field, and the fully polarized state suggest that at low temperatures the Wiedemann-Franz law is fulfilled:

$$\frac{K_\mathrm{th}(h,T)}{D_\mathrm{s}(h,T)} = L_0 T \,. \tag{4.82}$$

The prefactor L_0 is different in all three cases, but a constant with respect to the field *within* the regimes (i) and (ii) *within mean-field theory* [see also Eq. (4.49)]:

$$L_0^\mathrm{MF} = \begin{cases} \pi^2/3 & h \le h_{c2} \\ A_{11}A_{22} - A_{21}^2/A_{11}^2 \quad \text{for} & h = h_{c2} \\ 3/2 & h > h_{c2} \end{cases} . \tag{4.83}$$

Finally, note that $D_{22} \propto \exp(-G/T)/\sqrt{T}$ has been argued to be a generic feature of all gapped systems with a finite thermal Drude weight [55]. In the same work, a $T^{3/2}$-dependence of D_{22} has been found at the saturation field within a continuum theory suggested to describe low-energy features of spin ladders.

Mean-field theory for $\Delta > 0$

The results from mean-field theory are discussed for $\Delta > 0$, starting with the spin Drude weight D_s, which is one ingredient in Eqs. (4.16) and (4.17) needed to compute K_th under

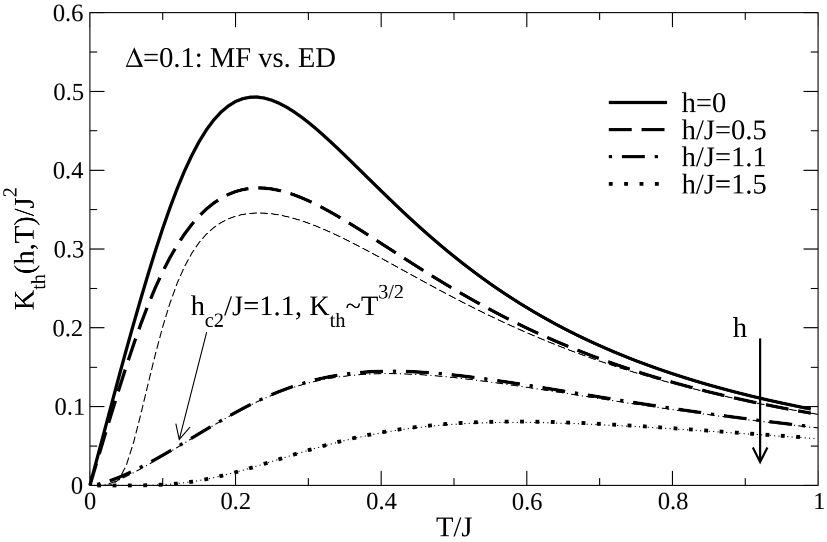

Figure 4.8: Thermal Drude weight $K_{\mathrm{th}}(h, T)$, mean-field theory for finite magnetic fields $h/J = 0, 0.5, 1.1, 1.5$ [ix]. The curve for $h = 0$ is the exact result from Ref. [78]. Comparison with exact diagonalization for $N = 18$ sites (thin lines). Mean-field theory results are denoted by thick lines. The thick arrow indicates increasing magnetic field Δ.

the condition of $\langle j_{\mathrm{s}} \rangle = 0$. The temperature dependence of D_{s} is shown in Fig. 4.7 for $\Delta = 0.1$ and $h/J = 0, 0.5, 1.1, 1.5$ and compared to exact diagonalization data for $N = 18$ sites (thin lines). The agreement is poor for small fields, similar to the case of $h = 0$ shown in Fig. 4.6, but for $h \geq h_{c2}$ and $T/J \lesssim 0.5$, only small deviations between MF and ED are found.

Figure 4.8 shows $K_{\mathrm{th}}(h, T)$ for $\Delta = 0.1$ and $h/J = 0, 0.5, 1.1, 1.5$ (thick lines). The main features are: (i) a suppression of the thermal Drude weight by the magnetic field; (ii) a shift of the maximum to higher temperatures for $h/J > 0.5$ compared to $h = 0$; (iii) a change in the low-temperature behavior which resembles the findings for the free-fermion case.

For comparison, the results from exact diagonalization (ED) for $N = 18$ sites are included in Fig. 4.8 (thin lines) and the agreement is very good. Deviations at low temperatures for $h = 0$ and $h = 0.5$ are due to finite-size effects, i.e., the ED results are not yet converged to the thermodynamic limit. For larger fields $h \geq h_{c2} = 1.1J$, deviations between ED and MF are negligibly small.

Within the massless phase $0 \leq h < h_{\mathrm{sat}}$, the mean-field theory results confirm that $K_{\mathrm{th}}(h, T) = V(h, \Delta)T$ for $\Delta > 0$ and low temperatures. However, we expect that the prefactor $V(h, \Delta)$ will be renormalized if interactions are fully accounted for.

From Eq. (4.61), one can derive the critical field h_{c2} within the Hartree-Fock approximation. The behavior of both Ω and the average local magnetization m as a function of temperature and for various magnetic fields are depicted in Fig. 4.4(a) and (b), respectively. At $T = 0$ and $h = h_{c2}$, the ground state is the fully polarized state with $n = \langle c_i^\dagger c_i \rangle = 1$, i.e., the parameter Ω from Eqs. (4.61) and (4.62) vanishes. Consequently, we find $h_{c2}/J = 1 + \Delta$ in accordance with the exact result [243]. From the point of view of bosonization it is evident that the low-energy theories along the line $h/J = 1 + \Delta$ and for $\Delta = 0$ are equivalent in the sense that they are characterized by the same radius of compactification [241, 242, 272]. Within bosonization, the line $h = h_{c2}$ is special since the velocity of the elementary excitations vanishes here.

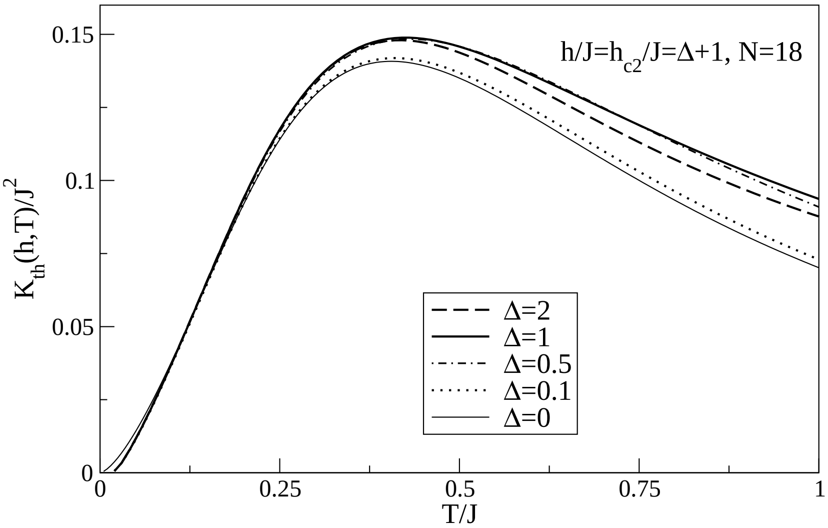

Figure 4.9: Thermal Drude weight $K_{\mathrm{th}}(h,T)$ at the critical field $h_{c2}/J = 1+\Delta$ for $\Delta = 0, 0.1, 0.5, 1, 2$ [ix]. For $\Delta \neq 0$, we show numerical results for $N = 18$ sites, while the curve for the free-fermion case (thin solid line) is valid in the thermodynamic limit. This comparison confirms that $K_{\mathrm{th}} = AT^{3/2}$ for $h = h_{c2}$ with A being independent of Δ for $\Delta > -1$.

Regarding the low-temperature behavior of the thermal Drude weight for $h = h_{c2}$ one can then infer that it is given by Eqs. (4.73) and (4.75), independently of Δ. This picture is further substantiated by additional exact diagonalization data for $\Delta = 0.1, 0.5, 1, 2$ shown in Fig. 4.9 and the respective critical fields $h_{c2}/J = 1+\Delta$. The curve for $\Delta = 0$ is of course exact in the thermodynamic limit and has been evaluated from Eqs. (4.64)–(4.66). Small deviations visible at very low temperatures are due to the presence of finite size gaps in the exact diagonalization data. Note, however, that the case of $\Delta = -1$ and $h = 0$ might be exceptional, since exact diagonalization results point to $K_{\mathrm{th}}(h=0) \propto T$ at low temperatures. This will be discussed in more detail in Sec. 4.6. In the case of the ferromagnetic Heisenberg chain, the existence of many low-lying excitations might complicate the situation.

In the ferromagnetic state $h > h_{c2}$ and for low temperatures, the parameter Ω from Eq. (4.62) is exponentially suppressed and the average local magnetization is $m = 1/2$, which is illustrated in Fig. 4.4. Thus, to leading order in T the low-temperature dependence of $K_{\mathrm{th}}(h,T)$ is independent of Δ, similar to the case of $h = h_{c2}$, and the thermal Drude weight is exponentially suppressed

$$K_{\mathrm{th}}(h,T) \propto T^{\nu} e^{-G/T} \quad \text{for} \quad h > h_{c2}\,. \tag{4.84}$$

The mean-field theory as well as ED results are compatible with $\nu = 3/2$ even for $\Delta \neq 0$.

In summary, mean-field theory provides the leading low-temperature contributions to K_{th} in the regimes (i) and (ii) of Fig. 4.1. Moreover, a reasonable quantitative description of the transport coefficients is found first, for small Δ and $h > 0$ and second, for $h \geq h_{c2}$.

4.5 The spin Drude weight (ED)

For the spin Drude weight D_s of the XXZ chain, numerical results are presented for zero magnetic field in Sec. 4.5.1 and for finite magnetic fields in Sec. 4.5.2. For the latter case, a proof of $D_\mathrm{s}(h > 0, T > 0) > 0$ exists [61], while no such proof has been found for zero magnetic field. Therefore, the discussion in Sec. 4.5.1 starts with the finite-size scaling of the Drude weight in the limit $\beta = 0$, which allows one to access this aspect from the numerical point of view. Conclusions regarding the temperature dependence and a comparison of D_s^I and D_s^{II} complete the discussion of the zero field case. For finite magnetic fields, preliminary results for the zero-temperature Drude weight will be presented showing that this quantity probes the phase diagram Fig. 4.1. Furthermore, the field and temperature dependence is studied. Finally, it is shown to which extent Mazur's inequality Eq. (2.80) is exhausted by considering j_th as the only conserved quantity. Note that the Drude weight D_s is needed as an input in Eqs. (4.16) and (4.17) to obtain the magnetothermal correction to the thermal Drude weight.

4.5.1 Zero magnetic field

Scaling of the Drude weight in the high-temperature limit

Broad numerical evidence exists supporting the conclusion of a finite spin Drude weight in the massless regime at *finite* temperatures [83–86, 88–90], corresponding to the absence of spin diffusion [151, 152]. Field theoretical [87] as well as Bethe ansatz studies [75–77] reach the same conclusion, finding, however, different results for the *low*-temperature behavior. The issue of the $SU(2)$-symmetric case is unsettled. Numerical studies are partially interpreted in favor of a finite Drude weight [85,86], while, e.g., the Bethe ansatz results by Zotos [75] predict a vanishing Drude weight. In the gapped regimes $|\Delta| > 1$, the Drude weight is believed to vanish [83, 89, 250].

Numerical results for the Drude weight are presented in the limit $\beta = 0$. Noting that $D_\mathrm{s} \propto T^{-1}$ at high temperatures, one defines [see Eq. (2.53)]:

$$C_\mathrm{s}(N) = \lim_{\beta\to 0}[T\, D_\mathrm{s}(T)]\,. \tag{4.85}$$

This first coefficient of a high-temperature expansion of D_s fulfills the relation $C_\mathrm{s}(\Delta) = C_\mathrm{s}(-\Delta)$, which can be inferred from the following argument: Changing the sign of Δ is an anti-unitary transformation and essentially turns $H(-\Delta) = -H(\Delta)$ and $E_n(-\Delta) = -E_n(\Delta)$ while the eigenvectors remain unchanged. This follows from an additional rotation by π about the z axis on all sites with even site index. The spin-current operator j_s from Eq. (4.19) does not depend on Δ and therefore, the matrix elements in Eq. (4.85) do not change under this transformation. Due to this relation, it is sufficient to concentrate on $\Delta \geq 0$ in the limit of $\beta = 0$.

Numerical results for $C_\mathrm{s}(N)$ and several values of the anisotropy are shown in Fig. 4.10(a) for system sizes $N \leq 19$.[19] To fix the absolute values we note that $C_\mathrm{s} = \pi/8$ in our notation

---

[19] The figure also contains a result for $N = 20$ sites for $\Delta = 1$.

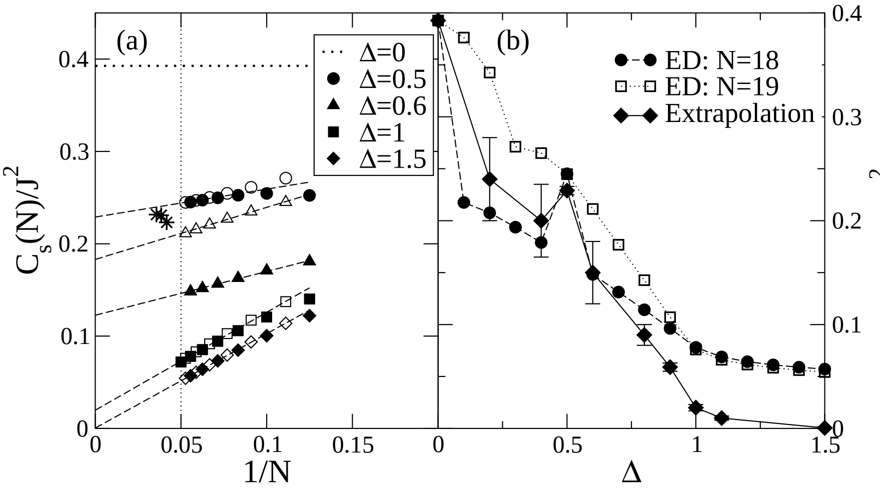

Figure 4.10: Finite-size scaling of the spin Drude weight in the high-temperature limit $\beta = 0$ [iii]. Panel (a) shows $C_\mathrm{s}(N)$ versus $1/N$ for $\Delta = 0, 0.5, 0.6, 1, 1.5$ (symbols). Open symbols denote odd N and solid symbols even N. The largest system sizes are $N = 19$ for $\Delta = 0.5, 0.6, 1.5$ and $N = 20$ for $\Delta = 1$. For $\Delta = 0$, C_s can be computed for system sizes of the order of $N = 5000$ sites without much effort, and C_s does not exhibit any finite-size effects in the limit $\beta = 0$ in this case. Thus, only a straight horizontal line is shown for $\Delta = 0$ (dotted line). In addition, the results of Ref. [90] for $\Delta = 0.5$ and $N = 24, 26, 28$ are included for comparison (stars). The straight dashed lines are fits to the data according to Eq. (4.86). The vertical line marks $N = 20$. (b): Extrapolated values for C_s (diamonds) and the ED results for $N = 18$ (solid circles) and $N = 19$ (open squares). Lines are guides to the eyes.

for the free-fermion case $\Delta = 0$. For all anisotropies that can be written as $\Delta = \cos(\pi/\nu)$, ν being an integer, $C_\mathrm{s}(N)$ follows the form

$$C_\mathrm{s}(N) = a + \frac{b}{N} + \dots\,. \tag{4.86}$$

Both the subset of even- and odd-numbered system sizes extrapolate to the same value for $N \to \infty$. This is not the case for intermediate values of Δ such as $\Delta = 0.6$, where both subsets exhibit a $1/N$-scaling with different coefficients $a_\mathrm{even}, b_\mathrm{even}$ and $a_\mathrm{odd}, b_\mathrm{odd}$. In order to estimate the value C_s in the thermodynamic limit, the following procedure is applied. In the subtle cases, i.e., $\Delta = 0.2, 0.4, 0.6, 0.8, 0.9$, fits are separately performed to the subsets with even and odd N. C_s is then estimated by averaging the results from the fits, while in the case of $\Delta = 0.5$ and $\Delta = 1$, all system sizes were included in a single fit according to Eq. (4.86). Following this procedure, one obtains $C_\mathrm{s} = (0.15 \pm 0.03)J^2$ for $\Delta = 0.6$ while the extrapolation of the even-numbered systems yields $C_\mathrm{s} = (0.123 \pm 0.001)J^2$. The latter value compares well to the data published in Ref. [84] ($C_\mathrm{s} = (0.119 \pm 0.004)J^2$). The strong differences between even- and odd-numbered systems, however, indicate that additional finite-size corrections apart from a simple $1/N$-term must become relevant for larger N if the sequences of even and odd N converge to the same value in the thermodynamic limit. A difference in the extrapolated value for large N of these two subsets does not seem to be plausible. This subtle behavior will further be elucidated below by analyzing the integrated spectral weight of the spin conductivity.

The results of the extrapolation are shown in Fig. 4.10(b), including the data points for $N = 17$ and $N = 18$ sites for comparison. The large error bars for $\Delta = 0.2, 0.4, 0.6, 0.8, 0.9$

N_{min}	N_{max}	$C_{\mathrm{s}}^{\mathrm{fit}}(\infty)$	N_{min}	N_{max}	$C_{\mathrm{s}}^{\mathrm{fit}}(\infty)$
8	19	0.030 ± 0.003	8	20	0.028 ± 0.003
9	19	0.023 ± 0.002	9	20	0.023 ± 0.003
10	19	0.024 ± 0.003	10	20	0.023 ± 0.002
11	19	0.020 ± 0.003	11	20	0.019 ± 0.002
12	19	0.022 ± 0.003	12	20	0.021 ± 0.003
13	19	0.018 ± 0.003	13	20	0.018 ± 0.003
14	19	0.018 ± 0.003	14	20	0.020 ± 0.003

Table 4.2: Extrapolation of the spin Drude weight in the limit $\beta = 0$ for the case of $\Delta = 1$ using $C_{\mathrm{s}}(N) = C_{\mathrm{s}}^{\mathrm{fit}}(\infty) + b/N$. Here, the range of the system sizes included in the fit was varied, i.e., $N_{\mathrm{min}} \leq N \leq N_{\mathrm{max}}$.

are due to the large differences in the extrapolated values of subsets with even and odd N. This analysis confirms the conclusion of $D_{\mathrm{s}}(T > 0) > 0$ for $|\Delta| < 1$ of Refs. [83,84]. The plot further suggests that $D_{\mathrm{s}}(T) = 0$ for $\Delta \geq 1.5$ within the numerical accuracy. For intermediate Ising-like anisotropies, i.e., $1 < \Delta < 1.5$, the system sizes may still be too small for an unambiguous confirmation of the conjecture $D_{\mathrm{s}}(\Delta > 1) = 0$ [83,89,250]. In particular, the possibility of a finite Drude weight in the gapped regime cannot be ruled out on the basis of the numerical data even though the Drude weight is zero at $T = 0$. An example for such a scenario, i.e., $D_{\mathrm{s}}(T = 0) = 0$ but $D_{\mathrm{s}}(T > 0) > 0$ has been given in Ref. [94] for the half-filled integrable $t - U$ Hubbard model.

The most interesting case is the Heisenberg chain $\Delta = 1$ for which the extrapolation also indicates a *finite* spin Drude weight. To estimate the reliability of the fit, the system sizes included were varied. The details are shown in Table 4.2. We find $C_{\mathrm{s}} = (0.020 \pm 0.003)J^2$ for $N_{\mathrm{min}} = 14$ and $N_{\mathrm{max}} = 20$, indicating a finite Drude weight in the thermodynamic limit. This result is smaller than the data reported in Ref. [84], where one finds $C_{\mathrm{s}} = (0.046 \pm 0.005)J^2$ there for $N = 6, 8, \ldots, 14$. The latter is regained if we use our data for $N = 6, \ldots, 14$. The analysis implies $D_{\mathrm{s}}(T > 0) > 0$ for the isotropic, ferromagnetic chain also since $C_{\mathrm{s}}(\Delta) = C_{\mathrm{s}}(-\Delta)$.

In Ref. [90], results for $C_{\mathrm{s}}(N)$ were published for system sizes as large as $N \leq 28$ using a finite-temperature Lanczos method (MCLM) by Long and coworkers. Astonishingly, their data points for $N = 24, 26, 28$ do suddenly no longer follow the $1/N$ scaling, which is always observed if exact diagonalization data are used. See Figure 4.10(a) for a direct comparison in the case of $\Delta = 0.5$. This observation casts some doubts on the reliability of the MCLM approach to study spin transport. Note that this method also computes the transport coefficient from a single microstate only, constructed to have the proper mean energy. Analytically, an expression for C_{s} was derived from the Bethe ansatz by Klümper, which can be found in Ref. [90]. The results presented here agree with this formula for $\Delta < 1$ and integer values of ν, but deviate for ν noninteger and in particular, also for $\Delta = 1$, for which a vanishing Drude weight is predicted from this expression.

Finally, one can elaborate somewhat more on the strange finite-size scaling for intermediate values of $\Delta = \cos(\pi/\nu)$; ν non-integer. It is instructive to study the integrated spectral

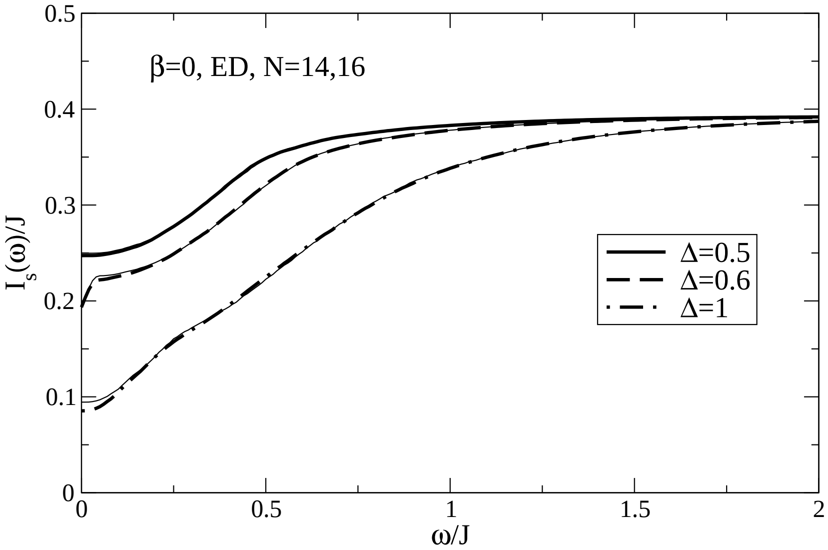

Figure 4.11: Integrated spectral weight $I_{\mathrm{s}}(\omega)$ of the XXZ chain for $\Delta = 0.5, 0.6, 1$ at $\beta = 0$ for $N = 14$ (thin lines) and $N = 16$ (thick lines). See also Ref. [89].

weight

$$I_{\mathrm{s}}(\omega) = D_{\mathrm{s}} + 2\int_{0^+}^{\omega} d\omega\,\mathrm{Re}\,\sigma_{\mathrm{reg}}(\omega)\,, \tag{4.87}$$

which is plotted versus ω for $\beta = 0$, $\Delta = 0.5, 0.6, 1$, and $N = 14, 16$ in Fig. 4.11. Note that $I(\omega)$ is well converged with respect to system size; in particular for $\omega \to \infty$. The interesting feature of incommensurate values of Δ (non-integer ν) is that there is a *depletion* of weight at low frequencies for even system sizes, which can be seen in the case of $\Delta = 0.6$. On grounds of this observation Zotos and coworkers [89] have suggested to add some spectral weight from low, but finite frequencies $\omega/J > 10^{-8}$ to the spin Drude weight. If one does so by varying the cut-off ϵ_{cut}, it seems that the extrapolation of $C_{\mathrm{s}}(N)$ to $N \to \infty$ from *odd* system sizes gives a better estimate of the true $C_{\mathrm{s}}(\infty)$. It should, however, be stressed that such procedure goes beyond the standard definition Eq. (4.12) of the Drude weight. Sticking to its definition, the obvious conclusion is that D_{s} seems to exhibit a non-continuous dependence on system size for ν non-integer [89].

Massless regime $-1 < \Delta \leq 1$

The spin Drude weight of XXZ chains with $\Delta = 0.5$ and $\Delta = 1$ is shown in Figs. 4.12 and 4.13, respectively. In the case of $\Delta = 0.5$, a comparison of D_{s}^{I} and D_{s}^{II} is presented. Note that the results for $D_{\mathrm{s}}^{I}(N,T)$ agree with the data for $\Delta = 0.4$ (not shown in the figures) and $N \leq 14$ published in Ref. [84].

The discussion starts with the case of $\Delta = 0.5$, representative for $0 \leq \Delta < 1$. In Fig. 4.12, $D_{\mathrm{s}}^{I}(N,T)$ [dashed lines] and $D_{\mathrm{s}}^{II}(N,T)$ [solid lines] are compared confirming that these two expressions are equivalent at high temperatures. In Fig. 4.12, they agree for temperatures $T/J \gtrsim 0.5$, depending on system size.

At low temperatures, $D_{\mathrm{s}}^{I}(N,T)$ shows much slower convergence with N and essential features of the temperature dependence are only present in the data for $D_{\mathrm{s}}^{II}(N,T)$. These

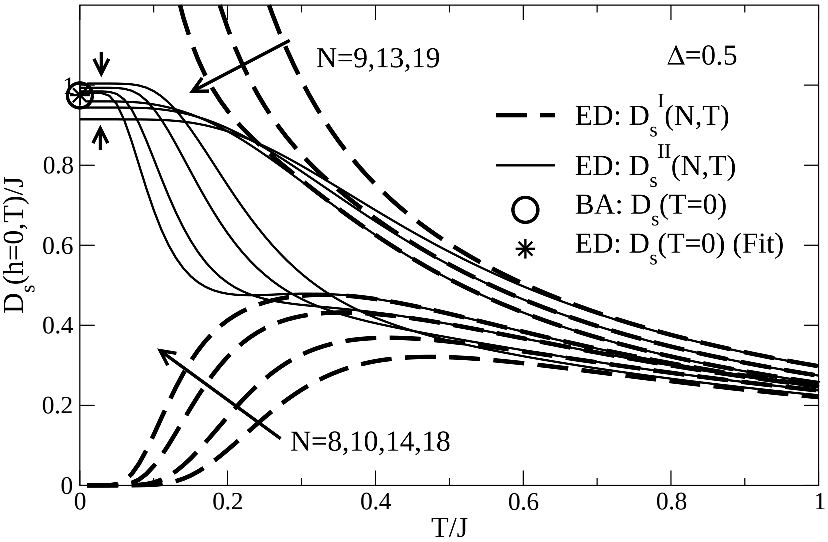

Figure 4.12: Spin Drude weight for $\Delta = 0.5$ and $N = 8, 9, 10, 13, 14, 18, 19$ sites [iii]. Dashed lines: D_s^I, solid lines: D_s^{II}. The open circle at $T = 0$ denotes the exact result for $D_\mathrm{s}(h = 0, T = 0)$ from Eq. (4.20) [79], while the star represents an extrapolation of ED data. Arrows indicate increasing system size.

are the finite value at $T = 0$ and the vanishing slope of $D_\mathrm{s}^{II}(N,T)$ for $T \to 0$. The latter observation, i.e., $dD_\mathrm{s}^{II}(N,T)/dT = 0$ at $T = 0$, is consistent with the Bethe ansatz by Klümper et al. [76, 77]. In general, the functional form of $D_\mathrm{s}(T)$ at low T for $|\Delta| < 1$ is

$$D_\mathrm{s}(T) = D_\mathrm{s}(T = 0) - \mathrm{const} \cdot T^\mu \tag{4.88}$$

where the exponent μ depends on the anisotropy. In Ref. [75], the expression $\mu = \frac{2}{\nu-1}$ was derived for integer values of ν in $\Delta = \cos(\pi/\nu)$. Taking this result, Eq. (4.88) would imply $D_\mathrm{s}(T) = D_\mathrm{s}(T = 0) - \mathrm{const} \cdot T$ for $\Delta = 0.5$ which is not consistent with the numerical data of Fig. 4.12. Should the numerical data obtained on finite systems finally converge to Zotos' result, nontrivial finite-size effects at low temperatures must necessarily become relevant. For $|\Delta| < 1$ and low T, the temperature dependence seems to be described by the expressions derived by Fujimoto and Kawakami [87] which are compatible with QMC [85, 86] and the ED presented here.

In addition, $D_\mathrm{s}^{II}(N, T = 0)$ was numerically determined by evaluating Eq. (4.9) in the subspace containing the ground state, and the results are depicted in the inset of Fig. 4.13. Using Eq. (2.54), one could go to larger systems than $N = 18$ since only the curvature of the ground state is needed. However, the main objective of this work is the Drude weight at finite temperatures while the finite-size corrections for the zero-temperature Drude weight have been computed in Ref. [261] for very large systems $N \sim 10^4$.

The results for $D_\mathrm{s}^{II}(N, T = 0)$ are plotted versus $1/N$ in the inset of Fig. 4.13 for $\Delta = 0.5$ (diamonds) and $\Delta = 1$ (squares). The data from finite systems with an even number of sites form a monotonically decreasing sequence in N at $T = 0$ and small temperatures, which can be seen in Fig. 4.12 for $T/J \lesssim 0.2$, while the data for odd N are a monotonically increasing sequence. Thus, the results for $D_\mathrm{s}^{II}(N,T)$ and even N provide an *upper* bound and those from systems with odd N a *lower* bound for $D_\mathrm{s}(T)$ at low temperatures.

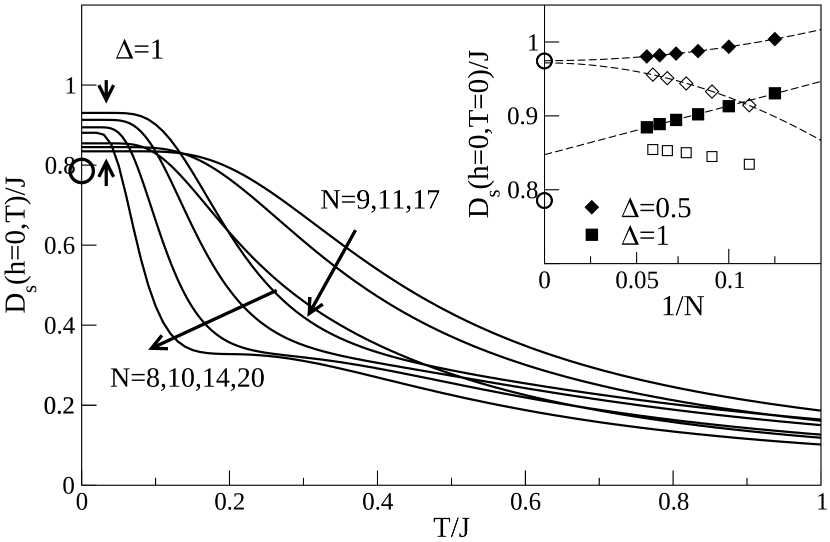

Figure 4.13: Spin Drude weight D_{s}^{II} for $\Delta = 1$ for $N = 8, 9, 10, 11, 17, 20$ sites [iii]. The inset shows the Drude weight at $T = 0$ for $\Delta = 0.5$ (diamonds) and $\Delta = 1$ (squares). Open(solid) symbols are used for odd(even) N. Open circles at $T = 0$ denote the exact results for $D_{\mathrm{s}}(T = 0)$ from Eq. (4.20) [79]. The dashed lines are fits to the numerical results according to Eq. (4.89). Arrows indicate increasing system size.

From Ref. [261], the leading finite-size corrections at $T = 0$ are available:[20]

$$D_{\mathrm{s}}^{II}(N, T = 0) = D_{\mathrm{s}}(T = 0) + \frac{B}{N^{\mu}} + \dots \tag{4.89}$$

with $\mu = 2$ for $\Delta \lesssim 0.5$. Performing fits according to Eq. (4.89) at $T = 0$ separately for even(odd) N results in $D_{\mathrm{s}}(T = 0) = 0.9747(0.9717)J$ for $\Delta = 0.5$ which is in very good agreement with the exact result $D_{\mathrm{s}}(T = 0)/J = 0.97428$ [79].

Turning now to the case of the isotropic chain with $\Delta = 1$, the analysis will be solely based on D_{s}^{II}, since this quantity describes the temperature dependence best, in particular at low temperatures. The curves shown in Fig. 4.13 display similar features as those shown in the main panel of Fig. 4.12 for $\Delta = 0.5$: (i) a vanishing slope for $T \to 0$, (ii) a monotonic decrease at high temperatures, and (iii) $D_{\mathrm{s}}^{II}(2N, T) < D_{\mathrm{s}}^{II}(2N - 2, T)$ $[D_{\mathrm{s}}^{II}(2N + 1, T) > D_{\mathrm{s}}^{II}(2N - 1, T)]$ at low temperatures $T/J \lesssim 0.1$.

However, the finite-size data at the isotropic point and $T = 0$ seem to follow

$$D_{\mathrm{s}}^{II}(N, T = 0) = A + B/N \tag{4.90}$$

in contrast to the case of $\Delta = 0.5$ as can be seen in the inset of Fig. 4.13. For A, one finds $A/J \approx 0.847$ which compares well with numerical results obtained by the Lanczos method reported in Ref. [260]. Admittedly, a good approximation to the exact value of $D_{\mathrm{s}}(T = 0)$ at $\Delta = 1$ for $N \to \infty$ *cannot* be obtained from the numerical data since the system sizes are far too small. In fact, from the work of Laflorencie et al. [261] it is known that the relevant and leading finite-size correction at $T = 0$ and $\Delta = 1$ is a logarithmic term. This is so because umklapp scattering is a marginally irrelevant perturbation in this case. Similar to the susceptibility $\chi(T)$ [248, 261], $D_{\mathrm{s}}(T)$ is expected to show a sharp drop for $T \to 0$

---

[20] The finite-size scaling of the spin Drude weight was also studied in Ref. [216].

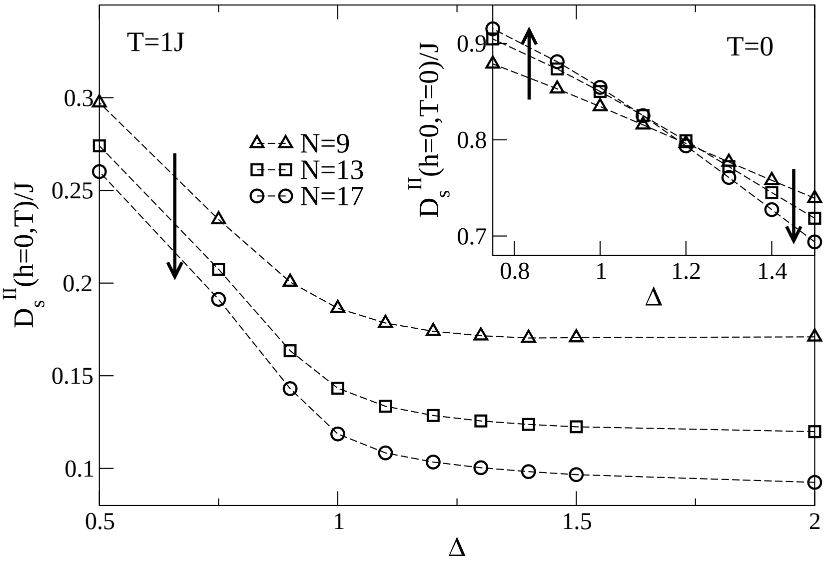

Figure 4.14: Spin Drude weight $D_{\mathrm{s}}^{II}(h = 0, T)$ in the antiferromagnetic gapped regime $\Delta > 1$, shown as a function of anisotropy at $T/J = 1$ for $N = 9, 13, 17$ [iii]. The inset shows results at $T = 0$ for the same system sizes. Lines are guides to the eyes. Arrows indicate increasing system size.

accompanied with a diverging slope at $T = 0$ in the thermodynamic limit [247].

At sufficiently large temperatures, we believe that the numerical data for $\Delta = 1$ presented in Fig. 4.13 give the correct picture of the temperature dependence of the Drude weight. However, Fujimoto and Kawakami [87] have recently obtained an analytic expression for $D_{\mathrm{s}}(T)$ in the low-energy limit with conformal field theory which is compatible with the numerical data for $|\Delta| < 1$ but not for $\Delta = 1$. For $\Delta = 1$, Fujimoto and Kawakami find $D_{\mathrm{s}}(T) < D_{\mathrm{s}}(T = 0)$ while the data shown in Fig. 4.13 seemingly support the opposite relation. Despite of this discrepancy, our results do nevertheless support the notion of a *finite* $D_{\mathrm{s}}(T > 0)$ at $\Delta = 1$. This is substantiated by the analysis of the high-temperature prefactor $C_{\mathrm{s}}(N)$ defined in Eq. (4.85), which has been discussed in detail above.

Antiferromagnetic regime $\Delta > 1$

In the massive, antiferromagnetic regime $\Delta > 1$, the monotonic increase of $D_{\mathrm{s}}^{II}(N, T)$ at low temperatures observed before for odd N changes to a monotonic decrease. This is illustrated in the inset of Fig. 4.14 where $D_{\mathrm{s}}^{II}(N, T = 0)$ is plotted versus Δ for $N = 9, 13, 17$; compare Refs. [261, 262]. The crossover in the monotony occurs at $\Delta \approx 1.2$, i.e., in the gapped regime. Since $D_{\mathrm{s}}^{II}(N, T)$ is almost constant at small temperatures, the behavior at $T = 0$ is characteristic for the low-temperature regime. At larger temperatures, $D_{\mathrm{s}}^{II}(N, T)$ is a monotonically decreasing function for both even and odd N which can be seen in Fig. 4.14 for odd N and $T/J = 1$.

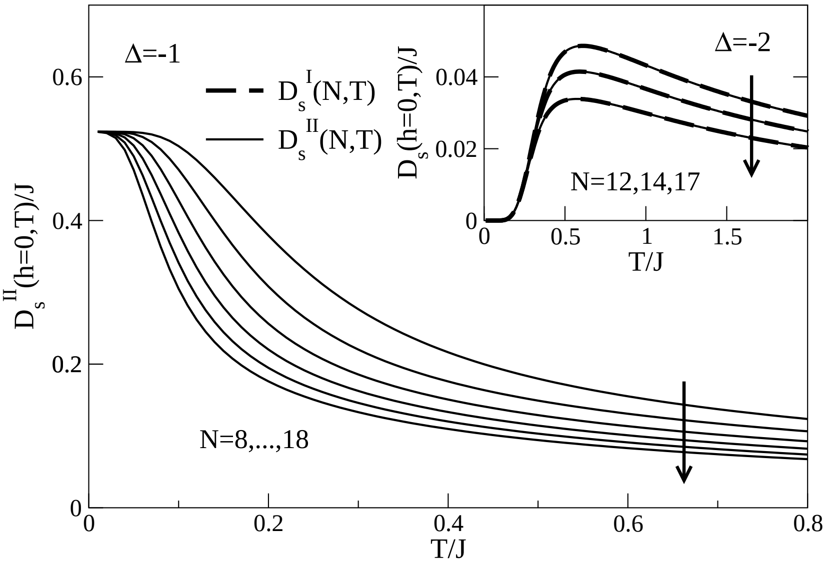

Figure 4.15: Main panel: Spin Drude weight $D_s^{II}(h=0,T)$ for the $SU(2)$-symmetric ferromagnetic chain ($\Delta=-1$), plotted as a function of temperature and for $N=8,\ldots,18$ [iii]. The inset shows results for both $D_s^I(h=0,T)$ and $D_s^{II}(h=0,T)$ at $\Delta=-2$ (dashed lines: D_s^I, solid lines: D_s^{II}). Arrows indicate increasing system size.

Ferromagnetic regime $\Delta \leq -1$

Regarding the ferromagnetic regime, i.e., $\Delta \leq -1$, the examples of $\Delta=-1$ and $\Delta=-2$ are studied. The results for $\Delta=-1$ plotted in Fig. 4.15 indicate a constant $D_s^{II}(N,T)$ at low temperatures with $D_s(T=0)/J \approx 0.523(5)$. However, since the low-energy spectrum for $\Delta=-1$ is of comparable complexity as for $\Delta=1$, one may expect nontrivial finite-size corrections which could lead to a different temperature dependence at low T. If the latter is true, then the system sizes are too small to draw conclusions about the behavior of $D_s^{II}(N,T)$ at very low temperatures.

The Drude weight in the gapped, ferromagnetic regime is expected to show a behavior similar to that of $\Delta>1$. For instance, $D_s^{II}(N,T)$ is monotonically decreasing with N at all temperatures irrespective of odd-even effects. Interestingly, $D_s^I(N,T)$ and $D_s^{II}(N,T)$ turn out to be indistinguishable for $\Delta<-1$ and N large enough which is illustrated in the inset of Fig. 4.15. This plot shows $D_s^{I,II}(N,T)$ for $N=12,14,17$ at $\Delta=-2$ where dashed lines show $D_s^I(N,T)$ from Eq. (4.8) and solid lines stem from $D_s^{II}(N,T)$ [Eq. (4.9)].

4.5.2 Finite magnetic fields

Zero temperature

The Drude weight of systems of electrons at zero temperature is, according to the criteria suggested by Kohn [64] and Scalapino et al. [127], a useful quantity to investigate metal-insulator transitions. Though we are dealing with spinless fermions in the case of the XXZ

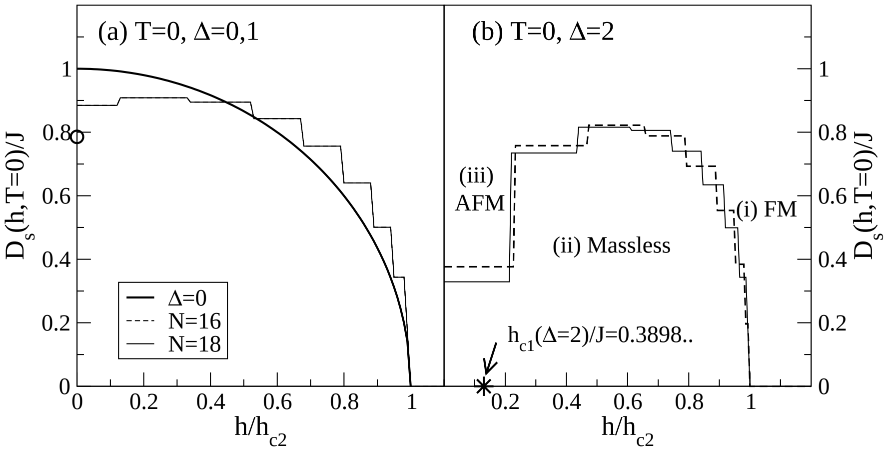

Figure 4.16: Spin Drude weight $D_\mathrm{s}(h, T = 0)$ at zero temperature for $\Delta = 0, 1$ [panel (a)] and $\Delta = 2$ [panel (b)] as a function of h/h_{c2}. The result for $\Delta = 0$ is for $N \to \infty$ and $T = 0$; $D_\mathrm{s}(h, T = 0) = \sqrt{J^2 - h^2}$. The circle in panel (a) marks the exact value of $D_\mathrm{s}(h = 0, T = 0)$ for $\Delta = 1$ and $N \to \infty$ [79]. The star in panel (b) denotes the critical field h_{c1} for $\Delta = 2$, taken from Ref. [243].

chain, the picture still applies to this case as well and it is therefore of interest to investigate the field dependence of the zero-temperature spin Drude weight $D_\mathrm{s}(h, T = 0)$. Technically, the best way to study this limit is to consider a flux-dependent Hamiltonian, or to introduce twisted boundary conditions, equivalently. The Drude weight then follows from

$$D_\mathrm{s}(h, T = 0) = \pi \, N \, \frac{\partial E_0^2}{\partial \Phi^2}\bigg|_{\Phi=0} \tag{4.91}$$

where E_0 denotes the ground-state energy assuming that the ground state is unique. This allows one to study large systems sizes since Lanczos techniques provide an excellent tool to determine extremal eigenvalues. This approach was used in, e.g., Refs. [252, 260] for the frustrated chain and Hubbard rings. However, we will proceed differently, since this section's chief case is to discuss qualitative aspects of the Drude weight. Preliminary results from using full exact diagonalization will be shown.

First, one has to identify the subspace that contains the ground state. Then, analogously to the case of zero magnetic field discussed in Sec. 4.5.1, the Drude weight is given by:

$$D_\mathrm{s}^{II}(h, T = 0) = \frac{\pi}{N}\left[\langle 0| - \hat{T}|0\rangle - 2 \sum_{E_n \neq E_0} \frac{|\langle n|j_\mathrm{s}|0\rangle|^2}{E_n - E_0}\right]. \tag{4.92}$$

Results for $D_\mathrm{s}^{II}(h, T = 0)$ as a function of h/h_{c2} computed for $N = 16$ and 18 sites are shown in Fig. 4.16(a) for $\Delta = 0$ and $\Delta = 1$ and in Fig. 4.16(b) for $\Delta = 2$. The curve for $\Delta = 0$ is of course computed exactly at $T = 0$ and for $N \to \infty$, and the result is $D_\mathrm{s}(h, T = 0) = \sqrt{J^2 - h^2}$.

The Drude weight is clearly finite in the massless regime indicating ideal metallic behavior while it vanishes at the quantum critical line $h = h_{c2}$. The same features, modulated by finite-size effects are present in the numerical data for $\Delta = 1$. Since a chain with $N = 18$ sites has 10 subspaces with $S^z_\mathrm{tot} = 0, \ldots, 9$, there are 10 plateaus in $D_{11} = D_\mathrm{s}(h, T = 0)$, including the one for $h > h_{c2}$. $D_\mathrm{s}(h, T = 0)$ drops to zero exactly at $h = h_{c2}$. The reason is that the one-magnon state is an exact eigenstate both for finite systems and in the thermodynamic limit. The difference in the ground-state energies of $S^z_\mathrm{tot} = N/2$ and $S^z_\mathrm{tot} = N/2 - 1$ (N even)

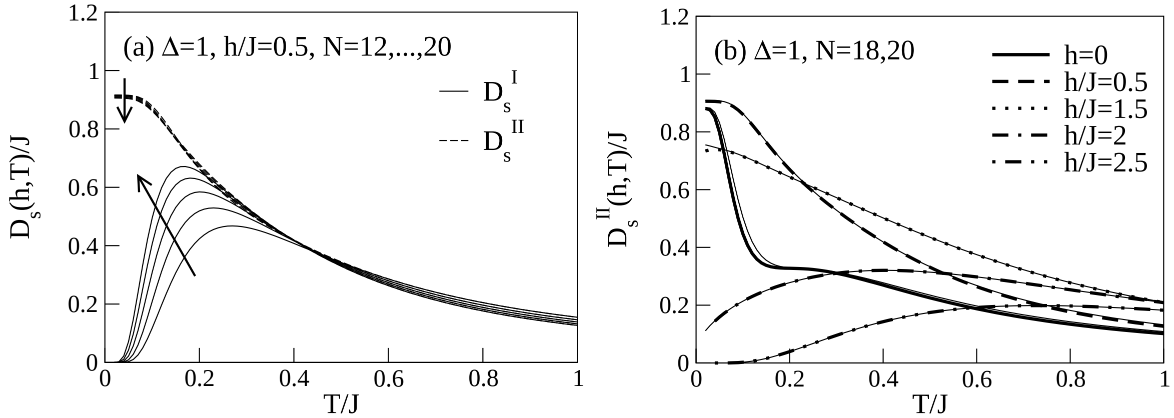

Figure 4.17: (a): Finite-size scaling of the spin Drude weight for $\Delta = 1$, $N = 12, \dots, 20$ and for $h/J = 0.5$. Solid lines denote D_{s}^{I} and dashed ones D_{s}^{II}. Arrows indicate increasing system size. (b): Spin Drude weight $D_{\mathrm{s}}^{II}(h,T)$ for $\Delta = 1$ versus temperature for various magnetic fields $h/J = 0, 0.5, 1.5, 2, 2.5$ for $N = 18$ (thin solid lines) and $N = 20$ sites (thick lines).

is the critical field:

$$h_{c2} = E_0(S^z_{\mathrm{tot}} = N/2) - E_0(S^z_{\mathrm{tot}} = N/2 - 1)\,. \tag{4.93}$$

Thus, in the fully polarized state, the Drude weight is found to be zero even on finite system sizes indicating insulating behavior, as expected. The star at $h = 0$ marks the exact result for $D_{\mathrm{s}}(h = 0, T = 0)$ from Ref. [79].

The case of $D_{\mathrm{s}}(h, T = 0)$ and $\Delta = 2$ is even more interesting, since both critical lines are crossed. While it is evident from Fig. 4.16(b) that $D_{\mathrm{s}}(h, T = 0) > 0$ in the massless regime, finite values of the zero temperature Drude weight are still found in the antiferromagnetic regime $h < h_{c1}$. These finite values decrease as a function of system size indicating a vanishing Drude weight $D_{\mathrm{s}}(h, T = 0)$ in the thermodynamic limit. A precise determination of h_{c1} from the numerical results for $D_{\mathrm{s}}(h, T = 0)$ is not possible without further extrapolations. On the contrary, the behavior at the second critical field resembles that of Fig. 4.16(a): finite-size effects become small. The examples discussed here show that $D_{\mathrm{s}}(T = 0, h)$ reflects the different ground states of the model in the (Δ, h) plane.

Finite temperatures

Turning now to finite temperatures, four aspects will be discussed, and the main focus will be on the case of the Heisenberg chain. First, D_{s}^{I} and D_{s}^{II} are compared on finite systems with $N \leq 20$ and $\Delta = 1$ in Fig 4.17(a). Second, results for the Drude weight $D_{\mathrm{s}}^{II}(h, T)$ as a function of temperature and for several magnetic fields are shown in Fig. 4.17(b). Next, the Drude weight is plotted versus h/h_{c2} for $T/J = 0.5, 1$ in Fig. 4.18. Finally, some remarks on Mazur's inequality will be made.

A behavior similar to the case of $h = 0$ is found regarding the finite-size dependence of D_{s}^{I} as compared to D_{s}^{II} in the massless regime. We find $D_{\mathrm{s}}^{II}(h, T = 0) > 0$ and a vanishing slope of $D_{\mathrm{s}}^{II}(h, T)$ if the temperature is lowered. Prominent finite-size effects of $D_{\mathrm{s}}^{II}(h, T)$ are not found at low temperatures. It would be desirable to compare the numerical results with exact expressions for $D_{\mathrm{s}}(h, T = 0)$, from, e.g., bosonization. Unfortunately, values for

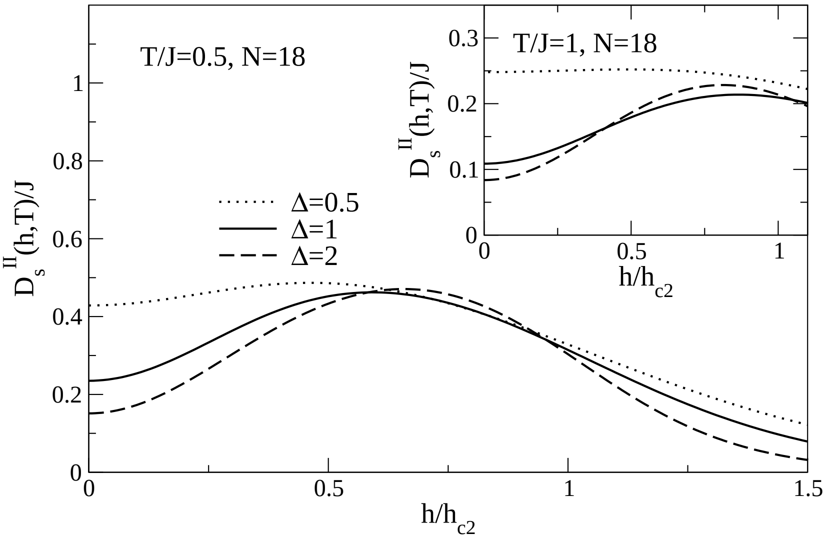

Figure 4.18: Spin Drude weight $D_{\mathrm{s}}^{II}(h,T)$ versus magnetic field h/h_{c2} at $T/J=0.5$ (main panel) and $T/J=1$ (inset) for $\Delta=0.5,1,2$ and $N=18$ sites.

the velocity $v(h)$ and the Luttinger parameter $K(h)$ are rarely known, their computation involving the solution of nonlinear integral equations, and at present, this is left as a future project. The conclusion from the comparison of D_{s}^{I} and D_{s}^{II} is that D_{s}^{II} results in the more reliable low-temperature behavior in the massless phase. In the fully polarized state, we find $D_{\mathrm{s}}^{I}\approx D_{\mathrm{s}}^{II}$ anyway.

Regarding the temperature dependence of $D_{\mathrm{s}}^{II}(h,T)$ in the massless phase, it is worth noting that finite-size effects are small down to very low temperatures. Note the good agreement between the results for $N=18$ and $N=20$ in Fig. 4.17(b). At low temperatures, the numerical data for $N=20$ sites are compatible with the following functional forms:

$$\begin{aligned}
D_{\mathrm{s}}(h,T) &= D_{\mathrm{s}}^{II}(h,T=0)-b\,T^{4.2} && \text{for} \quad h/J=0.5\,,\\
D_{\mathrm{s}}(h,T) &= \exp(-0.546)\,T^{0.43} && \text{for} \quad h/J=h_{c2}/J=2.0\,,\\
D_{\mathrm{s}}(h,T) &= \exp(0.115)\,T^{0.47}\,e^{-0.5/T} && \text{for} \quad h/J=2.5\,,
\end{aligned} \tag{4.94}$$

which have been extracted by fitting the numerical data using functions motivated from mean-field theory [see Sec. 4.4 and Eqs. (4.88), (4.76), and (4.78)]. At very high temperatures, one always finds $D_{\mathrm{s}}\approx C_{\mathrm{s}}/T$ and C_{s} is *independent* of the magnetic field. Note that in the fully polarized regime, one the one hand, $D_{\mathrm{s}}(h,T=0)=0$ is found, but one the other hand, $D_{\mathrm{s}}(h,T>0)>0$ implying that an *ideal insulator* at $T=0$ *can* evolve into an ideal *conductor* at finite temperatures, in contrast to one of Zotos's and coworkers' conjectures [83].

Plotting $D_{\mathrm{s}}^{II}(h,T)$ versus magnetic field h/h_{c2} at fixed temperatures reveals that $D_{\mathrm{s}}^{II}(h,T)$ exhibits a broad maximum at roughly $h\approx 0.7h_{c2}$, seen in all cases shown in Fig. 4.18, both for $T/J=0.5$ and $T/J=1$. At such high temperatures, no clear indications of the critical lines are found.

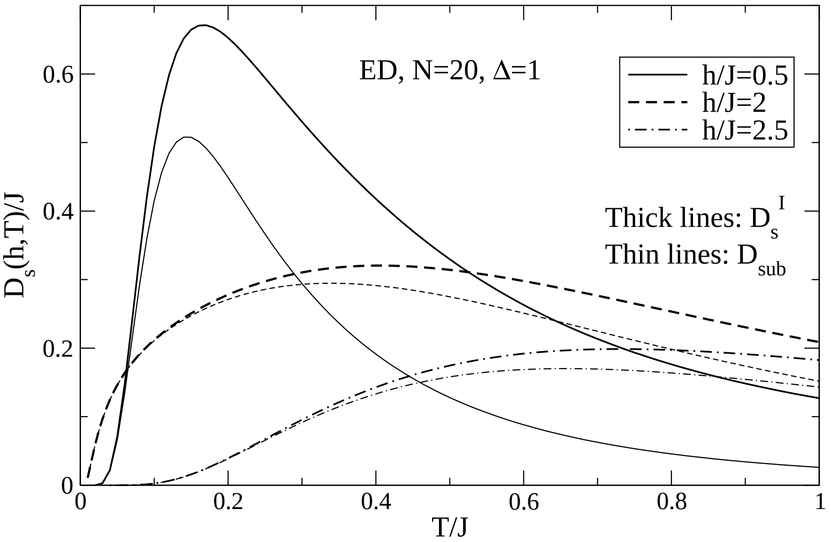

Figure 4.19: Comparison of the spin Drude weight $D_{\mathrm{s}}^{I}(h,T)$ [thick lines] and its lower bound $D_{\mathrm{sub}}(h,T)$ [Eq. (4.96)] (thin lines; see text for further details). The figure shows results for $\Delta = 1$, N=20, and $h/J = 0.5, 2, 2.5$ [ix].

Mazur's inequality

Finally, let us turn to the inequality Eq. (2.80) for the spin Drude weight $D_{11}(h,T) = D_{\mathrm{s}}(h,T)$ introduced in Sec. 2.3.1:

$$D_{\mathrm{s}}^{I}(h,T) \geq \frac{\pi}{N\,T} \sum_{m} \frac{\langle j_{\mathrm{s}} Q_m \rangle^2}{\langle Q_m^2 \rangle}\,. \tag{4.95}$$

Here, we want to discuss to which extent the inequality Eq. (4.95) is exhausted by j_{th} at finite magnetic fields and finite temperatures. An analogous analysis for $\beta = 0$ has been presented in Ref. [61]. To this end $D_{\mathrm{s}}^{I}(h,T)$ and

$$D_{\mathrm{sub}}(h,T) := \frac{\pi}{T\,N} \frac{\langle j_{\mathrm{s}} j_{\mathrm{th}} \rangle^2}{\langle j_{\mathrm{th}}^2 \rangle} = \frac{1}{T} \frac{D_{\mathrm{th,s}}^2(h,T)}{D_{\mathrm{th}}(h,T)} \tag{4.96}$$

are compared in Fig. 4.19. The relation $D_{\mathrm{s}}(h,T) \geq D_{\mathrm{sub}}(h,T)$ is equivalent to the positivity of the thermal Drude weight $K_{\mathrm{th}}(h,T) \geq 0$ as defined in Eq. (4.17). Second, $D_{\mathrm{s}}(h,T) \approx D_{\mathrm{sub}}(h,T)$ implies a very small thermal Drude weight and thus, the comparison provided in Fig. 4.19 also reveals the relative size of the two contributions to $K_{\mathrm{th}}(h,T)$ in Eq. (4.17), namely $D_{\mathrm{th}}(h,T)$ and the magnetothermal correction $D_{\mathrm{th,s}}^2(h,T)/[T\,D_{\mathrm{s}}^{I}(h,T)]$. In Fig. 4.19, results are shown for $\Delta = 1$, $N = 20$ sites, and $h/J = 0.5, 2, 2.5$. For the sake of clarity, data for smaller system sizes are not included in the figure. Differences between the curves for $N = 18$ and $N = 20$ are anyway only pronounced for temperatures $T/J \lesssim 0.1$ and become smaller as the magnetic field h increases.

Figure 4.19 allows for three major observations: (i) $D_{\mathrm{s}}^{I}(h,T) \approx D_{\mathrm{sub}}(h,T)$ at low temperatures and for all cases shown in the figure; (ii) $D_{\mathrm{sub}}(h,T)$ approximates $D_{\mathrm{s}}^{I}(h,T)$ the better the larger the magnetic field is; and (iii) significant deviations are present for high temperatures implying that for a quantitative description of $D_{\mathrm{s}}(h,T)$ using Eq. (4.95), more conserved quantities need to be considered.

This comparison provides, at least for finite system sizes, a quantitative measure of the temperature range where $D_{\mathrm{s}}^{I} \approx D_{\mathrm{sub}}$. Observation (i) indicates that analytical approaches can make use of $D_{\mathrm{sub}}(h, T)$ for a quantitative description of $D_{\mathrm{s}}(h, T)$ at low temperatures as it has been done by Fujimoto and Kawakami within a continuum theory in Ref. [87]. The quantities that appear on the right hand side of Eq. (4.95) are less involved than Eqs. (4.8) and (4.9) for $D_{\mathrm{s}}(h, T)$ since the former are static correlators. Furthermore, for finite magnetic fields, we suggest to compute $D_{\mathrm{s}}(h, T)$ analytically from Eq. (4.95), taking into account some more of the conserved quantities Q_m, which are in principle known (see, e.g., Ref. [244]). Such a procedure is applicable to $h \neq 0$ and might circumvent the ambiguities in the results encountered in recent computations of $D_{\mathrm{s}}(h = 0)$ including different Bethe ansatz approaches [75–77, 87, 90]. The latter have used Eq. (4.9) directly or Kohn's formula [60, 64], equivalently. Regarding the relative size of $D_{\mathrm{th}}(h, T)$ and the magnetothermal correction, we see that the latter becomes more relevant the larger the magnetic field is, which leads to the strong suppression of $K_{\mathrm{th}}(h, T)$. This is consistent with results of the mean-field theory treatment.

4.6 The thermal Drude weight (ED)

4.6.1 Zero magnetic field

In contrast to the spin Drude weight D_{s}, which has been discussed in the previous section, the thermal Drude weight $K_{\mathrm{th}} = D_{\mathrm{th}}$ of the XXZ chain at zero magnetic field is a static correlator of the current operator

$$D_{\mathrm{th}}(h = 0, T) = \frac{\pi}{N T^2} \langle j_{\mathrm{th}}^2 \rangle \, . \tag{4.97}$$

Therefore, one does not need to care about degenerate states since only a trace has to be evaluated. In the following, numerical results for $D_{\mathrm{th}}(T)$ will be presented for $\Delta = 1, 2, -0.5, -1, -2$, covering the different phases of the model. Technically, it is helpful to realize that the results for negative anisotropies $\Delta < 0$ can be obtained from the spectrum of positive Δ by computing the correlators at negative temperatures, i.e.,

$$D_{\mathrm{th}}(-\Delta, T) = D_{\mathrm{th}}(\Delta, -T) \, . \tag{4.98}$$

Thus, once the matrix elements of the thermal current j_{th} and the eigenenergies are known for $\Delta > 0$, no additional computational effort is needed to obtain results for negative anisotropies.

Antiferromagnetic chains $\Delta > 0$

First of all, the numerical implementation can be checked in the limit of free fermions $\Delta = 0$, for which the Drude weights can be evaluated both in the thermodynamic limit, on finite systems and, also for specific subspaces labeled by total S^z and momentum k. Such technical checks have been done but will not be discussed in detail.

Next it is important to check the convergence of the numerical data with respect to system size. Figure 4.20(a) shows the curves for finite systems with even N (dashed lines)

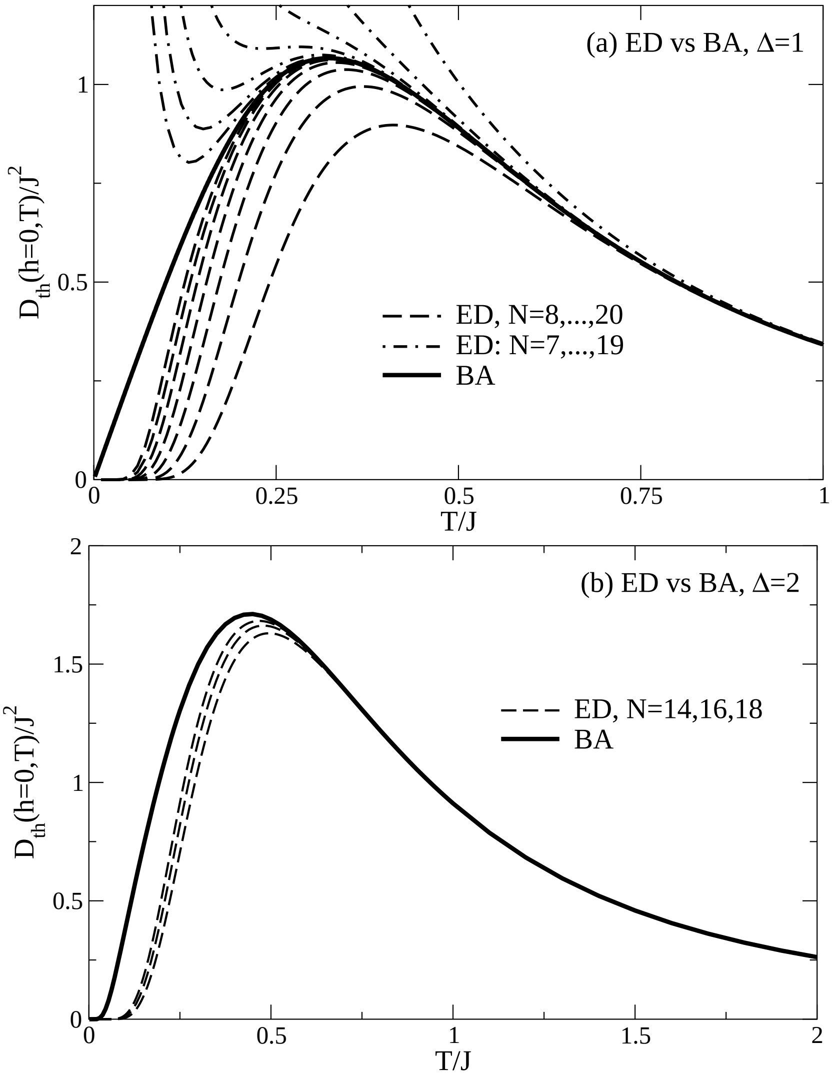

Figure 4.20: Thermal Drude weight $K_{\text{th}}(h=0,T) = D_{\text{th}}(h=0,T)$ of the Heisenberg chain ($\Delta = 1$) [panel (a)] and for $\Delta = 2$ [panel (b)] [i, iii]. Dashed lines are the ED results for finite systems with $N = 8, \ldots, 20$ sites, dot-dashed lines in panel (a) are the odd system sizes $N = 7, \ldots, 19$. For comparison, the exact results for $N \to \infty$ from Refs. [78, 82] are also shown (solid lines, BA). See also Ref. [54] for numerical results for $\Delta = 1$, $N \leq 14$.

and odd N (dot-dashed lines) for $N = 7, \ldots, 20$ and $\Delta = 1$ together with the exact result from Ref. [78]. One should pay attention to the fact that at high temperatures $T/J \gtrsim 0.5$, no finite-size effects are visible within the line-width of the plot. From the numerical data, it is even possible to determine the position of the maximum quite accurately. A strong difference between even and odd N becomes obvious from the figure: for even N, D_{th} is always suppressed by finite-size gaps at low temperatures and the curves exhibit a maximum while for odd N, $D_{\text{th}}(N,T)$ diverges for $T \to 0$. The physical reason is that the ground state for even N lies in the subspaces with $S^z_{\text{tot}} = 0$ and $k = 0, \pi$, while for odd N, the ground state is found at finite momentum $k \neq 0, \pi$. A finite slope of the dispersion and thus a finite matrix element $\langle 0 | j_{\text{th}} | 0 \rangle$ is therefore expected for odd N. In other words, in a system with an odd number of sites with periodic boundary conditions, there is always one domain wall, or spinon excitation, respectively. The comparison with the Bethe ansatz result proves the correct implementation of the current operator and it shows that the numerical approach is well suited to study transport properties. In fact, the results can even be improved using standard extrapolation schemes,[21] which allow one to reach lower temperatures. This works well if the dependence on system size is monotonous.

Having demonstrated that the method works, the focus will be on the behavior of D_{th} as a function of anisotropy Δ. From Ref. [78] as well as from conformal field theory outlined in Sec. 4.3, one knows that $D_{\text{th}} = (\pi^2/3)vT$ at low temperatures. This regime, however, turns out to be out of reach for exact diagonalization in the massless phase. One might expect that the presence of the gap in the antiferromagnetic gapped regime improves the convergence of D_{th} at low temperatures. This, however, is not the case as can be seen in Fig. 4.20(b), where numerical data for $N = 14, 16, 18$ is compared with the Bethe ansatz result for $\Delta = 2$ from Ref. [82]. Rapid convergence is found at high temperatures, but deviations remain present for $T/J \lesssim 0.5$, similar to the case of $\Delta = 1$. At low temperatures, the thermal Drude weight is exponentially activated with a power-law prefactor [55, 82]:

$$D_{\text{th}} \propto e^{-G/T}/\sqrt{T}\,. \tag{4.99}$$

In experiment, the square root divergence of D_{th} will be compensated by the mean value of the velocity, for which one finds $\langle v\rangle \propto \sqrt{T}$ for a gapped spectrum. Interestingly, the gap G_{ED} that one can extract from the numerical data for finite systems at low temperatures is very close to the *two*-spinon gap. For instance, for $\Delta = 10$, one obtains $G_{\text{ED}}/J = 8.056$ [i], which is close to the value of the two-spinon gap $G_{2\text{sp}}/J = 8.055126$ [277]. For the thermodynamic limit, however, one can show, that the gap that enters in Eq. (4.99) is the *one*-spinon gap [82].

Ferromagnetic chains $\Delta < 0$

Turning now to the case of negative Δ, i.e., to the region $-1 \leq \Delta < 0$, note that no results for $N \to \infty$ are yet available in the literature. When Δ decreases, starting from the free-fermion case, the convergence with system size quickly improves when $\Delta = -1$ is approached. This is not so clear for the case of $\Delta = -0.5$ shown in Fig. 4.21(a), but becomes quite obvious for the $SU(2)$-symmetric ferromagnetic chain and the case of $\Delta = -2$, which is presented in Fig. 4.21(b). While the numerical data for $\Delta = -0.5$ do not allow for a conclusion about the low-temperature behavior, the thermal Drude weight at $\Delta = -1$ most likely exhibits a linear T-dependence, although $(\Delta = -1, h = 0)$ is the starting point of the quantum critical line $h/J = \Delta + 1$ in Fig. 4.1, for which mean-field theory and conformal field theory predict a universal $T^{3/2}$-power law.

In the gapped ferromagnetic state, the Drude weight at low temperatures follows the form of Eq. (4.99) [82], where the gap is now the one-triplet gap $G = -J(1 + \Delta)$, that can easily be determined from a spin-wave computation. From the numerical data for $\Delta = -2$ shown in Fig. 4.21(b), one obtains $G/J = 0.97$, in good agreement with the exact expression.

---

[21] Here the Vanden-Broeck-Schwartz algorithm was used for this purpose [276], which is provided by *diagonalize* [263]. Results are not shown in the figures.

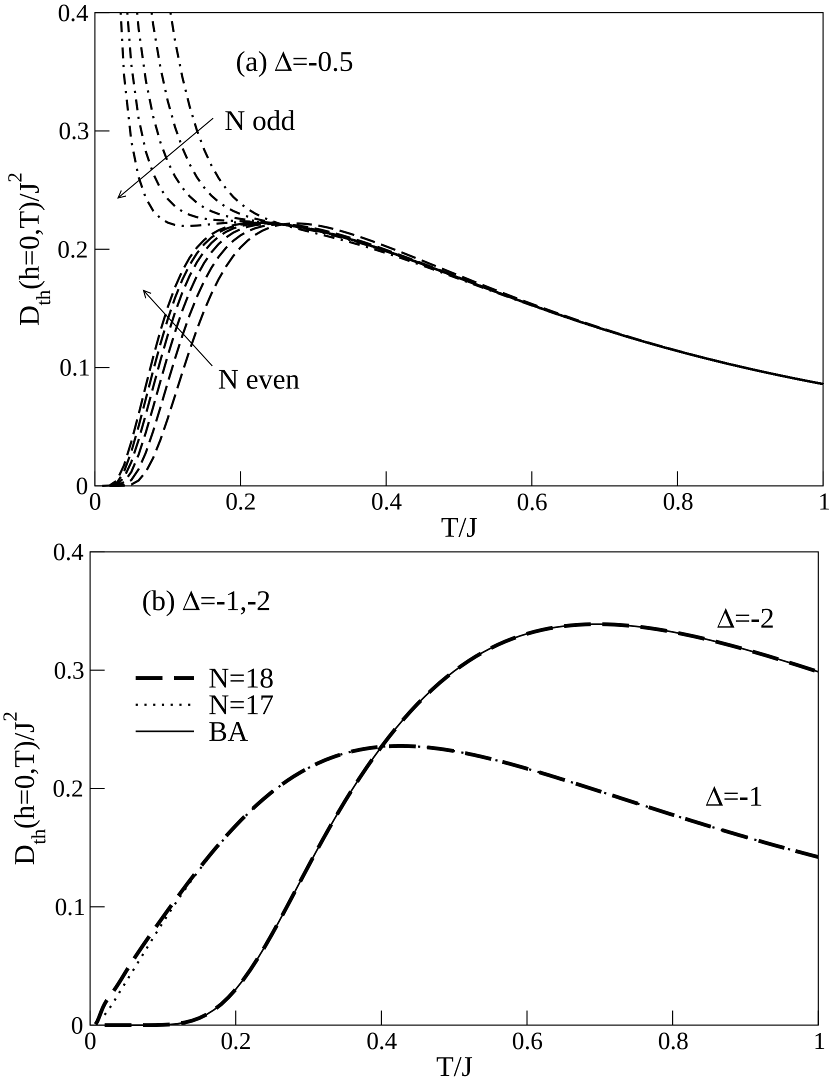

Figure 4.21: Thermal Drude weight $K_{\text{th}}(h = 0, T) = D_{\text{th}}(h = 0, T)$ of a chain with ($\Delta = -0.5$) [panel (a)] and for $\Delta = -1, -2$ [panel (b)] [iii, i]. In panel (a), results for $N = 8, 9, \dots, 18$ are shown. Dashed lines are the results from ED for even N; dot-dashed lines denote odd N. Panel (b): Dashed lines are the results from ED for $N = 18$ sites; the dotted line denotes $N = 17$ sites. For comparison, the exact result for $N \to \infty$ from Ref. [82] is also shown for $\Delta = -2$ (solid line, BA).

Position of the maximum and scaling in the high-temperature limit

To illustrate the qualitative dependence of D_{th} on the anisotropy Δ, the position of the maximum T_{max} and the maximum value of the thermal Drude weight $D_{\text{th}}(T_{\text{max}})$ are plotted versus Δ in Fig. 4.22(a). From this figure one infers that the smallest values for the Drude weight are expected close to $\Delta = -1$. Furthermore, the position of the maximum T_{max} is smallest in the vicinity of $\Delta \gtrsim -1$. Both T_{max} and $D_{\text{th}}(T_{\text{max}})$ are not symmetric with respect to $\Delta = 0$, and both quantities increase steadily for increasing $|\Delta| > 1$. In contrast to the low-temperature regime, the symmetry with respect to Δ is restored in the high-temperature limit, i.e., $C_{\text{th}}(\Delta) = C_{\text{th}}(-\Delta)$. $C_{\text{th}}(\Delta)$ is the coefficient of the leading term in an expansion

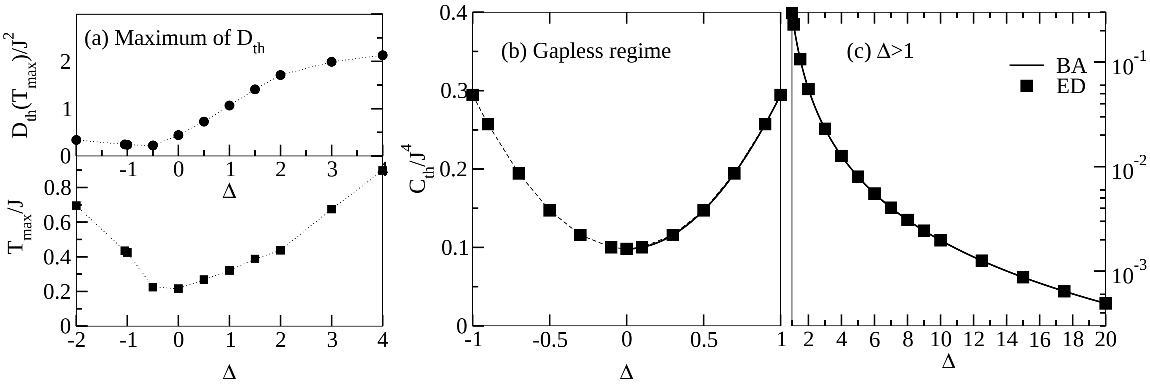

Figure 4.22: (a): Position $T_{\max}$ of the maximum of $D_{\text{th}}(T)$ versus anisotropy Δ [lower panel in (a)]. In the upper panel, $D_{\text{th}}(T_{\max})$ is plotted versus anisotropy. Where available, the data points were extracted from the Bethe ansatz results from Refs. [78, 82] [$\Delta = 0, 0.5, 1, 2, 3, 4$]. In the other cases, the results for $N = 18$ sites are shown. (b), (c): High-temperature prefactor C_{th} of the thermal Drude weight $K_{\text{th}}(h = 0, T) = D_{\text{th}}(h = 0, T)$; plotted as a function of anisotropy in the massless regime $|\Delta| < 1$ in panel (b) and in the massive regime $\Delta > 1$ in panel (c) [iii]. Solid lines in panels (b) and (c) represent the result from Refs. [78, 82] [see Eq. (4.101)].

of D_{th} in $1/T$:

$$C_{\text{th}} = \lim_{T\to\infty} [T^2\, D_{\text{th}}(T)]\,. \tag{4.100}$$

The coefficient C_{th} is plotted versus Δ in Figs. 4.22(b) and 4.22(c) for the massless regime $|\Delta| \leq 1$ and the gapped regime $\Delta > 1$, respectively. In the massless regime, there is a minimum at $\Delta = 0$, in contrast to spin transport where the corresponding coefficient C_{s} is maximal in the XY case.

Figures 4.22(b) and 4.22(c) also contain solid lines which are analytically exact results for $C_{\text{th}}(\Delta)$ [78, 82]:

$$C_{\text{th}}(\Delta) = \frac{\pi\, J^4}{64}\left[3 + \frac{\sin(3\arccos\,\Delta)}{\sin(\arccos\,\Delta)}\right]. \tag{4.101}$$

The ED data points, computed for systems of only 12 sites, are in perfect agreement with this exact expression.

In the limit of $\Delta/J \to \infty$, one approaches the one-dimensional Ising model, where no transport is possible, since all excitations are local spin flips which cannot propagate. Thus, all transport coefficients must vanish in this limit, and in order to observe this, C_{th} is scaled on Δ instead of J for $\Delta > 1$ in Fig. 4.22(c).

Truncation of the spectrum; contribution of subspaces with fixed S^z_{tot} to D_{th}

Finally, having discussed the finite-size as well as the temperature dependence of $K_{\text{th}} = D_{\text{th}}$ at zero magnetic field, one can conclude that exact diagonalization is a very good tool to study the thermal Drude weight of the XXZ chain. However, one might be interested in overcoming the restrictions regarding the system sizes that could be studied so far. Two ways out have been tested: (i) truncation of the spectrum in the largest subspaces, e.g., $S^z = 0$ for even N; and (ii) restriction to the subspaces with given magnetization $\langle M\rangle = S^z_{\text{tot}}$. Without much computational effort, it is possible to compute only low-lying eigenenergies and states in the largest subspaces for, e.g., $N = 22, 24$. However, this immediately leads to errors at high temperatures, while no significant improvement at low temperatures could be achieved. Therefore, this strategy was not further pursued.

If one diagonalizes only subspaces with given magnetization $\pm S^z_{\mathrm{tot}}$ at zero magnetic field to ensure $\langle M \rangle = 0$, one finds that these sets also converge to the same curve in the thermodynamic limit that one obtains if all subspaces are included. While the total CPU time requirements are reduced, the convergence with system size is unfortunately much slower compared to the full diagonalization and summation of contributions from all subspaces. Also, the largest subspaces need to be diagonalized completely, still limiting the accessible system sizes. Having these observations in mind, the analysis of the thermal Drude weight K_{th} in the presence of finite magnetic fields will be done with complete diagonalization.

A very efficient way of improving the exact diagonalization analysis consists of exploiting conservation of the total spin S^2_{tot} also in the $SU(2)$-symmetric cases, e.g., $\Delta = 1$. Basically, it is possible to construct eigenenergies of, e.g., the $S^z_{\mathrm{tot}} = 1$ subspace for even N from the eigenenergies found for $S^z_{\mathrm{tot}} = 0$. This would on the one hand reduce the number of subspaces that need to be diagonalized, and on the other hand, one would still take into account the full spectrum.

Note that a finite-temperature Lanczos method developed in Ref. [90] was proposed to investigate transport properties. This numerical approach allows one to study system sizes as large as $N = 28$ [57,90]. However, the comparison of this Lanczos technique with brut-force exact diagonalization in the case of spin transport presented in Fig. 4.10 casts some doubts on the reliability of these results (see the discussion in Sec. 4.5). Unfortunately, no direct comparison between ED and this Lanczos method for the thermal Drude weight of the XXZ chain was presented in the literature.

4.6.2 Finite magnetic field

In the previous sections of this chapter, first the spin Drude weight $D_{11} = D_{\mathrm{s}}(h, T)$ at zero and finite magnetic field and second, the thermal Drude weight $K_{\mathrm{th}}(h = 0, T) = D_{\mathrm{th}}(h = 0, T)$ have been discussed. This is now extended to the case of thermal transport at finite magnetic fields under the condition of zero spin current flow, i.e., $\langle j_{\mathrm{s}} \rangle = 0$. This condition leads to Eq. (4.17) for the thermal Drude weight $K_{\mathrm{th}}(h, T)$. In practice, since the currents j_{s} and j_{th} have already been implemented for the zero field case, it is most straightforward to compute $D_{\mathrm{th}}, D_{\mathrm{th,s}}$, and D_{s} from the matrix elements of the current operators. To be economic, these matrix elements are stored, thus the diagonalization needs only to be done once, while the results at finite magnetic fields are obtained by replacing the eigenvalues $E_n^{h=0}$ of H without field by $E_n^{h=0} - hS^z_{\mathrm{tot}}$ in each subspace.

The use of Eq. (4.17) implicitly presumes that an equation of continuity holds for spin transport. Note that Shimshoni et al. [59] have argued that in any real material conservation of spin is broken due to, for instance, spin-orbit coupling. Then, no magnetothermal corrections would arise and the thermal conductivity is rather described by[22]

$$\mathrm{Re}\,\kappa(h, T, \omega) = D_{\mathrm{th}}(h, T)\delta(\omega)\,. \tag{4.102}$$

In order to cover both cases, i.e., either a coupling of j_{th} to j_{s} or no such coupling, the field dependence of K_{th}, given by Eq. (4.17), will frequently be contrasted to that of the pure

---

[22] In a real material, there will of course not be any finite Drude weight.

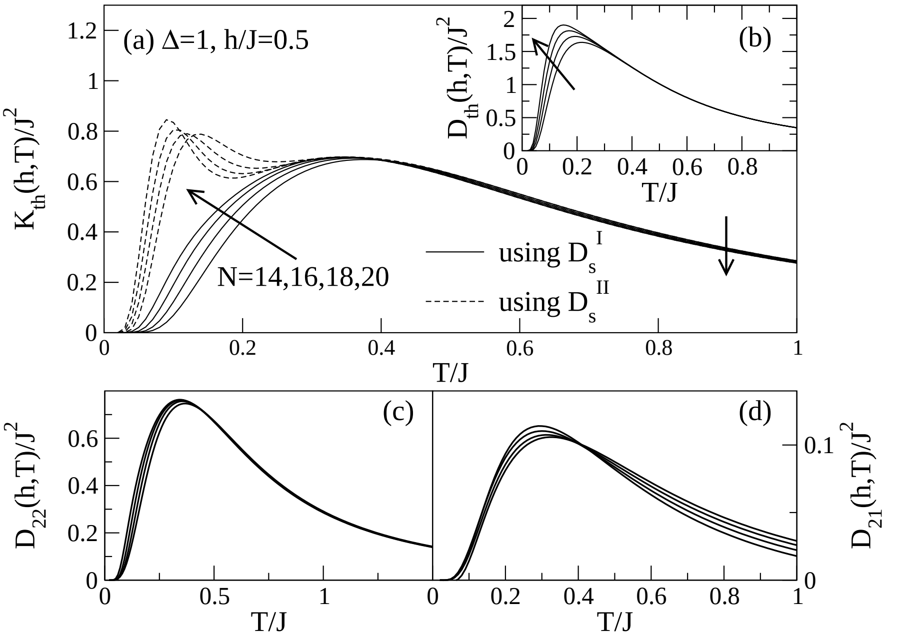

Figure 4.23: Finite-size scaling of the different Drude weights of the Heisenberg chain ($\Delta = 1$) at $h/J = 0.5$ [ix]. (a): $K_{\mathrm{th}}(h,T)$; (b): $D_{\mathrm{th}}(h,T)$; (c): D_{22}; (d): D_{21}. ED results are shown for $N = 14, 16, 18, 20$; arrows indicate increasing system size. For the solid lines in panel (a), $D_s = D_{\mathrm{s}}^I$ was used in Eq. (4.17) and for the dashed lines, $D_s = D_{\mathrm{s}}^{II}$.

thermal Drude weight D_{th}.

In principle, any other combination of transport coefficients that can be derived from Eq. (2.7) can conveniently be studied using exact diagonalization in the case of the XXZ chain, since at finite magnetic field, all Drude weights are finite.[23] At the end of this section, numerical results for the field dependence of the *magnetic thermopower*

$$S = \frac{D_{12}}{D_{11}} = \frac{1}{T}\frac{D_{21}}{D_{11}} \tag{4.103}$$

are presented. This quantity has previously been studied by Louis and Gros [91] in the limit of small magnetic fields both analytically and numerically with QMC simulations and ED. A qualitative comparison with their results is performed.

Scaling with system size

The main focus of this section is on the $SU(2)$-symmetric antiferromagnetic chain, and the discussion starts with the finite-size scaling of the various Drude weights in the massless regime. As an example, Fig. 4.23 shows results for $D_{21}, D_{22}, D_{\mathrm{th}}$, and K_{th} for $\Delta = 1$ and $h/J = 0.5$. The finite-size scaling of $D_{11}(h,T) = D_{\mathrm{s}}(h,T)$ has been addressed in Sec. 4.5.2; see Fig. 4.17(a).

Since $[H, j_{\mathrm{th}}] = 0$, both D_{th}, shown in Fig. 4.23(b), and $D_{\mathrm{th,s}}$, not shown in the figures, rapidly converge at high temperatures, resembling the behavior of the zero-field thermal

---

[23] See the discussion in Chapter 2, Secs. 2.2.1, 2.2.3, and 2.3.1.

Drude weight $D_{\rm th}(h=0,T)$. All other quantities, i.e., D_{21}, D_{22}, and $K_{\rm th}$ exhibit a weak monotonous decrease with system size at high temperatures, which in all cases is due to $D_{\rm s}$ exhibiting a dependence on system size. At low temperatures, D_{21}, D_{22}, and $D_{\rm th}$, increase with system size as indicated by the arrows in Fig. 4.23.

When combining the various Drude weights, i.e., $D_{\rm th}, D_{\rm th,s}$, and $D_{\rm s}$ to compute $K_{\rm th}$ on finite systems, one has to decide which of the two spectral representations $D_{\rm s}^{I}$ or $D_{\rm s}^{II}$ for $D_{\rm s}$ is best suited. They do not differ at high temperatures [see Fig. 4.17(a)], but deviations are significant in the low-temperature regime $T/J \lesssim 0.3$. The thermal Drude weight $K_{\rm th}(h,T)$ resulting from inserting either $D_{\rm s}^{I}(h,T)$ or $D_{\rm s}^{II}(h,T)$ in Eq. (4.17) is shown in Fig. 4.23(a). Using $D_{\rm s}^{II}(h,T)$ leads to a double-peak structure in $K_{\rm th}(h,T)$, which is very likely artificial. The peak in $K_{\rm th}$ seen at lower temperatures $T/J < 0.1$ is expected to disappear in the limit of large system sizes, and indeed, it becomes evident from the results shown in Fig. 4.23(a) that this peak is strongly shifted towards $T=0$ when N grows. It has been checked that a similar scenario arises for $\Delta = 0$ for finite systems. In this case, the thermal Drude weight can be computed exactly in the thermodynamic limit and one finds that one of the two maxima disappears, namely the suspicious low-temperature peak. An analogous behavior is therefore expected for $\Delta > 0$, supporting the choice of $D_{\rm s}^{I}$ instead of $D_{\rm s}^{II}$. Inserting $D_{\rm s}^{I}$ in the numerical study is in fact important for consistency reasons, since then, all Drude weights entering in Eq. (4.17) have a similar finite-size dependence at low temperatures, characterized by the exponential suppression at low temperatures due to the finite-size gap.

Field dependence of the Drude weights $K_{\rm th}$ and $D_{\rm th}$

Having clarified technical issues, the next step is to make a tour through the phase diagram Fig. 4.1, starting from $(\Delta, h) = (1, 0)$. The thermal Drude weight $K_{\rm th}(h,T)$, used to probe the phase diagram, is shown as a function of temperature for $h/J = 0, 0.5, 1.5, 2, 2.5$ in Fig. 4.24(a), while Fig. 4.24(b) contains the corresponding curves for $D_{\rm th}(h,T)$. For $h=0$, the result for $N \to \infty$ from Ref. [78] is included in both plots (dotted line). Thick lines are used for $N=20$ sites and thin lines for $N=18$ sites.

The main features of the thermal Drude weight $K_{\rm th}(h,T)$ are: (i) the position of the maximum depends on the magnetic field; (ii) $K_{\rm th}(h,T)$ is strongly suppressed as the magnetic field is increased; (iii) for $h \geq h_{c2}$, finite-size effects are negligible; and (iv) a change in the low-temperature behavior is evident from the figure, if one compares the results for $h/J = 0, 2, 2.5$.

The vanishing of pronounced finite-size effects as the magnetic field approaches the line $h = h_{c2}$ can be ascribed to the fact that a description in terms of free fermions with parameters independent of Δ is valid here, as was mentioned in Sec. 4.4. In the fully polarized state $h > h_{c2}$, the elementary excitations are of spin-wave nature and the single-magnon excitations are exact eigenstates. The higher the field is, the less relevant are excitations with higher energy. Therefore, no prominent finite-size effects are expected and indeed, the curves shown in Fig. 4.24(a) for $N=20$ are practically indistinguishable from the corresponding ones for $N=18$ (not included in the figure) within the line width.

The non-monotonous behavior of the peak position of $K_{\rm th}$ and the strong suppression of $K_{\rm th}$ is a consequence of the two competing contributions, i.e., the pure Drude weight $D_{\rm th}$ and the magnetothermal correction $D_{\rm th,s}^2/[T\,D_{\rm s}]$. Note that in the massless regime, $D_{\rm th}$ is strongly enhanced by the magnetic field and it also develops a sharp maximum, which is shifted to very low temperatures. See, for instance, the curve for $h/J = 1.5$ shown in Fig. 4.24(b). In

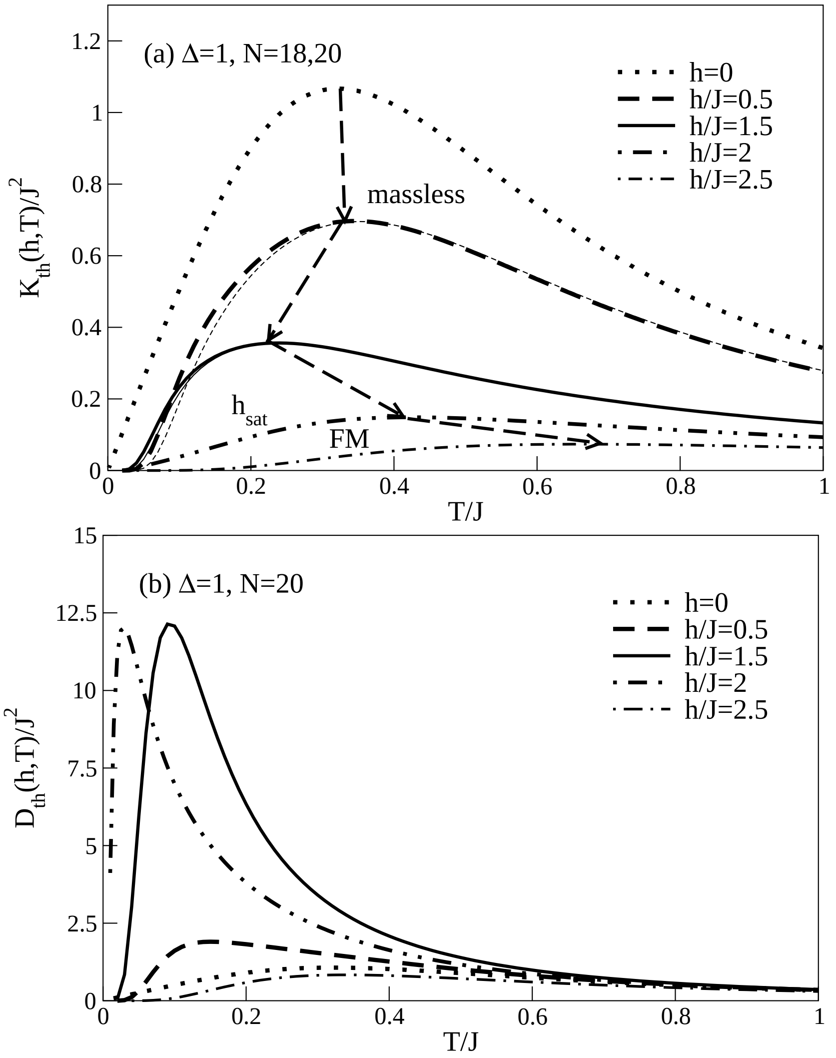

Figure 4.24: (a): Thermal Drude weight $K_{\mathrm{th}}(h,T)$ versus temperature for $\Delta = 1$ and different magnetic fields $h/J = 0, 0.5, 1.5, 2, 2.5$ for $N = 18$ (thin lines) and $N = 20$ (thick lines). The dashed arrows indicate the shift of the maximum of K_{th} as the magnetic field h increases. (b): For comparison, this panel shows the pure thermal Drude weight $D_{\mathrm{th}}(h,T)$ versus temperature for $\Delta = 1$ and $N = 20$ sites and the same parameters as in panel (a). The dotted lines represent the exact result for $h = 0$ taken from Ref. [78] in both figures.

the low-temperature limit and within the massless regime, conformal field theory predicts a divergence of D_{th} with T^{-1} [see Eq. (4.57)] and with $T^{-1/2}$ at the critical field h_{c2}, which follows from Eq. (4.77). Although such T-dependence cannot be seen directly on finite system sizes, the strong increase of D_{th} for $T/J \sim 0.1$ is compatible with Eqs. (4.57) and (4.77).

To elaborate more on the comparison of K_{th} and D_{th}, Fig. 4.25 shows both quantities as a function of h/h_{c2} at an intermediate temperature $T/J = 0.5$. First of all, the decrease of $K_{\mathrm{th}}(h,T)$ as a function of increasing magnetic field as mentioned for the Heisenberg chain is also observed for other choices for the anisotropy Δ, e.g, $\Delta = 0.5, 2$ for which results are included in Fig. 4.25. In contrast to $K_{\mathrm{th}}(h,T)$, $D_{\mathrm{th}}(h,T)$ grows with increasing magnetic field at intermediate temperatures and develops a maximum around $h/h_{c2} \sim 0.8$ for this

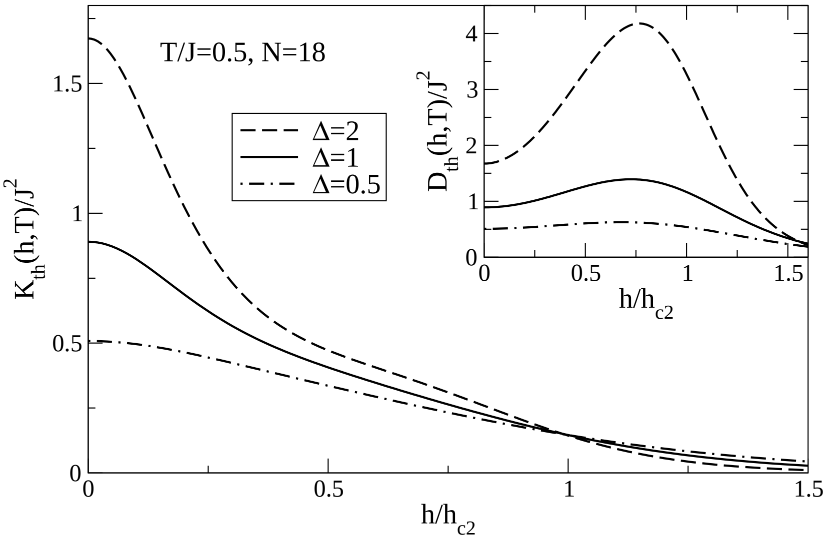

Figure 4.25: Main panel: Thermal Drude weight $K_{\mathrm{th}}(h,T)$ versus magnetic field h/h_{c2} for $\Delta = 0.5, 1, 2$ and $T/J = 0.5$ [ix]. Inset: Pure thermal Drude weight $D_{\mathrm{th}}(h,T)$ versus magnetic field h/h_{c2} for $\Delta = 0.5, 1, 2$ and $T/J = 0.5$.

temperature, which can be seen in the inset of Fig. 4.25. The position of this maximum seems to approach $h = h_{c2}$ when the temperature is lowered. Thus, indications of the transition to the ferromagnetic phase are visible in $D_{\mathrm{th}}(h,T)$, but not present in $K_{\mathrm{th}}(h,T)$. Note, however, that all three curves in the main panel of Fig. 4.25 almost pass through the same point for $h \approx h_{c2}$. For $T/J \lesssim 1$, $D_{\mathrm{th}}(h,T)$ is enhanced by the magnetic field and we can therefore conclude that the decrease of $K_{\mathrm{th}}(h,T)$ as a function of magnetic field is due to a cancellation of $D_{\mathrm{th}}(h,T)$ and the magnetothermal correction in Eq. (4.17).

Magnetothermal response, magnetic Seebeck coefficient

In this last part, a few words are said about the magnetothermal response, or the magnetic Seebeck coefficient, respectively:

$$S(h,T) = \frac{D_{12}}{D_{11}} = \frac{1}{T}\frac{D_{21}}{D_{11}} = \frac{1}{T}\left[\frac{D_{\mathrm{th,s}}}{D_{\mathrm{s}}} - h\right] . \qquad (4.104)$$

Obviously, $S = 0$ for $h = 0$ since $D_{\mathrm{th,s}}(h = 0, T) = 0$. For a discussion of an experimental setup that allows the measurement of S, see Ref. [91].

The magnetic Seebeck coefficient S has first been studied in Ref. [91] using ED and QMC in the limit of small fields. Furthermore, analytical expressions for S were derived for this limit. As a surprising result, Louis and Gros found that S can be negative in the low-temperature limit and for fields $h \ll h_{c2}$. The origin of this effect, however, remained unclear, and in particular, it could not be ruled out that this observation was only a finite-size effect, possibly caused by the choice of $D_{\mathrm{s}} = D_{\mathrm{s}}^I$ made in Ref. [91]. As was discussed before in this chapter, one has to be careful about the choice for D_{s}, since artificial finite-size effects may arise (see Figs. 4.12, 4.17(a), and 4.23(a) and the discussion there). Very recently, Sakai and Klümper have presented an analytical study of the Seebeck coefficient, which is exact in

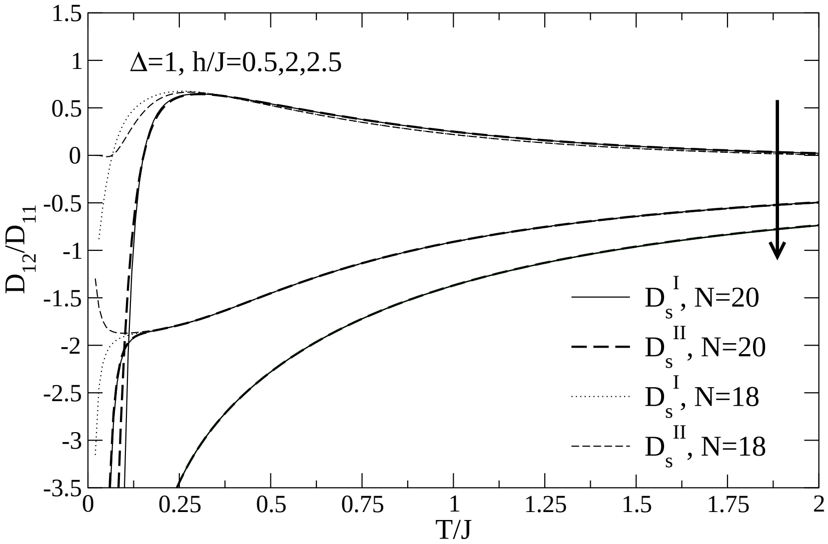

Figure 4.26: Magnetothermal response $S = D_{21}/D_{11}$ of the Heisenberg chain ($\Delta = 1$). ED data are plotted versus temperature for $N = 18$ and $N = 20$ sites and $h/J = 0.5, 2, 2.5$ (top to bottom). Increasing field is indicated by the arrow. At low temperatures and for finite systems, strong finite-size effects appear. Note that for the dashed curves, $D_\mathrm{s} = D_\mathrm{s}^{II}$ was used, while for the solid ($N = 20$) and dotted ones ($N = 18$), $D_\mathrm{s} = D_\mathrm{s}^{I}$ was inserted in Eq. (4.104). The arrow indicates increasing magnetic field. Compare also Refs. [91, 92].

the thermodynamic limit [92]. Their approach is limited to the low-temperature limit $T \ll h$ due to the problems of computing $D_\mathrm{s}(h, T)$, but not restricted with respect to the size of the field. To leading order in temperature, they find:

$$S(h, T) = B(h, \Delta)\, T\,, \tag{4.105}$$

where the coefficient B depends on both Δ and h. Furthermore, this coefficients changes its sign as a function of field; for instance, for the Heisenberg chain, $B > 0$ for $h/J \lesssim 0.6$ but $B < 0$ for $h/J \gtrsim 0.6$. The main point is that the analytical results of Ref. [92] confirm the findings of Ref. [91]. A similar behavior was found for the Seebeck effect of the Hubbard model [125].

Here, results for S are presented that are complementary to the other studies in the sense that both large fields and large temperatures can be studied, while the low-temperature limit is difficult to reach. Figure 4.26 shows numerical data for the Seebeck coefficient S of the Heisenberg chain as a function of temperature for $h/J = 0.5, 2, 2.5$. Both choices for D_s have been tried, and substantial differences arise in the low-field and low-temperature limit $T/J \lesssim 0.2$ as can be seen in the case of $h/J = 0.5$ and $N = 18$. This is also the regime, where substantial finite-size effects complicate the interpretation of the results.

The conclusion of a negative magnetothermal response, however, can clearly be confirmed for high temperatures $T/J \gtrsim 0.2$ and fields $h/J \gtrsim 1.5$. It would be interesting to take a closer look at the temperature dependence of S for moderate fields $h \sim 0.5J$ to see whether S changes its sign as a function of temperature as well. This is left for future work.

4.7 Summary

This chapter contains detailed results about transport properties of spin-1/2 XXZ chains. The Drude weights have been studied using conformal field theory, mean-field theory, and exact diagonalization. These methods are complementary, since the latter method works best at high temperatures while the analytical approaches give a proper description of the low-temperature behavior.

The comparison of mean-field theory for the thermal Drude weight with exact diagonalization and the Bethe ansatz in the massless regime results in a surprisingly good agreement indicating that a description of thermal transport in terms of quasi-particles is justified for this model. Furthermore, using mean-field theory and conformal field theory, the leading contributions to the Drude weights at low temperatures could be determined as a function of anisotropy and magnetic field. Exact results are obtained for the free-fermion case and the saturation field, where a universal behavior is found, and within the massless regime. These findings confirm those of other studies of transport in the Luttinger liquid [80] and of the thermal Drude weight of the XXZ chain [78, 82]. Similar predictions for the field dependence of the thermal Drude weight D_{22} of continuum theories can also be found in Ref. [55].

Numerically, the spin Drude weight has been studied in the entire phase diagram. The main results are: (i) A comparison between the two expressions for the spin Drude weight, i.e., $D_{\rm s}^{I}$ and $D_{\rm s}^{II}$, explicitely reveals their different finite-size dependence. (ii) For the Heisenberg chain, the numerical results indicate a *finite* spin Drude weight at zero magnetic field. (iii) Mazur's inequality [61, 146, 147] holds as an equality at low temperatures in good approximation. Taking into account more conserved quantities could be an interesting extension of recent analytical approaches. (iv) The spin Drude weight $D_{\rm s}^{II}$ at zero temperature is a probe of the various regimes, as expected from Kohn's original work [64].

Results for the thermal Drude weight from exact diagonalization are in excellent agreement with the Bethe ansatz [78, 82], where available, and previous numerical studies of the Heisenberg chain [54]. Combining the results from ED and the analytical approaches, the field, temperature, and anisotropy dependence could widely be clarified, with the exception of the antiferromagnetic gapped regime for nonzero magnetic field ($\Delta > 1, h < h_{c1}$), which is left for future work. As a result, the thermal Drude weight, computed under the condition of a vanishing spin current $\langle j_{\rm s} \rangle$, is suppressed by a magnetic field and its peak position exhibits a non-monotonous field dependence.

With respect to experiments it is interesting to study relations such as $\kappa \propto C_V$ or the Wiedemann-Franz law. In the massless regime and in the low-temperature limit, the thermal Drude weight is proportional to the specific heat, i.e., $K_{\rm th}(h,T)/C_V = \pi v^2$ [78, 92]. In this thesis, a Wiedemann-Franz type of relation is found to be fulfilled for $0 \leq \Delta \leq 1$ and $h \geq 0$, i.e., $K_{\rm th}(h,T)/D_{\rm s}(h,T) = L_0\, T$, where the constant L_0 was given in Eq. (4.83).

Regarding the Drude weights of the XXZ chain, one can identify three major open issues. First, it would be highly desirable to finally clarify whether spin transport of the Heisenberg chain is ballistic or not. Second, the temperature dependence of the Drude weight $D_{\rm s}$ is not yet completely understood. Third, the low-temperature behavior of the thermal Drude weight $K_{\rm th}$ in the antiferromagnetic regime ($\Delta > 1, 0 < h < h_{c1}$) and along the critical line $h = h_{c1}$ has not yet been studied.

Outlook: the Hubbard model

An obvious extension to the work done for the XXZ chain is the study of transport properties of the 1D Hubbard model, which is also integrable. This includes particle, charge, spin, and thermal transport (see the discussion in Ref. [17]). Zero-temperature features of, in particular, the charge Drude weight are well known [129–131,252], but a theory of the thermal conductivity remains an open issue. Zotos and coworkers have shown that the thermal Drude weight D_{th} is finite and they have proposed a certain form for the energy-current operator [61]. The dependence of D_{th} on temperature, filling, or onsite Coulomb correlations U is not known. Recently, the Seebeck effect in the one-dimensional Hubbard model has been studied numerically [125]. It would be very interesting to analyze other ratios of transport coefficients, such as the thermal conductivity (2.16) or the validity of the Wiedemann-Franz law. This could be relevant for the interpretation of recent transport measurements for the Beechgard salts [278].

CHAPTER 5

Transport in frustrated and dimerized 1D spin systems

This chapter deals with transport properties of several nonintegrable spin-1/2 models, including the frustrated chain, the dimerized chain, and the two-leg spin ladder. A finite-size scaling analysis of the finite-temperature Drude weights for spin and thermal transport is presented, which yields evidence for a vanishing of both quantities in the thermodynamic limit. This numerical result is corroborated by field-theoretical arguments. Furthermore, the frequency dependence of the conductivities is numerically studied and the regular parts are found to exhibit only small finite-size effects at high enough temperatures. In the high-temperature limit, the dc-limit is discussed and the zero-frequency thermal conductivity is extrapolated from the numerical data. This allows for a comparison with experiments in the case of two-leg ladders.

5.1 Overview: the λ-α chain

The model that is studied in this chapter is the λ-α chain:

$$H = \sum_{l=1}^{N} H_l = J \sum_{l=1}^{N} [\lambda_l \vec{S}_l \cdot \vec{S}_{l+1} + \alpha \vec{S}_l \cdot \vec{S}_{l+2}] \,, \tag{5.1}$$

where $J\lambda_l$ is an alternating nearest-neighbor interaction and $J\alpha$ is a next-nearest neighbor coupling. Antiferromagnetic interactions are assumed, i.e., $J, \lambda, \alpha > 0$. Dimerization is introduced through the alternation of the couplings: $\lambda_l = 1$ for even site-index l and $\lambda_l = \lambda$ for odd l. A nonzero value of α causes frustration. The model is sketched in Fig. 5.1. Its limiting cases are: (i) $\lambda = 1, \alpha = 0$: the Heisenberg chain; (ii) $0 \leq \lambda \neq 1, \alpha = 0$: the dimerized chain; (iii) $\lambda = 1, \alpha > 0$: the frustrated chain; and (iv) $\lambda = 0, \alpha \geq 0$: the two-leg spin ladder. The parameter space of (5.1) is depicted in Fig. 5.2. In relation with other notations frequently used in the literature, note that $J = J_\perp$ is the coupling on the rungs and $\alpha J = J_\|$ is the coupling along the legs of the ladder. The dimerization is often parameterized via δ:

$$J_l = \tilde{J}[1 + (-1)^l \delta] \quad \Rightarrow \quad J = \tilde{J}(1+\delta); \quad \lambda J = \tilde{J}(1-\delta) \,. \tag{5.2}$$

If not stated otherwise, the interaction is assumed to be $SU(2)$-symmetric. An exchange anisotropy Δ can be introduced by replacing the scalar products in (5.1):

$$\vec{S}_l \cdot \vec{S}_{l+i} \rightarrow \frac{1}{2}(S_l^+ S_{l+i}^- + \text{H.c.}) + \Delta S_l^z S_{l+i}^z \,. \tag{5.3}$$

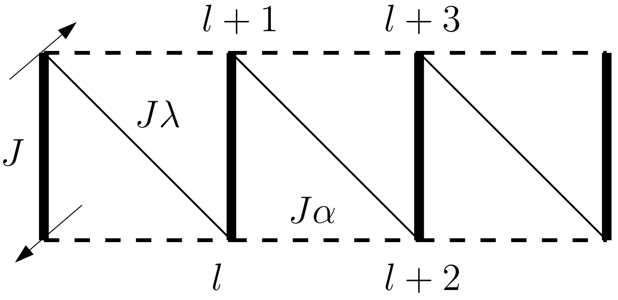

Figure 5.1: The λ-α chain. The model is equivalent to a zig-zag ladder. Its limiting cases are: (i) $\lambda = 1, \alpha = 0$: the Heisenberg chain. (ii) $0 \leq \lambda \neq 1, \alpha = 0$: the dimerized chain; (iii) $\lambda = 1, \alpha > 0$: the frustrated chain; (iv) $\lambda = 0, \alpha \geq 0$: the two-leg spin ladder.

The local energy density H_l is defined as indicated in Eq. (5.1), and for the magnetization density m_l, $m_l = S_l^z$ is the obvious choice. Using these definitions, the current operators j_s and j_th follow directly from Eqs. (2.35) and (2.36). However, the definition of the energy-current operator j_th of spin ladders is not consistent in the literature [iii,54,57]. This problem will be further discussed in Sec. 5.6.2. Except for the case of a dimerized XY chain, both current operators do not commute with the Hamiltonian:

$$[H, j_\mathrm{s}] \neq 0; \quad [H, j_\mathrm{th}] \neq 0\,. \tag{5.4}$$

In relation with the definition of the spin-current operator note that the kinetic-energy operator $\hat{T}$ is related, but not identical to the XY part of (5.1):

$$\begin{aligned}\hat{T} &= J\sum_{l=1}^{N}\left[\lambda_l\,(S_l^+S_{l+1}^- + \mathrm{H.c.}) + 4\alpha(S_l^+S_{l+2}^- + \mathrm{H.c.})\right]\\ &= J\sum_{l=1}^{N}\left[\frac{\lambda_l}{2}\,(c_l^\dagger c_{l+1} + \mathrm{H.c.}) + 4\,\frac{\alpha}{2}(c_l^\dagger c_{l+2} + \mathrm{H.c.})(1-n_{l+1})\right].\end{aligned} \tag{5.5}$$

One might have expected that the kinetic energy only involves direct nearest and next-nearest neighbor hopping of spinless fermions [see Eq. (2.5)]. In contrast to the XXZ chain, setting $\Delta = 0$ in the case of nonzero frustration α does not lead to a model of noninteracting fermions via the Jordan-Wigner transformation (2.2). Rather, for $\alpha \neq 0$, the phase factors appearing in the Jordan-Wigner transformation do not cancel, but give rise to correlated hopping terms such as $c_l^\dagger c_{l+2} n_{l+1}$ stemming from the XY part of the Hamiltonian [compare Eq. (2.5)]. Furthermore, note the appearance of the extra factor four in front of the term proportional to $\alpha\, J$ in Eq. (5.5). This factor can be understood by considering the limit of two decoupled chains ($J\alpha = \mathrm{const}; J \to 0$) of length $N/2$. To this end, the reader is referred to the derivation of $\hat{T}$ in Sec. 2.2.3. Rescaling the size-dependent prefactors on $N/2$ in the expression for $H(\Phi)$, i.e., Eq. (2.58), cancels the factor four and results in twice the Hamiltonian of a single chain with $N/2$ sites.

Apart from the case of the integrable XXZ chain ($\lambda = 1, \alpha = 0$), the model (5.1) possesses some limiting cases that are exactly solvable. First of all, for ($\lambda \neq 1, \alpha = 0$) but $\Delta = 0$, the Hamiltonian reduces to that of the dimerized XY chain, which is equivalent to free spinless, but massive fermions. Next, for ($\lambda = 0, \alpha = 0$), the system consists of noninteracting dimers only. The ground state is a spin singlet, and the elementary excitations are

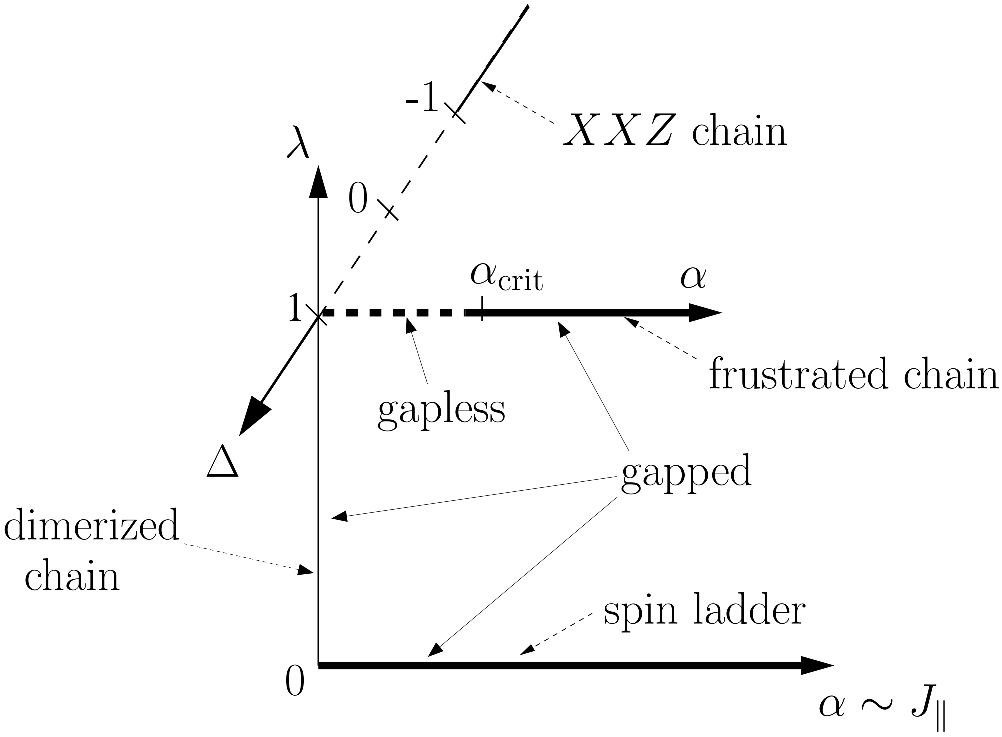

Figure 5.2: Parameter space of the λ-α chain. Dashed lines represent gapless phases of the model, while a spin gap exists along the solid lines.

local triplets that reside on the dimers. From this limit one can infer that the elementary excitations of both the dimerized chain and the two-leg spin ladder are triplet modes that are dispersive for $(\lambda \neq 0, \alpha = 0)$ and $(\lambda = 0, \alpha \neq 0)$, respectively. Values for the spin gap have numerically been obtained to high accuracy for the spin ladder by QMC simulations [279] and for the dimerized chain using DMRG [183, 280]. In a seminal work on the spin gap of the dimerized chain, Cross and Fisher found that the gap opens with $\Delta_{\mathrm{sp}} \propto \delta^{2/3}$ [281, 282]. The dispersion of the triplets has intensely been studied using perturbative approaches for ladders [283, 284] and chains [285, 286], using high-order series expansions [183, 287], and several numerical methods [28, 279, 280, 283, 288–292]. The low-energy physics of spin ladders is closely related to that of Haldane chains (see, e.g., Ref. [27] and references therein) and both systems possess a spin gap of comparable size.[1]

In contrast to dimerized systems, the elementary excitations of the frustrated chain are spinons, similar to the XXZ chain. The spectrum of the frustrated chain is gapless below a critical value of $\alpha = \alpha_{\mathrm{crit}}$, but a gap opens for larger α [294, 295].[2] A special case is the Majumdar-Gosh point $\alpha = 0.5$, for which the ground state, which is twofold degenerate, can exactly be given as a product of singlets [296]. Thus, studying transport properties of the λ-α chain allows one to compare different types of elementary excitations.

Ground state, spectral, dynamical as well as thermodynamical properties of the dimerized chain, the spin ladder, and the frustrated chain have very intensely been studied over the last years. For a review and further references the reader may consult Refs. [19–21, 28].

---

[1] The gap of the isotropic Haldane chain ($\Delta = 1$) is $\Delta_{\mathrm{sp}} \approx 0.41J$ [215], while that of the ladder with equal couplings along legs and rungs, i.e., $J_\perp = J_\parallel$, is $\Delta_{\mathrm{sp}} \approx 0.5J_\perp$ [288, 293].

[2] For values for $\alpha_{\mathrm{crit}} = \alpha_{\mathrm{crit}}(\Delta)$, see, e.g., Ref. [235].

Thermal transport properties of spin ladders and frustrated chains have attracted strong theoretical interest [54–58] after the experimental observation of significant contributions from magnetic excitations to the thermal conductivity. An extended discussion of experiments can be found in Chapter 3. In a first study by Alvarez and Gros [54, 58], the results from exact diagonalization for $N \leq 14$ sites were interpreted in favor of a *finite* thermal Drude weight both for spin ladders and frustrated chains. This picture was suggested to hold also for dimerized chains. Subsequent numerical studies on larger system sizes could not confirm this conjecture, neither for frustrated chains [i, iii, iv, v, viii], dimerized chains [iii, v], nor for spin ladders [iii, 57]. In fact, it will be argued that the conclusion of a finite thermal Drude weight does neither arise when larger system sizes of $N \leq 20$ using full diagonalization [iii, iv, viii] or $N \leq 28$ sites using the MCLM method [57, 90] are included nor when the analysis of smaller system sizes is carefully revisited [iii, iv]. The conclusion of normal transport and a vanishing thermal Drude weight for spin ladders and more generally, nonintegrable systems agrees with Zotos' and coworkers' original conjecture for transport in nonintegrable models [83] as well as with a theory of transport in one-dimensional systems within the Mori-Zwanzig formalism [59, 95, 97, 143] and with a numerical study of Haldane chains [96].

It should be stressed that the reason for using exact diagonalization to study transport properties lies in the problem of treating conservation laws properly. Many theories to describe low-energy properties of, e.g., spin ladders exist, including a mapping on Majorana fermions [297], hard-core bosons [98], or bosonization [27]. While the neglect of some or all interactions of these particles or fields still allows one to make safe statements about, e.g., ground-state properties, a mapping onto noninteracting particles introduces artificial conservation laws, often including the current operators themselves. This is, for instance, the case in Ref. [55]. Furthermore, one has to pay much attention which interactions must be included in an effective low-energy theory to arrive at a reliable description of transport [95]. This aspect will be discussed in more detail within bosonization in the next section of this chapter, where the framework of Ref. [59, 95] is applied to this thesis' chief cases of interest, i.e., thermal and spin transport of spin systems.

For spin transport, the influence of integrability breaking terms added to the Hamiltonian of the XXZ model has extensively been investigated using exact diagonalization [83, 84, 88] and QMC simulations [85, 86]. These studies focused on additional longer-ranged Ising terms such as[3]

$$H_i^{zz} \propto J_i^z \sum_{l=1}^{N} S_l^z S_{l+i}^z ; \quad i = 2, 3 . \tag{5.6}$$

The common conclusion is that spin transport in nonintegrable models is characterized by a vanishing Drude weight D_s. Transport in nonintegrable systems is often discussed in relation with changes in the level-spacing distribution [84, 88], the existence of degenerate, current carrying states [84, 88], and in connection with ergodicity [144].

In this thesis, spin transport is numerically analyzed for frustrated chains, dimerized chains, and ladders, mainly focusing on the $SU(2)$-symmetric cases. Thus, the previous studies are extended by considering next-nearest neighbor XY interactions. Finally, note that analogous studies have been performed for the extended Hubbard model, e.g., in Ref. [94]. For the sake of easy reference, Table 5.1 lists some recent theoretical studies of spin and thermal transport in nonintegrable, purely one-dimensional spin systems.

---

[3] Note that QMC cannot handle frustrating next-nearest neighbor XY terms due to the so-called sign problem.

Authors & Ref.	Model	Method	Results
Thermal transport			
Alvarez, Gros [54,58]	Frust. chain	ED, $N \leq 14$	$D_{\mathrm{th}} > 0$
	2-leg ladder		
Saito [56]	Frust.& dim. chain	BOS	$D_{\mathrm{th}} > 0$
Orignac et al. [55]	2-leg ladder	LE	$D_{\mathrm{th}} > 0$
	Dim. XY chain		$D_{\mathrm{th}} = D_{\mathrm{th}}(T)$,
			$D_{22} = D_{22}(h, T)$
Zotos [57]	2-leg ladder	ED, MCLM	$D_{\mathrm{th}} \to 0$, $\kappa_{\mathrm{reg}}(\omega)$
Karadamoglou, Zotos [96]	$S = 1$ chain	ED, MCLM	$D_{\mathrm{th}} \to 0$, $\kappa_{\mathrm{reg}}(\omega)$
H.-M. et al. [i, iii, iv, v, viii]	Frust. chain	ED	$D_{\mathrm{th}} \to 0$, $\kappa_{\mathrm{reg}}(\omega)$
	2-leg ladder	ED	$D_{\mathrm{th}} \to 0$
	Dim. chain	ED	$D_{\mathrm{th}} \to 0$
Spin transport			
Zotos, Prelovšek [83]	XXZ+H_2^{zz}	ED, $N \leq 16$	$D_{\mathrm{s}} \to 0$
Narozhny et al. [84]	XXZ+H_2^{zz}	ED, $N \leq 14$	$D_{\mathrm{s}} \to 0$
Alvarez, Gros [85,86]	XXZ+H_3^{zz}	QMC	$D_{\mathrm{s}} \to 0$
Rabson et al. [88]	XXZ+H_2^{zz}	ED, $N \leq 20$	$D_{\mathrm{s}} \to 0$
Fujimoto, Kawakami [87]		BOS	$D_{\mathrm{s}} > 0$
Karadamoglou, Zotos [96]	$S = 1$ chain	ED, MCLM	$D_{\mathrm{s}} \to 0$, $\sigma_{\mathrm{reg}}(\omega)$
H.-M. et al. [iii, v]	λ-α chain	ED	$D_{\mathrm{s}} \to 0$

Table 5.1: This table lists several theoretical studies of transport properties of nonintegrable spin models or equivalent models of spinless fermions. If not stated otherwise, $h = 0$ and $\Delta = 1$ was considered. All studies focused on finite temperatures. The following abbreviations are used: ED (exact diagonalization), QMC (Quantum-Monte-Carlo simulations), BOS (bosonization), MCLM (micro-canonical Lanczos method), LE (effective low-energy theory). Regarding the models studied in Refs. [83–86,88], note that "XXZ+H_i^{zz}" stands for: "XXZ chain plus an additional Ising interaction H_i^{zz}"; see Eqs. (4.1) and (5.6).

The structure of this chapter is the following. In Sec. 5.2, bosonization is used to argue that in generic spin lattice models, transport of both energy and spin is non-ballistic. This implies that in general, the Drude weights should vanish in the thermodynamic limit. Section 5.3 outlines the program of the numerical study of Secs. 5.4, 5.5, and 5.6, and it addresses the issue of degeneracies in nonintegrable models. In Secs. 5.4, 5.5, and 5.6, numerical results for transport properties of frustrated chains, dimerized chains, and spin ladders, respectively, are presented. For each model, a finite-size scaling analysis of the Drude weights is performed. No evidence for a finite Drude weight in the thermodynamic limit is found, neither for spin nor for thermal transport. Therefore, the frequency dependence of the regular part is computed for representative examples, namely frustrated chains in the massless and massive regime ($\lambda = 1, \alpha = 0.2, 1$), a dimerized chain in the strong-coupling limit ($\lambda = 0.1, \alpha = 0$), and the spin ladder with equal couplings along both legs and rungs ($\lambda = 0, \alpha = 1$). In the high-temperature regime it is possible to extract the dc-conductivity κ_{dc} from $\kappa_{\mathrm{reg}}(\omega)$. For the spin ladder, a comparison with experimental data is suggested. Section 5.7 summarizes this chapter and contains suggestions for extensions of this study.

Some of the results presented in this chapter have already been published in Refs. [i,iii,iv,v] and [viii].

5.2 Bosonization

The starting point for the description of one-dimensional spin-1/2 systems is the XY chain, which is described by the Luttinger liquid Hamiltonian introduced in Eq. (4.26):[4]

$$H_{\mathrm{LL}} = \frac{v}{2}\int dx \left(K(\partial_x\theta)^2 + \frac{1}{K}(\partial_x\phi)^2 \right) . \tag{5.7}$$

Many additional terms are present when passing from the lattice to the continuum limit. The low-energy physics and, in particular, the question whether a gap opens in the spectrum or not depends on the presence or absence of relevant perturbations. The terms relevant, marginally relevant, and irrelevant have their meaning in the renormalization group sense: the coupling in front of a relevant perturbation increases during the renormalization flow, while the coupling in front of an irrelevant perturbation scales to zero (see, e.g., Ref. [27] for a discussion and further references). Irrelevant perturbations to (5.7) are thus usually discarded. In addition, incommensurate perturbations are also typically not incorporated in effective low-energy theories. To see which operators in principle appear when passing from the lattice to the continuum limit, one inserts Eq. (4.33) for S^z and Eq. (4.34) for $S^{\pm}$ into the Hamiltonian (5.1). The Hamiltonian is then expanded in powers of the lattice constant. We mention some examples for the usual effective, low-energy Hamiltonians. The low-energy physics of the XXZ chain in the massless phase as well as the frustrated chain for $\alpha < \alpha_{\mathrm{crit}}$ is modeled by Eq. (5.7) with K, v depending on Δ or Δ and α, respectively. In the case of the dimerized chain or of the XXZ in its massive phase, the Hamiltonian is extended by one relevant operator, resulting in a Sine-Gordon model.

In this section, qualitative arguments are given to highlight the importance of incommensurate umklapp scattering terms for a correct description of transport properties [59, 95]. Neglecting incommensurate umklapp scattering terms introduces artificial conservation laws, which give rise to finite Drude weights in effective low-energy theories. The discussion extends the framework of Ref. [95] to the case of thermal transport in spin systems; see also Refs. [59, 97]. In Ref. [95], a hydrodynamic description of electrical transport in a clean wire was proposed. The theory, using the Mori-Zwanzig formalism [63], was built up in a 2 × 2 subspace of the Liouville space, spanned by the particle-current operator and a second current operator, which is directly proportional to the energy-current operator j_{th}. The latter identification of the second current as the energy current was not explicitely mentioned in Ref. [95]. For an algebraic interpretation of j_{th}, see Ref. [87].

For the Luttinger-liquid Hamiltonian, the currents have been derived from the equation of continuity in Sec. 4.3:

$$j_{\mathrm{s}} = \frac{-vK}{\sqrt{\pi}} \int dx\, \partial_x\theta(x) \,, \quad j_{\mathrm{th}} = v^2 \int dx\, \partial_x\phi(x)\partial_x\theta(x) \tag{5.8}$$

---

[4] See the discussion in Sec. 4.3 for details and references.

and they commute with $H_{\rm LL}$:

$$[H_{\rm LL}, j_{\rm th[s]}] = 0\,. \tag{5.9}$$

Let us now discuss what happens if perturbations are added to $H_{\rm LL}$. Such perturbations are divided into two groups: a relevant perturbation $H_{\rm rel}$ and all irrelevant ones, summed up in $H_{\rm irr}$. First, we consider relevant perturbations, as they arise for the frustrated chain for $\alpha > \alpha_c$ and for the dimerized chain for $\lambda \neq 1$:

$$H_{\rm LL} \to H_{\rm LL} + H_{\rm rel}; \quad H_{\rm rel} = g(\Delta, \alpha, \lambda, \dots) \int dx \cos(c\,\phi)\,. \tag{5.10}$$

c is a constant that we do not need to specify further for the present purpose. While such perturbations break the conservation of the spin current $j_{\rm s}$, the conservation of the energy-current operator is not affected by this type of operator [56]:

$$[H_{\rm LL} + H_{\rm rel}, j_{\rm th}] = 0\,. \tag{5.11}$$

Note that the dependence of the current operators on the fields is not changed by adding $H_{\rm rel}$ to $H_{\rm LL}$.

In the next step, the Hamiltonian is extended by adding one irrelevant *and* incommensurate operator. Among the irrelevant operators, the incommensurate ones can degrade the currents. They are, in the case of pure spin models, generically of the form [275]

$$\begin{array}{rcl} H & \to & H_{\rm LL} + H_{\rm rel} + \mathbf{1} \times H_{\rm irr} \\ H_{\rm irr} & \sim & \displaystyle\sum_{n,m} \int dx\, \mathcal{O}_{nm}(x) = \int dx\, g_{nm} \cos(p\,n\,\phi + k_{nm}x)\,. \end{array} \tag{5.12}$$

$g_{n,m}$ are coupling constants, p is just a trivial constant depending on the notation, $k_{nm} = 2nk_{\rm F} - mG$ where $k_{\rm F}$ is the Fermi momentum, and G is a reciprocal lattice vector. n, m are integer numbers. In a fermionic representation, n is the number of fermions which change chirality under the action of the operator $\mathcal{O}_{n,m}(x)$. It can be shown that $H_{\rm irr}$ breaks the conservation of the energy-current operator due to its incommensurability:

$$[H_{\rm irr}, j_{\rm th}] \neq 0\,. \tag{5.13}$$

One of the main results of Ref. [95] is that in the presence of one operator of the type (5.12), a conserved current can still be constructed:

$$j_{\rm conserved} = k_{nm} j_{\rm s} + 2n j_{\rm th}\,. \tag{5.14}$$

The crucial observation, however, is that many operators of the type (5.12) exist:

$$H_{\rm LL} \to H_{\rm LL} + H_{\rm rel} + \text{many} \times H_{\rm irr}\,. \tag{5.15}$$

While for each of them, a conserved current can be found, all conservation laws are usually broken, if at least two operators $\mathcal{O}_{nm}$ are added to the Hamiltonian [95]. Therefore, transport in nonintegrable models is expected to show no anomalous features and is characterized by vanishing Drude weights. Since incommensurate operators have neither been considered in Ref. [55] nor in Ref. [56] it is not clear whether their results of a finite thermal Drude weight in the low-energy limit provide a proof of $D_{\rm th}(T > 0) > 0$ for the respective nonintegrable lattice models, i.e., frustrated and dimerized chains [56], as well as spin ladders [55]. It should be stressed that explicit computations of $\sigma(\omega)$ [95] and $\kappa(\omega)$ [59] within low-energy theories have only been carried out for the massless case. The general physical picture, however, is not expected to change in the massive regime.

In contrast to the main result of this section, note that in Ref. [87], anomalous transport properties of various nonintegrable models have been proposed based on field-theoretical computations. Since the incommensurate operators of Eq. (5.12) are explicitly excluded in Ref. [87], the result of this work does neither contradict the arguments given above nor our numerical indications for a vanishing Drude weight D_{s} in nonintegrable spin-lattice models to be presented in the following sections.

Some criticism against the line of reasoning of this section has been raised stating that no proper mathematical rule exists to decide which operators must be added to the Hamiltonian for a given problem or not [298]. A guideline as to how to formulate a low-energy theory correctly in detail is, however, not the purpose of this section: here, the main objective has been to demonstrate that neglecting irrelevant operators leads to artificial conservation laws and should therefore not *a priori* be discarded.

While some authors have speculated about ballistic transport in nonintegrable models [54–56, 58, 87], it seems that this is not the correct picture. Rather, the missing stone in the puzzle about ballistic transport is a deeper understanding why spin transport in the integrable XXZ chain is ballistic at zero magnetic field; a conclusion for which no formal proof has been found so far.[5] Since the type of operators that are present either in the massless phase of the XXZ or the frustrated chain is similar, integrability must arise due to a certain *fine-tuning* of the parameter-dependence of coupling constants in any order of the lattice constant [132].

5.3 Preliminaries

In the next three sections, numerical results for the transport coefficients of frustrated chains, dimerized chains, and spin ladders are presented, including an extensive scaling analysis of the Drude weights D_{s} and D_{th} as well as a discussion of the frequency dependence of the spin conductivity $L_{11}(\omega) = \sigma(\omega)$ and the thermal conductivity $L_{22}(\omega) = \kappa(\omega)$. If not stated otherwise, the magnetic field is zero, and the coupling J is set to unity in all explicit computations, defining the energy scale. Therefore, the first argument of the transport coefficients, i.e., the magnetic field h, is suppressed in this chapter. Also, the thermal Drude weight is uniquely denote by D_{th} in the following.

The expressions for the Drude weights D_{s}^{I}, D_{s}^{II}, and D_{th} have been given in Eqs. (2.43),

---

[5] See also the discussion in Chapter 4.

(2.55), and (2.44) in Sec. 2.2.3, but for the sake of quick reference, they are quoted below:[6]

$$
\begin{aligned}
D_{\mathrm{s}}^{I}(T) &= \frac{\pi\beta}{N} \sum_{\substack{m,n \\ E_m=E_n}} p_n \, |\langle m|j_{\mathrm{s}}|n\rangle|^2 \,, & (5.16)\\
D_{\mathrm{s}}^{II}(T) &= \frac{\pi}{N} \left[\langle -\hat{T} \rangle - 2 \sum_{\substack{m,n \\ E_m \neq E_n}} p_n \frac{|\langle m|j_{\mathrm{s}}|n\rangle|^2}{E_m - E_n} \right] , & (5.17)\\
D_{\mathrm{th}}(T) &= \frac{\pi\beta^2}{N} \sum_{\substack{m,n \\ E_m=E_n}} p_n \, |\langle m|j_{\mathrm{th}}|n\rangle|^2 \,. & (5.18)
\end{aligned}
$$

Spectral representations for the regular part of the frequency dependent transport coefficients $\sigma(\omega) = L_{11}(\omega)$ and $\kappa(\omega) = L_{22}(\omega)$ can be found in Eq. (2.24), which is also quoted for completeness:

$$
\begin{aligned}
\sigma_{\mathrm{reg}}(\omega) &= \frac{\pi}{N} \frac{1-e^{-\beta\omega}}{\omega} \sum_{\substack{m,n \\ E_m \neq E_n}} p_n \, |\langle m|j_{\mathrm{s}}|n\rangle|^2 \, \delta(\omega - (E_m - E_n)) \,, & (5.19)\\
\kappa_{\mathrm{reg}}(\omega) &= \frac{\pi\beta}{N} \frac{1-e^{-\beta\omega}}{\omega} \sum_{\substack{m,n \\ E_m \neq E_n}} p_n \, |\langle m|j_{\mathrm{th}}|n\rangle|^2 \, \delta(\omega - (E_m - E_n)) \,. & (5.20)
\end{aligned}
$$

Here, sums over δ-functions need to be performed. For the curves to be shown for $\sigma_{\mathrm{reg}}(\omega)$ and $\kappa_{\mathrm{reg}}(\omega)$ in Figs. 5.6, 5.9, 5.10, 5.12, 5.14, and 5.18, the spectral weight has been summed up in small frequency bins $\Delta\omega$ of the order of $\Delta\omega/J \sim 0.02$ instead of using an imaginary broadening.

The structure of Secs. 5.4 to 5.6 is the following: first, spin transport, and second thermal transport is discussed. For both types of transport, first, the overall temperature dependence of the Drude weight is analyzed. Second, a finite-size scaling analysis in the high-temperature limit is performed and extensive numerical results for the coefficients

$$
C_{\mathrm{s}} = \lim_{T\to\infty} [T \, D_{\mathrm{s}}(T)]; \quad C_{\mathrm{th}} = \lim_{T\to\infty} [T^2 \, D_{\mathrm{th}}(T)] \qquad (5.21)
$$

are presented. For an expression of these coefficients in terms of eigenenergies and eigenstates, see Eq. (2.53). Both their finite-size scaling and their dependence on parameters of the model, i.e., λ and α are studied. Since the scaling analysis of the Drude weights points to a vanishing of these quantities in most cases, the discussion will highlight features that are specific for each model in order to avoid a repetitive discussion. Finally, the frequency dependence of $\sigma_{\mathrm{reg}}(\omega)$ or $\kappa_{\mathrm{reg}}(\omega)$ is analyzed for some interesting examples. To this end, it is also useful to study the integrated spectral weight $I_{\mathrm{th[s]}}(\omega)$:

$$
I_{\mathrm{s}}(\omega) = D_{\mathrm{s}} + 2 \int_{0^+}^{\omega} d\omega \, \sigma_{\mathrm{reg}}(\omega) \,; \quad I_{\mathrm{th}}(\omega) = D_{\mathrm{th}} + 2 \int_{0^+}^{\omega} d\omega \, \kappa_{\mathrm{reg}}(\omega) \,. \qquad (5.22)
$$

The largest system size for which the Hamiltonian was completely diagonalized is $N = 20$ sites in the case of frustrated chains and $N = 18$ in the case of dimerized systems. Due to the dimerization for $\lambda \neq 1$, the unit cell of the model (5.1) is doubled, restricting the maximum system size in these cases to $N = 18$.

---

[6] See also Sec. 2.2.3 for the notation.

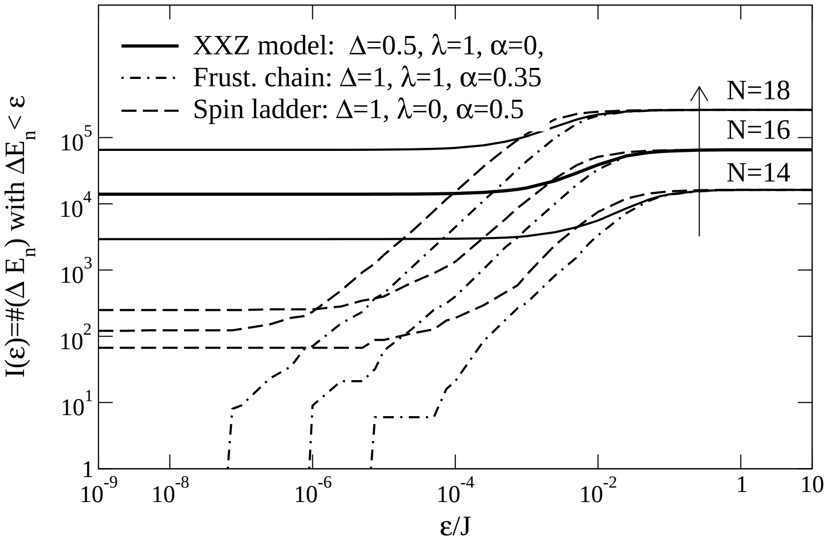

Figure 5.3: Distribution of level spacings in the spectrum of finite chains with $8 \leq N \leq 18$ (bottom to top as indicated by the arrow) for the XXZ chain, the frustrated chain, and the spin ladder. ΔE_n is the difference of adjacent energy levels in subspaces classified by total S^z_{tot} and momentum k. The number $I(\epsilon)$ of ΔE_n with $\Delta E_n < \epsilon$ summed over all subspaces is plotted versus ϵ (see also the discussion in Sec. 4.2). From Ref. [iii].

Degeneracies

For both the computation of the Drude weights $D^I_{\text{s}}(T)$, $D^{II}_{\text{s}}(T)$, and $D_{\text{th}}(T)$ from Eqs. (5.16), (5.17), and (5.18), respectively, and of the regular part of the conductivities from Eqs. (5.19) and (5.20), degenerate states need to be identified, analogous to the discussion in Sec. 4.2. The same criterion as in Chapter 4 is imposed, i.e., states are degenerate if they are separated by less than $\epsilon_{\text{cut}} = 10^{-8}J$. The integrated level-spacing distribution $I(\epsilon)$, defined in Eq. (4.24), is shown in Fig. 5.3 for frustrated chains and spin ladders and compared to that of the XXZ chain. In stark contrast to the integrable model, no degeneracies are found at all for frustrated chains on finite systems, neither in the massive regime $\alpha > \alpha_{\text{crit}}$ nor in the massless phase (not shown in the figure). Accidental exceptions exist for $\alpha = 0.5$ and $\alpha = 1$. At the Majumdar-Ghosh point, one degenerate state occurs if $N/2$ is even. In the latter case, i.e., $\alpha = 1$, there are degenerate states in the spectra of chains with $N = 10, 12, 14, 18$ which are, however, small in number. For instance there are approximately ten candidates for degeneracies for $N = 18$. The disappearance of degeneracies in nonintegrable models is consistent with the change from Poisson to Wigner statistics, since the low-energy tail of the level-spacing distribution disappears in the case of the Wigner distribution [88, 100, 150, 264].

In the cases of dimerized chains and spin ladders, the number of degeneracies is highly reduced compared to the integrable model. The example of $(\lambda = 0, \alpha = 0.5)$ shown in Fig. 5.3 is representative for all $\lambda \neq 1$ in Eq. (5.1). For example, there are approximately 10^2 degenerate states for $N = 18$ compared to more than 10^4 in the integrable case. It might be possible to further reduce the number of degenerate states by exploiting more symmetries.

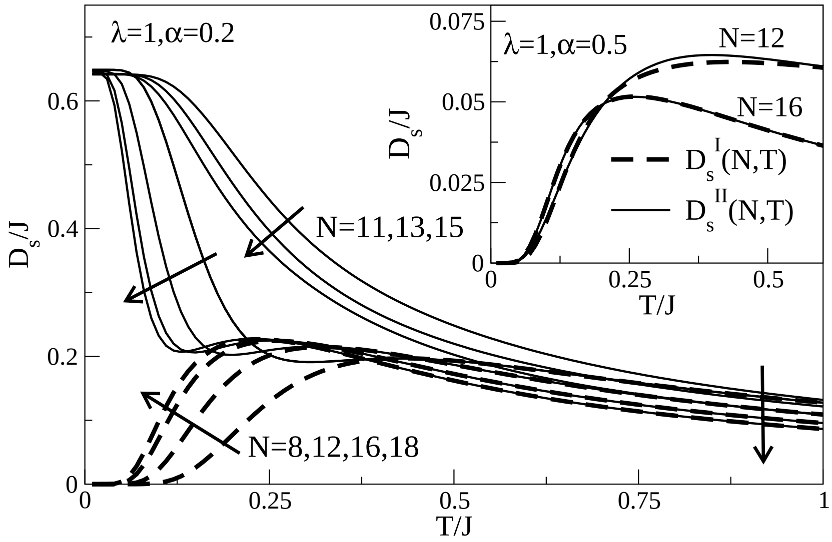

Figure 5.4: Spin transport, frustrated chain: Drude weight $D_{\mathrm{s}}^{I,II}(N,T)$ for $N=8,11,12,13,15,16,18$ and $(\lambda=1,\alpha=0.2)$ [dashed lines: $D_{\mathrm{s}}^{I}(N,T)$; solid lines: $D_{\mathrm{s}}^{II}(N,T)$]. Arrows indicate increasing systems size. Inset: Drude weight at the Majumdar-Ghosh point $(\lambda=1,\alpha=0.5)$ for $N=12,16$. From Ref. [iii].

5.4 The frustrated chain

5.4.1 Spin transport

The Drude weight $D_{\mathrm{s}}(T\geq 0)$

Figure 5.4 shows the Drude weights D_{s}^{I} and D_{s}^{II} of frustrated chains with $\alpha=0.2$ in the main panel and for $\alpha=0.5$ in the inset. Regarding the Drude weight in the massless phase, many features of the integrable case can still be found: (i) $D_{\mathrm{s}}^{I}\approx D_{\mathrm{s}}^{II}$ at high-temperatures; (ii) a finite value of D_{s}^{II} at $T=0$; (iii) significant differences in the temperature dependence of D_{s}^{II} between systems with an even or odd number of sites for $0.05<T/J<0.5$; and (iv) a monotonic decrease of D_{s} with N in the high-temperature limit. For comparison, see the data shown in Fig. 4.12 for the case of $\Delta=0.5,\lambda=1,\alpha=0$.

Spin transport at zero temperature was numerically studied in [260]. As a result, indications for a nonzero Drude weight $D_{\mathrm{s}}(T=0)$ for $\alpha\lesssim 0.5$ were found. This observation is likely to be mimicked by finite-size effects, since one would rather expect that any transition in $D_{\mathrm{s}}(T=0)$ occurs at $\alpha=\alpha_{\mathrm{crit}}$. Also, no proof for a finite Drude weight in the massless phase at zero temperature exists. An extension to larger systems at $T=0$, using, e.g., Lanczos techniques, could clarify whether $D_{\mathrm{s}}(T=0)>0$ is a property of the massless phase $\alpha<\alpha_{\mathrm{crit}}$ that survives in the thermodynamic limit. Note that the arguments of Sec. 5.2 in principle apply to $T=0$ also. In the massive phase, the spin Drude weight at $T=0$ vanishes on finite systems for some parameters, which can be seen in the inset of Fig. 5.4 taking the example of the Majumdar-Ghosh chain. In this particular case, the numerical results further indicate that $D_{\mathrm{s}}^{I}(N,T)\approx D_{\mathrm{s}}^{II}(N,T)$ for $N\gtrsim 16$. For $\alpha=1$, negative values of $D_{\mathrm{s}}^{II}(T=0)$ are found (not shown in the figures).

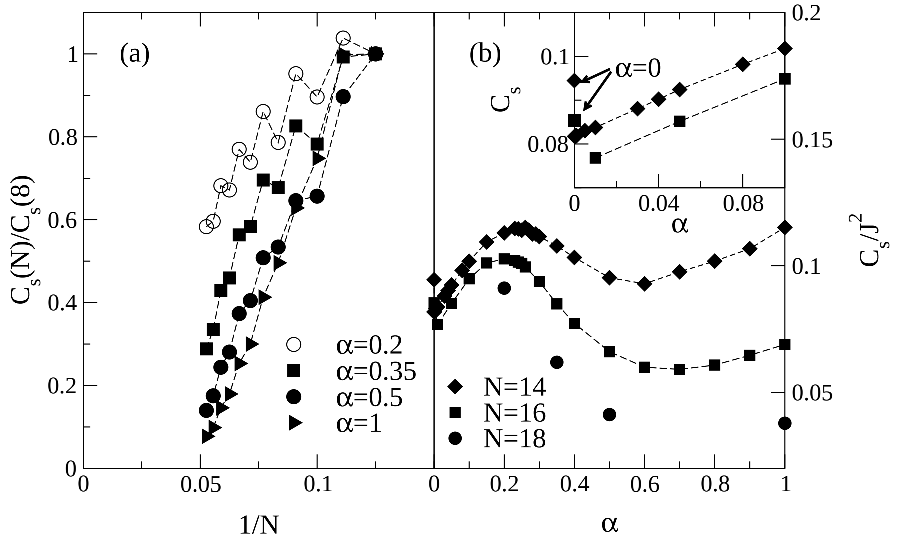

Figure 5.5: Spin transport: High-temperature prefactor $C_\mathrm{s}(N)$ for frustrated chains [iii]. (a): $C_\mathrm{s}(N)/C_\mathrm{s}(8)$ versus $1/N$ for several values of α both in the gapless and gapped regime ($N = 8, 9, ..., 19$). (b): $C_\mathrm{s}(N)$ for $N = 14, 16, 18$ as a function of frustration α. The inset shows a blow-up for small α and $N = 14, 16$. Lines are guides to the eye.

Scaling of D_s in the limit $\beta = 0$

Figure 5.5 depicts results for the high-temperature prefactor $C_\mathrm{s}(N)$ as a function of system size for $\alpha = 0.2, 0.35, 0.5, 1$ in panel (a) and as a function of frustration α for $N = 14, 16, 18$ in panel (b). First, $C_\mathrm{s}(N)$ monotonically decreases with system size, except for odd-even effects, for all values of α presented in Fig. 5.5(a) and exhibits a discontinuity at $\alpha = 0$. Second, the data for $\alpha = 0.2$ may in principle be extrapolated to a finite value in the thermodynamic limit. Regarding the discontinuity of $C_\mathrm{s}(N)$ at $\alpha = 0$, note that a small, but finite value of the frustration, e.g., $\alpha = 10^{-4}$, has the effect that degeneracies are lifted while the values of diagonal matrix elements $|\langle n\,|j_\mathrm{s}|\,n\rangle|^2$ are almost unaffected. This leads to the substantial difference between C_s at $\alpha = 0$ compared to small, but finite $\alpha > 0$, which can be seen in the inset of Fig. 5.5(b).

For the system sizes contained in Fig. 5.5(b), $C_\mathrm{s}(N)$ first grows with α and exhibits a maximum around $\alpha \approx 0.2$, followed by a minimum around $\alpha \approx 0.6$. For larger $\alpha \gtrsim 0.7$, $C_\mathrm{s}(N)$ increases with α again, analogous to the case of the thermal Drude weight, see Fig. 5.8(b). In the massive regime $\alpha > \alpha_\mathrm{crit}$, $C_\mathrm{s}(N)$ decreases rapidly with N and faster than $1/N$.

The data for $\alpha > \alpha_\mathrm{crit}$ indicate a vanishing Drude weight in the thermodynamic limit $N \to \infty$. For the gapless regime, the possibility of a nonzero value of C_s in the thermodynamic limit cannot be ruled out by our data although the absence of degeneracies supports the conclusion of $C_\mathrm{s}(N \to \infty) = 0$ for all $\alpha > 0$.

Frequency dependence of $\sigma_\mathrm{reg}(\omega)$

The analysis of the frequency dependence of $\sigma_\mathrm{reg}(\omega)$ points to additional interesting differences between the massless and massive regimes. Numerical results for $\sigma_\mathrm{reg}(\omega)$ are shown in Fig. 5.6 for $\alpha = 0.2$ [$N = 18$, panel (a)] and $\alpha = 1$ [$N = 20$, panel (b)]. While the values

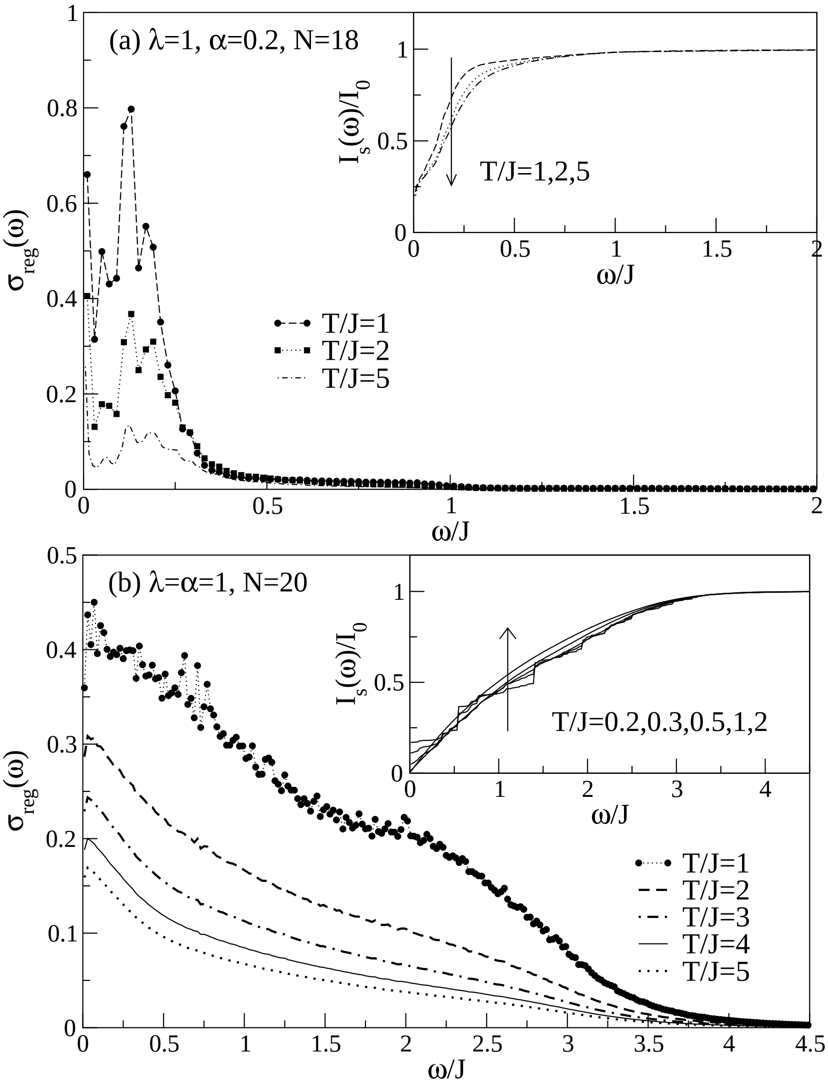

Figure 5.6: Spin conductivity $\sigma_{\mathrm{reg}}(\omega)$ of frustrated chains. (a) $\alpha = 0.2$, (b) $\alpha = 1$. The insets show the integrated spectral weight $I_{\mathrm{s}}(\omega)/I_0$ [see Eq. (5.22)]. Arrows in the insets indicate increasing temperature.

of $\sigma_{\mathrm{reg}}(\omega)$ at low frequencies are of comparable magnitude at $T/J = 1$, the most striking difference between $\alpha = 0.2$ and $\alpha = 1$ is the distribution of the spectral weight. In the former case, significant weight is only found for $\omega/J \lesssim 0.5$, while for $\alpha = 1$, $\sigma_{\mathrm{reg}}(\omega)$ has a very broad, mainly featureless peak that extends between $0 \leq \omega/J \lesssim 4.5$. A closer inspection of the integrated spectral weight $I_{\mathrm{s}}(\omega)/I_0$, which is normalized on the total weight I_0 and shown in the insets, further reveals that the Drude weight is a large fraction of the total weight I_0 in the case of $\alpha = 0.2$, while it is negligible in the massive regime. While the main panels only show the regular part, the Drude weight is included into both $I_{\mathrm{s}}(\omega)$ and I_0, and we can therefore read of its contribution to the total $\mathrm{Re}\,\sigma(\omega)$ from the offset at $\omega = 0$.

In the thermodynamic limit for $\alpha = 1$, the spin gap is $\Delta_{\mathrm{sp}}/J \approx 0.25$ [210]. The temperatures considered in the inset of Fig. 5.6(b) are, however, still too large, and therefore, the existence of the excitation gap is not yet reflected in the behavior of $I_{\mathrm{s}}(\omega)$.

5.4.2 Thermal transport

The Drude weight $D_{\text{th}}(T > 0)$

The thermal Drude weight of frustrated chains has first been studied in Ref. [54] using exact diagonalization. The main conclusion of Ref. [54] was that the behavior of D_{th} as a function of system size both in the low- and in the high-temperature regime points to a finite thermal Drude weight. The examples investigated include $\alpha = 0.1, 0.24$, and 0.35 for $N \leq 14$. As a main result of this section, it is demonstrated that numerical data for D_{th} yield no evidence for the conclusion of ballistic transport in frustrated chains.

Figures 5.7(a) and 5.7(b) show the thermal Drude weight $D_{\text{th}}(N, T)$ for $\alpha = 0.2$ and $\alpha = 0.35$, respectively. Additional results for the specific heat C_V for $\alpha = 0.2$ and $N = 8, 10, 12, 14, 16, 18$ are included in Fig. 5.7(a). Comparing the massless and massive regime, no significant differences are found and therefore, the discussion of the temperature dependence can be done in parallel for both examples.

For chains of finite length, the data at low temperatures are dominated by finite-size gaps. Hence the Drude weight and the specific heat are exponentially suppressed for small temperatures. While the specific heat converges to the thermodynamic limit at temperatures $T/J \gtrsim 0.25$, strong finite-size effects are present in the data for the Drude weight at all temperatures. At low temperatures, $D_{\text{th}}(N, T)$ monotonically increases with system size in both cases, i.e., $\alpha = 0.2$ and $\alpha = 0.35$. This observation might hint at a finite thermal Drude weight for $N \to \infty$, as it was concluded in Ref. [54] for the case of $\alpha = 0.35$. However, the notion of an increasing Drude weight at low temperatures does not support the conjecture [54] of a finite D_{th} for $N \to \infty$ either for $\alpha = 0.2$ or $\alpha = 0.35$. In fact, a crossover temperature T^* can be defined by

$$D_{\text{th}}(N + 2, T^*) = D_{\text{th}}(N, T^*) \tag{5.23}$$

for even system sizes N. At this temperature, the monotony behavior of the thermal Drude weight changes from an increase with system N at low temperatures $T < T^*$ to a decrease with N at high temperatures $T > T^*$. The crossover temperature T^* seems to extrapolate to zero as a function of system size, which is evident from the inset of Fig. 5.7(b), implying that the temperature range where one observes a Drude weight that increases with system size, could vanish for $N \to \infty$. To summarize the discussion of the low-temperature regime, finite-size effects are typically too pronounced to allow for any reliable conclusion about the thermodynamic limit.

Scaling of D_{th} in the limit $\beta = 0$

In Figure 5.8(a), the high-temperature prefactor $C_{\text{th}}(N)$ is presented for several values of α both in the gapless ($\alpha = 0.1, 0.2$, open symbols) and the gapped regime ($\alpha = 0.25, 0.35, 0.5, 1$, solid symbols). Finite systems with up to $N = 20$ sites have been analyzed. While $C_{\text{th}}(N)$ is almost constant in the case of $\alpha = 0.1$ and small system sizes, a substantial decrease with system size is observed for larger α and sufficiently large N. This is especially obvious for $\alpha = 1$. As far as thermal transport is concerned, the data at the Majumdar-Ghosh point $\alpha = 0.5$ do not point to any peculiarities.

In Figure 5.8(b), $C_{\text{th}}(N)$ is plotted versus α for $N = 14, 16, 18$. Starting at small α,

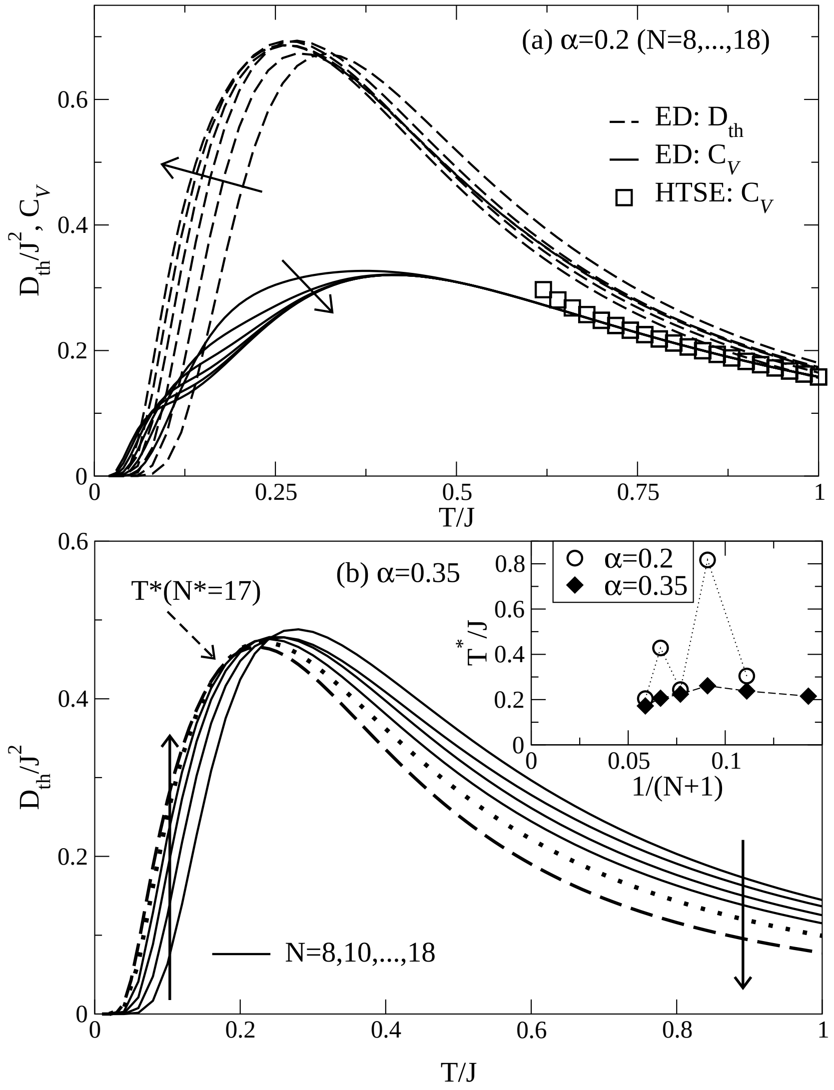

Figure 5.7: Thermal transport, frustrated chain [i,iii,iv]. (a): Drude weight $D_{\rm th}(N,T)$ [dashed lines] and specific heat C_V (solid lines) for $\alpha = 0.2$ and $N = 8, ..., 18$ sites (arrows indicate increasing system size). The plot includes data for C_V from a high-temperature series expansion (HTSE) reproduced from Ref. [299]. Note that only the bare high-temperature series up to order 10 in J/T is shown. By means of extrapolation schemes, the HTSE can be extended to significantly lower temperatures. For details, see Ref. [299]. (b): Drude weight $D_{\rm th}(N,T)$ of frustrated chains with $\alpha = 0.35$ for $N = 8, \dots, 14$ sites (solid lines). The dotted curve is for $N = 16$ and the dashed one for $N = 18$ sites. $T^*(N^*)$ is the temperature where the monotony behavior changes from a decrease with N at high-temperatures $T > T^*$ to an increase with N at low temperatures $T < T^*$. T^* is thus defined by $D_{\rm th}(N+2, T^*) = D_{\rm th}(N, T^*)$ for even N and $N^* = N + 1$. Inset: T^* versus $1/N^* = 1/(1 + N)$ for $\alpha = 0.2$ (open symbols) and $\alpha = 0.35$ (solid symbols).

one observes that $C_{\rm th}(N)$ is discontinuous at $\alpha = 0$ similar to the behavior of $C_{\rm s}$ shown in Fig. 5.5(b). The curve further decreases with α and exhibits a minimum at $\alpha \approx 0.4$ for $N = 14$ and $\alpha \approx 0.5$ for $N = 16$. The position of the minimum seems to be shifted towards larger α as N grows. Further increasing the next-nearest neighbor interaction drives the system into the limit of two decoupled chains with $N/2$ sites each and interchain interaction α. Exactly

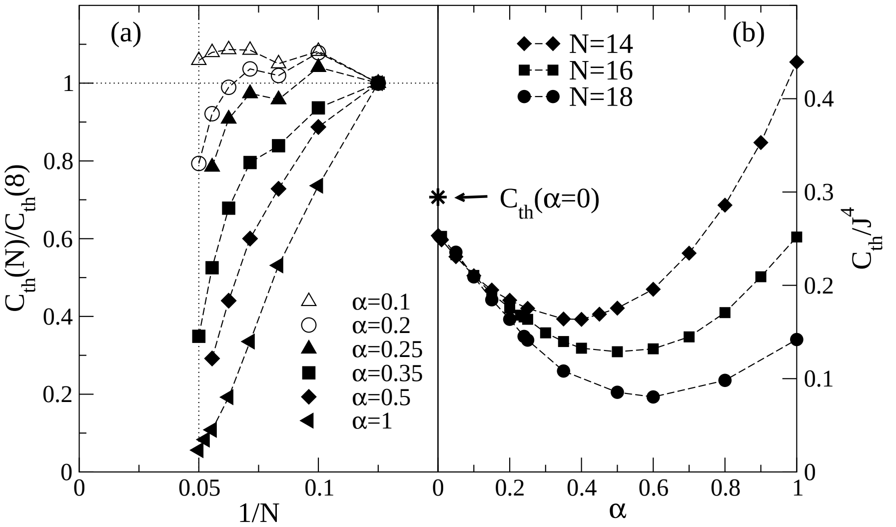

Figure 5.8: Thermal transport: High-temperature prefactor $C_{\text{th}}(N)$ for frustrated chains [iii,iv]. (a): $C_{\text{th}}(N)/C_{\text{th}}(8)$ versus $1/N$ for several values of α both in the gapless and gapped regime ($N = 8, ..., 20$) [iii, iv]. Compare also Ref. [54]. (b): $C_{\text{th}}(N)$ for $N = 14, 16, 18$ as a function of frustration α. The arrow indicates the system-size independent value of C_{th} at $\alpha = 0$ (marked by the star).

for $J \to 0$; $J\alpha = \text{const}$, the energy-current operator j_{th} is again conserved. Consequently, one expects the Drude weight to increase for large α at finite and fixed N. This feature is indeed found for $\alpha \gtrsim 0.5$ in Fig. 5.8(b).

Figure 5.8(b) indicates a difference between the gapped and gapless regimes: the decrease of $C_{\text{th}}(N)$ with N is weaker for $\alpha < \alpha_{\text{crit}}$. The following two scenarios for the thermodynamic limit are suggested for further discussion: (i) The Drude weight is nonzero in the gapless regime and zero in the gapped regime. (ii) The Drude weight is zero for all $\alpha > 0$, but, depending on α, there is a characteristic system size $N(\alpha)$ with a more or less constant $C_{\text{th}}(N)$ for $N < N(\alpha)$ and a monotonically decreasing $C_{\text{th}}(N)$ for $N > N(\alpha)$. The first interpretation might be plausible in view of the significant differences in the low-energy properties for $\alpha < \alpha_{\text{crit}}$ and $\alpha > \alpha_{\text{crit}}$, using an effective Hamiltonian such as (5.10). However, since C_{th} is essentially the Drude weight at *infinite* temperature where all states contribute with equal weight, it is not clear why low-energy features should play a crucial role for the finite-size scaling in the limit $\beta \to 0$.

A second objection against the first scenario arises from the analysis of the level-spacing distribution both in the gapped and gapless regime. Exploiting translational invariance and conservation of total S^z_{tot} already lifts all degeneracies on finite systems as is obvious from Fig. 5.3, showing the integrated level-spacing distribution $I(\epsilon)$. Again, the striking difference to the spectrum of the integrable model is emphasized: no candidates for degenerate states appear in the case of $\alpha = 0.2$ and this feature is characteristic for $\alpha > 0$, which supports the conjecture that transport properties in the gapped and gapless regimes should not be different at high-temperatures.[7]

Note that the results for $N = 20$ sites for $\alpha = 0.1, 0.2, 0.35, 1$ have not been published in Refs. [iii, iv]. The inclusion of these additional data points supports the main conclusion of a vanishing Drude weight.

---

[7] See Sec. 5.3 for a detailed discussion of Fig. 5.3.

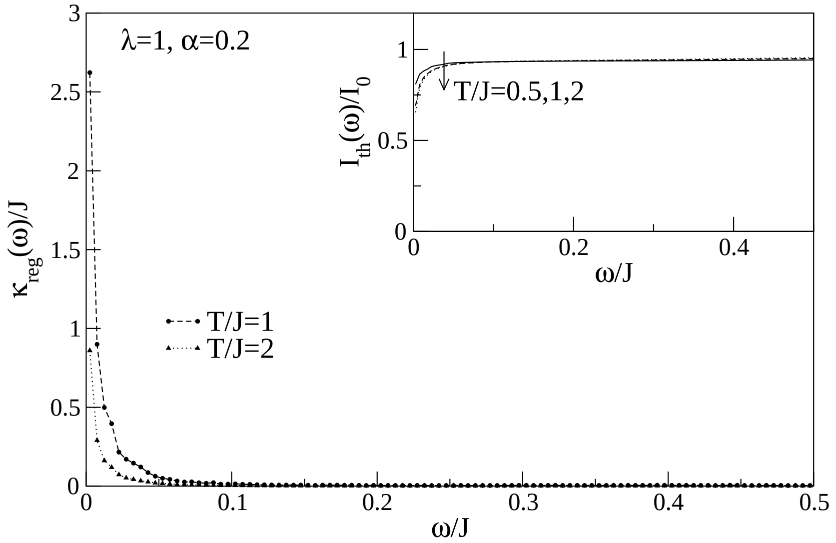

Figure 5.9: Thermal conductivity of frustrated chains with $\alpha = 0.2$ [see Eq. (5.20)]. Main panel: Regular part of $\mathrm{Re}\,\kappa(\omega)$ versus ω for $T/J = 1, 2$ for $N = 18$. Lines are guides to the eyes. Inset: Integrated weight $I_{\mathrm{th}}(\omega)/I_0$ [see Eq. (5.22)] versus ω for $T/J = 1, 2$. The arrow in the inset indicates increasing temperature.

Frequency dependence of $\kappa_{\mathrm{reg}}(\omega)$

Since the scaling analysis of the thermal Drude weight D_{th} has not yielded evidence for a finite thermal Drude weight, the next step is to study the frequency dependence of the regular part of $\kappa(\omega)$. Such a study allows one to estimate the ratio of the Drude weight to the total weight I_0 and furthermore, one can estimate the dc-conductivity in the high-temperature limit. Two examples are analyzed: $\alpha = 0.2$ and $\alpha = 1$. The numerical results are shown in Figs. 5.9 and 5.10.

Qualitatively, the curves for $\kappa_{\mathrm{reg}}(\omega)$ of frustrated chains with $\alpha = 0.2$ and $\alpha = 1$ differ even stronger than the corresponding ones for the spin conductivity $\sigma_{\mathrm{reg}}(\omega)$ shown in Fig. 5.6. In the massless phase, there is only a very narrow peak at low frequencies $\omega/J \lesssim 0.1$. More than 50% of the integrated weight $I_{\mathrm{th}}(\omega)$ shown in the inset of Fig. 5.9 is concentrated in the thermal Drude weight for the temperatures analyzed in this plot.

In contrast to the massless regime, $\kappa_{\mathrm{reg}}(\omega)$ of the chain with $\alpha = 1$ consists of a broad, structureless peak that extends up to frequencies of the order of $\omega/J \sim 4$. Depending on temperature, the data are well converged down to frequencies $\omega/J \lesssim 0.25$ while deviations between $N = 18$ and $N = 20$ sites become visible at lower frequencies. Furthermore, we observe a characteristic down-turn of $\kappa_{\mathrm{reg}}(\omega)$ at low frequencies which is also present for spin ladders [57] (see Fig. 5.18). In relation with possible ballistic transport, note that the Drude weight amounts to less than 3% of the total weight I_0 from Eq. (2.75) for $N = 20$ sites and $T/J = 1$. Thus, the scenario of ballistic thermal transport is unlikely for the massive regime of frustrated chains. While the down-turn at low frequencies renders it difficult to draw precise conclusions about the functional form of the frequency dependence, we can, however, fairly well estimate the absolute value of $\kappa_{\mathrm{dc}} = \lim_{\omega\to 0}\kappa_{\mathrm{reg}}(\omega)$. For instance, the data shown in Fig. 5.10(a) indicates $\kappa_{\mathrm{dc}}/J \approx (0.27 \pm 0.3)$ for $T/J = 2$.

Next we comment on the integrated spectral weight $I_{\mathrm{th}}(\omega)$ of the chain with $\alpha = 1$, which

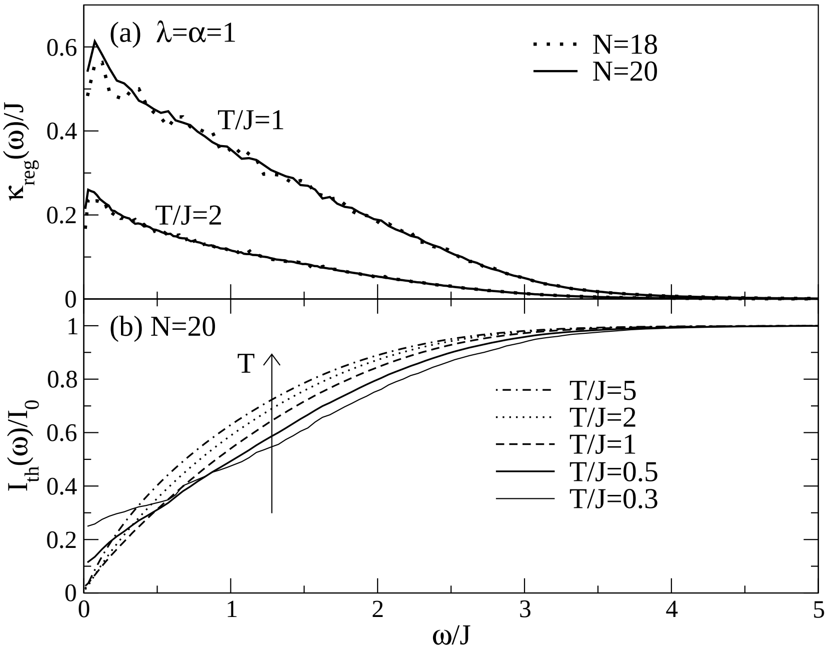

Figure 5.10: Thermal conductivity of frustrated chains with $\alpha = 1$ [see Eq. (5.20)]. (a): Regular part of $\mathrm{Re}\, \kappa(\omega)$ versus ω for $T/J = 1, 2$ for $N = 18$ and $N = 20$ sites. (b): Integrated weight $I_{\mathrm{th}}(\omega)/I_0$ [see Eq. (5.22)] versus ω for several temperatures. The arrow in panel (b) indicates increasing temperature. From Ref. [viii].

is shown as $I_{\mathrm{th}}(\omega)/I_0$ in Fig. 5.10(b) for $N = 20$ sites and several temperatures $T/J \geq 0.3$. Here, we see that first, $I_{\mathrm{th}}(\omega)/I_0$ approaches 1 the faster the larger the temperature is, and it is evident from the figure that the spectral weight is widely distributed over the range of frequencies $0 \leq \omega/J \leq 4$. Second, the curve for $T/J = 0.3$ is less smooth than the others indicating the limitations of an exact diagonalization study with respect to the accessible temperature and frequency range. No suppression of spectral weight at low frequencies due to the spin gap is observed for the parameters of Fig. 5.10(b). A smooth curve for $\kappa_{\mathrm{reg}}(\omega)$ is obtained for $T/J > 0.5$ and $N = 20$. Finally, we mention that $I_0 \propto T^{-2}$ for high-temperatures, as expected for thermal transport.

To summarize the analysis of thermal transport of frustrated chains, the numerical data indicate a vanishing thermal Drude weight for the *massive* regime at high temperatures, in agreement with the qualitative arguments given in Sec. 5.2. On the one hand, the scaling analysis of C_{th} for large values $\alpha \sim 0.2$ within the massless regime resembles the behavior seen in the gapped regime. On the other hand, the spectra of $\kappa_{\mathrm{reg}}(\omega)$ for $\alpha < \alpha_{\mathrm{crit}}$ and $\alpha > \alpha_{\mathrm{crit}}$ are qualitatively quite different, calling for an extended study including larger system sizes and further values of α. In particular, one should compute the spectra for values of α slightly above α_{crit} and compare them to the case of $\alpha = 0.2$. A possible scenario to explain the finite-size scaling in the massless regime could be that a "hidden" length scale exists, and that the system sizes need to be larger than this scale to allow for an unambiguous observability of non-ballistic behavior. A similar proposal for such a crossover system size has been put forward in Ref. [88] to explain the level-spacing distribution of XXZ spin chains plus next-nearest neighbor Ising interactions close to the integrable point.

5.5 The dimerized chain

5.5.1 Spin transport

While for the frustrated chain and the spin ladder the fermionized Hamiltonian, Eq. (2.5), contains interaction terms even at $\Delta = 0$, the case of the dimerized XY model ($\Delta = 0, \lambda \neq 1, \alpha = 0$) corresponds to a model of free, but massive fermions which can be solved exactly, allowing for a calculation of D_s in the thermodynamic limit. For details, the reader may consult, e.g., Ref. [55], where the analogous computation for D_th was done. The section starts with a discussion of this limiting case where a finite Drude weight D_s exists in the thermodynamic limit.

Drude weight of the dimerized XY chain

The Hamiltonian in terms of spinless fermions reads [see Eq. (2.5)]:

$$H^{XY} = J \sum_l \frac{\lambda_l}{2} \left(c^\dagger_{l+1} c_l + \text{H.c.}\right). \tag{5.24}$$

As usual, $\lambda_l = 1$ for l even and $\lambda_l = \lambda$ otherwise. A straightforward computation diagonalizes H^{XY}:

$$H^{XY} = J \sum_k \epsilon_k \left(a^\dagger_{k,+} a_{k,+} - a^\dagger_{k,-} a_{k,-}\right). \tag{5.25}$$

To species of new fermion operators $a^{(\dagger)}_{k,\pm}$ are necessary, and correspondingly, two modes with a gapped dispersion exist for $\Delta = 0$:

$$\epsilon_k = J\sqrt{(1-\lambda)^2/4 + \lambda \cos(k)}\,. \tag{5.26}$$

Obviously, the spin-current operator $j_\mathrm{s} = \sum_k v_k (a^\dagger_{k,+} a_{k,+} - a^\dagger_{k,-} a_{k,-})$ is conserved. $v_k = \partial_k \epsilon_k$ is the velocity. The Drude weight can exactly be computed from

$$D_\mathrm{s}(T) = \frac{1}{4T} \int dk\, \frac{v_k^2}{\cosh^2[\epsilon_k/(2T)]}\,. \tag{5.27}$$

The Drude weight $D_\mathrm{s}(T > 0)$ and its scaling in the limit $\beta = 0$

In Figure 5.11(a), the Drude weight on finite systems is plotted for a dimerized chain with $\lambda = 0.5$ and both $\Delta = 0$ (inset) and $\Delta = 1$ (main panel). In the former case, we see that the numerical data for 16 sites agree with the exact expression for $N \to \infty$ [Eq. (5.27)] at temperatures $T/J \gtrsim 0.2$. The same holds for smaller system sizes (not shown in the figure) for high temperatures. This is in contrast to the curves for $\Delta = 1$ (main panel), where no convergence with N is observed at any temperature.

For $\Delta = 1$, both $D^I_\mathrm{s}(N,T)$ [dashed lines] and $D^{II}_\mathrm{s}(N,T)$ [solid lines] have been evaluated proving their equivalence at high temperatures. Small systems ($N = 10, 12$) still exhibit

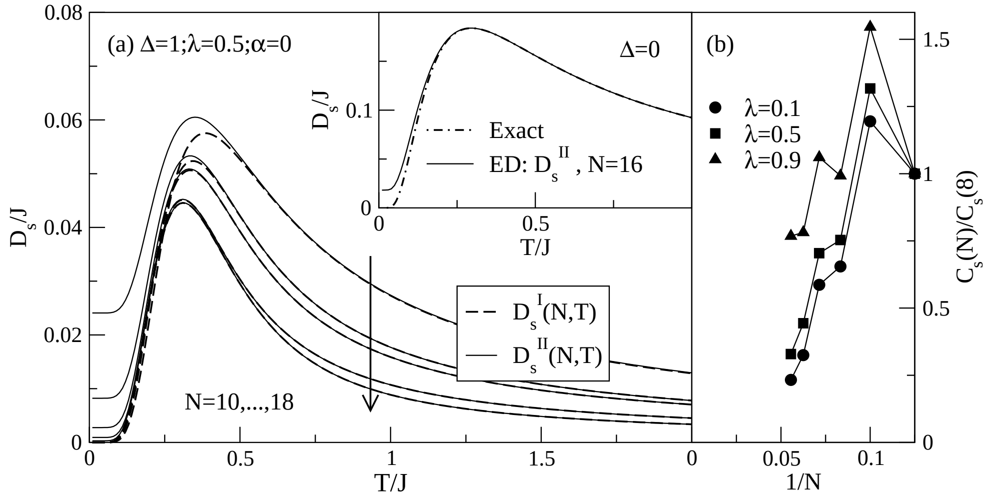

Figure 5.11: Spin transport, dimerized chain [iii]. (a): Drude weight $D_{\rm s}^{I,II}(N,T)$ for $N = 10, ..., 18$ (top to bottom as indicated by the arrow) and ($\lambda = 0.5, \alpha = 0$) [dashed lines: $D_{\rm s}^{I}(N,T)$; solid lines: $D_{\rm s}^{II}(N,T)$]. In the inset, the exact result from Eq. (5.27) [dot-dashed line] for the Drude weight of a dimerized XY chain with $\Delta = 0, \lambda = 0.5, \alpha = 0$, and numerical data (solid line) for $N = 16$ sites are shown. (b): Scaling of the high-temperature prefactor $C_{\rm s}$ of the Drude weight $D_{\rm s}$ for $\lambda = 0.1, 0.5, 0.9$ and $N = 8, 10, 12, 14, 16, 18$.

a large nonzero value of the zero-temperature Drude weight $D_{\rm s}^{II}(N, T = 0)$ which rapidly decreases with system size.

Numerical results for the high-temperature prefactor $C_{\rm s}(N)$ of $D_{\rm s}$ are shown in Fig. 5.11(b) for $\lambda = 0.1, 0.5, 0.9$ and $N = 10, 12, 14, 16, 18$ sites. An overall decrease of $C_{\rm s}$ with system size is evident from the plot. Strong oscillations of $C_{\rm s}$ are found in the case of $\lambda = 0.9$, which is very close to the integrable point $\lambda = 1$. On grounds of our numerical data, we do not find any evidence for a finite Drude weight in the limit of large system sizes.

Frequency dependence of $\sigma_{\rm reg}(\omega)$

In the case of the dimerized chain, the discussion of both $\sigma_{\rm reg}(\omega)$ and $\kappa_{\rm reg}(\omega)$ focuses on the limit of strong dimerization $\lambda \ll 1$, and we consider the isotropic case $\Delta = 1$ only. In this limit, one expects the influence of triplet-triplet interactions to be weak. Furthermore, the spin gap is very large in units of the exchange coupling J, and the spectra should reflect this.

The example chosen is $\lambda = 0.1$, for which $\sigma_{\rm reg}(\omega)$ has been computed for $N = 16$ and $N = 18$ and several temperatures. Figure 5.12 contains the results. Significant spectral weight in $\sigma_{\rm reg}(\omega)$ is only found in the frequency window $0.9 \lesssim \omega/J \lesssim 1.1$, including the energy range of the one-triplet dispersion, which, to first order in λ (and for $\Delta = 1$), is [285, 286, 300]:

$$\epsilon_k = J[1 - \frac{\lambda}{2}\cos(k)]\,. \qquad (5.28)$$

A very small and narrow peak exists at low frequencies $\omega/J \lesssim 0.1$ [shown in the inset of Fig. 5.12(a)], which stems from nonzero matrix-elements between states inside the one-triplet band. The inverse width of this peak can be interpreted as being related to the current

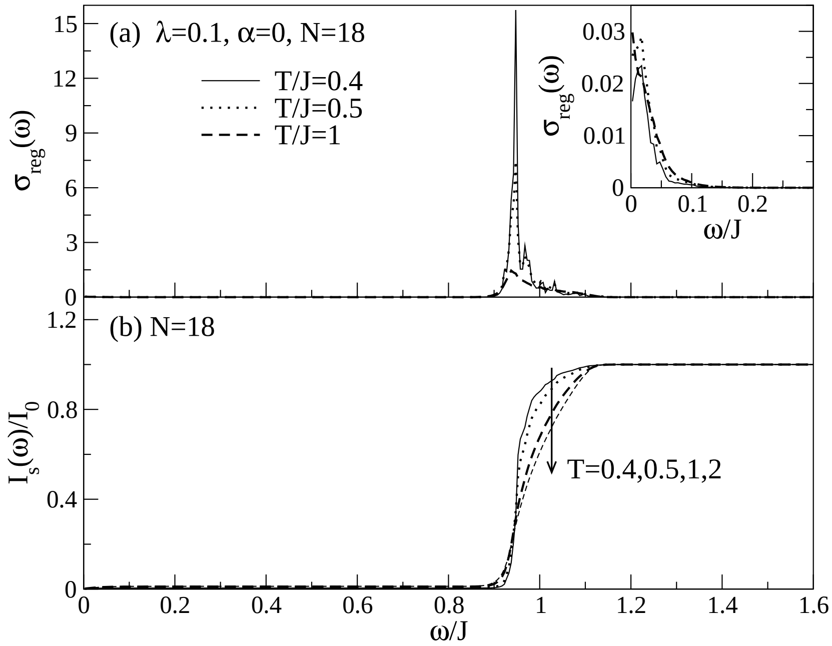

Figure 5.12: Spin conductivity of a dimerized chain with $\lambda = 0.1$ [see Eq. (5.19)]. (a): Regular part of $\mathrm{Re}\,\sigma(\omega)$ versus ω for $T/J = 0.4, 0.5, 1$ for $N = 18$ sites. (b): Integrated weight $I_{\mathrm{s}}(\omega)/I_0$ [see Eq. (5.22)] versus ω for various temperatures. The arrow indicates increasing temperature. Inset of (a): Zoom in the low-frequency region for the same data sets shown in panel (a).

lifetime and it would be very interesting to compare this measure of the lifetime to the results of an analytical computation for the current-current correlation function. This is left as a future project. Finally, the distribution of the spectral weight is clearly seen in the integrated spectral weight also, which is depicted in Fig. 5.12(b).

5.5.2 Thermal transport

The Drude weight $D_{\mathrm{th}}(T > 0)$ and its scaling in the limit $\beta = 0$

The findings for the thermal Drude weight of dimerized chains are quite similar to the spin Drude weight of the same model. The curves are plotted in Fig. 5.13 for the case of $\lambda = 0.5$ and $N = 8, \dots, 18$ sites. In the thermodynamic limit, a chain with this ratio of the alternating couplings has a spin gap of $\Delta_{\mathrm{sp}} \approx 0.6J$ [183]. At moderate temperatures $T/J \sim 0.3$, the Drude weight $D_{\mathrm{th}}(N, T)$ exhibits the typical maximum and a non-monotonous dependence on system size. A similar behavior is found in the high-temperature limit, for which the first two coefficients of an expansion of D_{th} in β are depicted in the inset of Fig. 5.13. The general trend of both $C_{\mathrm{th}} = C_{\mathrm{th},1}$ and $C_{\mathrm{th},2}$ is a decrease with system size, modulated by some oscillations. This behavior is consistent with a vanishing of D_{th} in the thermodynamic limit.

Regarding the dependence of $D_{\mathrm{th}}(N, T)$ on λ, note that C_{th} is a monotonously decreasing function of λ. Such behavior is expected, since in the limit $\lambda = 0$, the triplets are local objects that cannot propagate, which is reflected in the narrowing of the one-triplet band upon decreasing λ.

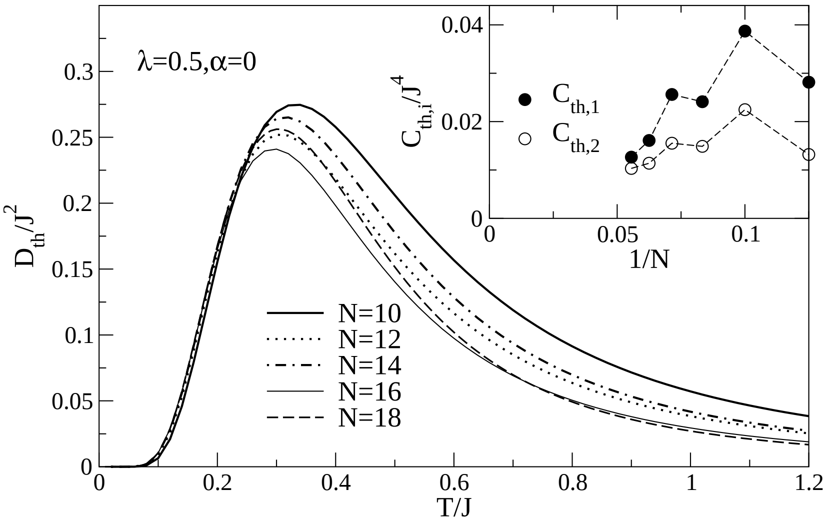

Figure 5.13: Thermal Drude weight $D_{\text{th}}(N, T)$ of dimerized chains with $N = 8, ..., 18$ sites for $(\lambda = 0.5, \alpha = 0)$ [v]. Inset: Leading coefficients $C_{\text{th},1}$ and $C_{\text{th},2}$ of a high-temperature expansion of $D_{\text{th}}(N, T) = \sum_{i=1} C_{\text{th},i}/T^{1+i}$.

The frequency dependence of $\kappa_{\text{reg}}(\omega)$

Figure 5.14 depicts our results for the regular part of the thermal conductivity $\kappa(\omega)$ for the case of $\lambda = 0.1$ and $N = 18$. Similar to the spin conductivity shown in Fig. 5.12, the regular part of the thermal conductivity only has spectral support in the low-frequency region $\omega/J \lesssim 0.1$ and in the vicinity of the one-triplet band $0.9 \lesssim \omega/J \lesssim 1.1$. There are, however, two clear-cut differences. First, the bare values found for $\kappa_{\text{reg}}(\omega)$ in units of J are an order of magnitude smaller than those for $\sigma_{\text{reg}}(\omega)$. Second, the distribution of the weight is almost reversed. At moderate temperatures $T/J \sim 0.3$, approximately 80% of the weight is found in the low-frequency peak, and the remaining fraction is concentrated around $\omega/J \approx 0.9$. This is very well reflected in the frequency dependence of the integrated spectral weight $I_{\text{th}}(\omega)$ shown in Fig. 5.14(b), which one should compare to Fig. 5.12(b).

As a first step towards an analysis of the low-frequency peak, the integral $I(\omega/J = 0.5)$ of this peak is depicted as a function of temperature in the inset of Fig. 5.14(a) for $N = 16$ and $N = 18$ sites. One observes a maximum at roughly $T/J \approx 0.35$ and a $1/T^2$-dependence at high temperatures.

5.6 The two-leg spin ladder

5.6.1 Spin transport

The Drude weight $D_{\text{s}}(T > 0)$ and its scaling in the limit $\beta = 0$

Our discussion of spin transport of spin ladders focuses on the low-temperature behavior of $D_{\text{s}}^{II}(T)$ and on the scaling of D_{s} in the limit $\beta = 0$. Figure 5.15 shows the spin Drude weight $D_{\text{s}}^{II}(T)$ of spin ladders with $\alpha = 0.5$ and $N = 10, 12, 14, 16, 18$ sites, including $D_{\text{s}}^{I}(T)$ for

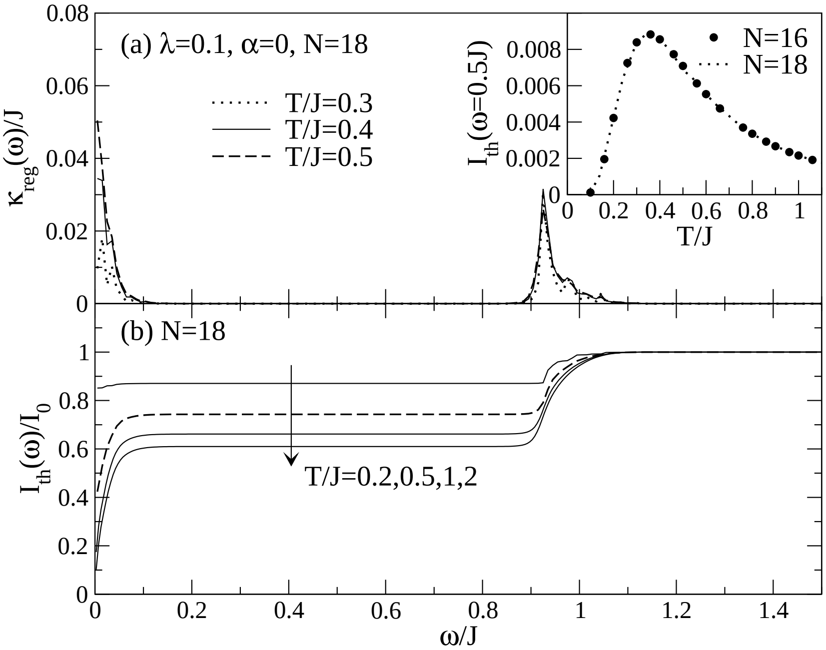

Figure 5.14: Thermal conductivity of a dimerized chain with $\lambda = 0.1$ [see Eq. (5.20)]. (a): Regular part of $\mathrm{Re}\,\kappa(\omega)$ versus ω for $T/J = 1, 2$ for $N = 18$ sites. (b): Integrated weight $I_{\mathrm{th}}(\omega)$ [see Eq. (5.22)] versus ω for several temperatures. The inset depicts the temperature dependence of the integrated spectral weight $I_{\mathrm{th}}(\omega)$ for $\omega/J = 0.5$ and $N = 16, 18$.

$N = 16$ sites. In this case, i.e., $N = 16$, we find $D_{\mathrm{s}}^{I}(T) \approx D_{\mathrm{s}}^{II}(T)$ for $T/J \gtrsim 0.5$. $D_{\mathrm{s}}^{II}(N,T)$ has a maximum for each fixed N, and its position strongly depends on N. The most interesting feature of $D_{\mathrm{s}}^{II}(N,T)$ is the zero-temperature value which is *negative* for ladders with an odd number of rungs, i.e., $N = 10, 14, 18$ sites, while $D_{\mathrm{s}}^{II}(N,T=0) > 0$ for even $N/2$. A similar observation of negative zero-temperature Drude weights has been reported in the literature for small Hubbard rings with $4n$ sites; n integer [94, 252] and for the frustrated square lattice antiferromagnet [301]. A positive zero-temperature Drude weight implies that the system is stable against changes in the boundary conditions, while a negative value signals a tendency towards a different ground state. Thus, in this case, the ground state in the thermodynamic limit is incommensurate with the structure of the finite system.

Regarding the scaling of D_{s} in the limit of $\beta = 0$, a monotonic decrease of C_{s} with increasing system size is evident from the inset of Fig. 5.15, which contains results for C_{s} for $8 \leq N \leq 18$ sites and $\alpha = 0.5, 1, 2$. In a nutshell, no evidence for ballistic spin transport is found in spin ladders on grounds of our numerical data, obtained from system sizes with $N \leq 18$ sites.

5.6.2 Thermal transport

The thermal current operator

Numerical results for the thermal conductivity of spin ladders at finite temperatures have been published by three groups [iii, 54, 57]. All authors have studied the temperature dependence

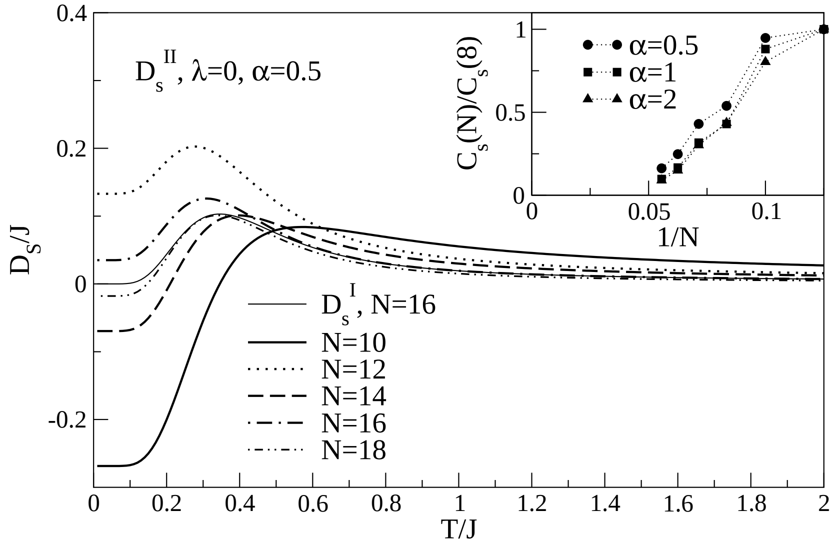

Figure 5.15: Spin transport, spin ladder. Main panel: Drude weight $D_{\mathrm{s}}^{II}(N,T)$ for $N = 10, \ldots, 18$ and $\alpha = 0, \lambda = 0.5$. The thin solid line shows $D_{\mathrm{s}}^{I}(N,T)$ for $N = 16$ sites. Inset: Finite-size scaling of the high-temperature prefactor $C_{\mathrm{s}}(N)/C_{\mathrm{s}}(8)$ for $\alpha = 0.5, 1, 2$ and $N = 8, 10, 12, 14, 16, 18$.

and the finite-size scaling of the thermal Drude weight, while in the most recent publication, Ref. [57], additional results for $\kappa_{\mathrm{reg}}(\omega)$ were presented. Further data for $\kappa_{\mathrm{reg}}(\omega)$ are shown in this thesis.

In contrast to Ref. [54], both Ref. [iii] and Ref. [57] arrive at the same main conclusion, i.e., a vanishing thermal Drude weight at finite temperatures in the limit $N \to \infty$. Still, the present situation is very unsatisfactory since the results for the Drude weight from all three groups differ pairwise. The same holds for the results for $\kappa_{\mathrm{reg}}(\omega)$ from Ref. [57] and this thesis. One possible reason for this discrepancy could lie in the different definitions for the energy-current operator j_{th} used in Refs. [iii, 54, 57]. This can be traced back to different choices for the local energy density H_l since the energy-current operator is a sum of commutators of local energy densities on different sites [see Eq. (2.36)]. The energy densities underlying the numerical computations of Refs. [iii, 54, 57] are depicted in Fig. 5.16. Both Ref. [54] and [57] start from a doubled unit cell in real space, i.e., the site label is assigned to rungs instead of single spins. In this chapter, the spin ladder is treated as a limiting case of the λ-α chain, thus the site l corresponds to a single spin. This adopts the philosophy of Ref. [45] to the present problem. Since the λ-α chain has controlled limiting cases where the Drude weight can be computed analytically and exactly,[8] there is good reason to believe in the correctness of the numerical results for the case of the spin ladder also, i.e., $\lambda = 0, \alpha > 0$.

Using an independent[9] implementation of the Hamiltonian and the energy-current operator that allows one to derive the energy-current operator from different local energies, *no* quantitative differences are found for the thermal Drude weight if different local energy densities are chosen. At present, the origin for the different quantitative results published for the thermal Drude weight remains unclear.

---

[8] These cases are the XXZ chain discussed in Chapter 4 and the dimerized XY chain discussed in Sec. 5.5.

[9] Independent means that this implementation is different from the programs used to compute the numerical results presented in the figures.

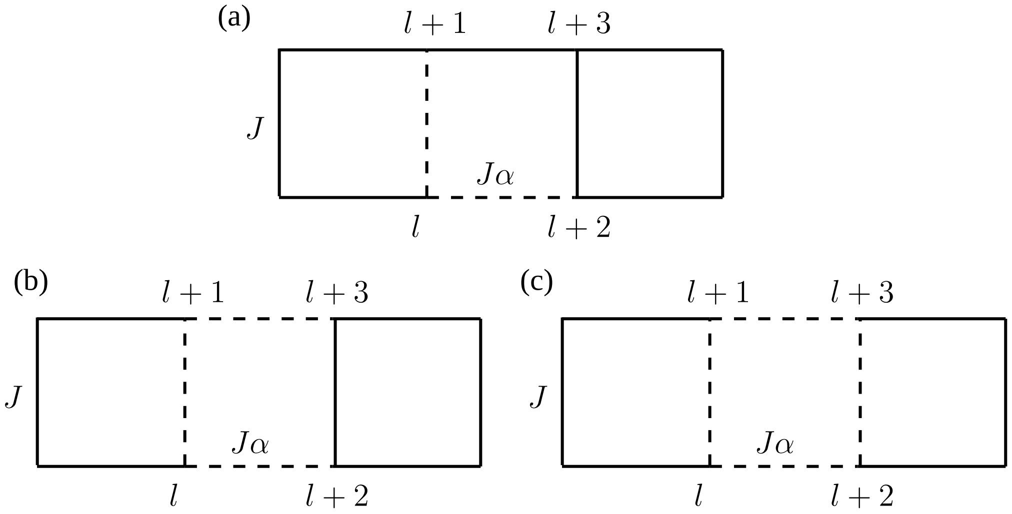

Figure 5.16: Sketch of the local energy densities underlying the definition of the energy-current operator in Refs. [iii] [panel (a), this chapter], [54] [panel (b)], and [57] [panel (c)]. The lines representing couplings that belong to the local energy at site l are dashed. The index l runs over the sites of single spins in panel (a)–(c). Note that Refs. [54] and [57] use a different real space representation. In their notation, the site index runs over rungs. In this thesis, the spin ladder is treated as a limiting case of the λ-α chain.

The thermal Drude weight $D_{\text{th}}(T > 0)$

First, it is quite instructive to discuss the finite-size scaling of the Drude weight $D_{\text{th}}(N, T)$ in comparison to thermodynamic quantities such as the susceptibility χ or the specific heat C_V. Second, the results from a finite-size analysis of the high-temperature prefactor C_{th} are detailed. Third, the dc-conductivity κ_{dc} is extracted from the frequency dependence of the thermal conductivity in the high-temperature limit. Finally, we comment on possible implications of our results for the interpretation of recent experiments [8]. With respect to experiments, further details can be found in Sec. 3.2.

The specific heat C_V, the susceptibility χ, and the thermal Drude weight $D_{\text{th}}(N, T)$ are plotted versus temperature in Fig. 5.17 for $N = 8, 10, 12, 14, 16, 18$ and $(\lambda = 0, \alpha = 0.5)$. Panel (a) contains C_V and χ, while in panel (b), $D_{\text{th}}(N, T)$ is shown. The main characteristics are the following: (i) From the comparison with QMC data, we see that finite-size effects are small for the specific heat and negligible for the susceptibility. (ii) The data for $D_{\text{th}}(N, T)$ display strong finite-size effects at all temperatures. (iii) $D_{\text{th}}(N, T)$ is monotonically decreasing for $N > 8$ and $T/J \gtrsim 0.6$. (iv) The positions of the maxima of the specific heat and the Drude weight are different. (v) For $N/2$ even(odd), the data are monotonically increasing(decreasing) at low temperatures. The latter may be attributed to the fact that $D_{\text{th}}(N, T)$ diverges for $T \to 0$ for decoupled chains and odd chain length.

It should be stressed that the restricted number of system sizes analyzed here precludes any definite conclusions from the finite-size scaling at temperatures $T/J \lesssim 0.6$; in particular, since the N-dependence is non-monotonic. Note that even a monotonic increase of $D_{\text{th}}(N, T)$ with system size at low temperatures as observed in the case of frustrated chains with, e.g., $\alpha = 0.35$, does not unambiguously point to a finite Drude weight. In this context, see also Ref. [57] and the discussion of $D_{\text{th}}(N, T)$ of frustrated chains in Sec. 5.4.

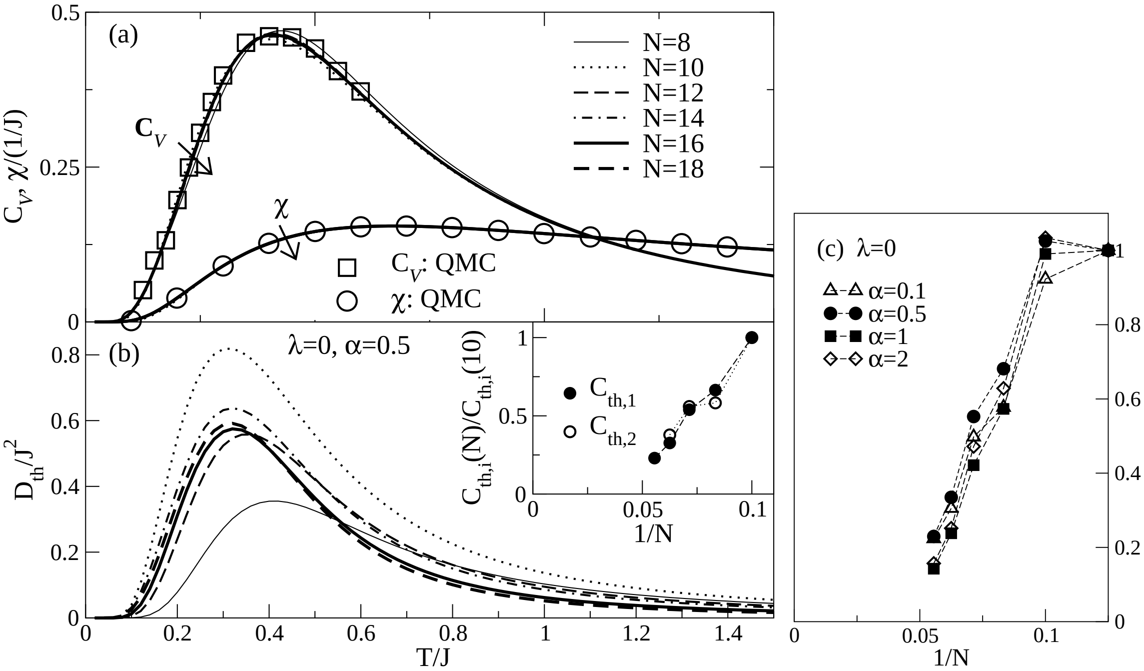

Figure 5.17: Spin ladder, ($\lambda = 0.5, \alpha = 0$). (a): Thermodynamic quantities: susceptibility χ (circles, Ref. [28]) and specific heat C_V (squares, Ref. [54]). (b): Thermal Drude weight $D_{\text{th}}(N, T)$ for $N = 8, ..., 18$ sites. Inset: Leading coefficients of a high-temperature expansion of $D_{\text{th}}(N, T) = \sum_{i=1} C_{\text{th},i}/T^{1+i}$. (c): Scaling of the thermal Drude weight in the limit $\beta = 0$. The panel shows $C_{\text{th}}(N) = C_{\text{th},1}(N)$ versus $1/N$ for $\alpha = 0.1, 0.5, 1, 2$ and $N = 8, \ldots, 18$ sites. See Ref. [iii].

While the numerical data for the specific heat are in quantitative agreement with the QMC results from Ref. [54] for the same choice of parameters, only qualitative consistency is found for the thermal Drude weight regarding points (ii)–(iv). Note that the Drude weight D_{th} in Ref. [54] is measured in units of $J_{\|} \sim \alpha J$ instead of $J_{\perp} = J$ used in this work. The specific heat, however, is dimensionless. Also, compared to point (v), the opposite monotony behavior is observed at low temperatures in Ref. [54]. This difference is very likely mainly due to the use of twisted boundary conditions and maybe also due to a different definition for the energy-current operator j_{th} in Ref. [54].

Scaling of the Drude weight D_{th} in the limit $\beta = 0$

We turn to the scaling of the thermal Drude weight with system size in the limit $\beta = 0$. The leading and next-to-leading coefficients $C_{\text{th}} = C_{\text{th},1}$ and $C_{\text{th},2}$ of an expansion of D_{th} in powers of β are plotted versus $1/N$ in the inset of Fig. 5.17(b) for ($\lambda = 0, \alpha = 0.5$). The figure reveals that the monotonic decrease with system size, modulated by odd-even effects, is present for both coefficients. In fact, the qualitative behavior does not change down to temperatures $T/J \sim 1$. Further results for C_{th} and other choices of parameters are included in Fig. 5.17(c) for $J_{\|}/J_{\perp} = \alpha = 0.1, 0.5, 1, 2$ and $N = 8, 10, 12, 14, 16, 18$ spins. A systematic decrease with system size is found for $N > 8$ from the finite-size analysis. In particular, by normalizing the data on the respective values for $C_{\text{th}}(N = 8)$, the finite-size dependence of the data for the

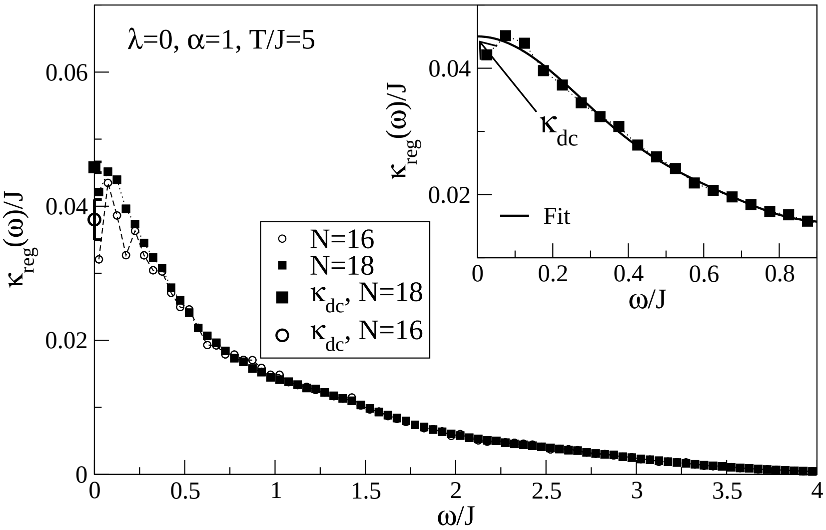

Figure 5.18: Spin ladder with equal couplings along both legs and rungs ($\lambda = 0, \alpha = 1$). (a): Regular part $\kappa_{\text{reg}}(\omega)$ of the thermal conductivity at $T/J = 5$ for $N = 16$ and $N = 18$ sites. The symbols at $\omega = 0$ denote the results from extrapolations of $\kappa_{\text{reg}}(\omega)$ to the dc-limit for $N = 16$ (circle) and $N = 18$ (square). Inset: $\kappa_{\text{reg}}(\omega)$ is fitted with a 10th-order even polynomial to estimate κ_{dc}.

spin ladder appears to be almost independent of the interchain coupling $\alpha = J_{\|}/J_{\perp}$ for the choice of parameters considered here, including the ladder with equal couplings along both legs and rungs ($\lambda = 0, \alpha = 1$).

To summarize the finite-size analysis, one can exclude the possibility of a finite thermal Drude weight of spin ladders for $N \to \infty$. In particular, this includes spin ladders with $J_{\perp} = J_{\|}$ ($\lambda = 0$,$\alpha = 1$), which is of relevance because the magnetic properties of $La_5Ca_9Cu_{24}O_{41}$ are well described by $J_{\perp} \approx J_{\|}$ [177, 178].

The regular part of $\kappa(\omega)$ and comparison with experiments

Having convinced ourselves that no evidence for $D_{\text{th}}(T > 0) > 0$ exists either from the field-theoretical or from the numerical point of view, we turn to the regular part of the thermal conductivity. As a major objective, a comparison with experimental data is suggested, connecting the results presented in this chapter with Chapter 3.

Before addressing implications for the interpretation of experiments, some words should be said about the numerical results for $\kappa_{\text{reg}}(\omega)$ itself. These are presented in Fig. 5.18 for the ladder with $\alpha = 1$, $N = 16, 18$ sites, and $T/J = 5$. An important feature of the curves is emphasized: while the curves for $N = 16$ and $N = 18$ sites differ in the low-frequency regime $\omega/J \lesssim 0.2$, no strong finite-size effects are present at higher frequencies. This is in stark contrast to the behavior of the thermal Drude weight at high temperatures, and it strongly supports the conclusion that $\kappa_{\text{reg}}(\omega)$ is a quantity that survives in the thermodynamic limit while D_{th} scales to zero. Furthermore, the typical low-frequency dip of $\kappa_{\text{reg}}(\omega)$ is also found in the present example. This feature seems to be less pronounced on larger system sizes, implying that spectral weight from the Drude weight is shifted to low, but finite frequencies.

The dc-conductivity κ_{dc} is estimated by fitting a 10th-order, even polynomial to $\kappa_{\text{reg}}(\omega)$ at low frequencies. The values obtained for κ_{dc} depend on system size, increasing with N.

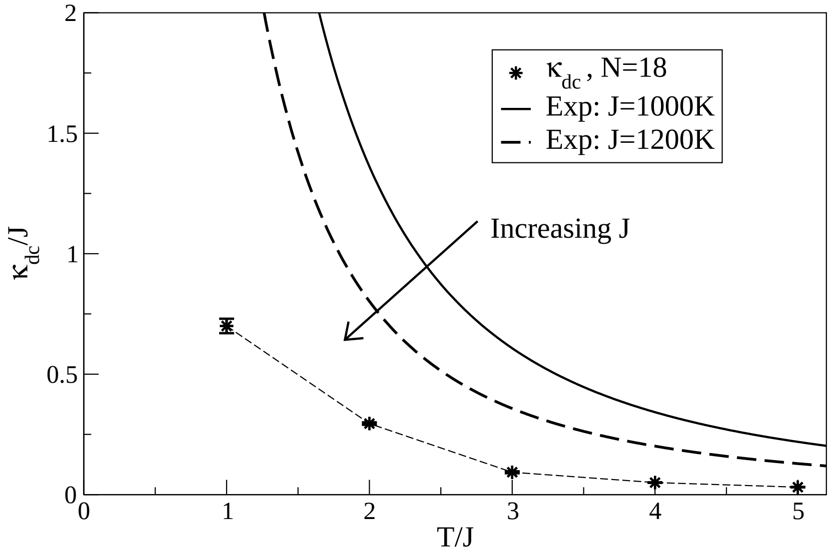

Figure 5.19: Spin ladder, $(\lambda = 0, \alpha = 1)$. Comparison with experimental data. The solid lines are extrapolations of Eq. (5.29) [54] to high temperatures. Equation (5.29) is a phenomenological fit-formula of the experimental data for $La_5Ca_9Cu_{24}O_{41}$ [8]. Note that T and κ are scaled in units of J. The two curves are obtained by using different values for J. The stars denote values of κ_{dc} extracted from $\kappa_{\mathrm{reg}}(\omega)$ and $N = 18$ spins. The line connecting the symbols is a guide to the eye.

The procedure has been carried out down to $T/J \approx 1$ where error-bars become large.

Figure 5.19 contains results for κ_{dc} for $N = 18$ sites and $T/J = 1, 2, 3, 4, 5$. Furthermore, the plot shows two lines representing the experimental data. These lines have been obtained in the following way. In Ref. [54], a fit formula was given that describes the experimental κ_{mag} of $La_5Ca_9Cu_{24}O_{41}$ very well for temperatures $T \leq 300$ K. Lacking a theory of the temperature dependence of κ_{mag}, we have used this fit-formula, which is given by:[10]

$$\kappa_{\mathrm{mag}} = \frac{A}{B + C\, e^{D/T} + (T/E)^2} \,. \tag{5.29}$$

Extrapolating this expression to high temperatures yields $\kappa_{\mathrm{mag}} \propto 1/T^2$. In order to compare κ_{mag} with theoretical data, Eq. (5.29) needs to be scaled on units of J. Since there is an experimental uncertainty about the value of $J = J_\perp$ in $La_5Ca_9Cu_{24}O_{41}$, Fig. 5.19 contains two curves, resulting from either setting $J = 1000$ K or $J = 1200$ K. Note that smaller values for κ_{mag} are obtained, if a larger value for J is used.

The comparison with the theoretical results demonstrates that the *order of magnitude* of the numerical data for κ_{dc} is comparable to the extrapolated experimental data. Apparently, the regular part contributes a major part of the dc-thermal conductivity in the ladder materials. This seems to be the case even at high temperatures, implying that extrinsic scattering gives only rise to a weak perturbation of the intrinsic thermal conductivity.

Despite the assumptions underlying this comparison, the general picture agrees well with the experimental evidence for both weak triplet-triplet and triplet-phonon interactions [153]. Therefore, it would be very interesting to supplement the present numerical study by an analytical theory of scattering mechanisms of spin ladder materials, designed to model the

---

[10] The values for the fit parameters reported in Ref. [54] are: $A = 444.2$ WK^{-1}m^{-1}, $B = 1.0, C = 0.093, D = 419.6$ K$, E = 156.4$ K.

properties of $\mathrm{La_5Ca_9Cu_{24}O_{41}}$. Such a study will hopefully further elucidate the impact of external scattering on the thermal conductivity of these materials.

5.7 Summary

The main objective of this chapter was to demonstrate that the results from an extended exact diagonalization study of both spin transport and thermal transport in nonintegrable one-dimensional spin-1/2 models do not allow for the conclusion of ballistic transport, i.e., finite Drude weights in the thermodynamic limit. This result is based on a finite-size scaling analysis of the Drude weights in the high-temperature limit, a discussion of the level-spacing distribution, and the study of the regular part of the conductivities. The situation is particularly clear for all gapped phases of the λ-α chain, i.e., frustrated chains with $\alpha > \alpha_{\text{crit}}$, the dimerized chain $(\lambda < 1, \alpha = 0)$, and the spin ladder $(\lambda = 0, \alpha > 0)$. On the contrary, in the massless regime of the frustrated chain the regular parts of the conductivities show a peculiar behavior with only a narrow peak at low frequencies. On the one hand the Drude weights are monotonically decreasing with system size in the high-temperature limit for sufficiently large systems, but on the other hand the decrease is weaker than in the gapped regime. This might be a consequence of the proximity to the integrable XXZ chain, implying that larger system sizes are needed to shed more light on this case. From the point of view of bosonization, ballistic transport is neither expected in the massless nor in the massive regimes, in agreement with the conclusions of Refs. [59, 95].

The analysis of the regular part of the conductivities reveals several interesting features and allows for extensions of the present study. First, while no convergence of the thermal Drude weight with system size is found at all, the spectra of both $\sigma_{\text{reg}}(\omega)$ and $\kappa_{\text{reg}}(\omega)$ clearly converge to finite values in the thermodynamic limit, with small finite-size effects at high temperatures and frequencies. Second, we mention the dimerized chain in the strong coupling limit $\lambda \ll 1$, where both $\kappa_{\text{reg}}(\omega)$ and $\sigma_{\text{reg}}(\omega)$ exhibit spectral weight only at very low frequencies and in the vicinity of the one-triplet band. A comparison with analytical computations of transport coefficients in this limiting case may reveal to which extent transport can be understood in a quasi-particle picture. Technically, bond-operator theory [221] combined with the Mori-Zwanzig formalism [63, 302] provides a framework for the study of, e.g., current-current life-times within an approximative scheme. Third, dc-conductivities can reliably be extracted from the numerical results in the high-temperature limit. This has been exemplified in the case of thermal transport of frustrated chains with $(\lambda = 1, \alpha = 1)$ and spin ladders with $(\lambda = 0, \alpha = 1)$. In the latter case, i.e., thermal transport of spin ladders, a comparison with experimental data for the thermal conductivity of $\mathrm{La_5Ca_9Cu_{24}O_{41}}$ has been suggested. As a result, the dc-conductivities extracted from the numerical data are of the same order of magnitude as the experimental data. This conclusion and the general statement that thermal transport of spin ladders is non-ballistic agrees with another numerical study [57].

Chapter 6

Disordered spin systems

Introducing disorder into pure spin models is a key step to arrive at realistic models for materials. While crystallographic defects or weak disorder in the interactions may be present even in very clean crystals, interesting physics arises if controlled doping experiments are performed. As an example, we mention the Zn-doping experiments discussed in Secs. 3.2.3 and 3.4.2.

In this chapter, two models are discussed: bond-disordered XY chains in Sec. 6.1, and bond-disordered spin ladders in Sec. 6.2. Bond disorder in the present context means that spatial randomness is introduced into the exchange interactions J_l of the spin Hamiltonians. In contrast to that, the replacement of ions such as Cu by Zn in the CuO_2 planes of the cuprates leads to site impurities, which will not be studied in this chapter.

In Sec. 6.1, preliminary numerical results are presented for transport properties of disordered XY chains, focusing on the frequency dependence of the spin and the heat conductivity. Being a model of noninteracting free lattice fermions, the Hamiltonian can be diagonalized completely on very large systems with $N \sim 10^4$ sites. The single-impurity case, binary distributions as well as continuous distributions of impurities are studied.

Section 6.2 mainly focuses on the appearance of mid-gap states in the spectrum of two-leg ladders upon doping. A comparative study of diagrammatic and numerical methods is presented, covering the cases of single impurities as well as binary distributions. The theory is set up in the strong-coupling limit, which is the limit of strongly coupled legs of the two-leg ladder. The existence of impurity-induced bound states is demonstrated and detailed features of the density of states of the one-triplet excitation of spin ladders are discussed. The results may be of relevance for ladder materials in the strong-limit such as $(C_5H_{12}N)_2CuBr_4$ [303] or CaV_2O_5 [304, 305].

Some aspects of Sec. 6.2 have already been published in Refs. [vi] and [vii].

6.1 Transport properties of disordered XY chains

6.1.1 Outline: model and numerical method

The field of transport in disordered spin and electron systems has a very long tradition, in particular due to its relation to localization phenomena [306]. For a review, we refer the reader to Ref. [307]. Transport of disordered one-dimensional systems has recently attracted renewed interest within mesoscopic physics due to the existence of persistent currents in finite systems (see, e.g., Refs. [133–137, 308–313]), which are reduced in the presence of disorder. As a measure of the persistent currents one studies the (spin) Drude weight [137]. Furthermore, the zero-temperature phases of disordered XY and XXZ chains are probed by the spin Drude weight (or the spin stiffness, respectively) [311]. In this section we investigate disordered XY chains with bond disorder and periodic boundary conditions. In principle, one distinguishes between diagonal and off-diagonal disorder. Diagonal disorder is realized by randomly distributed onsite energies (e.g., a randomly varying magnetic field), while off-diagonal disorder is introduced into spin systems through a random variation of the exchange couplings in the XY part of the Hamiltonian.

Without disorder, the XY model is in the massless phase of the XXZ chain (see, e.g., Fig. 4.1), extending between $-1 < \Delta < 1$, which possesses a nonzero Drude weight $D_{\mathrm{s}}(T = 0)$ [79]. For $-1/2 < \Delta < 1$, disorder is a relevant perturbation in the renormalization group sense and the system is driven into a random-singlet phase [314, 315]. This phase is characterized by a vanishing zero-temperature Drude weight in the thermodynamic limit (see, e.g., Refs. [316,317]). Even the presence of a single impurity in, e.g., the spin-1/2 XXZ chain, is sufficient to destroy the ideally conducting behavior [257, 313]. Diagonal disorder leads to complete localization of the wave-function (see Ref. [307] and further references therein). Then, we are dealing with a metal-insulator transition that is of the Anderson localization type.

In the present study, we focus on off-diagonal disorder. The breaking of translational invariance gives rise to vanishing Drude weights. However, the system may still exhibit metallic behavior at finite temperatures with finite dc-conductivities. We therefore first concentrate on the regular parts of the spin and the thermal conductivities at finite frequencies and temperatures, while the main objective of our study is to access the dc-conductivities. References [316] and [317] provide for recent results for the finite-size scaling of the spin stiffness of disordered XY and XXZ chains at zero temperature, while Refs. [311,312] contain numerical studies of dynamics and transport properties of random XXZ spin-1/2 chains, including a renormalization group treatment of the XY case.

We now turn to an outline of the numerical approach to our problem. The Hamiltonian reads:

$$H = \sum_{l=1}^{N} \frac{J_l}{2}(S_l^+ S_{l+1}^- + \mathrm{H.c.})\,. \tag{6.1}$$

The couplings J_l are randomly chosen according to a distribution $P(J_l)$. Via the Jordan-Wigner transformation [81], which is explicitely given in Eq. (2.2), the Hamiltonian is equivalent to free spinless fermions with random nearest-neighbor hopping matrix elements $t_l = J_l/2$:

$$H = \sum_{l=1}^{N-1} \frac{J_l}{2}(c_l^\dagger c_{l+1} + \mathrm{H.c.}) + [-e^{i\pi n_F} c_N^\dagger c_1 + \mathrm{H.c.})]\,. \tag{6.2}$$

The fermion creation and annihilation operators on site l are $c_l^\dagger$ and c_l. n_F denotes the number of fermions in the system, N the number of sites, and $n_l = c_l^\dagger c_l$, as usual. In principle, a random magnetic field corresponding to random onsite energies could easily be incorporated into the Hamiltonian. At present, we focus on the case of random hopping matrix elements in zero magnetic field. The current operators in terms of spinless fermions are:

$$j_{\mathrm{s}} = \sum_l \frac{J_l}{2}(ic_l^\dagger c_{l+1} + \mathrm{H.c.});\quad j_{\mathrm{th}} = \frac{1}{4}\sum_l J_l J_{l+1}(ic_l^\dagger c_{l+2} + \mathrm{H.c.})\,. \tag{6.3}$$

We now detail how the single-particle subspace is diagonalized numerically, and second, how finite-temperature transport coefficients can be computed from the single-particle eigenstates, following Refs. [316, 318–320].

A technical subtlety arises concerning the boundary conditions for the fermions, which is why the boundary term has explicitely been given in (6.2). While the spin operators satisfy periodic boundary conditions, the sign of the boundary term in Eq. (6.2) depends on the number of fermions, denoted by n_F:

$$\left.\begin{array}{c} n_F \text{ odd} \\ n_F \text{ even} \end{array}\right\} \Rightarrow \left\{\begin{array}{c} \text{PBC} \\ \text{APBC} \end{array}\right. , \tag{6.4}$$

where (A)PBC stands for (anti-)periodic boundary conditions. The number of fermions is determined by the z-component of the total spin:

$$S^z_{\text{tot}} = \sum_{l=1}^{N} n_l - \frac{N}{2} = n_F - \frac{N}{2} . \tag{6.5}$$

However, since the goal of this study is to express all transport coefficients in terms of single-particle states for very large system sizes, the dependence of the boundary conditions on the number of fermions will be neglected. Rather, either periodic or anti-periodic boundary conditions are used in the single-particle subspace. This approximation is justified since in the thermodynamic limit, the effect of boundary conditions should vanish. It has been checked that in the case of the clean XY chain the results for the Drude weights obtained from finite chains of spinless fermions with either PBC or APBC converge to the same curve, which one obtains if boundary conditions are correctly implemented for each S^z_{tot} subspace.

The Hamiltonian H can be written as

$$H = \Psi^\dagger \mathcal{A} \Psi \tag{6.6}$$

where $\mathcal{A}$ is a symmetric $N \times N$ band-matrix with nonzero entries $\mathcal{A}_{i,i+1} = J_l/2$ and $\mathcal{A}_{1N}, \mathcal{A}_{N1}$ due to the boundary conditions. $\Psi^\dagger$ is a row-vector:

$$\Psi^\dagger = (c_1^\dagger, \ldots, c_N^\dagger) . \tag{6.7}$$

Let U be the unitary transformation that diagonalizes $\mathcal{A}$. Then, transforming to a new set of fermion operators

$$\eta_\mu = \sum_l U_{l\mu} c_l \tag{6.8}$$

we arrive at:

$$H = \sum_\mu \epsilon_\mu \eta_\mu^\dagger \eta_\mu . \tag{6.9}$$

Applying the unitary transformation (6.8) to the current operators yields:

$$j_{\text{th[s]}} = \vec{\eta}^{\,\dagger} \mathcal{J}_{\text{th[s]}} \vec{\eta} \tag{6.10}$$

where we use the definition $\vec{\eta}^{\,\dagger} = (\eta_1^\dagger, \ldots, \eta_N^\dagger)$. $\mathcal{J}_{\text{th[s]}}$ are $N \times N$ matrices. Since the currents are in general not diagonal in the index μ, the explicit knowledge of eigenvectors of $\mathcal{A}$ is necessary. In the numerical implementation, the matrices representing the current operators are diagonalized in subspaces of the Hilbert space in which the Hamiltonian is degenerate.

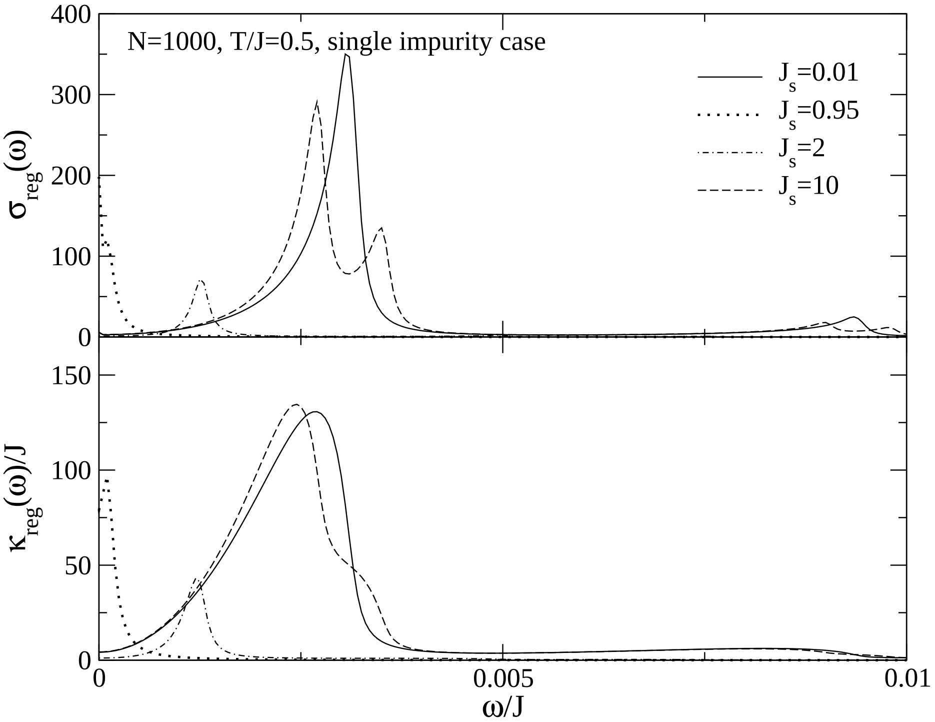

Figure 6.1: XY chain with a single impurity, $N = 1000$ sites, and $T/J = 0.5$. (a): Spin conductivity, $\sigma_{\rm reg}(\omega)$. (b): Thermal conductivity, $\kappa_{\rm reg}(\omega)$. The parameters are: $J_{\rm s} = 0.01, 0.95, 2, 10$ and $T/J = 0.5$. The spectra for $J_{\rm s} = 0.95, 2$ have been multiplied by 0.1.

Transport coefficients for noninteracting particles

The transport coefficients can be expressed in terms of single-particle eigenenergies ϵ_μ. To this end, we exploit the property that all multi-particle states are simply products of single-particle states, which is inherent to noninteracting systems. For the Drude weights $D_{\rm s}$ and $D_{\rm th}$ one obtains:

$$D_{\rm th[s]}(T) = \frac{\pi\beta^{r+1}}{N} \sum_{\mu\nu} \mathcal{J}_{\mu\mu}\mathcal{J}_{\nu\nu}\, f(\epsilon_\mu)\, f(\epsilon_\nu)\, [\delta_{\mu\nu} e^{\beta\epsilon_\mu} + 1] \,. \tag{6.11}$$

The corresponding expressions for the regular parts of $L_{11}(\omega) = \sigma(\omega)$ and $L_{22}(\omega) = \kappa(\omega)$ read [307]

$$\kappa[\sigma]_{\rm reg}(\omega) = \frac{\beta^r}{\omega} \sum_{\epsilon_\mu \neq \epsilon_\nu} |\mathcal{J}_{\nu\mu}|^2 \, [f(\epsilon_\mu) - f(\epsilon_\nu)]\, \delta(\omega - (\epsilon_\nu - \epsilon_\mu)) \,. \tag{6.12}$$

The exponent r is $r = 0$ for spin and $r = 1$ for thermal transport. $\mathcal{J}_{\nu\mu}$ denote the matrix elements of $\mathcal{J}_{\rm th}$ and $\mathcal{J}_{\rm s}$, respectively.

6.1.2 Frequency dependence of the thermal and the spin conductivity

Preliminary results for $\kappa_{\rm reg}(\omega)$ and $\sigma_{\rm reg}(\omega)$ are presented for three types of disorder: (i) the single-impurity case; (ii) binary distributions of impurities; and (iii) a Gaussian distribution

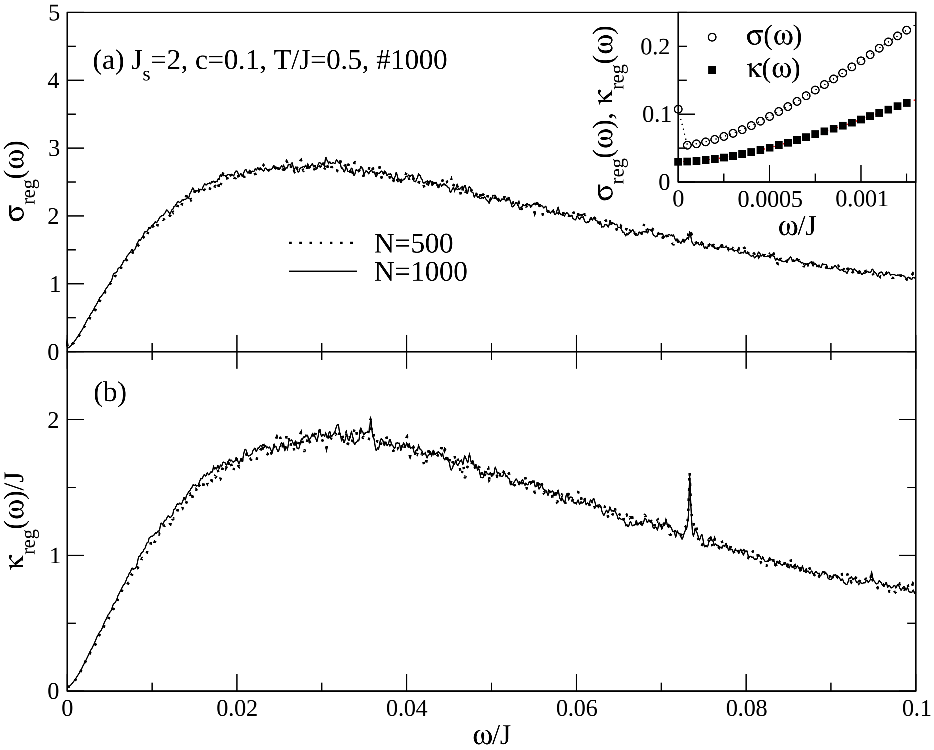

Figure 6.2: XY chain with a binary distribution of impurities. (a): Spin conductivity. (b): Thermal conductivity. The parameters are: $J_\mathrm{s} = 2$, concentration $c = 0.1$, and $T/J = 0.5$. The plots contain results for $N = 500$ (dotted lines) and $N = 1000$ (solid lines) sites, averaged over 1000 random realizations. The inset shows a zoom of the low-frequency region for $\sigma_\mathrm{reg}(\omega)$ [circles] and $\kappa_\mathrm{reg}(\omega)$ [squares] for $N = 1000$ sites.

of impurities. For the spectra shown in Figs. 6.1, 6.2, and 6.3, an imaginary broadening of $\eta = 10^{-4}$ is used.

Single-impurity case

We now discuss the case of a single impurity in a XY chain, i.e.,

$$J_1 = J_\mathrm{s}; \quad J_l = J \quad \forall l \neq 1 \, . \tag{6.13}$$

For a single impurity, an arbitrary site can be chosen for the impurity, e.g., $l = 1$. This case can also be treated analytically, for instance, by computing the T-matrix. We use this approach in Sec. 6.2 to analyze the impurity-induced bound states of disordered spin ladders. For the present problem, the discussion is restricted to a purely numerical treatment.

Both the spin and the thermal conductivity of XY chains with 1000 sites and a single impurity with $J_\mathrm{s} = 0.01, 0.95, 2, 10$ are shown in Fig. 6.1(a) and Fig. 6.1(b), respectively, for $T/J = 0.5$. Note that the spectra for $J_\mathrm{s} = 0.95, 2$ have been multiplied by 0.1. Mainly, the spectra consist of one peak that is shifted away from $\omega = 0$ as a function of J_s. Additional oscillations are visible in both quantities. In the extreme limits of either $J_\mathrm{s} = 0$ or $J_\mathrm{s} \to \infty$, no transport through the modified link is possible. Qualitatively, we observe a stronger reduction of the dc-conductivities the more J_s deviates from $J = 1$. For small perturbations, i.e., $J_\mathrm{s} = 0.95, 2$, finite dc-conductivities are found for both $\kappa_\mathrm{reg}(\omega)$ and $\sigma_\mathrm{reg}(\omega)$.

Binary distribution of impurities

We now proceed by a discussion of a binary distribution $P(J_l)$ of impurities:

$$P(J_l) = c\,\delta(J_l - J_\mathrm{s}) + (1 - c)\,\delta(J_l - J)\,. \tag{6.14}$$

The concentration of impurities is denoted by c and J is set to unity.

Figure 6.2(a) and 6.2(b) contain the numerical results for $\sigma_\mathrm{reg}(\omega)$ and $\kappa_\mathrm{reg}(\omega)$, respectively. The parameters are: $J_\mathrm{s} = 2$, $c = 0.1$, $N = 500, 1000$, and $T/J = 0.5$. The spectra have been sampled over 1000 random realizations for both system sizes. We observe that the larger the system size is, the less random realizations are necessary to suppress statistical fluctuations.[1] Regarding the dependence on system size, only small differences between the two curves for $N = 500$ and $N = 1000$ shown in the figure are found. The origin of smaller features seen in $\sigma_\mathrm{reg}(\omega)$ at small frequencies (see the inset) and in $\kappa_\mathrm{reg}(\omega)$ at $\omega/J \approx 0.075$ is at present unclear, but it is believed that these are only statistical artefacts.[2]

Both $\sigma_\mathrm{reg}(\omega)$ and $\kappa_\mathrm{reg}(\omega)$ exhibit a broad, structureless peak, with a maximum around $\omega/J \approx 0.03$. No fingerprint of the single-impurity peak is visible in the plot (compare the curves for $J_\mathrm{s} = 2$ shown in Fig. 6.1). In the zero-frequency limit, both conductivities possess finite values, which is evident from the inset of Fig. 6.2(a). Furthermore, the slopes of the conductivities at $\omega = 0$ seem to vanish in both cases.

Continuous distributions of impurities

Finally, we turn to the case of a continuous distribution of impurities, namely the Gaussian distribution:

$$P(J_l) \propto e^{-(J_l - J)^2/w^2}\,. \tag{6.15}$$

The width of $P(J_l)$ is denoted by w and the center J of $P(J_l)$ is set to unity. The conductivities are plotted in Figure 6.3 for $w = 0.2$, $T/J = 0.5$, and $N = 1000, 5000$. The number of random realizations is 1000 and 10, respectively.

The general shape of the spin and the thermal conductivity for this type of distribution is quite similar to the case of a binary distribution of impurities. Again, $\sigma_\mathrm{reg}(\omega)$ and $\kappa_\mathrm{reg}(\omega)$ exhibit only a single broad maximum located around $\omega/J = 0.015$. In the limit of vanishing frequency, the conductivities extrapolate to finite values, which is illustrated in the inset of Fig. 6.3(a). This implies that bond-disordered XY chains conduct both spin and heat at finite temperatures.

Renormalization group studies have shown that physical properties of disordered systems do not depend on the specific form of the random distribution [314,315]. On the one hand, one should therefore formulate the results independently of specific distributions. As a measure

---

[1] For a discussion of *self-averaging* in the present context, we refer the reader to Refs. [307, 311].

[2] Reference [311] predicts a logarithmic divergence of $\sigma_\mathrm{reg}(\omega)$ at $T = 0$. It remains to be checked whether the low-temperature feature of $\sigma_\mathrm{reg}(\omega)$ seen in the inset of Fig. 6.2(a) is reminiscent of this divergence.

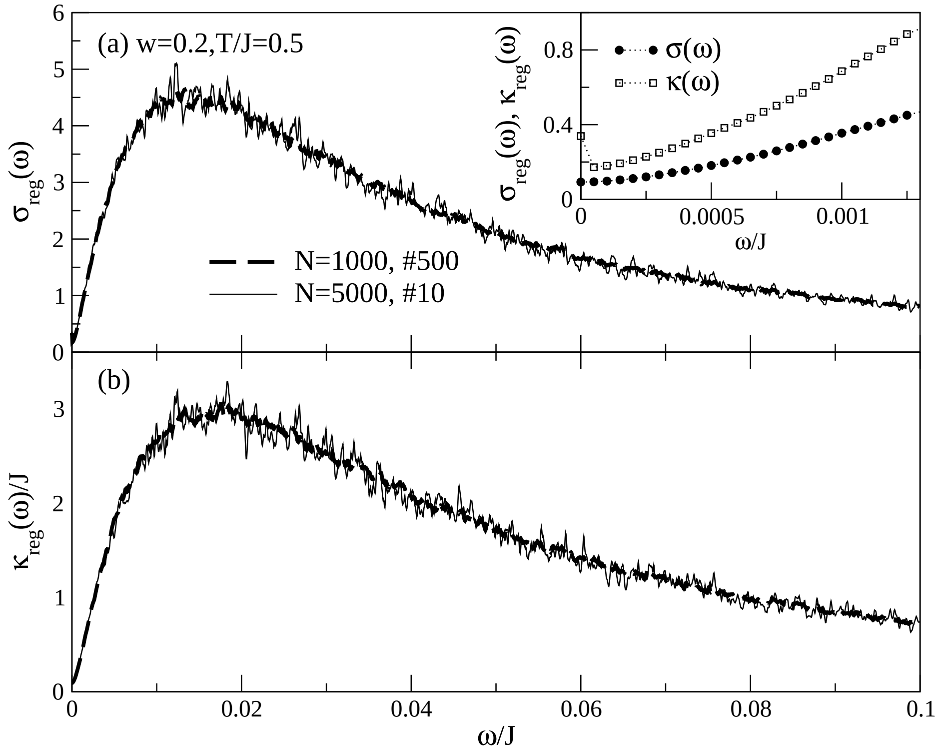

Figure 6.3: XY chain with a Gaussian distribution of impurities, centered around $J = 1$ with width $w = 0.2$. (a): Spin conductivity, $\sigma_{\mathrm{reg}}(\omega)$. (b): Thermal conductivity, $\kappa_{\mathrm{reg}}(\omega)$. The system sizes in this figures are $N = 1000$, sampled over 1000 random realizations, and $N = 5000$, sampled over 10 random realizations. The inset shows a zoom of the low-frequency region for $\sigma_{\mathrm{reg}}(\omega)$ [circles] and $\kappa_{\mathrm{reg}}(\omega)$ [squares].

of disorder, which may allow one to compare different distributions, one often introduces the variance of the distribution of the couplings (see, e.g., [316]):

$$\mathcal{D} = \overline{(J_l)^2} - \left(\overline{J_l}\right)^2 . \tag{6.16}$$

In this equation, $\overline{J_l}$ denotes the ensemble-average of J_l. This may help to identify the correct scaling of the numerical data both with system size and disorder strength.

On the other hand, in order to make direct contact with the existing literature, diagonal disorder, i.e., randomly distributed onsite potentials or magnetic fields should be included in the study. Very often, a box-distribution is considered:

$$P(J_l) = \begin{cases} 1/W & \text{for } J - (W/2) \leq J_l \leq J + (W/2) \\ 0 & \text{otherwise} \end{cases} , \tag{6.17}$$

which can easily be implemented. These extensions are left for future work.

6.1.3 Summary

In this section, first results for transport properties of disordered XY chains have been shown. Since this is a model of noninteracting spinless fermions, the transport coefficients can be expressed in terms of single-particle states, allowing one to study fairly large system sizes of the order of 10^4 sites. The largest system size studied in this thesis is $N = 5000$.

Numerical results for three types of disorder were presented, including the single-impurity case and a binary as well a Gaussian distribution of impurities. In all cases, the Drude weights vanish in the thermodynamic limit both at zero and at finite temperatures, but the dc-conductivities are nonzero at finite temperatures. This result needs to be further substantiated by a refined analysis of the scaling with both system size N and imaginary broadening η. The general form of the frequency dependence of the spin conductivity resembles the results of Ref. [312] for zero temperature. We stress that the form of either $\sigma_{\mathrm{reg}}(\omega)$ or $\kappa_{\mathrm{reg}}(\omega)$ is not simply a broadened Drude peak. It remains to be checked whether the total weight evolves continously from the homogenous case for weak disorder.

Our results are intended to extend the existing literature for disordered one-dimensional systems in two directions: first, finite temperatures and frequencies are considered, and second, the thermal conductivity has been computed. An extension of the present study could comprise a more detailed analysis of the dependence of the conductivities on temperature and further parameters such as the width w in the case of the Gaussian distribution. As a major objective, we aim at the extrapolation to the zero-frequency limit. The inclusion of larger system sizes will clarify whether the results for $\omega \to 0$ hold in the thermodynamic limit.

6.2 Bond-disordered spin ladders

6.2.1 Outline and motivation

In this section, we turn to the discussion of bond disorder in spin ladders. Being a realization of a spin liquid with a quantum disordered ground state and a large spin gap $\Delta_{\mathrm{sp}} \sim 0.5 J_\perp$ for the ladder with equal couplings along legs and rungs, an interesting aspect of disorder is the possibility to find mid-gap bound states. For the pure, homogeneous spin ladder $S = 0$ bound states of triplet excitations have intensely been studied during the past years and their relevance for optical properties of spin ladders was proposed [218,321–326] and experimentally verified; for instance for $\mathrm{La_6Ca_8Cu_{24}O_{41}}$ [178].

In this section, we discuss the effect of impurity-induced bound states of triplets. This type of bound states is different from those mentioned above: here, we are dealing with one-triplet wave-functions that are localized in the vicinity of the impurity site. In contrast to a large fraction of the literature dealing with localization phenomena, we are primarily interested in the existence of mid-gap states, and, at least in the first place, not in the physics of *mid-band* states at the center of the band which are usually studied in connection with impurity-induced metal-insulator transitions (see Ref. [307] for a review).

This thesis' main interest lies in transport properties of spin models. An extension of Chapter 5 naturally comprises thermal transport properties of bond-disordered spin ladders. In this section, we will, however, rather establish a number of useful methods that allow us to investigate disordered systems. This includes numerical impurity-averaging and diagrammatic techniques. The focus is on the eigenenergies of single-impurity and cluster bound states and on features of the density of states originating from impurities at finite concentrations. Technically, a mapping onto bond-boson operators [98] is performed, followed by a projection on the single-triplet subspace. Thus, the interactions of the triplets are accounted for on the level of first-order perturbation theory in $J_\parallel / J_\perp$. A comparison with a Lanczos study of spin ladders [vi] with one impurity reveals that the results are qualitatively relevant for ratios of $J_{\|}/J_{\perp}$ that are larger than 0.1. The study is intended to serve as a basis for future research on transport properties of disordered ladder systems. Furthermore, the physics of bond disorder in spin ladders is also directly important for doping experiments in realistic materials that are currently studied. In the next paragraph, we will elaborate more on this aspect.

Let us briefly give a more precise definition of the type of disorder we are interested in since in general, one may distinguish between different kinds of impurities. First, magnetic ions such as the Cu^{2+} ions in $SrCu_2O_3$ can be replaced by nonmagnetic ones such as Zn (see Ref. [327] and references therein), effectively removing a spin-1/2 moment, or by other ions with the same or a different effective magnetic moment. The replacement of the spin-carrying ion will be referred to as a site impurity. Note that it is also conceivable that a site impurity leads to modifications of the exchange couplings to neighboring sites. Second, and this is what we mainly have in mind in this study, the exchange paths themselves can be modified by doping the bridging X-ions in, e.g., Cu-X-Cu bonds, realizing what we call a bond impurity, or simply impurity, in the following. Such a situation is described in Ref. [328] for the alternating spin chain system $(CH_3)_2CHNH_3Cu(Cl_xBr_{1-x})_3$ where Cl and Br ions are substituted with each other. Furthermore, a spin ladder material exists, namely $(C_5H_{12}N)_2CuBr_4$ [303], where one could think of analogous doping experiments. This material is suggested to contain two-leg spin ladders in the strong-coupling limit, i.e., the coupling constant along the legs $J_{\mathrm{L}} = J_{\|}$ is small compared to the coupling along the rungs $J_{\mathrm{R}} = J_{\perp}$ [303]. Moreover, there are a number of further candidates for organic spin ladder materials in the strong-coupling limit, see, e.g., Ref. [329]. As an example for an inorganic system, we mention CaV_2O_5 for which a ratio of $J_{\mathrm{L}}/J_{\mathrm{R}} \sim 0.1$ is discussed [304, 305].

In the literature, bond randomness in spin ladder systems has been studied both in the weak and strong disorder limit using the real-space renormalization group method [330, 331], bosonization [332], and a mapping onto random-mass Dirac fermions [333]. Most of these studies have focused on the stability of the ground state and the gap against disorder and they find that disordered spin ladders exhibit nonuniversal thermodynamic properties (see, e.g., Ref. [331]), which is similar to the physics of disordered dimerized spin-1/2 chains [334].

6.2.2 Strong-coupling limit: bond-boson operators

Although the Hamiltonian of the pure two-leg spin ladder has frequently been discussed in the preceding chapters, we repeat its definition, since in this section the notation for the couplings slightly deviates from Chapter 5, with the intention to keep the consistency with Refs. [vi, vii]:

$$H_0 = \sum_{l=1}^{N} \left[J_{\mathrm{R}} \vec{S}_{l,1} \cdot \vec{S}_{l,2} + J_{\mathrm{L}} (\vec{S}_{l,1} \cdot \vec{S}_{l+1,1} + \vec{S}_{l,2} \cdot \vec{S}_{l+1,2}) \right] . \tag{6.18}$$

$\vec{S}_{l,1(2)}$ are spin-1/2 operators acting on rung l and on leg 1(2) and N is the number of rungs. In contrast to Chapter 5, the couplings along rungs is denoted by $J_{\perp} = J_{\mathrm{R}}$ and that along legs by $J_{\|} = J_{\mathrm{L}}$. J_{R} is set to unity in all explicit computations, but kept in the equations for the sake of clarity. In the presence of disorder we adopt the following notation:

$$H = H_0 + H'; \quad H' = \sum_{n=1}^{N_{\mathrm{imp}}} \delta H_n \,, \tag{6.19}$$

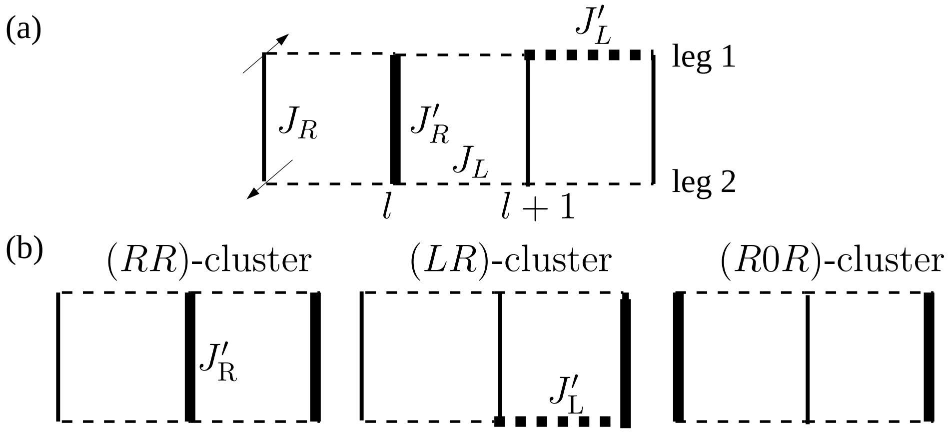

Figure 6.4: (a): Sketch of a two-leg spin ladder with one bond impurity J_{R}' on a rung site (thick solid lines) and one bond impurity J_{L}' (thick dashed lines) on one leg. J_{R} (thin solid lines) denotes the coupling along rungs and J_{L} (dashed lines) denotes the couplings along the legs. (b): Examples for small impurity clusters. (RR) stands for two rung impurities on neighboring rungs, (LR) denotes a modified rung coupling in combination with one leg coupling being modified on an adjacent leg site. In the case $(R0R)$, the modified rungs are separated by one non-perturbed site.

where N_{imp} is the number of modified couplings and δH_n is the local perturbation at site l_n leading to either a modified onsite rung interaction $J_{\mathrm{R}}' = J_{\mathrm{R}} + \delta J_{\mathrm{R}}$ or a modified leg coupling $J_{\mathrm{L}}' = J_{\mathrm{L}} + \delta J_{\mathrm{L}}$, connecting sites l_n and l_n+1. For the cases of disorder on a rung or a leg site, δH_n explicitly reads

$$\begin{aligned} \delta H_n &= \delta J_{\mathrm{R}}\, \vec{S}_{l_n,1} \cdot \vec{S}_{l_n,2} && (6.20)\\ \delta H_n &= \delta J_{\mathrm{L}}\, \vec{S}_{l_n,j} \cdot \vec{S}_{l_{n+1},j}; \quad j = 1,2\,. && (6.21) \end{aligned}$$

For an illustration, see Fig. 6.4.

The effect of modified interactions on the one-triplet dispersion is discussed in the strong-coupling limit $J_{\mathrm{L}} \ll J_{\mathrm{R}}$ by projecting on the one-triplet subspace. Therefore, all terms contained in H_0 destroying or creating two triplet excitations are neglected. For the later application of diagrammatic techniques, it is useful to map the spin operators onto so-called bond-boson operators $s_l^{(\dagger)}, t_{\alpha,l}^{(\dagger)}$; $\alpha = x, y, z$ [98,335,336]. $s_l^\dagger$ creates a singlet on the lth rung out of the vacuum state $|\,0\rangle$ and $t_{\alpha,l}^\dagger$ creates a triplet excitation with orientation α, respectively. The exact representation of $S_{l,1(2)}^\alpha$, $\alpha = x, y, z$, in terms of bond-boson operators reads [98]

$$S_{l,j}^\alpha = (1/2)\{\pm s_l^\dagger t_{\alpha,l} \pm t_{\alpha,l}^\dagger s_l - i\epsilon_{\alpha\beta\gamma} t_{\beta,l}^\dagger t_{\gamma,l}\}\,. \tag{6.22}$$

The plus sign corresponds to $j = 1$ and the minus sign to $j = 2$; j labeling the leg. To avoid unphysical double occupancies one has to impose the local constraint

$$s_l^\dagger s_l + t_{\alpha,l}^\dagger t_{\alpha,l} = 1\,. \tag{6.23}$$

Summation over repeated indices is implied in this equation and in the following ones. Projecting onto the one-triplet subspace and thereby applying a Holstein-Primakoff type of approximation $s_l = s_l^\dagger \approx 1$ [335,337] results in the effective Hamiltonian

$$H_{0,\mathrm{eff}} = J_{\mathrm{R}} \sum_l t_{\alpha,l}^\dagger t_{\alpha,l} + \frac{J_{\mathrm{L}}}{2} \sum_l (t_{\alpha,l+1}^\dagger t_{\alpha,l} + \mathrm{H.c.})\,, \tag{6.24}$$

where we have dropped irrelevant additive constants. $H_{0,\mathrm{eff}}$ is diagonalized by a Fourier transformation $t^\dagger_{\alpha,l} = (1/\sqrt{N})\sum_k e^{-ikl} t^\dagger_{\alpha,l}$ leading to

$$H_{0,\mathrm{eff}} = \sum_k \epsilon_k t^\dagger_{\alpha,k} t_{\alpha,k} \tag{6.25}$$

and the dispersion relation of one-triplet excitations is [283]

$$\epsilon_k = J_\mathrm{R} + J_\mathrm{L}\cos(k)\,. \tag{6.26}$$

The perturbations δH_n caused by modifications of the exchange couplings are expressed in terms of bond-boson operators as follows

$$\delta H_n = \frac{1}{N}\sum_{k,k_1} v_{\mathrm{R(L)}}(k,k_1)\, t^\dagger_{\alpha,k} t_{\alpha,k_1} \tag{6.27}$$

with the potentials $v_{\mathrm{R(L)}}(k,k_1)$ given by

$$\begin{aligned} v_\mathrm{R}(k,k_1) &= \delta J_\mathrm{R}\, e^{il_n\Delta k} && (6.28)\\ v_\mathrm{L}(k,k_1) &= \frac{\delta J_\mathrm{L}}{4}(e^{il_n\Delta k}e^{ik_1} + e^{-il_n\Delta k}e^{-ik})\,. && (6.29)\end{aligned}$$

$\Delta k = k_1 - k$ is the momentum transferred in a scattering process. All together, the effective Hamiltonian takes the form

$$H_\mathrm{eff} = H_{0,\mathrm{eff}} + H'_\mathrm{eff}\,; \quad H'_\mathrm{eff} = \sum_{n=1}^{N_\mathrm{imp}} \delta H_n. \tag{6.30}$$

6.2.3 Single-impurity case: T-matrix

Several methods exist to treat the single-impurity problem exactly. First, Schrödinger's equation in real space may be written as:

$$\left[I - G^0(E)\, H'_\mathrm{eff}\right]|\psi\rangle = 0\,. \tag{6.31}$$

A solution of this equation for the eigenenergies and eigenfunctions of states above or below the one-triplet band is straightforward. A general discussion can be found in [338], while the application to the current problem is outlined in Refs. [vi, 339]. The advantage of the real-space calculation is that not only the single-impurity problem can be analyzed, but also the case of *impurity clusters* can be treated analogously. Furthermore, one also obtains direct information about the impurity wave-function. In this section, we prefer to only quote the results derived in Refs. [vi, 339], and the discussion will rather focus on how the single-impurity bound states can be calculated using diagrammatic techniques.

The main technical problem is that disorder destroys translational invariance, implying that working in a momentum-space representation lacks the advantage of a diagonal representation. Nevertheless, the one-impurity problem can be formulated in k-space, although, in principle, the one-triplet Green's-function $G_{kk'}(E)$ is not diagonal in k. The Green's function $G^s_{kk'}(E)$ of the impurity problem can be expressed in terms of the free Green's function $G^0_k(E) = 1/(E - \epsilon_k)$ and the T-matrix

$$G^s_{kk'}(E) = \delta_{kk'} G^0_k(E) + G^0_k(E)\, T_{kk'}\, G^0_{k'}(E) \tag{6.32}$$

where the T-matrix is given by

$$T_{kk'} = \frac{2\, V_{k'}}{I - (1/N) \sum_{k''} V_{k''}\, G^0_{k''}(E)} \,. \tag{6.33}$$

We are mainly interested in the diagonal part T_{kk} of the T-matrix. In the case of onsite disorder, i.e., a rung impurity, V_k is given by

$$V_k = v_{\mathrm{R}}(k,k) = \delta J_{\mathrm{R}} \,, \tag{6.34}$$

which is independent of momentum. For an impurity located on a leg site, all quantities in Eq. (6.32) become 2 × 2 matrices, indicated by an underscore, since the modified coupling connects two sites. We then have:

$$\underline{V}_k = \frac{\delta J_{\mathrm{L}}}{2} \begin{pmatrix} \cos(k) & 1 \\ 1 & \cos(k) \end{pmatrix} . \tag{6.35}$$

Equations (6.34) and (6.35) follow directly from Eqs. (6.28) and (6.29). The free Green's function matrix in Eq. (6.33) is $\underline{G}^0_k(E) = G^0_k(E)\underline{I}$, where $\underline{I}$ is the 2×2 unit matrix.

The positions of the bound states are determined by the zeros of the determinant of the denominator of the T-matrix, and we find for the eigenenergies of the single-rung impurity problem:

$$E_{1,\mathrm{R}} = J_{\mathrm{R}} \pm \sqrt{J_{\mathrm{L}}^2 + (\delta J_{\mathrm{R}})^2}; \quad \delta J_{\mathrm{R}} \gtrless 0 \,. \tag{6.36}$$

The plus(minus) sign in Eq. (6.36) corresponds to $\delta J_{\mathrm{R}} > 0$ ($\delta J_{\mathrm{R}} < 0$). Therefore, a bound state in the spin gap, i.e., below the original one-triplet band, appears for $\delta J_{\mathrm{R}} < 0$. Conversely, for $\delta J_{\mathrm{R}} > 0$, there is an anti-bound state above the one-triplet band.

For the single leg-impurity problem $\delta J_R = 0, \delta J_L \neq 0$, one arrives at:

$$E_{1,\mathrm{L}} = J_{\mathrm{R}} \pm \frac{J_{\mathrm{L}} + \frac{\delta J_{\mathrm{L}}}{2}(1 + \frac{\delta J_{\mathrm{L}}}{4 J_{\mathrm{L}}})}{1 + \frac{\delta J_{\mathrm{L}}}{2 J_{\mathrm{L}}}}; \quad \delta J_{\mathrm{L}} > 0 \,. \tag{6.37}$$

For $\delta J_{\mathrm{L}} > 0$, there are always both a bound and an anti-bound state. On the other hand, note that there are no states outside the one-triplet band for $-4J_{\mathrm{L}} < \delta J_{\mathrm{L}} < 0$ [339]; instead, one expects the appearance of resonant modes inside the band [see Sec. 6.2.4, Fig. 6.8(f)]. Finally, for a strong ferromagnetic coupling $\delta J_L < -4J_L$, Eq. (6.37) again has two solutions; however, we will restrict the discussion to the case of antiferromagnetic couplings. These results, i.e., Eqs. (6.36) and (6.37) agree with the real-space computation outlined in Refs. [vi, 339]. The T-matrix approach is well suited to be extended to the case of small, but finite concentrations providing approximative analytical results in the thermodynamic limit.

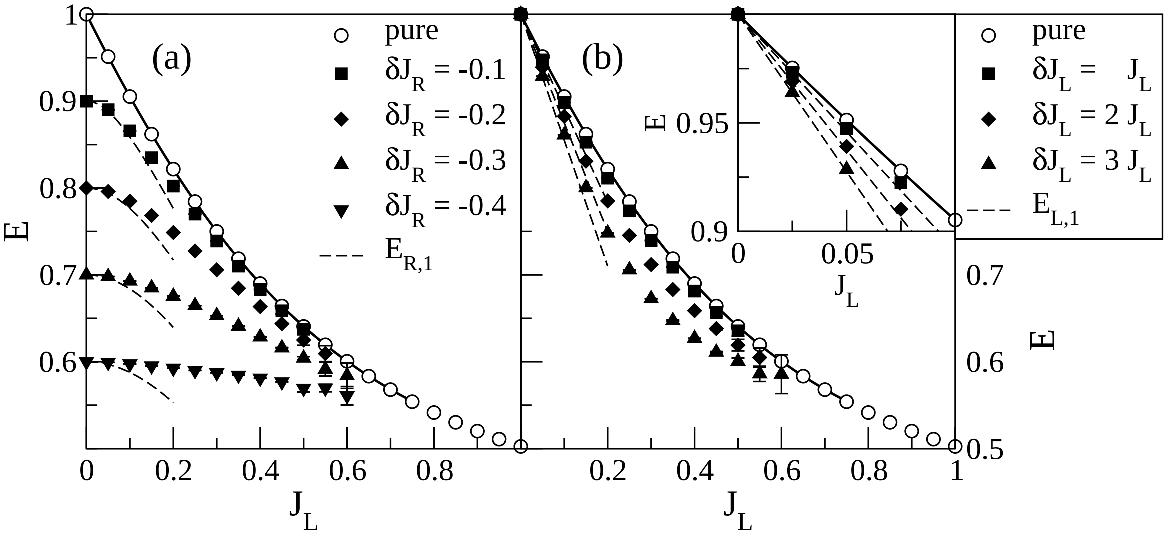

Figure 6.5: Comparison of the analytical results for the excitation energy E of the lowest level with a Lanczos study [vi], done for the full spin ladder Hamiltonian (6.19). (a): One rung impurity $J'_{\mathrm{R}} = J_{\mathrm{R}} + \delta J_{\mathrm{R}}$. (b): One leg impurity $J'_{\mathrm{L}} = J_{\mathrm{L}} + \delta J_{\mathrm{L}}$. In all cases, the normalization is fixed to $J_{\mathrm{R}} = 1$. Symbols are obtained by extrapolation of Lanczos diagonalization on finite systems. Open circles are for the pure system ($\delta J_{\mathrm{R}} = 0$ and $\delta J_{\mathrm{L}} = 0$) and correspond to the spin gap; the solid line is a [7,6] Padé approximant to the 13th order strong-coupling series from Ref. [340] for the spin gap of the pure ladder. Dashed lines display the analytical result for the position of the bound state in the effective Hamiltonian Eq. (6.30), namely Eq. (6.36) [panel (a)] and Eq. (6.37) [panel (b)].

Comparison with exact diagonalization (Lanczos)

So far we have seen that for both locations of single impurities, mid-gap states may appear. The results derived in first order in $J_{\mathrm{L}}/J_{\mathrm{R}}$ are now compared to a Lanczos study of the full Hamiltonian (6.19) with either one modified leg or rung coupling [vi]. The systems analyzed include ladders with $N = 4, 6, 8, 10, 12,$ and 14 rungs. The eigenenergies obtained on finite systems were then extrapolated to the thermodynamic limit by application of the Vanden-Broeck-Schwartz-algorithm [276]. For details, see Sec. IIIC of Ref. [vi]. Results of such extrapolations are shown in Fig. 6.5. There, the eigenenergy E of the lowest two states is plotted versus J_{L} for $\delta J_{\mathrm{R}} \neq 0, \delta J_{\mathrm{L}} = 0$ in Fig. 6.5(a) and for $\delta J_{\mathrm{R}} = 0, \delta J_{\mathrm{L}} \neq 0$ in Fig. 6.5(b). The open symbols in both panels are the spin gap of the pure ladder. Its value is expected to be independent of the presence of a single impurity if the extrapolation to $N \to \infty$ is taken [vi]. The full symbols are the energies of the impurity-induced bound state, while the dashed lines show $E_{1,\mathrm{R}}$ and $E_{1,\mathrm{L}}$ from Eqs. (6.36) and (6.37). While a good quantitative agreement between the Lanczos results and the perturbative calculation is found for small $J_{\mathrm{L}} \lesssim 0.1$, the qualitative behavior is still correctly described for larger values of J_{L}. Note that the extrapolation of the numerical data becomes uncertain for leg couplings of the order of $J_{\mathrm{L}} \sim 1$, and it is not obvious whether the bound state survives for large J_{L} or whether it will merge into the band [vi]. The Lanczos study clearly confirms the presence of the bound states below the one-triplet band in a wide parameter range. The fair agreement motivates us to extend the strong-coupling approximation to the case of finite concentrations of impurities, which is studied in the next section.

6.2.4 Finite impurity concentrations

In this section, binary distributions of impurities are studied:

$$P(J_l) = c_{\mathrm{R,L}}\delta(J_l - J'_{\mathrm{R,L}}) + (1 - c_{\mathrm{R,L}})\delta(J_l - J_{\mathrm{R,L}})\,. \tag{6.38}$$

In both cases, i.e., $c_{\mathrm{R}} > 0$ and $c_{\mathrm{L}} > 0$, the perturbations are assumed to be uncorrelated. Furthermore, the concentrations of rung impurities c_{R} and of leg impurities c_{L} are independent. Note that in the case of impurities on the legs, we set $c_{\mathrm{L}} = 1$ if all $2N$ couplings are modified.

Before turning to the discussion of the methods and the results, it is instructive to list the limiting cases: (i) the pure system ($c_{\mathrm{R}} = c_{\mathrm{L}} = 0$); (ii) the single-impurity case (see Sec. 6.2.3); and (iii) the case $c_{\mathrm{R}} = c_{\mathrm{L}} = 1$ where all couplings are equal to $J_{\mathrm{R}} + \delta J_{\mathrm{R}}$ or $J_{\mathrm{L}} + \delta J_{\mathrm{L}}$, respectively. In the latter case and for $\delta J_{\mathrm{R}} \neq 0, \delta J_{\mathrm{L}} = 0$, a one-triplet band with the dispersion

$$E_k = (J_R + \delta J_R) + J_{\mathrm{L}} \cos(k)$$

will result, i.e., its center is shifted by δJ_R with respect to the center of the original band for $c_{\mathrm{R}} = 0$. Therefore, the single-impurity (anti-) bound state should develop into a dispersive band as the concentration increases while for $\delta J_{\mathrm{R}} < 0$, the center $\epsilon(c)$ of the band lies in the interval [compare Eq. (6.36)]

$$J_{\mathrm{R}} - \sqrt{J_{\mathrm{L}}^2 + (\delta J_{\mathrm{R}})^2} < \epsilon(c) < J_{\mathrm{R}} + \delta J_{\mathrm{R}}\,. \tag{6.39}$$

An analogous scenario arises for $\delta J_{\mathrm{R}} > 0$.

For $\delta J_{\mathrm{R}} = 0, \delta J_{\mathrm{L}} > 0$, the triplet dispersion in the limit of $c_{\mathrm{L}} = 1$, reads

$$E_k = J_{\mathrm{R}} + (J_{\mathrm{L}} + \delta J_{\mathrm{L}}) \cos(k)\,. \tag{6.40}$$

Thus, the bound and anti-bound states appear symmetrically with respect to the center of the original band. On increasing the concentration c_{L}, additional impurity levels will appear and eventually, they will merge in the original band. Finally, there will be one broadened band possessing a bandwidth of $(J_{\mathrm{L}} + \delta J_{\mathrm{L}})$. The combined analytical and numerical analysis to be presented in the next section validates this picture.

In analogy to Secs. 6.2.2 and 6.2.3 we will concentrate on the single-triplet subspace. Apart from integrating out the singlet, the hardcore constraint Eq. (6.23) is automatically satisfied within this approximation, i.e., first-order perturbation theory in $J_{\mathrm{L}}/J_{\mathrm{R}}$.

Diagrammatic techniques

Based on a diagrammatic expansion of the one-triplet Green's function in the presence of impurities, a number of useful methods exist to obtain approximate results for the self-energy $\Sigma(E)$. First, we briefly comment on the low-concentration approximation and second, the coherent-potential approximation is introduced.

Low-concentration approximation (LCA) - Technically, the key ingredient is to perform an impurity-averaging, i.e., the Green's function is sampled over many impurity configurations by varying the sites of all impurities at a given concentration. As a main consequence of the

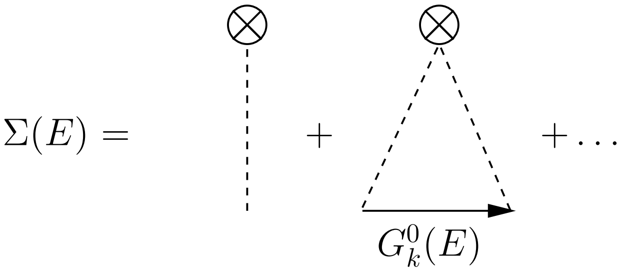

Figure 6.6: Sketch of the diagrammatic expansion of the self-energy $\Sigma(E)$ in the low-concentration limit. $G^0_k(E) = 1/(E - \epsilon_k)$ is the free one-triplet Green's function.

averaging procedure translational invariance is restored allowing one to express the Green's function in terms of a Dyson equation. The formalism is explained in detail in standard textbooks [341] and review articles [342]. A detailed discussion of this technique can also be found in Ref. [231], where a two-dimensional square lattice antiferromagnet with impurities was studied.

Following Ref. [341], the Green's function may be written as:

$$G_k(E) = \frac{1}{E - \epsilon_k - c_{\mathrm{R[L]}}\Sigma(E)}\,. \tag{6.41}$$

Keeping only terms linear in $c_{\mathrm{R[L]}}$ implies that the self-energy $\Sigma(E)$ is equal to the T-matrix of the one-impurity problem derived in Sec. 6.2.3. The diagrammatic expansion of the self-energy in the low-concentration approximation is sketched in Fig. 6.6. In the case of $c_\mathrm{L} > 0$, all quantities in Eq. (6.41) become 2×2 matrices again.

The spectral function $A_k(E) = -(1/\pi)\mathrm{Im}G_k(E)$ is plotted in Fig. 6.7 for (a) $J_\mathrm{L} = 0.1, \delta J_\mathrm{R} = -0.1, c_\mathrm{R} = 0.01$ and (b) for $J_\mathrm{L} = 0.1, \delta J_\mathrm{L} = 0.5, c_\mathrm{L} = 0.01$. In accordance with the results of Sec. 6.2.3 one finds one bound state in case (a) and a bound and an anti-bound state in case (b). Figure 6.7 further reveals that first, the impurity levels exhibit a small dispersion and second, the spectral weight is concentrated around $k = \pi$ for the bound states while it vanishes in the center of the zone, and vice-versa for the anti-bound states.

Coherent-potential approximation (CPA) - The coherent-potential approximation allows one to interpolate between the two limits of $c = 0$ and $c = 1$. Here, we apply this method to the case of $\delta J_\mathrm{R} < 0, \delta J_\mathrm{L} = 0$, i.e., $c_\mathrm{R} > 0$ and $c_\mathrm{L} = 0$. The self-energy is obtained from a self-consistent solution of the equation [342]:

$$\Sigma(E) = \frac{c_\mathrm{R}\,\delta J_\mathrm{R}}{1 - G(E)\,[\delta J_\mathrm{R} - \Sigma(E)]}\,. \tag{6.42}$$

Rather than deriving this equation,[3] some important features of this method are mentioned: (i) the self-energy is symmetric under exchange of host and impurity sites, i.e., c_R and $1 - c_\mathrm{R}$ and the respective replacement of the coupling constants; and (ii) it gives qualitatively correct results for the density of states for intermediate concentrations. Note that in contrast to the low-concentration approximation [see, e.g., Fig. 6.7(a)], the CPA does not lead to a sharp peak in the density of states at the position of the impurity level even for low concentrations. This can, for example, be seen in Fig. 6.8(b) for $c_\mathrm{R} = 0.1$. It has been checked that in both

---

[3] See Ref. [342] for details.

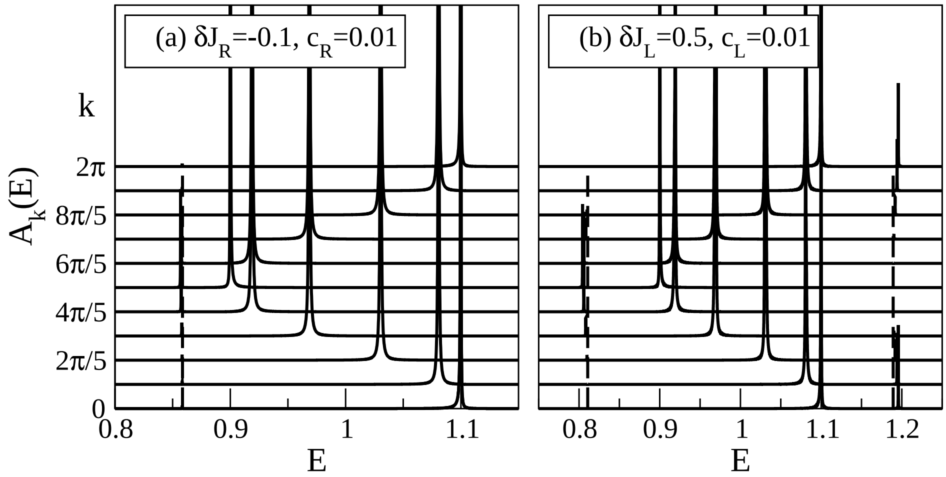

Figure 6.7: Spectral function $A_k(E)$ in low-concentration approximation (LCA) for (a) perturbed rung couplings with $\delta J_{\rm R} = -0.1$, $c_{\rm R} = 0.01$; (b) perturbed leg couplings with $\delta J_{\rm L} = 0.5$, $c_{\rm L} = 0.01$. The dashed lines mark the positions of the (anti-) bound states from Eqs. (6.36) and (6.37). $J_{\rm R} = 1$ and $J_{\rm L} = 0.1$ in both cases. See Ref. [vi].

diagrammatic approaches, the total weight in the impurity levels is the same and that it grows linearly with the impurity concentration, as expected.

Comparison with numerical impurity averaging

Now we compare the analytical results with a numerical diagonalization of the effective Hamiltonian (6.30) on large systems, sampled over typically a few thousand random realizations at fixed concentration. The effective Hamiltonian $H_{\rm eff}$ is diagonalized on finite systems with $N = 10^3$ rungs for different choices of impurity concentrations c for both types of bond impurities. The density of states (DOS) is obtained from binning the eigenvalues, the bin-width of typically $\Delta E \sim 10^{-3} J_{\rm R}$ determining the resolution in Figs. 6.8 and 6.9. The numerical data are taken from Refs. [vi, vii, 339].

Results are shown for $J_{\rm L} = 0.1, \delta J_{\rm R} = -0.1$ in Fig. 6.8 (panel (a): $c_{\rm R} = 0.01$; (b): $c_{\rm R} = 0.1$; (c): $c_{\rm R} = 0.3$). According to Eq. (6.36), the position of the single-impurity level is $E_{1,{\rm R}} = 0.8586 J_{\rm R}$. The following features are observed: (i) Upon increasing concentration, additional peaks appear in the vicinity of the one-impurity level. They stem from impurity clusters, i.e., impurities occupying neighboring sites. (ii) The bound state level develops into a band centered around $J_{\rm R} + \delta J_{\rm R} = 0.9$ as a function of concentration $c_{\rm R}$. Notice that larger concentrations $c_{\rm R} > 0.5$ are conveniently realized by setting $c_{\rm R} \to 1 - c_{\rm R}, J_{\rm R} \to J_{\rm R} + \delta J_{\rm R}$, and $\delta J_{\rm R} \to -\delta J_{\rm R}$. (iii) Inside the original band, the curve is not smooth, but displays small oscillations. These features are neither due to finite-size effects nor due to low statistics. The origin of these oscillations can also be related to the effect of impurity clusters, see Sec. IVC of Ref. [vi] and Ref. [339].

Let us now comment on the comparison of the numerical with the analytical results. By integrating $A_k(E)$ over the momentum k, the density of states $n(E)$ is obtained. Results from the LCA are compared to the numerical impurity averaging in the case of $J_{\rm L} = 0.1, \delta J_{\rm R} = -0.1, c_{\rm R} = 0.01$ in Fig. 6.8(a). Both approaches agree well with regard to the position of the

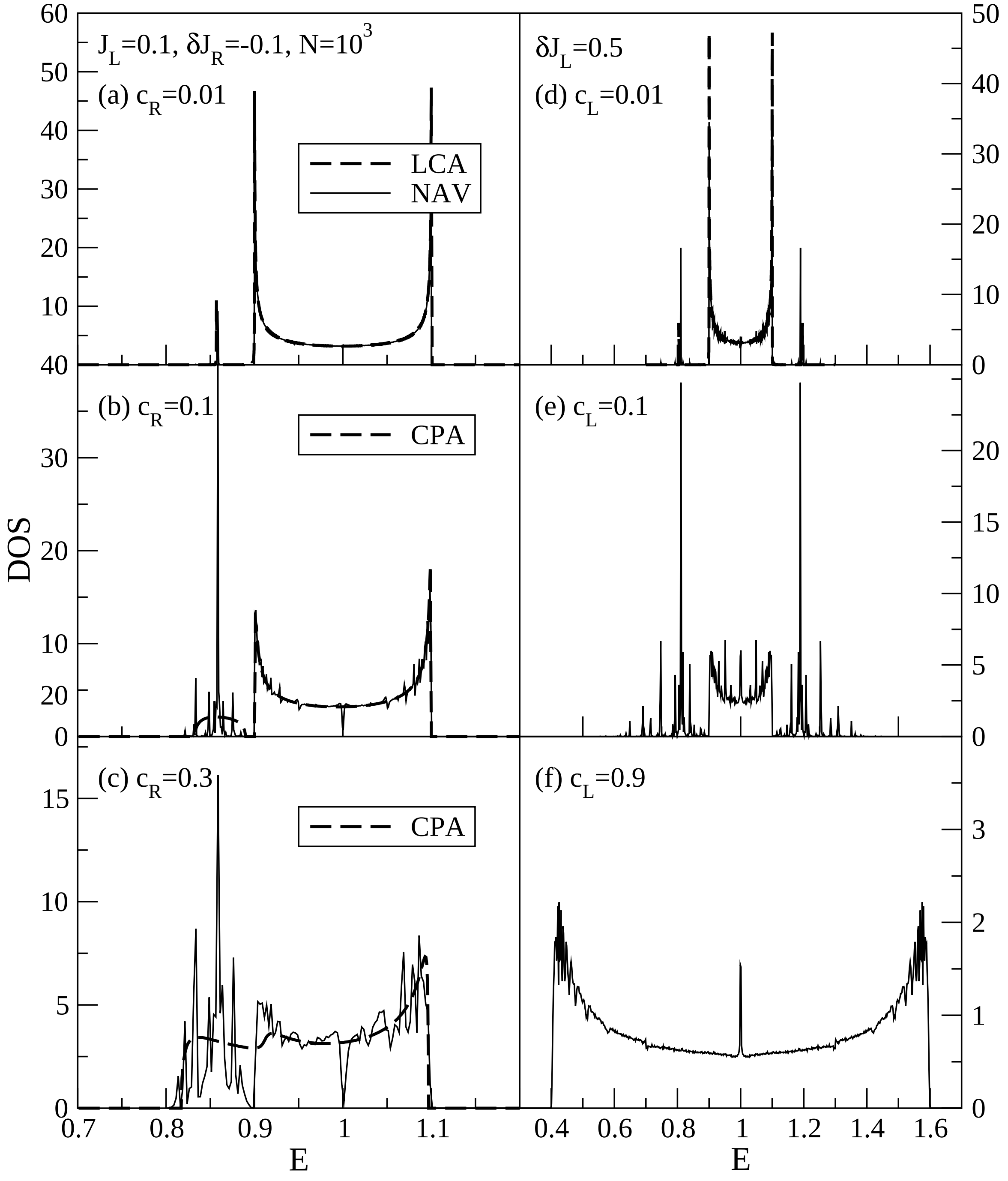

Figure 6.8: Density of states (DOS) at finite concentrations of modified rung couplings $J'_{\rm R}$ [$\delta J_{\rm R} = -0.1$, panel (a)–(c)] and of modified leg couplings [$\delta J_{\rm L} = 0.5$, panel (d)–(f)]. The figure contains numerical data (NAV, solid line) for spin ladders with $N = 10^3$ rungs and $J_{\rm R} = 1, J_{\rm L} = 0.1$ [panel (a)–(f)]. In detail, the parameters are: (a) $c_{\rm R} = 0.01$, (b) $c_{\rm R} = 0.1$, (c) $c_{\rm R} = 0.3$, (d) $c_{\rm L} = 0.01$, (e) $c_{\rm L} = 0.1$, (f) $c_{\rm L} = 0.9$. Dashed line in (a) and (d): Low-concentration approximation (LCA); in panel (b) and (c): CPA. (f): Note the resonance modes inside the band for $c_{\rm L} = 0.9$; the case shown here is equivalent to $J_{\rm L} = 0.6$, $\delta J_{\rm L} = -0.5 < 0$, and $c_{\rm L} = 0.1$. See Ref. [vi].

main impurity level. The comparison with the CPA for $c_{\mathrm{R}} = 0.1$ [Fig. 6.8(b)] and $c_{\mathrm{R}} = 0.3$ [Fig. 6.8(c)] shows that this approach gives qualitatively reasonable results even at fairly large concentrations such as $c_{\mathrm{R}} = 0.3$ or $c_{\mathrm{R}} = 0.5$ (not shown in the figures, see Ref. [vii]). At $c_{\mathrm{R}} = 0.3$, the impurity levels and the original band start to merge.

For a finite concentration of leg couplings, the numerical results confirm the qualitative expectations. The data are shown in Fig. 6.8 for $J_{\mathrm{L}} = 0.1, \delta J_{\mathrm{L}} = 0.5$ (panel (d): $c_{\mathrm{L}} = 0.01$; (e): $c_{\mathrm{L}} = 0.1$; (f): $c_{\mathrm{L}} = 0.9$). For the sake of clarity, note that the possible impurity configurations are: (i) one modified coupling on one leg, connecting, e.g., rungs l and $l + 1$; and (ii) both couplings between rungs l and $l + 1$ modified. Both cases are taken into account in the numerical implementation.

The impurity levels occur symmetrically with respect to the center of the band. On increasing the concentration c_{L}, the original band widens and eventually includes all impurity levels as can be seen in Fig. 6.8(f) for $c_{\mathrm{L}} = 0.9$. The influence of impurities is also visible as resonance modes inside the band. Note that the last case is equivalent to $J_{\mathrm{L}} = 0.6$, $\delta J_{\mathrm{L}} = -0.5$, and $c_{\mathrm{L}} = 0.1$. Comparing to the LCA from Eq. (6.41) for the case of $J_{\mathrm{L}} = 0.1, \delta J_{\mathrm{L}} = 0.5, c_{\mathrm{L}} = 0.01$, shown in Fig. 6.8(d), we see that the positions of the highest peaks seen in the numerical data and the analytical result almost coincide, similar to the case shown in Fig. 6.8(a).

In summary, the analytical approaches give fair results for the overall structure of the density of states even at large concentrations as exemplified in the case of $\delta J_{\mathrm{R}} < 0, \delta J_{\mathrm{L}} = 0, c_{\mathrm{R}} = 0.3$.

Impurity cluster

In the diagrammatic description, the effects of impurity clusters are not taken into account [342]. The presence of impurity clusters, such as (RR) or $(R0R)$ [see Fig. 6.4(b)], lead to further energy levels outside the one triplet band, which are discrete for finite systems. Such levels can be seen in Fig. 6.8(a)–(f). By solving Schrödinger's equation (6.31) in real space for the effective model containing one cluster, the respective eigenenergies can be derived [vi, vii, 339]. To illustrate this matching of certain peaks visible in the DOS with impurity clusters, we consider the example of both finite concentrations $c_{\mathrm{R}} > 0$ and $c_{\mathrm{L}} > 0$ for the following choice of parameters: $N = 10^3, c_{\mathrm{R}} = 0.1, c_{\mathrm{L}} = 0.05, J_{\mathrm{L}} = 0.2, \delta J_{\mathrm{R}} = -0.2, \delta J_{\mathrm{L}} = 0.3$. Numerical results are shown in Fig. 6.9. The spectrum consists of the remnant of the one-triplet band and several discrete peaks for $E > 1.2$ and $E < 0.8$. Some of these peaks are labeled by letters which denote certain impurity clusters as listed in the legend of Fig. 6.9. For instance, (LLL) stands for a cluster of three leg impurities between four adjacent rung sites. Only one of the legs is modified between each pair of two neighboring rung sites. Note that within the effective model, there is no difference between the eight possible distributions of these three impurities on the six leg couplings existing between four rungs.

This comparison shows that details of the one-triplet DOS of the effective disordered Hamiltonian (6.30) can be interpreted. At present, it remains unclear whether the spiky structure outside the one-triplet band observed for small concentrations will survive in the thermodynamic limit or whether a completely smooth curve will arise. For the system sizes investigated, i.e., $N \lesssim 10^4$, the peak structure is very stable.

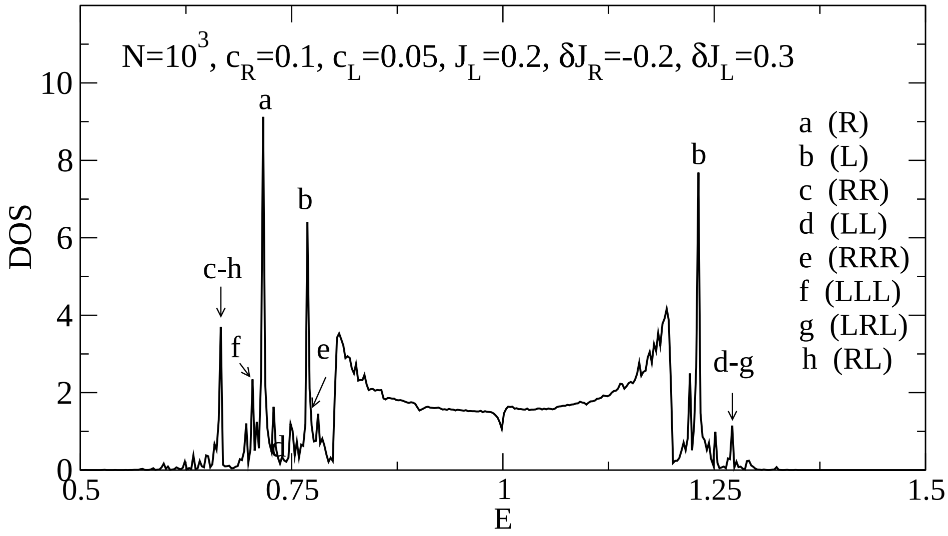

Figure 6.9: Numerical impurity-averaged results for bond-impurities on both rungs and legs. The letters label peaks originating from certain impurity clusters as indicated in the legend. See text and Fig. 6.4 for more details. See Ref. [vii].

6.2.5 Summary

In this section, we have addressed the issue of bond disorder in two-leg spin ladders. The problem has been treated by a mapping onto bond-boson operators and a subsequent projection on the one-triplet subspace, equivalent to first-order perturbation theory in $J_\mathrm{L}/J_\mathrm{R}$. It has been shown that for certain choices of model parameters, bound states appear below the one-triplet band. Their eigenenergies have been derived from the poles of the T-matrix. Furthermore, binary distributions of bond impurities on either rung or leg sites have been studied using diagrammatic techniques, focusing on the density of states. The comparison with numerical-impurity averaging has shown that in particular CPA is well suited to tackle the problem of finite impurity concentrations for the given one-dimensional problem.

Extensions of this study comprise the computation of observable quantities such as the structure factor. Furthermore, transport properties of a disordered *free* boson gas can be investigated along the lines of Sec. 6.1. The most important correlation that needs to be taken into account is the hardcore constraint (6.23) [see, e.g., Refs. [322, 323, 343]]. In the presence of disorder, this constraint can be ensured by an explicit numerical construction of many-triplet states, allowing one to go beyond the strong-coupling limit.[4]

---

[4] For an analytical construction of two-triplet states, see, e.g., Chapter 2 of Ref. [344].

Chapter 7

Summary and Conclusion

In this thesis, transport properties of low-dimensional spin systems were studied theoretically. A strong motivation for this work came from recent thermal transport experiments which gave profound evidence that magnetic excitations of low-dimensional spin systems contribute significantly to the thermal conductivity. Most of the experimental results were analyzed using phenomenological approaches in the literature. As an example, a Boltzmann-type of equation was chosen to estimate the magnetic mean-free paths of Zn-doped $\mathrm{La_2CuO_4}$ from the experimental data for the thermal conductivity [71]. Interestingly, the mean-free paths scale linearly with the inverse Zn-content, which is a measure of the distance of Zn-dopants [71].

The main part of this work was devoted to thermal and spin transport of translationally invariant one-dimensional spin models. This pertains to the integrable spin-1/2 XXZ chain on the one hand, and to several nonintegrable systems on the other hand. Detailed results were obtained for the temperature and field-dependence of the transport coefficients. In this summary we emphasize the main aspects, while the details are contained in the concluding sections of Chapters 4, 5, and 6.

The transport properties of the XXZ chain were investigated with complementary methods. While exact diagonalization provides for converged results in the high-temperature limit, conformal field theory as well as mean-field theory allow one to compute the transport coefficients at low temperatures. Numerically, the Hamiltonian of chains with up to twenty sites was completely diagonalized, which is possible after exploiting symmetries of the models. Transport in the XXZ model is characterized by finite Drude weights in the thermodynamic limit [61], leading to diverging conductivities. As a main result, the study elucidated the dependence of the thermal Drude weight on temperature, magnetic field, and exchange anisotropy. Perfect agreement with other theoretical studied was found [78, 82, 92], and in a wide temperature range, the thermal Drude weight could be obtained in the thermodynamic limit. An analogous analysis was performed for the spin Drude weight. At zero magnetic field, the finite-size scaling of this quantity is of particular interest, since until now no proof has been found for a finite spin Drude weight in the thermodynamic limit. The numerical results of this work agree with previous theoretical contributions to this field [75,84,85,87,89], as they confirm the conclusion of a finite spin Drude weight in the massless regime. This also includes the $SU(2)$-symmetric Heisenberg chain, for which the existence of a nonzero finite-temperature Drude weight is controversially debated in the literature [75,84–90,152]. Further aspects of the finite-size scaling, the temperature, and the field dependence were discussed in Chapter 4. Finally, ratios of transport coefficients are of particular interest. The validity of a Wiedemann-Franz type of relation could be established in the low-temperature limit for a large part of the phase diagram of the XXZ chain.

As an extension to the present work, the methods can be applied to another integrable quantum model as well, the one-dimensional Hubbard model. Due to its integrability, this system also possesses finite Drude weights [61]. In this case, four types of transport exist: particle, charge, energy, and spin transport. Several aspects of finite-temperature transport could be of interest: first, a theory for the dependence of the thermal Drude weight on temperature, on filling, and on the onsite Coulomb correlation is lacking and second, the knowledge of ratios of the transport coefficients is important for the interpretation of experimental results (see, e.g., Ref. [278]).

Stimulated by the experimental observation of extremely large magnetic mean-free paths in several quasi low-dimensional materials [7, 8, 14], some authors have speculated about possible ballistic thermal transport of nonintegrable spin models such as frustrated chains or spin ladders [54–56, 58]. As a major result of this work, it was shown that the conclusion of ballistic transport, i.e., finite Drude weights in the thermodynamic limit, is clearly not supported by the finite-size scaling analysis of numerical data, neither for spin, nor for thermal transport. Rather, the opposite conclusion must be favored for all systems investigated, which includes the two-leg spin ladder, the dimerized chain, and the frustrated chain. Other recent numerical studies arrive at the same conclusion [57, 96]. More generally, the picture of dissipative intrinsic transport of nonintegrable spin models is corroborated by field-theoretical arguments along the lines of Refs. [59, 95]. While the Drude weights scale to zero as a function of system size, the regular parts of both the spin and the thermal conductivity exhibit very small finite-size effects in the high-frequency and high-temperature regime. This indicates that the regular parts are the relevant quantities which describe the intrinsic transport properties of nonintegrable spin systems. Results were presented for the frequency dependence of the thermal conductivity for the frustrated chain, the dimerized chain, and the two-leg ladder. In the first case, the focus was on a comparison of the massless and the massive regime. For the dimerized chain, the limit of weakly coupled dimers is interesting, since interactions of the elementary excitations are suppressed. In this limit, a comparison of mean-free paths extracted from the numerical results and analytical computations would allow one to validate or invalidate a quasi-particle picture for thermal transport in dimerized systems. This would also establish the first direct comparison of independent analytical and numerical calculations for the thermal conductivity. The most relevant model with respect to experiments is the spin ladder, for which the dc-thermal conductivity can be estimated from the numerical results. Comparing the values with experimental data for $\mathrm{La_5Ca_9Cu_{24}O_{41}}$ [8], one finds the same order of magnitude. This implies that transport in the telephone-number compounds is largely determined by intrinsic scattering, while external scattering is likely to be only a weak perturbation. This picture agrees with the analysis of experimental data in terms of phenomenological expressions [153].

Apart from translationally invariant spin models, bond disordered XY chains and spin ladders were analyzed in Chapter 6. Spin-1/2 XY chains are equivalent to free, spinless fermions; thus the transport coefficients can be written in terms of the single-particle eigenenergies and -states [307]. This allows one to study very large system sizes of the order of 10^4 sites numerically. First results for the spin and the thermal conductivity have been presented for three different types of off-diagonal disorder: the single-impurity case, binary distributions of impurities, and a Gaussian distribution of impurities. While the Drude weights vanish for any type of randomness, the dc-conductivities are finite in all three cases. An extension of the current study could pertain to a refined analysis of the scaling with system size, the dependence on temperature, and the inclusion of diagonal disorder.

As a consequence of disorder, both localization of the wave-function and bound states may result. For the cases of diagonal and off-diagonal disorder in spin ladders, it was demonstrated that bound states appear within the spin gap. The study of the bound state structure and the density of states both for the single-impurity problem and for finite impurity concentrations was based on a mapping on bond-boson operators [98] and a subsequent projection onto the single-triplet subspace. The methods applied to this problem were first, diagrammatic techniques such as the coherent-potential approximation and second, exact diagonalization. The results are of relevance for doping experiments with spin ladder materials in the strong-coupling limit. The approach can easily be extended to the case of bond-disordered three-dimensional dimer systems such as $TlCuCl_3$ and $KCuCl_3$ (see, e.g., Refs. [345, 346]).

In conclusion, this work has provided many numerical results which may serve as a basis for future analytical studies of transport properties. In general, the theoretical understanding of intrinsic transport properties of low-dimensional spin systems has recently been improved by several theoretical contributions; however, many important issues have not yet fully been elucidated. In particular, a realistic modeling of materials including external channels of scattering is required. While an exact diagonalization study reaches its limitations if the Hilbert space is enlarged by additional degrees of freedom, promising results for magnetic transport including a coupling to phonons were recently obtained analytically using either the Boltzmann equation [158] or a hydrodynamic description [59]. One problem for which theoretical studies are very rare is thermal transport in two-dimensional spin systems on different topologies. Such a study would be of relevance for the interpretation of the transport experiments done for cuprates such as La_2CuO_4 [ii, 2], and might be accessible by a combination of numerical and analytical techniques.

The large number of open questions in the field of transport of low-dimensional quantum systems arising both from theory and experiment guarantee that this field is very likely to receive much attention in the future, hopefully with some surprising physics to be discovered.

Bibliography

[1] H. K. Onnes, Akad. van Wetenschapen (Amsterdam) **14**, 818 (1911).

[2] Y. Nakamura, S. Uchida, T. Kimura, N. Motohira, K. Kishio, K. Kitazawa, T. Arima, and Y. Tokura, Physica C **185-189**, 1409 (1991).

[3] X. F. Sun, J. Takeya, S. Komiya, and Y. Ando, Phys. Rev. B **67**, 104503 (2003).

[4] R. Jin, Y. Onose, Y. Tokura, D. Mandrus, P. Dai, and B. C. Sales, Phys. Rev. Lett. **91**, 146601 (2003).

[5] M. Hofmann, T. Lorenz, K. Berggold, M. Grüninger, A. Freimuth, G. S. Uhrig, and E. Brück, Phys. Rev. B **67**, 184502 (2003).

[6] K. Kudo, S. Ishikawa, T. Noji, T. Adachi, Y. Koike, K. Maki, S. Tsuji, and K. Kumagai, J. of Low Temp. Phys. **117**, 1689 (1999).

[7] A. V. Sologubenko, K. Gianno, H. R. Ott, U. Ammerahl, and A. Revcolevschi, Phys. Rev. Lett. **84**, 2714 (2000).

[8] C. Hess, C. Baumann, U. Ammerahl, B. Büchner, F. Heidrich-Meisner, W. Brenig, and A. Revcolevschi, Phys. Rev. B **64**, 184305 (2001).

[9] K. Kudo, S. Ishikawa, T. Noji, T. Adachi, Y. Koike, K. Maki, S. Tsuji, and K. Kumagai, J. Phys. Soc. Jpn. **70**, 437 (2001).

[10] C. Hess, U. Ammerahl, C. Baumann, B. Büchner, and A. Revcolevschi, Physica B **312-313**, 612 (2002).

[11] C. Hess, H. ElHaes, B. Büchner, U. Ammerahl, M. Hücker, and A. Revcolevschi, Phys. Rev. Lett. **93**, 027005 (2004).

[12] A. V. Sologubenko, E. Felder, K. Gianno, H. R. Ott, A. Vietkine, and A. Revcolevschi, Phys. Rev. B **62**, R6108 (2000).

[13] A. V. Sologubenko, K. Gianno, H. R. Ott, A. Vietkine, and A. Revcolevschi, Phys. Rev. B **64**, 054412 (2001).

[14] A. V. Sologubenko, H. R. Ott, G. Dhalenne, and A. Revcolevschi, Europhys. Lett. **62**, 540 (2003).

[15] A. V. Sologubenko, S. M. Kazakov, H. R. Ott, T. Asano, and Y. Ajiro, Phys. Rev. B **68**, 094432 (2003).

[16] S. Lepri, R. Livi, and A. Politi, Phys. Rep. **377**, 1 (2003).

[17] X. Zotos and P. Prelovšek, *in: "Strong Interactions in Low Dimensions"*, chapter 11, Physics and Chemistry of Materials with Low-Dimensional Structures, Kluwer Academic Publishers, 2004, cond-mat/0304630.

[18] T. M. Rice, Z. Phys. B **103**, 165 (1997).

[19] E. Dagotto, Rep. Prog. Phys. **62**, 1525 (1999).

[20] E. Dagotto and T. M. Rice, Science **271**, 618 (1996).

[21] H.-J. Mikeska and A. K. Kolezhuk, Lect. Notes Phys. **645**, 1 (2004).

[22] U. Schollwoeck, to appear in Rev. Mod. Phys., cond-mat/0409292 (unpublished).

[23] M. Troyer, F. Alet, S. Trebst, and S. Wessel, AIP Conf. Proc. **690**, 156 (2003).

[24] H. G. Evertz, Adv. in Physics **52**, 1 (2003).

[25] N. Laflorencie and D. Poilblanc, Lect. Notes Phys. **645**, 227 (2004).

[26] H. Bethe, Z. Phys. **71**, 205 (1931).

[27] D. C. Cabra and P. Pujol, Lect. Notes Phys. **645**, 253 (2004).

[28] D. C. Johnston, M. Troyer, S. Miyahara, D. Lidsky, K. Ueda, M. Azuma, Z. Hiroi, M. Takano, M. Isobe, Y. Ueda, M. A. Korotin, V. I. Anisimov, A. V. Mahajan, and L. L. Miller, cond-mat/0001147 (unpublished).

[29] D. C. Johnston, R. K. Kremer, M. Troyer, X. Wang, A. Klümper, S. L. Bud'ko, A. F. Panchula, and P. C. Canfield, Phys. Rev. B **61**, 9558 (2000).

[30] A. Assa and A. Auerbach, *Interacting Electrons and Quantum Magnetism*, Springer-Verlag, Berlin Heidelberg New York, 1998.

[31] P. Fazekas, *Lecture Notes on Electron Correlations and Magnetism*, World Scientific Publishing Co. Pte. Ltd., Singapore, 1999.

[32] J. G. Bednorz and K. A. Müller, Z. Phys. B **64**, 189 (1986).

[33] E. Manousakis, Rev. Mod. Phys. **63**, 1 (1991).

[34] W. Brenig, Phys. Rep. **251**, 153 (1995).

[35] E. M. McCarron, M. A. Subramanian, J. C. Calabrese, and R. L. Harlow, Mater. Res. Bull. **23**, 1355 (1988).

[36] H. Fröhlich and W. Heitler, Proc. Roy. Soc. (London) **A135**, 640 (1936).

[37] H. Sato, Prog. Theor. Phys. **13**, 119 (1955).

[38] D. L. Huber, Prog. Theor. Phys. **39**, 1170 (1968).

[39] D. L. Huber and J. S. Semura, Phys. Rev. **182**, 602 (1969).

[40] D. L. Huber, J. S. Semura, and G. Windsor, Phys. Rev. **186**, 534 (1969).

[41] D. Krueger, Phys. Rev. B **3**, 2348 (1971).

[42] C. Kittel and E. Abrahams, Rev. Mod. Phys. **25**, 233 (1953).

[43] T. Wolfram and J. Callaway, Phys. Rev. **130**, 2207 (1963).

[44] J. Callaway, Phys. Rev. **132**, 2003 (1963).

[45] K. Kawasaki, Prog. Theor. Phys. **29**, 801 (1963).

[46] C. M. Bhandari and G. S. Verma, Phys. Rev. **152**, 152 (1966).

[47] A. Kumar, Phys. Lett. **85A**, 173 (1981).

[48] A. Kumar, Phys. Rev. B **25**, 3369 (1982).

[49] A. Kumar, Phys. Lett. **87A**, 421 (1982).

[50] M. A. Continentino and R. P. Pacheco, Phys. Rev. B **32**, 3234 (1985).

[51] R. L. Douglass, Phys. Rev. **129**, 1132 (1963).

[52] D. Walton, J. E. Rives, and Q. Khalid, Phys. Rev. B **8**, 1210 (1973).

[53] H. Miike and K. Hirakawa, J. Phys. Soc. Jpn. **38**, 1279 (1975).

[54] J. V. Alvarez and C. Gros, Phys. Rev. Lett. **89**, 156603 (2002).

[55] E. Orignac, R. Chitra, and R. Citro, Phys. Rev. B **67**, 134426 (2003).

[56] K. Saito, Phys. Rev. B **67**, 064410 (2003).

[57] X. Zotos, Phys. Rev. Lett. **92**, 067202 (2004).

[58] C. Gros and J. V. Alvarez, Phys. Rev. Lett. **92**, 069704 (2004).

[59] E. Shimshoni, N. Andrei, and A. Rosch, Phys. Rev. B **68**, 104401 (2003).

[60] H. Castella, X. Zotos, and P. Prelovšek, Phys. Rev. Lett. **74**, 972 (1995).

[61] X. Zotos, F. Naef, and P. Prelovšek, Phys. Rev. B **55**, 11029 (1997).

[62] G. D. Mahan, *Many-Particle Physics*, Plenum Press, New York London, 1990.

[63] D. Forster, *Hydrodynamic Fluctuations, Broken Symmetry and Correlation Functions*, Addison-Wesley Publishing, Reading, Massachusetts, 1990.

[64] W. Kohn, Phys. Rev **133**, A171 (1964).

[65] Y. Ando, J. Takeya, D. L. Sisson, S. G. Doettinger, I. Tanaka, R. S. Feigelson, and A. Kapitulnik, Phys. Rev. B **58**, R2913 (1998).

[66] J. Takeya, I. Tsukada, Y. Ando, T. Masuda, and K. Uchinokura, Phys. Rev. B **62**, R9260 (2000).

[67] J. Takeya, I. Tsukada, Y. Ando, T. Masuda, K. Uchinokura, I. Tanaka, R. S. Feigelson, and A. Kapitulnik, Phys. Rev. B **63**, 214407 (2001).

[68] A. N. Vasil'ev, V. V. Pryadun, D. I. Khomskii, G. Dhalenne, A. Revcolevschi, M. Isobe, and Y. Ueda, Phys. Rev. Lett. **81**, 1949 (1998).

[69] M. Hofmann, T. Lorenz, A. Freimuth, G. S. Uhrig, H. Kageyama, Y. Ueda, G. Dhalenne, and A. Revcolevschi, Physica B **312-313**, 597 (2002).

[70] M. Hofmann, T. Lorenz, G. S. Uhrig, H. Kierspel, O. Zabara, A. Freimuth, H. Kageyama, and Y. Ueda, Phys. Rev. Lett. **87**, 047202 (2001).

[71] C. Hess, *Thermischer Transport in Übergangsmetalloxiden mit niedrigdimensionalen Ladungs- und Spinstrukturen*, Dissertation, Universität zu Köln, 2002.

[72] F. Heidrich-Meisner, *Wärmeleitfähigkeit niedrigdimensionaler Spinsysteme*, Diplomarbeit, Technische Universität Braunschweig, 2001.

[73] P. Prelovšek and X. Zotos, AIP Conf. Proc. **629**, 161 (2002).

[74] T. Niemeyer and H. van Vianen, Phys. Lett. **34A**, 401 (1971).

[75] X. Zotos, Phys. Rev. Lett. **82**, 1764 (1999).

[76] S. Glocke, *Elektrische Leitfähigkeit wechselwirkender quantenmechanischer Vielteilchensysteme bei endlichen Temperaturen*, Diplomarbeit, Universität Dortmund, 2002.

[77] A. Klümper, private communication.

[78] A. Klümper and K. Sakai, J. Phys. A **35**, 2173 (2002).

[79] B. Shastry and B. Sutherland, Phys. Rev. Lett. **65**, 243 (1990).

[80] C. I. Kane and M. P. A. Fisher, Phys. Rev. Lett. **76**, 3192 (1996).

[81] P. Jordan and E. Wigner, Z. Phys. **47**, 631 (1928).

[82] K. Sakai and A. Klümper, J. Phys. A **36**, 11617 (2003).

[83] X. Zotos and P. Prelovšek, Phys. Rev. B **53**, 983 (1996).

[84] B. N. Narozhny, A. J. Millis, and N. Andrei, Phys. Rev. B **58**, R2921 (1998).

[85] J. V. Alvarez and C. Gros, Phys. Rev. Lett. **88**, 077203 (2002).

[86] J. V. Alvarez and C. Gros, Phys. Rev. B **66**, 094403 (2002).

[87] S. Fujimoto and N. Kawakami, Phys. Rev. Lett. **90**, 197202 (2003).

[88] D. A. Rabson, B. N. Narozhny, and A. J. Millis, Phys. Rev. B **69**, 054403 (2004).

[89] F. Naef and X. Zotos, J. Phys. C **10**, L183 (1998).

[90] M. W. Long, P. Prelovšek, S. ElShawish, J. Karadamoglou, and X. Zotos, Phys. Rev. B **68**, 235106 (2003).

[91] K. Louis and C. Gros, Phys. Rev. B **67**, 224410 (2003).

[92] K. Sakai and A. Klümper, cond-mat/0410192.

[93] H. Castella and X. Zotos, Phys. Rev. B **54**, 4375 (1996).

[94] S. Kirchner, H. G. Evertz, and W. Hanke, Phys. Rev. B **59**, 1825 (1999).

[95] A. Rosch and N. Andrei, Phys. Rev. Lett. **85**, 1092 (2000).

[96] J. Karadamoglou and X. Zotos, Phys. Rev. Lett. **93**, 177203 (2004).

[97] N. Andrei, E. Shimshoni, and A. Rosch, AIP Conf. Proc. **695**, 315 (2004).

[98] S. Sachdev and R. N. Bhatt, Phys. Rev. B **41**, 9323 (1990).

[99] J. M. Luttinger, Phys. Rev. **135**, A1505 (1964).

[100] K. Saito, S. Takesue, and S. Miyashita, Phys. Rev. E **54**, 2404 (1996).

[101] K. Saito, Europhys. Lett. **61**, 34 (2002).

[102] K. Saito and S. Miyashita, J. Phys. Soc. Jpn. **71**, 2485 (2002).

[103] M. Michel, M. Hartmann, J. Gemmer, and G. Mahler, Eur. Phys. J B **34**, 325 (2003).

[104] J. Gemmer, M. Michel, and G. Mahler, Lect. Notes Phys. **657**, 221 (2005).

[105] M. Hartmann, G. Mahler, and O. Hess, Phys. Rev. Lett. **93**, 080402 (2004).

[106] M. Hartmann, G. Mahler, and O. Hess, Phys. Rev. E **70**, 066148 (2004).

[107] M. Hartmann and G. Mahler, cond-mat/0410526.

[108] A. Dhar, cond-mat/0210470.

[109] X. Zhou and M. Iwamoto, J. Phys. A **37**, 11123 (2004).

[110] J. M. Deutsch and O. Narayan, Phys. Rev. E **68**, 041203 (2003).

[111] S. Lepri, R. Livi, and A. Politi, Phys. Rev. E **68**, 067102 (2003).

[112] L. Yang and P. Grassberger, cond-mat/0306173.

[113] B. Li and J. Wang, Phys. Rev. Lett. **91**, 044301 (2003).

[114] A. Pereverzev, Phys. Rev. E **68**, 056124 (2003).

[115] B. Li, G. Casati, J. Wang, and T. Prosen, Phys. Rev. Lett. **92**, 254301 (2004).

[116] R. Metzler and I. M. Sokolov, Phys. Rev. Lett. **92**, 089401 (2004).

[117] V. N. Likhachev, J. Szavits-Nossan, and G. A. Vinogradov, cond-mat/0404223.

[118] L. W. Lee and A. Dhar, cond-mat/0410067.

[119] B. Li, J. Wang, and G. Casati, Phys. Rev. Lett. **93**, 184301 (2004).

[120] F. Meier and D. Loss, Phys. Rev. Lett. **90**, 167204 (2003).

[121] S. Datta, *Electronic Transport in Mesoscopic Systems*, Cambridge University Press, Cambridge, 1995.

[122] W. Brenig, Phys. Rev. B **56**, 2551 (1997).

[123] N. W. Ashcroft and N. D. Mermin, *Solid State Physics*, Saunders College Publishing, 1976.

[124] P. L. Taylor, *A Quantum Approach to the Solid State*, Prentice-Hall, Englewood Cliffs, New York, 1970.

[125] M. M. Zemljic and P. Prelovšek, Phys. Rev. B **71**, 085110 (2005).

[126] E. Dagotto, Rev. Mod. Phys. **66**, 763 (1994).

[127] D. J. Scalapino, S. R. White, and S. Zhang, Phys. Rev. B **47**, 7995 (1993).

[128] D. J. Scalapino, S. R. White, and S. Zhang, Phys. Rev. Lett. **68**, 2830 (1992).

[129] F. D. Haldane, Phys. Lett. **81A**, 153 (1981).

[130] H. Schulz, Phys. Rev. Lett. **64**, 2831 (1990).

[131] N. Kawakami and S. Yang, Phys. Rev. B **44**, 7844 (1991).

[132] A. Honecker, private communication.

[133] F. Schütz, P. Kopietz, and M. Kollar, Eur. Phys. J. B **41**, 557 (2004).

[134] F. Schütz, M. Kollar, and P. Kopietz, Phys. Rev. Lett. **91**, 017205 (2003).

[135] F. Schütz, M. Kollar, and P. Kopietz, Phys. Rev. B **69**, 035313 (2004).

[136] D. Schmeltzer, A. Saxena, A. R. Bishop, and D. L. Smith, cond-mat/0405659.

[137] T. Giamarchi and B. S. Shastry, Phys. Rev. B **51**, 10915 (1995).

[138] N. Byers and C. N. Yang, Phys. Rev. Lett. **7**, 46 (1961).

[139] P. F. Maldague, Phys. Rev. B **16**, 2437 (1977).

[140] D. Baeriswyl, C. Gros, and T. M. Rice, Phys. Rev. B **35**, 8391 (1987).

[141] X. Zotos, J. of Low Temp. Phys. **126**, 1185 (2002).

[142] M. Garst and A. Rosch, Europhys. Lett. **55**, 66 (2001).

[143] A. Rosch and N. Andrei, J. of Low Temp. Phys. **126**, 1195 (2002).

[144] T. Prosen, Phys. Rev. Lett. **80**, 1808 (1998).

[145] W. Brenig, Z. Phys. B **89**, 187 (1992).

[146] P. Mazur, Physica **43**, 533 (1969).

[147] M. Suzuki, Physica **51**, 277 (1971).

[148] M. Oshikawa, Phys. Rev. Lett. **90**, 236401 (2003), Phys. Rev. Lett. **91**, 109901(E) (2003).

[149] A. Klümper, Lect. Notes Phys. **645**, 349 (2004).

[150] D. Poilblanc, T. Ziman, J. Bellissard, F. Mila, and G. Montambaux, Europhys. Lett. **22**, 537 (1993).

[151] B. N. Narozhny, Phys. Rev. B **54**, 3311 (1996).

[152] K. Fabricius and B. M. McCoy, Phys. Rev. B **57**, 8340 (1998).

[153] C. Hess, C. Baumann, and B. Büchner, J. Mag. Mag. Mat. **290-291**, 322 (2005).

[154] C. Hess, H. ElHaes, P. Ribeiro, G. Roth, B. Büchner, U. Ammerahl, and A. Revcolevschi, (unpublished).

[155] B. C. Sales, R. Jin, and D. Mandrus, cond-mat/0401154.

[156] A. V. Sologubenko and H. R. Ott, *in: "Strong Interactions in Low Dimensions"*, chapter 12, Physics and Chemistry of Materials with Low-Dimensional Structures, Kluwer Academic Publishers, 2004.

[157] H. Ibach and I. Lüth, *Festkörperphysik*, Springer-Verlag, Berlin, Heidelberg, New York, 1995.

[158] A. V. Rozhkov and A. L. Chernyshev, cond-mat/0407257.

[159] A. V. Rozhkov and A. L. Chernyshev, Phys. Rev. Lett. **94**, 087201 (2005).

[160] K. Kumagai, S. Tsuji, M. Kato, and Y. Koike, Phys. Rev. Lett. **78**, 1992 (1997).

[161] K. Magishi, S. Matsumoto, Y. Kitaoka, K. Ishida, K. Asayama, M. Uehara, T. Nagata, and J. Akimitsu, Phys. Rev. B **57**, 11533 (1998).

[162] R. S. Eccleston, M. Uehara, J. Akimitsu, H. Eisaki, N. Motoyama, and S. Uchida, Phys. Rev. Lett. **81**, 1702 (1998).

[163] S. Katano, T. Nagata, J. Akimitsu, M. Nishi, and K. Kakurai, Phys. Rev. Lett. **82**, 636 (1999).

[164] B. Shastry and B. Sutherland, Physica B **108**, 1069 (1981).

[165] K. Kudo, T. Noji, Y. Koike, T. Nishizaki, and N. Kobayashi, J. of Low Temp. Phys. **131**, 725 (2003).

[166] K. Kudo, T. Noji, Y. Koike, T. Nishizaki, and N. Kobayashi, J. Phys. Soc. Jpn. **72**, 2551 (2003).

[167] A. V. Sologubenko, R. Dell'Amore, H. R. Ott, and P. Millet, Eur. J. Phys. B **42**, 549 (2004).

[168] M. Nishi, O. Fujita, and J. Akimitsu, Phys. Rev. B **50**, 6508 (1994).

[169] J. Riera and A. Dobry, Phys. Rev. B **51**, 16098 (1995).

[170] K. Fabricius, A. Klümper, U. Löw, B. Büchner, T. Lorenz, G. Dhalenne, and A. Revcolevschi, Phys. Rev. B **57**, 1102 (1998).

[171] I. A. Zaliznyak, H. Woo, T. G. Perring, C. L. Broholm, C. D. Frost, and H. Takagi, Phys. Rev. Lett. **93**, 087202 (2004).

[172] N. Motoyama, H. Eisaki, and S. Uchida, Phys. Rev. Lett. **76**, 3212 (1996).

[173] H. Suzuura, H. Yasuhara, A. Furusaki, N. Nagaosa, and Y. Tokura, Phys. Rev. Lett. **76**, 2579 (1996).

[174] T. Ami, M. K. Crawford, R. L. Harlow, Z. R. Wang, D. C. Johnston, Q. Huang, and R. W. Erwin, Phys. Rev. B **51**, 5994 (1995).

[175] I. Tsukada, Y. Sasago, K. Uchinokura, A. Zheludev, S. Maslov, G. Shirane, K. Kakurai, and E. Ressouche, Phys. Rev. B **60**, 6601 (1999).

[176] M. Takigawa, T. Asano, Y. Ajiro, and M. Mekata, Phys. Rev. B **52**, R13087 (1995).

[177] M. Matsuda, K. Katsumata, R. S. Eccleston, S. Brehmer, and H.-J. Mikeska, Phys. Rev. B **62**, 8903 (2000).

[178] M. Windt, M. Grüninger, T. Nunner, C. Knetter, K. P. Schmidt, G. Uhrig, T. Kopp, A. Freimuth, U. Ammerahl, B. Büchner, and A. Revcolevschi, Phys. Rev. Lett. **87**, 127002 (2001).

[179] S. M. Hayden, G. Aeppli, R. Osborn, A. D. Taylor, T. G. Perring, S.-W. Cheong, and Z. Fisk, Phys. Rev. Lett. **67**, 3622 (1991).

[180] X. F. Sun, S. Komiya, and Y. Ando, Phys. Rev. B **67**, 184512 (2003).

[181] B. C. Sales, M. D. Lumsden, S. E. Nagler, D. Mandrus, and R. Jin, Phys. Rev. Lett. **88**, 095901 (2002).

[182] G. Liu and J. Greedan, J. Solid State Chem. **114**, 499 (1995).

[183] C. Knetter, A. Bühler, E. Müller-Hartmann, and G. S. Uhrig, Phys. Rev. Lett. **85**, 3958 (2000).

[184] U. Ammerahl, *Einkristallherstellung und physikalische Eigenschaften niedrigdimensionaler Kuprate: Spin-Ketten, -Leitern und -Ebenen*, Dissertation, Universität zu Köln, 2000.

[185] T. Osafune, N. Motoyama, H. Eisaki, and S. Uchida, Phys. Rev. Lett. **78**, 1980 (1997).

[186] T. Osafune, N. Motoyama, H. Eisaki, S. Uchida, and S. Tajima, Phys. Rev. Lett. **82**, 1313 (1999).

[187] N. Nücker, M. Merz, C. A. Kuntscher, S. Gerhold, S. Schuppler, R. Neudert, M. S. Golden, J. Fink, D. Schild, S. Stadler, V. Chakarian, J. Freeland, Y. U. Idzerda, K. Conder, M. Uehara, T. Nagata, J. Goto, J. Akimitsu, N. Motoyama, H. Eisaki, S. Uchida, U. Ammerahl, and A. Revcolevschi, Phys. Rev. B **62**, 14384 (2000).

[188] L. P. Regnault, J. P. Boucher, H. Moudden, J. E. Lorenzo, A. Hiess, U. Ammerahl, G. Dhalenne, and A. Revcolevschi, Phys. Rev. B **59**, 1055 (1999).

[189] M. Matsuda, T. Yosihama, K. Kakurai, and G. Shirane, Phys. Rev. B **59**, 1060 (1999).

[190] U. Ammerahl, B. Büchner, L. Colonescu, R. Gross, and A. Revcolevschi, Phys. Rev. B **62**, 8630 (2000).

[191] M. Uehara, T. Nagata, J. Akimitsu, H. Takahashi, N. Mori, and K. Kinoshita, J. Phys. Soc. Jpn. **65**, 2764 (1996).

[192] M. Isobe, T. Ohta, M. Onoda, F. Izumi, S. Nakano, J. Q. Li, Y. Matsui, E. Takayama-Muromachi, T. Matsumoto, and H. Hayakama, Phys. Rev. B **57**, 613 (1998).

[193] E. Dagotto, J. Riera, and D. Scalapino, Phys. Rev. B **45**, 5744 (1992).

[194] J. Callaway and H. C. von Baeyer, Phys. Rev. **120**, 1149 (1960).

[195] C. Hess, private communication.

[196] M. Troyer, H. Tsunetsugu, and D. Würtz, Phys. Rev. B **50**, 13515 (1994).

[197] B. Normand and T. M. Rice, Phys. Rev. B **56**, 8760 (1997).

[198] K. R. Thurber, K. M. Shen, A. W. Hunt, T. Imai, and F. C. Chou, Phys. Rev. B **67**, 094512 (2003).

[199] N. Nücker, C. Hess et al., unpublished.

[200] K. M. Shen, K. R. Thurber, A. W. Hunt, T. Imai, and F. C. Chou, Physica B **259-261**, 1032 (1999).

[201] H.-H. Klauss, W. Wagener, M. Hillberg, W. Kopmann, H. Walf, F. J. Litterst, M. Hücker, and B. Büchner, Phys. Rev. Lett. **85**, 4590 (2000).

[202] E. Benckiser, M. Grüninger, T. S. Nunner, T. Kopp, C. Sekar, and G. Krabbes, Magnetic excitations in the low-dimensional quantum spin systems $CaCu_2O_3$ and $Ba_2Si_3O_4Cl_2$, Verhandlungen der DPG Frühjahrstagung 2004, 08.-12.03.2004, Regensburg, Germany, 2004.

[203] I. V. Golosovsky, A. G. Gukasov, V. A. Polyakov, D. I. Zhigunov, and I. A. Zobkalo, J. Phys. C **11**, 6959 (1999).

[204] J. Qin, S. Feng, F. Yuan, and W. Y. Chen, Phys. Lett. **335A**, 477 (2005).

[205] J. Qin, Y. Song, S. Feng, and W. Y. Chen, Phys. Rev. B **65**, 155117 (2002).

[206] P. Ribeiro, C. Hess, P. Reutler, G. Roth, and B. Büchner, J. Mag. Mag. Mat. **290-291**, 334 (2005).

[207] C. Teske and H. Müller-Buschbaum, Z. Anorg. Allg. Chem. **371**, 325 (1969).

[208] C. Teske and H. Müller-Buschbaum, Z. Anorg. Allg. Chem. **379**, 234 (1970).

[209] T. M. Rice, S. Gopalan, and M. Sigrist, Europhys. Lett. **23**, 445 (1993).

[210] S. R. White and I. Affleck, Phys. Rev. B **54**, 9862 (1996).

[211] L. D. Faddeev and L. A. Takhtajan, Phys. Lett. **85A**, 375 (1981).

[212] J. des Cloizeaux and J. J. Pearson, Phys. Rev. **128**, 2131 (1962).

[213] P. Ribeiro, private communication.

[214] F. D. Haldane, Phys. Lett. **93A**, 464 (1983).

[215] E. S. Sørensen and I. Affleck, Phys. Rev. Lett. **71**, 1633 (1993).

[216] D. Loss and D. L. Maslov, Phys. Rev. Lett. **74**, 178 (1995).

[217] S. Sachdev and K. Damle, Phys. Rev. Lett. **78**, 943 (1997).

[218] K. Damle and S. Sachdev, Phys. Rev. B **57**, 8307 (1998).

[219] S. Fujimoto, J. Phys. Soc. Jpn. **68**, 2810 (1999).

[220] S. Fujimoto, J. Phys. Soc. Jpn. **69**, 2714 (2000).

[221] S. Sachdev and K. Damle, J. Phys. Soc. Jpn. **69**, 2712 (2000).

[222] R. M. Konik, Phys. Rev. B **68**, 104435 (2003).

[223] M. Takigawa, N. Motoyama, H. Eisaki, and S. Uchida, Phys. Rev. Lett. **76**, 4612 (1996).

[224] K. B. Lyons, P. A. Fleury, J. P. Remeika, A. S. Cooper, and T. J. Negran, Phys. Rev. B **37**, 2353 (1988).

[225] G. Aeppli, S. M. Hayden, H. A. Mook, Z. Fisk, S.-W. Cheong, D. Rytz, J. P. Remeika, G. P. Espinosa, and A. S. Cooper, Phys. Rev. Lett. **62**, 2052 (1989).

[226] S. M. Hayden, G. Aeppli, H. A. Mook, S.-W. Cheong, and Z. Fisk, Phys. Rev. B **42**, 10220 (1990).

[227] T. Thio, T. R. Thurston, N. W. Preyer, P. J. Picone, M. A. Kastner, H. P. Jenssen, D. R. Gabbe, C. Y. Chen, R. J. Birgeneau, and A. Aharony, Phys. Rev. B **38**, 905 (1988).

[228] R. Coldea, S. M. Hayden, G. Aeppli, T. G. Perring, C. D. Frost, T. E. Mason, S.-W. Cheong, and Z. Fisk, Phys. Rev. Lett. **86**, 5377 (2001).

[229] X. F. Sun, Y. Kurita, T. Suzuki, S. Komiya, and Y. Ando, Phys. Rev. Lett. **92**, 047001 (2004).

[230] B. Keimer, R. J. Birgeneau, A. Cassanho, Y. Endoh, M. A. Kastner, and G. Shirane, Z. Phys. B **373**, 91 (1993).

[231] W. Brenig and A. P. Kampf, Phys. Rev. B **43**, 12914 (1991).

[232] H. Anapa, K. Berggold, K. Kordonis, M. Kriener, J. Baier, T. Lorenz, A. Freimuth, and S. Barilo, Thermal conductivity of the layered cuprates R_2CuO_4 with R = Pr, Nd, Sm, Eu and Gd, Verhandlungen der DPG Frühjahrstagung 2004, 08.-12.03.2004, Regensburg, Germany, 2004.

[233] M. Hase, I. Terasaki, and K. Uchinokura, Phys. Rev. Lett. **70**, 3651 (1993).

[234] G. Castilla, S. Chakravarty, and V. J. Emery, Phys. Rev. Lett. **75**, 1823 (1995).

[235] K. Nomura and K. Okamoto, J. Phys. Soc. Jpn. **62**, 1123 (1993).

[236] M. Saint-Paul, G. Reményi, N. Hegmann, P. Monceau, G. Dhalenne, and A. Revcolevschi, Phys. Rev. B **52**, 15298 (1995).

[237] H. Kageyama, K. Onizuka, T. Yamauchi, Y. Ueda, S. Hane, H. Mitamura, T. Goto, Yoshimura, and K. Kosuge, J. Phys. Soc. Jpn. **68**, 1821 (1999).

[238] H. Kageyama, M. Nishi, N. Aso, K. Onizuka, T. Yosihama, K. Nukui, K. Kodama, K. Kakurai, and Y. Ueda, Phys. Rev. Lett. **84**, 5876 (2000).

[239] K. Kudo, T. Noji, Y. Koike, T. Nishizaki, and N. Kobayashi, J. Phys. Soc. Jpn. **73**, 3497 (2004).

[240] T. Ma and S. Feng, Phys. Lett. **328A**, 212 (2004).

[241] G. I. Dzhaparidze and A. A. Nersesyan, JETP Lett. **27**, 334 (1978).

[242] V. L. Pokrovsky and A. L. Talapov, Phys. Rev. Lett. **42**, 65 (1979).

[243] D. C. Cabra, A. Honecker, and P. Pujol, Phys. Rev. B **58**, 6241 (1998).

[244] M. P. Grabowski and P. Matthieu, Ann. Phys. **243**, 299 (1996).

[245] M. Takahashi, *Thermodynamics of One-Dimensional Solvable Models*, Cambridge University Press, Cambridge, 1999.

[246] S. Fujimoto and N. Kawakami, J. Phys. A **31**, 465 (1998).

[247] J. Benz, T. Fukui, A. Klümper, and C. Scheeren, cond-mat/0502516 (unpublished).

[248] S. Eggert, I. Affleck, and M. Takahashi, Phys. Rev. Lett. **73**, 332 (1994).

[249] A. Klümper and D. C. Johnston, Phys. Rev. Lett. **84**, 4701 (2000).

[250] N. M. R. Peres, P. D. Sacramento, D. K. Campbell, and J. M. P. Carmelo, Phys. Rev. B **59**, 7382 (1999).

[251] P. Prelovšek, S. ElShawish, X. Zotos, and M. W. Long, Phys. Rev. B **70**, 205129 (2004).

[252] R. M. Fye, M. J. Martins, D. J. Scalapino, J. Wagner, and W. Hanke, Phys. Rev. B **44**, 6909 (1991).

[253] G. S. Uhrig and D. Vollhardt, Phys. Rev. B **52**, 5617 (1995).

[254] N. M. R. Peres, R. G. Dias, P. D. Sacramento, and J. M. P. Carmelo, Phys. Rev. B **61**, 5169 (2000).

[255] T. Giamarchi, Phys. Rev. B **44**, 2905 (1991).

[256] T. Giamarchi and A. J. Millis, Phys. Rev. B **46**, 9325 (1992).

[257] C. I. Kane and M. P. A. Fisher, Phys. Rev. Lett. **68**, 1220 (1992).

[258] T. Giamarchi, T. Nattermann, and P. LeDoussal, cond-mat/0403487.

[259] P. Lou, W.-C. Wu, and M.-C. Chang, Phys. Rev. B **70**, 064405 (2004).

[260] J. Bonča, J. P. Rodriguez, J. Ferrer, and K. S. Bedell, Phys. Rev. B **50**, 3415 (1994).

[261] N. Laflorencie, S. Capponi, and E. S. Sørensen, Eur. Phys. J B **24**, 77 (2001).

[262] S.-J. Gu, V. M. Pereira, and N. M. R. Peres, Phys. Rev. B **66**, 235108 (2002).

[263] A. Honecker, http://www-public.tu-bs.de:8080/˜honecker/software/diagonalize.html.

[264] K. Kudo and T. Deguchi, Phys. Rev. B **68**, 052510 (2003).

[265] K. Kudo and T. Deguchi, Phys. Rev. B **69**, 132404 (2004).

[266] K. Kudo and T. Deguchi, cond-mat/0409761.

[267] P. DiFrancesco, P. Mathieu, and D. Sénéchal, *Conformal Field Theory*, Springer-Verlag, New York, 1999.

[268] T. Giamarchi, *Quantum Physics in One Dimension*, Clarendon Press, Oxford, 2004.

[269] S. Rao and D. Sen, *Field Theories in Condensed Matter Physics*, IOP Publishing, Bristol, 2002, cond-mat/0005492.

[270] H. Schulz, *in: Correlated Fermions and Transport in Mesoscopic Systems, edited by T. Martin, G. Montambaux, and J. Tran Thanh Van*, Editions Frontières, Gif-sur-Yvette, 1996.

[271] A. Klümper, Z. Phys. B **91**, 507 (1993).

[272] N. M. Bogoliubov, A. G. Izergin, and V. E. Korepin, Nucl. Phys. B **275**, 687 (1986).

[273] P. R. Hammar, M. B. Stone, D. H. Reich, C. Broholm, P. J. Gibson, M. M. Turnbull, C. P. Landee, and M. Oshikawa, Phys. Rev. B **59**, 1008 (1999).

[274] S. Qin, M. Fabrizio, L. Yu, M. Oshikawa, and I. Affleck, Phys. Rev. B **56**, 9766 (1997).

[275] D. C. Cabra, private communication.

[276] J.-M. vanden Broeck and L. W. Schwartz, Siam. J. Math. Anal. **10**, 658 (1979).

[277] J. des Cloizeaux and M. Gaudin, J. Math. Phys. **7**, 1384 (1966).

[278] T. Lorenz, M. Hofmann, M. Grüninger, A. Freimuth, G. S. Uhrig, M. Dumm, and M. Dressel, Nature **418**, 614 (2002).

[279] M. Greven, R. J. Birgeneau, and U.-J. Wiese, Phys. Rev. Lett. **77**, 1865 (1996).

[280] G. S. Uhrig, F. Schönfeld, M. Laukamp, and E. Dagotto, Eur. Phys. J. B **7**, 67 (1999).

[281] M. C. Cross and D. S. Fisher, Phys. Rev. B **19**, 402 (1979).

[282] M. C. Cross, Phys. Rev. B **20**, 4606 (1979).

[283] T. Barnes, E. Dagotto, J. Riera, and E. S. Swanson, Phys. Rev. B **47**, 3196 (1993).

[284] M. Reigrotzki, H. Tsunetsugu, and T. M. Rice, J. Phys. C **6**, 9235 (1994).

[285] A. B. Harris, Phys. Rev. B **7**, 3166 (1973).

[286] G. S. Uhrig, Phys. Rev. Lett. **79**, 163 (1997).

[287] J. Oitmaa, R. R. P. Singh, and W. Zheng, Phys. Rev. B **54**, 1009 (1996).

[288] T. Barnes and J. Riera, Phys. Rev. B **50**, 6817 (1994).

[289] R. Chitra, S. Pati, H. R. Krishnamurthy, D. Sen, and S. Ramasesha, Phys. Rev. B **52**, 6581 (1995).

[290] J. C. Bonner and H. W. J. Blöte, Phys. Rev. B **25**, 6959 (1982).

[291] Z. G. Soos, S. Kuwajima, and J. E. Mihalick, Phys. Rev. B **32**, 3124 (1985).

[292] T. Barnes, J. Riera, and D. A. Tennant, Phys. Rev. B **59**, 11384 (1999).

[293] S. R. White, R. Noack, and D. J. Scalapino, Phys. Rev. Lett. **73**, 886 (1994).

[294] F. D. Haldane, Phys. Rev. B **25**, 4925 (1982).

[295] K. Okamoto and N. Nomura, Phys. Lett. **169A**, 433 (1992).

[296] C. Majumdar and D. Ghosh, J. Math. Phys. **10**, 1399 (1969).

[297] D. G. Shelton, A. A. Nersesyan, and A. M. Tsvelik, Phys. Rev. B **53**, 8521 (1996).

[298] E. Orignac, private communication.

[299] A. Bühler, N. Elstner, and G. S. Uhrig, Eur. Phys. J. B **16**, 475 (2000).

[300] W. Brenig, Phys. Rev. B **56**, 14441 (1997).

[301] T. Einarsson and H. Schulz, Phys. Rev. B **51**, 6151 (1995).

[302] W. Götze and P. Wölfle, Phys. Rev. B **6**, 1226 (1972).

[303] B. C. Watson, V. N. Kotov, M. W. Meisel, D. W. Hall, G. E. Granroth, W. T. Montfrooij, S. E. Nagler, D. A. Jensen, R. Backov, M. A. Petruska, G. E. Fanucci, and D. R. Talham, Phys. Rev. Lett. **86**, 5168 (2001).

[304] M. J. Konstantinović, Z. V. Popović, M. Isobe, and Y. Ueda, Phys. Rev. B **61**, 15185 (2000).

[305] T. Ohama, M. Isobe, and Y. Ueda, J. Phys. Soc. Jpn. **70**, 1801 (2001).

[306] P. W. Anderson, Phys. Rev. **109**, 1492 (1958).

[307] B. Kramer and A. MacKinnon, Rep. Prog. Phys. **56**, 1469 (1993).

[308] G. Bouzerar, D. Poilblanc, and G. Montambaux, Phys. Rev. B **49**, 8258 (1994).

[309] K. J. Runge and G. T. Zimanyi, Phys. Rev. B **49**, 15212 (1994).

[310] H. Mori, Phys. Rev. B **51**, 12943 (1995).

[311] K. Damle, O. Motrunich, and D. A. Huse, Phys. Rev. Lett. **84**, 3434 (2000).

[312] O. Motrunich, K. Damle, and D. A. Huse, Phys. Rev. B **63**, 134424 (2001).

[313] T. M. R. Byrnes, R. J. Bursill, H.-P. Eckle, C. J. Hamer, and A. W. Sandvik, Phys. Rev. B **66**, 195313 (2002).

[314] C. A. Doty and D. S. Fisher, Phys. Rev. B **45**, 2167 (1992).

[315] D. S. Fisher, Phys. Rev. B **50**, 3799 (1994).

[316] N. Laflorencie and H. Rieger, Eur. Phys. J. B **40**, 201 (2004).

[317] N. Laflorencie, H. Rieger, A. W. Sandvik, and P. Henelius, Phys. Rev. B **70**, 054430 (2004).

[318] A. P. Young and H. Rieger, Phys. Rev. B **53**, 8486 (1996).

[319] P. Henelius and S. M. Girvin, Phys. Rev B **57**, 11457 (1998).

[320] F. Igloi, R. Juhasz, and H. Rieger, Phys. Rev. B **61**, 11552 (2000).

[321] C. Jurecka and W. Brenig, Phys. Rev. B **61**, 14307 (2000).

[322] O. P. Sushkov and V. Kotov, Phys. Rev. Lett. **81**, 1941 (1998).

[323] V. N. Kotov, O. P. Sushkov, and R. Eder, Phys. Rev. B **59**, 6266 (1999).

[324] S. Trebst, H. Monien, C. J. Hamer, W. Zheng, and R. R. P. Singh, Phys. Rev. Lett. **85**, 4373 (2000).

[325] W. Zheng, C. J. Hamer, R. R. P. Singh, S. Trebst, and H. Monien, Phys. Rev. B **63**, 144410 (2001).

[326] T. S. Nunner and T. Kopp, Phys. Rev. B **69**, 104419 (2004).

[327] M. Sigrist and A. Furusaki, J. Phys. Soc. Jpn. **65**, 2385 (1996).

[328] H. Manaka, I. Yamada, and H. A. Katori, Phys. Rev. B **63**, 104408 (2001).

[329] C. P. Landee, M. M. Turnbull, C. Galeriu, J. Giantsidis, and F. M. Woodward, Phys. Rev. B **63**, 100402(R) (2001).

[330] R. Melin, Y.-C. Lin, P. lajko, H. Rieger, and F. Igloi, Phys. Rev. B **65**, 104415 (2002).

[331] E. Yusuf and K. Yang, Phys. Rev. B **65**, 224428 (2002).

[332] E. Orignac and T. Giamarchi, Phys. Rev. B **57**, 5812 (1998).

[333] M. Steiner, M. Fabrizio, and A. O. Gogolin, Phys. Rev. B **57**, 8290 (1998).

[334] R. A. Hyman, K. Yang, R. N. Bhatt, and S. M. Girvin, Phys. Rev. Lett. **76**, 839 (1996).

[335] A. V. Chubukov, Pis‘ma Zh. Eksp. Teor. Fiz. **49**, 108 (1989), [JETP Lett. **49**, 129 (1989)].

[336] A. V. Chubukov and T. Jolicoeur, Phys. Rev. B **44**, 12050 (1991).

[337] O. A. Starykh, M. E. Zhitomirsky, D. I. Khomskii, R. R. P. Singh, and K. Ueda, Phys. Rev. Lett. **77**, 2558 (1996).

[338] R. White, *Quantum Theory of Magnetism*, McGraw-Hill, New York, 1970.

[339] M. Arlego, *Quantum Magnetism in Low-Dimensional Systems*, Dissertation, Universidad Nacional de La Plata, Argentina, 2004.

[340] W. Zheng, V. N. Kotov, and J. Oitmaa, Phys. Rev. B **57**, 11439 (1998).

[341] S. Doniach and E. H. Sondheimer, *Green's Functions for Solid State Physicists*, Imperial College Press, London, 1998.

[342] R. J. Elliott, J. A. Krumhansl, and P. L. Leath, Rev. Mod. Phys. **46**, 465 (1974).

[343] V. N. Kotov, O. P. Sushkov, Z. Weihong, and J. Oitmaa, Phys. Rev. Lett. **80**, 5790 (1998).

[344] C. Jurecka, *Excitations in Electron Systems with Strongly Dimerized Ground States*, Dissertation, Technische Universität Braunschweig, Cuiviller-Verlag, Göttingen, 2001.

[345] N. Cavadini, W. Henggeler, A. Furrer, H.-U. Güdel, K. Krämer, and H. Mutka, Eur. Phys. J. B **7**, 519 (1999).

[346] A. Oosawa, T. Kato, H. Tanaka, K. Kakurai, M. Müller, and H.-J. Mikeska, Phys. Rev. B **65**, 094426 (2002).

[i] F. Heidrich-Meisner, A. Honecker, D. C. Cabra, and W. Brenig, Phys. Rev. B **66**, 140406(R) (2002).

[ii] C. Hess, B. Büchner, U. Ammerahl, L. Colonescu, F. Heidrich-Meisner, W. Brenig, and A. Revcolevschi, Phys. Rev. Lett. **90**, 197002 (2003).

[iii] F. Heidrich-Meisner, A. Honecker, D. C. Cabra, and W. Brenig, Phys. Rev. B **68**, 134436 (2003).

[iv] F. Heidrich-Meisner, A. Honecker, D. C. Cabra, and W. Brenig, Phys. Rev. Lett. **92**, 069703 (2004).

[v] F. Heidrich-Meisner, A. Honecker, D. C. Cabra, and W. Brenig, J. Mag. Mag. Mat. **272-276**, 890 (2004).

[vi] M. Arlego, W. Brenig, D. C. Cabra, F. Heidrich-Meisner, A. Honecker, and G. Rossini, Phys. Rev. B **70**, 014436 (2004).

[vii] M. Arlego, W. Brenig, D. C. Cabra, F. Heidrich-Meisner, A. Honecker, and G. Rossini, to appear in Physica B, cond-mat/0411751 (unpublished).

[viii] F. Heidrich-Meisner, A. Honecker, D. C. Cabra, and W. Brenig, to appear in Physica B, cond-mat/0406378 (unpublished).

[ix] F. Heidrich-Meisner, A. Honecker, and W. Brenig, submitted to Phys. Rev. B, cond-mat/0408529 (unpublished).

Acknowledgment

It is my pleasure to acknowledge advice and support from several persons who have influenced this work.

First of all, I thank my supervisor Prof. Dr. W. Brenig for suggesting the very interesting and challenging problem of transport, for his constant interest in the progress of this work, his constructive criticism, and his support during the last years.

It is impossible to honor the impact that Dr. Andreas Honecker had on this work. I am indebted to him for countless discussions, for sharing his numerical expertise with me, for his infinite exactness, for having always found time to answer my questions, and for having been a good colleague.

Furthermore there are a number of scientific collaborations which I personally have highly enjoyed and from which this project has certainly strongly benefitted.

Prof. Dr. Daniel Cabra has taken over the task to introduce me to the field of bosonization. I also thank him for agreeing to review this thesis. Furthermore, I thank him as well as Prof. Dr. Gerardo Rossini and Dr. Marcelo Arlego for the very fruitful collaboration during several stages of this thesis. I had the privilege to enjoy their and their institutions' great hospitality during my visits at Universidad Nacional de La Plata, ENS Lyon, and Université Strasbourg.

On the experimental side, I am grateful for the delighting and successful collaboration with Prof. Dr. Bernd Büchner's group (Christoph Baumann, Dr. Christian Heß, Dr. Rüdiger Klingeler, Patrick Ribeiro, and others). In particular, I owe Dr. Christian Heß a great deal for his patience in explaining experimental aspects to me, for proofreading several of our manuscripts, countless discussions, and valuable suggestions.

It is a pleasure to acknowledge the exchange of results with Prof. Dr. Andreas Klümper and Dr. Kazumitsu Sakai and fruitful discussions on transport in the XXZ chain.

From Dr. Jochen Gemmer and Mathias Michael, I learned quite a bit about their approach to transport problems, and I enjoyed many conversations as well as my visit to Osnabrück.

Finally, I thank Dr. Thomas Lorenz for enlightening discussions on experimental aspects related to thermal transport.

Within the Institut für Theoretische Physik, I have experienced a stimulating environment for research and a very pleasant atmosphere with my present and former colleagues: Dr. Marcelo Arlego, Thorsten Bagdonat, Alexander Bößwetter, Andreas Friedrich, Dr. Noboru Fukushima, Jean-Mathias Grießmeier, Simon Grossjohann, Matthias Grzeschik, Dr. Andreas Honecker, Dr. Christoph Jurecka, Peter Kuehs, Dr. Marcus Renner, and Sven Simon. Special thanks go to Dr. Marcus Renner for solving so many of my soft- and hardware problems and for introducing me to the miracles of Linux and Solaris, and to Thorsten Bagdonat for many refreshing breaks and for all the discussions we had about exercise sheets. Renate Strassek, our institute's secretary, has helped me often with all the administration stuff, and she has supplied me with a good bunch of chocolate as well.

Dr. Marcelo Arlego, Jean-Mathias Grießmeier, Dr. Christian Heß, Dr. Andreas Honecker, and Ole Krüger have shared the tedious task of proofreading this thesis, for which I am deeply indebted to them.

Finally, I thank all my out-of-physics friends, my mother, my sister, and Kerstin for standing all my quircs and for their support. They have helped me to finish this work, too, and I thank them for being by my side.

Lebenslauf

Persönliche Daten

Name:	Fabian Heidrich-Meisner
Geburtsdatum:	22.07.1975
Geburtsort:	Hannover
Familienstand:	ledig
Staatsbürgerschaft:	deutsch

Schulbildung

1981 – 1982	Grundschule Ohle, Plettenberg
1982 – 1985	Grundschule Garssen, Celle
1985 – 1987	Orientierungsstufe Vorwerk, Celle
1987 – 1994	Kaiserin-Auguste-Viktoria-Gymansium, Celle
9. Jun. 1994	Abitur

Zivildienst

Aug. 1994 – Okt. 1995	Zivildient beim Deutschen Paritätischen Wohlfahrtsverband, Celle.

Studium

1995 – 2001	Studium der Physik an der TU Braunschweig
18. Sept. 1997	Vordiplom
13. Jul. – 17. Sept. 1999	Sommerstudent am CERN, Genf
Jul. 2000 – Jun. 2001	Diplomarbeit: *Wärmeleitfähigkeit niedrigdimensionaler Spinsysteme*, betreut von Prof. Dr. W. Brenig
1. Aug. 2001	Diplom in Physik
Seit Dez. 2001	Anfertigung der vorliegenden Dissertation, betreut von Prof. Dr. W. Brenig

Arbeitsverhältnisse

Okt. 1996 – Jun. 2001	Studentische Hilfskraft an verschiedenen Instituten der TU Braunschweig (mit Unterbrechungen)
Okt. – Nov. 2001	Wissenschaftliche Hilfskraft an den Instituten für Theoretische bzw. Mathematische Physik der TU Braunschweig
Seit Dez. 2001	Wissenschaftlicher Mitarbeiter am Institut für Theoretische Physik der TU Braunschweig

Weitere Veröffentlichungen

C. Hess, C. Baumann, U. Ammerahl, B. Büchner, F. Heidrich-Meisner, W. Brenig und A. Revcolevschi: *Magnon heat transport in* $(Sr,Ca,La)_{14}Cu_{24}O_{41}$, Phys. Rev. B **64**, 184305 (2001).